Deposition of Commercially Pure Titanium Powder Using Low Pressure Cold Spray and Pulsed Gas Dynamic Spray for Aerospace Repairs

By

Mathieu Bolduc

Thesis submitted to the Department of Mechanical Engineering
in partial fulfillment of the requirements for the degree of
Master of Applied Science (Engineering)

University of Ottawa

Ottawa, Ontario, Canada

January 17th, 2012

Abstract

The objective of this study is to investigate the feasibility of depositing 1.5 mm thick titanium coatings, as a repair method for aerospace Ti-6Al-4V substrates, using two new commercially available processes: Low Pressure Cold Spray (LPCS) and Pulsed Gas Dynamic Spray (PGDS). The coatings produced were examined and characterized by their porosity level, microhardness, adhesion strength, particle flattening ratio, wipe tests, fracture surface type and wear tests. Phases and chemical composition were determined using X-Ray diffraction analysis and energy dispersive spectroscopy, respectively. It was found that both spraying processes are capable of producing dense, hard and oxide-free coatings using specific parameters. Finally, as a first step towards repair implementation of these processes, damages were simulated on Ti-6Al-4V samples, which were successfully repaired with low porosity and high hardness levels. The feasibility of repairs was confirmed, the next step will consist in qualification testing to assess coating performances under real life application.

Acknowledgements

I would like to take this opportunity to thank Dr. Bertrand Jodoin for giving me the opportunity of pursuing graduate studies with such an interesting project. Thanks Dr. Jodoin for giving us such a great learning environment under your supervision. This amazing lab has been my home for the last two years, and I will surely miss it!

Special thanks to Dr. Mohammed Yandouzi for his help and Secondary Eletron Microscope (SEM) training. Your knowledge of material science and different point of view was precious to our lab filled with engineers.

I would also like to thank the technical officers in the Department of Mechanical Engineering machine shop at the University of Ottawa. Thank you John Perrins for your knowledge and James MacDermid for your advice and for making our machining projects a reality.

Thanks to my lab mates, for your insights, help and unrelated discussions: Jamil Assaad, Jean-Michel Roy, Daniel MacDonald, Jean-Louis Pelletier, Rubén Fernández, Patrick Trahan, Tyler Samson, Antoine Bacciochini as well as Deliand Goudl.

A special thank you to my parents, brother and sister who always believed in me and encouraged me throughout my projects and studies. I would also like to thank a special someone who coached me through my graduate studies. Finally to my beloved fiancé Malika, thank you for supporting me and always being there for me.

Table of Contents

List of Tables

List of Figures

Chapter 1. Introduction

1.1. Background

Over the past 20 years, the demand for higher performance parts and components has been continuously rising in the aerospace industry. Different coating technologies have been developed in order to meet these increasing needs. The objectives of the coatings are to either restore or improve the performance and properties of the component surface to be coated. Coatings are applied to increase a wide range of properties such as wear resistance, thermal insulation and oxidation resistance to name a few [1]. The thermal spray technology started in the 19th century, when Schoop presented a technique consisting in heating and melting metallic particles and propelling them at high velocities towards a substrate. The molten particles impact, deform and solidify onto the substrate, creating solid splats. The repeated process of the impacting particles sticking to the substrate ultimately forms a stratified structure coating. Since the first patent on thermal spray by Schoop in 1882, there has been a constant evolution of the deposition processes and their applications. Nowadays, thermal spray technology is composed of multiple techniques such as detonation spray, wire arc spray, plasma spray, flame spray, high-velocity oxygen-fuel (HVOF) and cold gas dynamic spray (CGDS). Other more specialized techniques with distinctive features can be derived from these main processes. Using the different thermal spray processes, a wide variety of feedstock materials can be deposited such as pure metals, alloys, polymers, cermets and ceramics. Coating thickness can be as thin as 25 μm and up to a few millimeters thick, depending on the application requirements and on the thermal spray process used.

The overlay coatings typically produced by thermal spray processes such as detonation spraying, HVOF, plasma spraying, flame spraying and wire arc spraying involve a molten or semi-molten state of the particles during the coating process. This state is achieved by the high heat produced through a combustion process, a plasma jet or an electric arc. The particles are then propelled when introduced into a high velocity gas stream. However, the particle velocity obtained varies greatly with the spraying process. The particles accelerate through drag forces resulting from the velocity difference between the propellant gas and the

particles, before impacting onto the substrate where they flatten and solidify to build up a coating.

The physical, chemical and mechanical properties of the coatings are strongly affected by the microstructural defects introduced during the deposition process [2], depicted in Figure 1.1. These detrimental microstructural defects are usually cracks, pores and oxides [2]. Their presence depends on the nature of the sprayed material, the spraying process and the spraying parameters chosen [2]. Most of these defects are generally due to the elevated temperatures required to melt the particles and form the coatings. The formation of cracks and pores are generally attributed to the lack of particles deformation upon substrate impact or thermal contraction upon solidification [3]. Low particle deformation levels can be attributed to the use of non-optimized spraying parameters. Thus, lower particles ductility and lower particle velocities decrease the particles deformation level and their ability to successfully comply with the uneven surface, affecting the final coating performances. Other defects, such as oxidation, generally occurs when heat sensitive materials are used in conjunction with a high temperature spraying process as it is a temperature dependant phenomenon. However, oxidation also requires the presence of oxygen in addition to the high process temperature. Therefore, it can be avoided by spraying in an inert environment; for instance, being under vacuum or in an inert gas chamber [4]. The use of inert propellant gases and lower process temperatures can also help reduce particle in-flight oxidation, as well as during coating formation. When oxidation is not avoided, the coatings properties decreases drastically; for example the tensile strength of stainless steel 316L decreases with higher oxide content and its elongation to failure drops from 40% with 2 wt.% oxide to 3% with 23 wt.% [5].

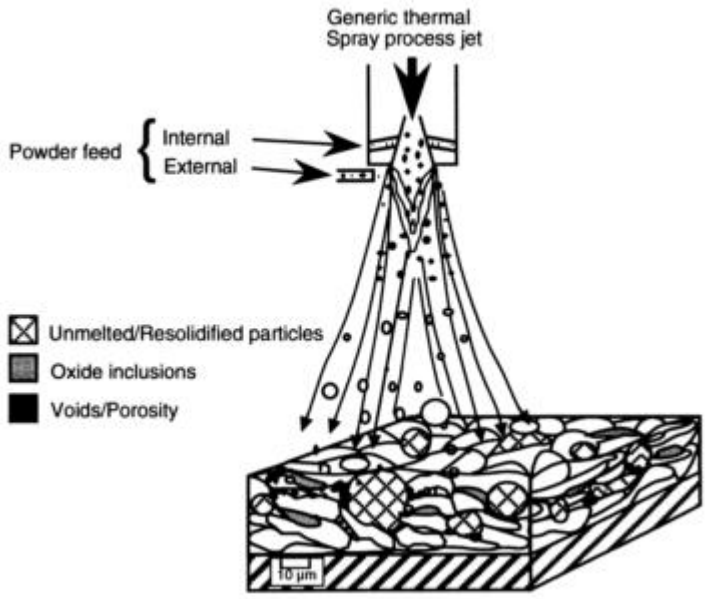

Figure 1.1 Schematic of a thermal spray coating process and coating formation from impacting particles on the substrate [6]

Further technology advancement, with the goal of reducing oxidation levels and reaching higher propellant gas velocities for enhanced deformation, has more recently led to new spray processes: vacuum plasma spray (VPS), warm spray (WS) and Cold Gas Dynamic Spray (CGDS). In VPS, the whole spraying process is conducted in a vacuum chamber, leading to lower coating oxidation and deposition of heat sensitive powder such as titanium [4]. In warm spray, a modified HVOF process, the propellant gas temperature is controlled and reduced by adding room temperature nitrogen into a post-combustion chamber before the spray nozzle [7]. Therefore, the deposition material is exposed to lower overall temperatures, considerably reducing oxidation levels.

In the late 1980's, CGDS was introduced as a new thermal spray process [8]. CGDS presented two major differences with other thermal spray processes addressing one of their major flaw: the high spraying temperatures. CGDS is considered to be an all solid state process since the gas temperatures used are always lower than the feedstock powder melting point. Each feedstock powder and substrate material combination has its own specific "critical particle velocity". The particles with sufficient impact velocity deform plastically upon impact with the substrate and adhere to create the typical coating microstructure [8] depicted in Figure 1.2.

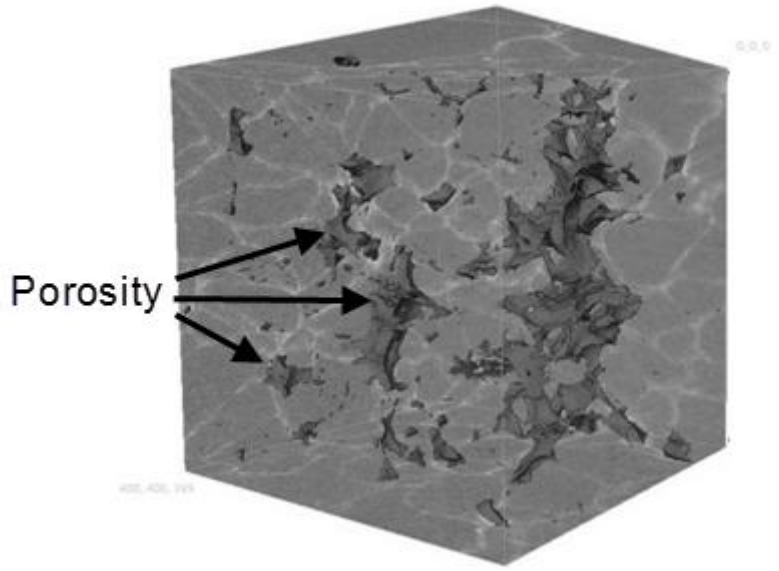

Figure 1.2 Three-dimension schematic of a CGDS coating showing porosity in between deformed particles [9]

CGDS relies solely on the sprayed particle kinetic energy and plastic deformation to form coatings. It minimizes oxidation, grain growth and tensile residual stresses [8]. The coatings produced using CGDS present a reduced number of defects, hence better mechanical and chemical coating properties. Using nitrogen or helium gas, particle velocities from 300 m/s up to 1200 m/s can be achieved with the acceleration of the propellant gas into a de Laval nozzle [2,10–15]. A distinction is made between two variants of the CGDS techniques: High Pressure Cold Spray (HPCS) and Low Pressure Cold Spray (LPCS). This nomenclature is based on the local gas pressure level at the powder injection port: before the throat (high pressure side) or after the throat (low pressure side). In summary, the use of lower spray temperature and inert propellant gases in HPCS or LPCS allows for the deposition of heat sensitive materials such as copper, magnesium and titanium [16–21] with low oxide and porosity levels.

The Pulsed Gas Dynamic Spray (PGDS) process has been developed and patented at the University of Ottawa Cold Spray Laboratory (Canada) [22]. This process is a variation of the CGDS process which uses a pulsed flow (unsteady flow) instead of a continuous flow (steady-state flow). Each pulse creates a shockwave that heats and propels the particles towards the substrate. The PGDS process experiences limited transfer of the gas thermal energy into kinetic energy since no de Laval nozzle is used. The particles are simultaneously

accelerated and heated up while travelling into a high intensity heat zone just behind the shockwave front [23]. The accelerated particles remain warm (although kept at temperatures below melting point) throughout the spraying process which promotes a high powder ductility and enhances powder deformation upon impact onto the substrate [24]. The PGDS process has shown its ability to spray hard materials [25,26] and the process has shown to keep the original powder phase [26]. Furthermore, this pulsing gas process could potentially lead to lower gas consumption than the continuous CGDS process. Thus, the PGDS system is a promising technique for deposition of heat sensitive materials.

Titanium is known for its high corrosion resistance as well as its superior strength to weight ratio. Particularly, titanium alloys have significantly higher performance than pure titanium, such as tensile strength. The most commonly used titanium alloy in the industry is Ti-6Al-4V grade 5. The potential weight savings by using titanium represents important improvements in term of energy efficiency and emission reductions for the automotive and aircraft industries [27]. For these reasons, the amount of titanium used commercially, especially in the aerospace field, has been rising constantly over the last decades [28]. However, titanium aerospace parts have currently no repair alternatives upon damage or wear. Replacement part prices are excessive due to the superior ingot and manufacturing costs of titanium [28]. As such, the aerospace industry is looking for a low cost, quick field reparation technique. LPCS and PGDS could be potential repair solutions [29]. As discussed previously, other techniques, such as traditional HVOF and Plasma Spray, involve high temperature gases in a non-inert spraying environment prohibiting these techniques to be used to deposit thermally sensitive materials. The coatings produced are either of bad quality or, worst, no coating build-up due to the in-flight oxidation of the powder. In the case of VPS, the deposition can be made under either vacuum or inert environment but the related costs for such equipment or procedure are usually too high for this to be a viable solution. For the HVOF, the addition of a mixing chamber with nitrogen (WS) can lead to intermediate gas temperatures and reduced oxidation. However, the reactive nature of the combusting gases used during the process makes it more susceptible of creating oxides, compared to the oxygen-free gases used in LPCS and PGDS techniques. For these reasons, LPCS and PGDS processes are promising techniques for deposition of heat sensitive materials such as titanium.

Commercially pure (CP) titanium is commonly referred to as pure titanium in the thermal spray industry. This name is employed in view of the fact that the material is not chemically pure, meaning that other elements are present inside its microstructure but at very low concentrations, usually below 1%. As such, CP titanium refers to a 99% purity level titanium.

1.2. Motivation of Research and Objectives

The present work was inspired by the potential capacity of LPCS and PGDS to deposit dense coatings made of heat sensitive materials. These processes have many advantages over other spraying techniques such as no masking required due to localised deposition and a much simpler and controllable gas heating method. In LPCS and PGDS, the gas heat is generated by an electrical heater rather than by the combustion of fuel and oxygen (Flame spray, HVOF and WS). The advantages of such a heating system are numerous: no hazardous gases involved, no combustion to control, characterize and optimize, no combustion products, the possibility of using inert driver gases such as nitrogen and helium, and lower gas temperatures are also possible. The lower process temperatures may lead to lower particle oxidation considered as coating defects making the LPCS and PGDS suitable for deposition of pure titanium onto titanium substrates. To date, many studies have been performed using LPCS and PGDS processes to spray a wide variety of materials but very few involved the deposition of titanium coatings.

In response to the industry needs, this project aims to be a first step towards the development of a repair method for titanium-based aerospace parts. The coating thickness required to perform such repairs is larger (around 1500 μm) than usual coatings (below 500 μm) used for corrosion or wear protection. This work aims at successfully depositing and characterizing pure titanium coatings onto Ti-6Al-4V substrates using commercially available LPCS and PGDS processes. In order to achieve this objective, the following procedure was developed:

1. Investigate the potential of LPCS and PGDS processes for deposition of CP titanium powder onto Ti-6Al-4V substrates using commercially available systems.

2. Optimize the spraying conditions for both LPCS and PGDS processes to obtain high quality CP titanium coatings based on coatings porosity level and microhardness.
3. Evaluate optimized CP titanium coating properties produced using both systems in terms of porosity level, microhardness, particle deformation level, adhesion strength and wear performance and compare with other potential repair techniques such as Warm Spray and High Pressure Cold Spray.
4. Investigate the adhesion mechanisms by single splat analysis and surface fracture analysis and compare with other potential repair techniques such as Warm Spray and High Pressure Cold Spray.
5. Identify and quantify oxygen/nitrogen content inside the sprayed coatings using X-Ray Diffraction analysis (XRD) and Energy Dispersive Spectroscopy (EDS) techniques and compare with other potential repair techniques such as Warm Spray (WS) and High Pressure Cold Spray (HPCS).
6. Assess the feasibility of repairing a simulated damaged part using both techniques and verify the repair microstructure.

1.3. Thesis Outline

The content of this research work has been divided and organized into eight chapters. Chapter 1 presents a brief introduction of the research topic and relevant background information, the motivation of the project as well as some details about the main objectives of the thesis.

Chapter 2 provides a detailed literature review and description of the principal thermal spray processes and the latest technology advancements. The principal spraying techniques considered in this study, LPCS and PGDS, are described more thoroughly. Finally, a summary of similar studies is presented.

In Chapter 3, a full description of the research objectives is presented in order to provide an overview of the procedure followed for the development of new aerospace parts repair techniques and further considerations related to the subject.

Chapter 4 provides key information on the coatings investigation approach. A description of the experimental equipment and procedures that were used throughout this study is presented. As such, the feedstock materials and processing, the descriptions of the two spraying systems available at the University of Ottawa Cold Spray Laboratory (LPCS and PGDS), the preparation of sprayed coatings for microstructural analysis and the coating characterization techniques are all described.

Chapter 5 describes the characterization of the different powders used in this work. The as-received powders in addition to different morphologies and size distributions obtained through sieving and milling are presented.

Chapter 6 presents the approach and methodology used in this study for the parameter optimization phase. The different spraying parameters of each system are presented into different categories. The importance of the various parameters on coatings microstructure are determined and the parameters are optimized based on coatings porosity level and microhardness. The list of optimized spray parameters, for each system, used throughout the rest of this study is presented.

Chapter 7 reports the results of the microstructural investigations and mechanical tests performed onto optimized CP titanium coatings produced by LPCS and PGDS techniques. Microstructural and mechanical properties such as porosity level, microhardness, particle deformation level, coating adhesion strength, single splat analysis, surface fracture analysis, element content analysis and wear performances of the coatings are examined and related to the coatings microstructure. The results are also compared to coatings produced using other thermal spraying devices, obtained from the literature. This chapter concludes on the feasibility of repairing a simulated damage part and the microstructural evaluation of the repair.

Finally, the conclusion provides a summary of the findings reported in this thesis and presents final remarks on the research. Recommendations and suggestions for future work are also provided.

Chapter 2. Literature Review

This chapter presents a broad review of the literature relevant to this research project. To begin with, an introduction to the thermal spray deposition processes is presented. Then, the emphasis is placed on the processes used throughout this work, namely the LPCS and the PGDS processes. The different powder manufacturing methods are presented as well as the resulting powder morphologies.

2.1. Thermal Spray Processes

As introduced in Chapter 1, after the invention of the first thermal spray process by Schoop in the 19th century, research and development efforts have led to various other coating deposition processes. For convenience, these techniques have been classified historically into categories with respect to their heat source used to melt or soften the material to be deposited: plasma, electric arc and combustion. The latter thermal spray category is called kinetic spraying, pointing at the main aspect of this technique, particle kinetic energy. Each category can also be divided into the sub-categories presented in Figure 2.1, based on specific characteristics of the processes.

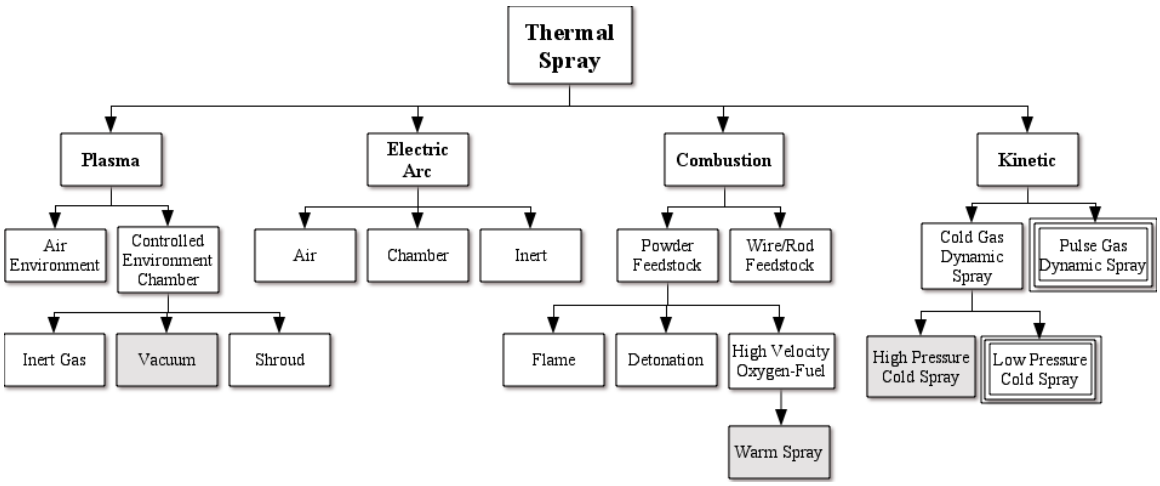

Figure 2.1 Thermal spraying process categories and their divisions; current titanium deposition processes shown in gray and techniques with triple borders are the ones used throughout this study (adapted from [6])

Each sub-category represents either improvement on or variations of the main category. The processes highlighted in gray in Figure 2.1 (Vacuum Plasma Spray, Warm Spray and HPCS) represent the promising thermal spray techniques to produce commercially pure titanium

coatings and the two with triple borders are the processes investigated throughout this study (LPCS and PGDS). The following sub-sections of this chapter describe each process category and the microstructural features of the coatings produced by these techniques.

2.1.1. Plasma Spraying

In this technique, the ionized gas stream (plasma jet) used is capable of melting most materials with temperatures ranging from 5,000 to 25,000°C [30]. In order to ionise the process gas and turn it into a plasma state, the gas flows through a direct current electric arc generated between an anode and a cathode where it heats up, by the Joule effect. Other energy sources such as radio-frequency, inductively-coupled or microwave discharges and alternate current arcs can be used to generate plasmas. The plasma gas expands and accelerates through a nozzle reaching high velocities ranging from 600 to 2,500 m/s [31]. Typically, plasma gases are mixtures of Ar, He, N_2 and H_2 carefully controlled to ensure uniform momentum and heat transfer to the particles to be sprayed. The feedstock powder is usually injected at the exit of the plasma torch as depicted in Figure 2.2.

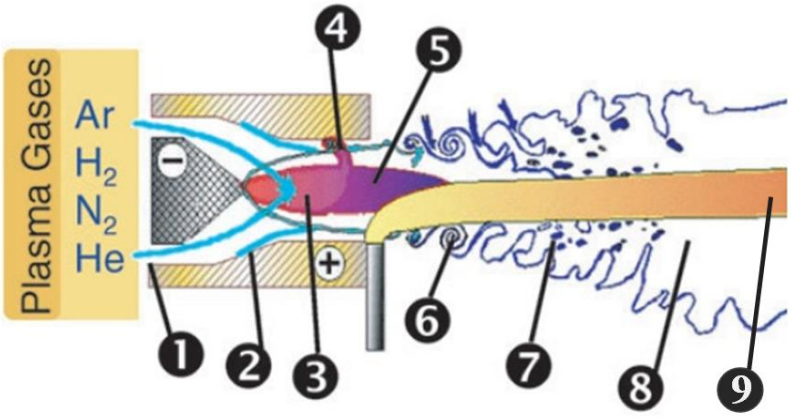

Figure 2.2 Schematic of a DC arc spray plasma torch. 1-plasma forming gas injection, 2-cold boundary layer, 3-Arc column, 4-connecting arc column, 5-plasma jet exiting nozzle, 6-large scale eddies, 7-surrounding atmosphere bubbles, 8-plasma plume, 9-powder injection (adapted from [31])

In this process, the injected particles would ideally reach high velocities and be completely molten prior to the impact with the substrate. However, as the particle velocity increases, the particles dwell time inside the plasma decreases, reducing heat transfer to the particles. Furthermore, the wide particle diameter range of the feedstock powders amplifies the difficulty of achieving the fully molten state as smaller particles are quickly accelerated out of the hot region. The molten particles, achieving velocities ranging from 10 to 600 m/s

[31], flatten and quickly solidify to form a coating. These coatings are generally porous and contain oxides as the particles can react with the oxygen from the environment after being heated by the plasma gases. To overcome this issue, plasma spray can be performed in an environmentally controlled chamber. The chamber can either be filled with an inert gas such as argon or be maintained under vacuum, reducing the amount of oxygen present to form oxides. While conventional plasma spray generally greatly oxidizes titanium feedstock powder in-flight resulting in no coating build-up, one study has shown that VPS process is able to produce Ti-6Al-4V coatings [4]. The very high temperatures of plasma spray combined with the high reactivity of titanium increases the complexity of spraying such coatings. The difficulty of creating a perfect vacuum to ensure that no oxidation occurs explains the lack of studies on titanium plasma spraying.

2.1.2. High Velocity Oxygen-Fuel (HVOF)

As its name suggests, the processes falling under this category obtain their thermal and kinetic energies by the combustion of fuel. Many variations of the gun configuration have been tested over the years, using different cooling media (air or water), combustion location (throat of chamber, shape, chamber length) and powder injection point (axial or radial). Different combustion gases (hydrogen, propane, acetylene or kerosene) can be used to reach different pressures and temperatures. The main gas stream is accelerated to supersonic velocity using a converging-diverging nozzle [32]. In HVOF, the gas velocity can reach up to 1,900 m/s and gas temperatures up to around 3,300K [33]. The particles are accelerated and particle velocities up to 1,000 m/s have been measured [2]. The particles are heated during the exposition to the hot gas and are either semi-molten or molten prior to impact with the substrate. A schematic cross-section view of the HVOF technique is presented in Figure 2.3.

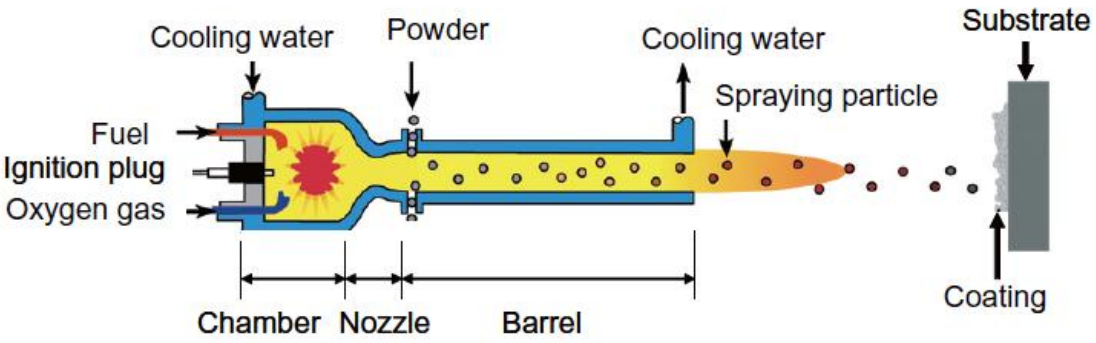

Figure 2.3 Schematic of HVOF spraying process [34]

Lately, some of the research focus in the thermal spray area has been on reducing the propellant gas temperature below the feedstock particle melting point to achieve lower oxide levels. A modified HVOF process known as Warm Spray (WS) was recently developed [34]. It consists in injecting nitrogen gas in a post-combustion mixing chamber located before the converging-diverging nozzle in order to reduce the gas temperature from 3000°C to 500°C [34]. This process has been used successfully to spray heat sensitive material such as titanium and polymers [7, 34]. A schematic cross-section of the Warm Spray technique is presented in Figure 2.4.

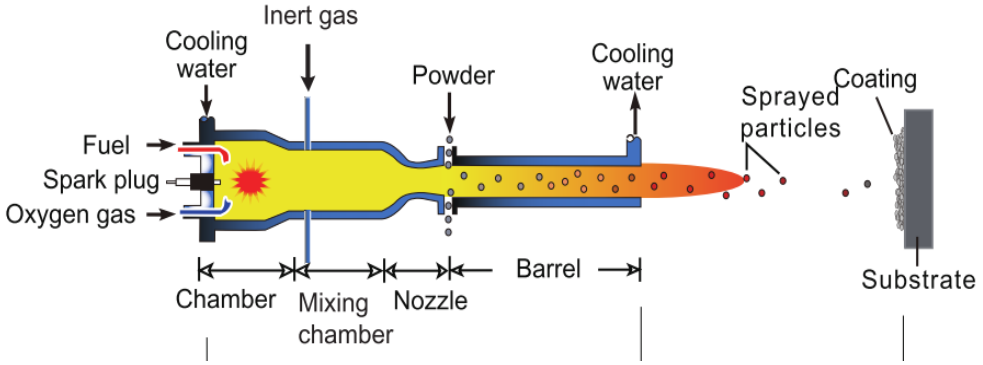

Figure 2.4 Schematic of the WS technique having an extra inert gas injection and a gas mixing chamber before the nozzle [34]

2.1.3. Kinetic Spray

The kinetic spraying processes rely on particle kinetic energy upon impact rather than thermal energy to deform the particles and produce coatings. Kinetic spray processes include Pulsed Gas Dynamic Spray (PGDS) and Cold Gas Dynamic Spray (CGDS) and processes derived from it: High Pressure Cold Spray (HPCS) and Low Pressure Cold Spray (LPCS). The lower thermal energy involved in these processes implies that the deposited particles retain a temperature below their melting point during the spraying process. As such, these processes are often referred to as solid state processes. In the CGDS processes, a converging-diverging nozzle is used to accelerate the gas stream to supersonic velocities by transforming the gas thermal energy into kinetic energy. Upon impact, the particles deform and adhere to the substrate. The powder injection is done either before the nozzle throat for the HPCS technique or after for the LPCS technique. The particles are accelerated by the drag forces and reach velocities between 200 m/s and 1,200 m/s [35]. Upon impact with the substrate, the particles deform and slowly build up a coating.

A variation of the CGDS process, called Laser-assisted CGDS [36], has been explored in the recent years. In this process, the setup is essentially the same as CGDS with the addition of a powerful laser to help deposition. The laser is used to increase the local temperature of the substrate, directly at the deposition location under the nozzle. The substrate microhardness is reduced due to its high temperature improving the deformation upon particle impact. However, the addition of the laser requires extensive safety equipment and operator training, a major drawback for process implementation in the industry. Furthermore, the high temperatures reached from the laser heating could be detrimental for heat treated substrates such as Ti-6Al-4V alloy.

In the PGDS technique, the main jet is pulsed using a quick opening and closing valve to create trains of shockwaves. In this case, no converging-diverging nozzle is required to accelerate the gas. The specific properties of the shockwave are described in Sections 2.3.3.1 and 2.3.3.2 which lead to higher particle temperatures throughout the spraying process. This higher temperature enhances the powder ductility and reduces the critical velocity, defined in Section 2.4, required to deposit a specific powder. Using these techniques, a large spectrum

of materials has been deposited. More details about the LPCS and PGDS techniques are presented in the upcoming sections.

2.1.4. Summary of Selected Thermal Spray Processes

The operating parameters of each process can be varied, but only to a certain extent due to various system limitations. Figure 2.5 presents the ranges of particle temperature and velocity that can be obtained by the different thermal spray processes.

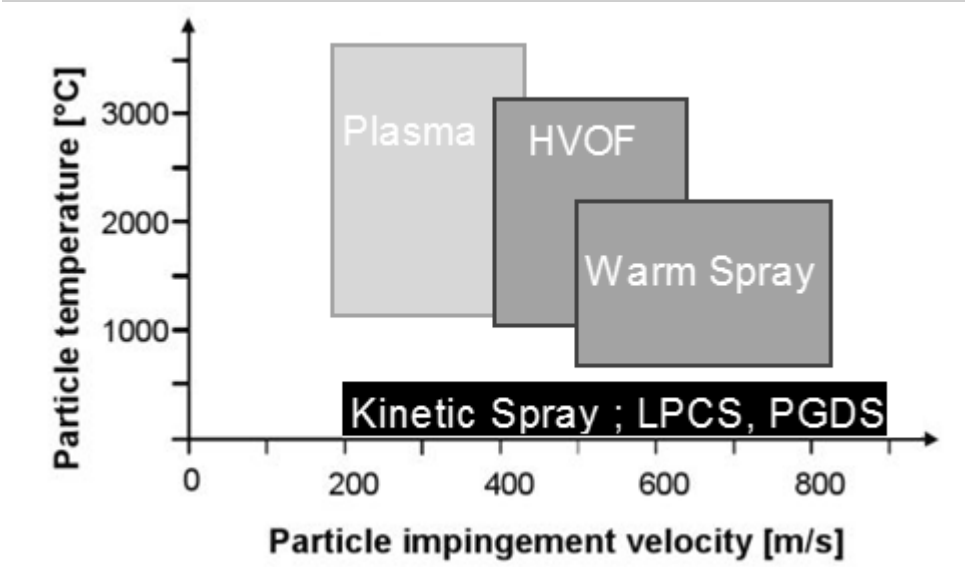

Figure 2.5 Ranges of particle temperature and velocity for different thermal spray processes (adapted from [37])

It can be seen from this figure that plasma spray process has the highest particle temperature and the lowest particle velocities. The complete opposite is observed for kinetic spraying processes, having low particle temperature and very high particle velocities. The combustion process lies between these two with moderate particle temperature and moderate particle velocities. The variety of particle temperature and particle velocity of the different processes makes them suitable for deposition of material of different natures.

As a result of the different particle temperatures and velocities of the various thermal spray processes, different microstructures are obtained upon deposition of the feedstock powders. Figure 2.6 illustrates various coatings produced by Warm Spray, Vacuum Plasma Spray and High Pressure Cold Spray.

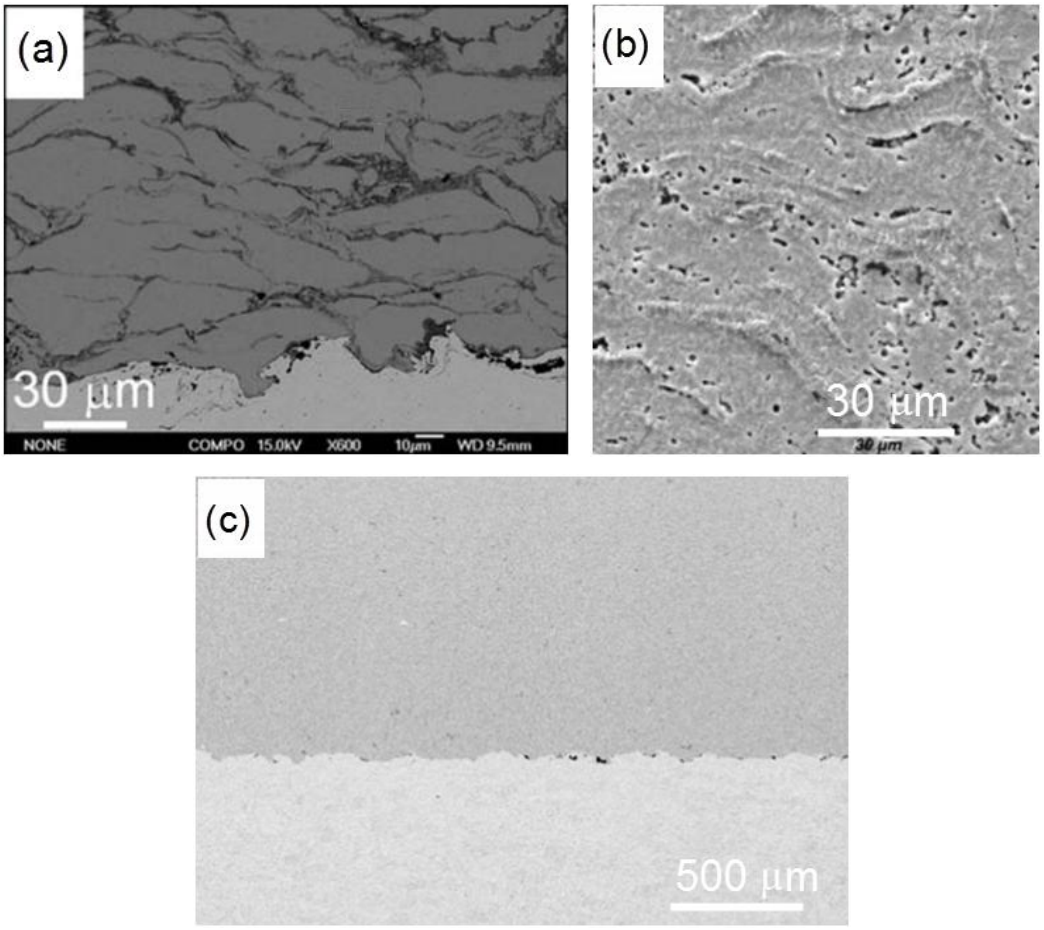

Figure 2.6 Different microstructures of (a) CP titanium coating using WS process [38]**, (b) Ti-6Al-4V coating VPS [4] and (c) CP titanium coating using HPCS process** [39]

As seen in Figure 2.6, coatings produced by WS can achieve high density levels. However, due to the nature of the gas used, the titanium powder can react with the gases and form oxidized coatings [38]. WS process has been developed fairly recently and the various properties such as adhesion strength are yet to be determined. Vacuum plasma spray can also reach low porosity level. The very high temperatures involved in plasma spray usually lead to powder oxidation for powders like titanium, thus very little literature can be found on such coatings [4]. Numerous studies have investigated the microstructure and mechanical properties of CP titanium coatings produced by HPCS, thus the coatings produced in this

work will be mainly compared with HPCS coatings. Typical HPCS coatings can reach high densities and their microhardness are slightly higher than the original powder due to plastic deformation. HPCS coatings typically present very low oxygen levels due to the inert nature of the gas used during the deposition process. The other kinetic spray processes (LPCS and PGDS) should produce coatings with comparable properties to HPCS, as they use similar processing gases and temperatures.

2.2. Cold Gas Dynamic Spraying (CGDS)

This section describes in more details the CGDS process, and more specifically the LPCS technique. The background of this invention is presented and followed by the distinction between HPCS and LPCS using schematics in the general process overview. Then, the basic gas dynamic principles employed by these techniques are explained in detail. Finally, the advantages and limitations of the LPCS are described.

2.2.1. Historical Background

The CGDS principle was found in the mid-1980s at the Institute of Theoretical and Applied Mechanics of the Siberian division of the Russian Academy of Science in Novosibirsk [27]. Researchers were conducting experiments in a supersonic wind tunnel adding solid tracer particles to simulate a two-phase flow around their aircraft models. After a short period, they observed that the metallic particles injected started to deposit onto the leading edges of the model [40]. Upon further investigations, it was found that aluminium particles would stick to the model if their velocities were above 400-450 m/s while bronze particles would erode the model [40]. Interest drove to a series of designs and ultimately, a system capable of accelerating particles up to velocities of 1,200 m/s was designed. This invention, the HPCS technique, was recognized as a technology advancement and patents were delivered in 1994 (USA) [8] and 1995 (Europe) [41]. A variant of this method, the LPCS technique, consisting in having the powder injected in the low pressure zone, after the throat, was developed only over the last two decades [42]. As of today, many commercial CGDS systems have been developed with different characteristics and advantages such as nozzle cooling.

2.2.2. General Process Overview of CGDS

Cold Gas Dynamic Spray is an all solid state process relying solely on the sprayed particle kinetic energy to form dense coatings. Using nitrogen or helium gas, particle velocities from 300 m/s up to 1,200 m/s can be achieved with the acceleration of the propellant gas through a converging-diverging nozzle [1, 9–14]. This technique accelerates particles above their critical velocity [43] by the conversion of thermal energy to kinetic energy through a de Laval nozzle. The critical velocity designation is described and explained in Section 2.4. In order to have more thermal energy to accelerate the gas to supersonic speeds, the gas is heated before entering the nozzle. The required heat is usually generated by an electrically resistive coil heater and the processing gas stays inert during the whole process, reducing the chances of contaminating the powder in-flight before deposition. The gas velocity at the nozzle exit is a function of the nozzle geometry, gas type, and gas stagnation pressure and temperature.

Up to now, the CGDS terminology has been widely used in journal papers and could have been more specific by using the terminology High Pressure Cold Spray (HPCS). The process typically called CGDS (or HPCS) is shown in Figure 2.7. The latest technique (Low Pressure Cold Spray, LPCS) involving a different powder injection site located after the throat, is schematically represented in Figure 2.8.

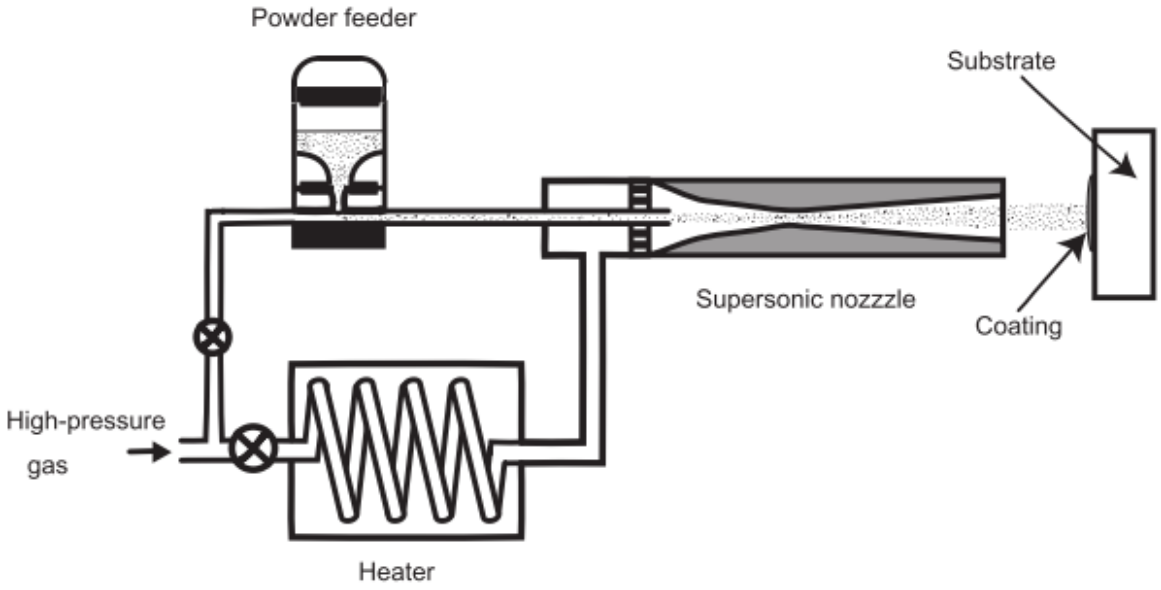

Figure 2.7 Schematic representation of HPCS system [34]

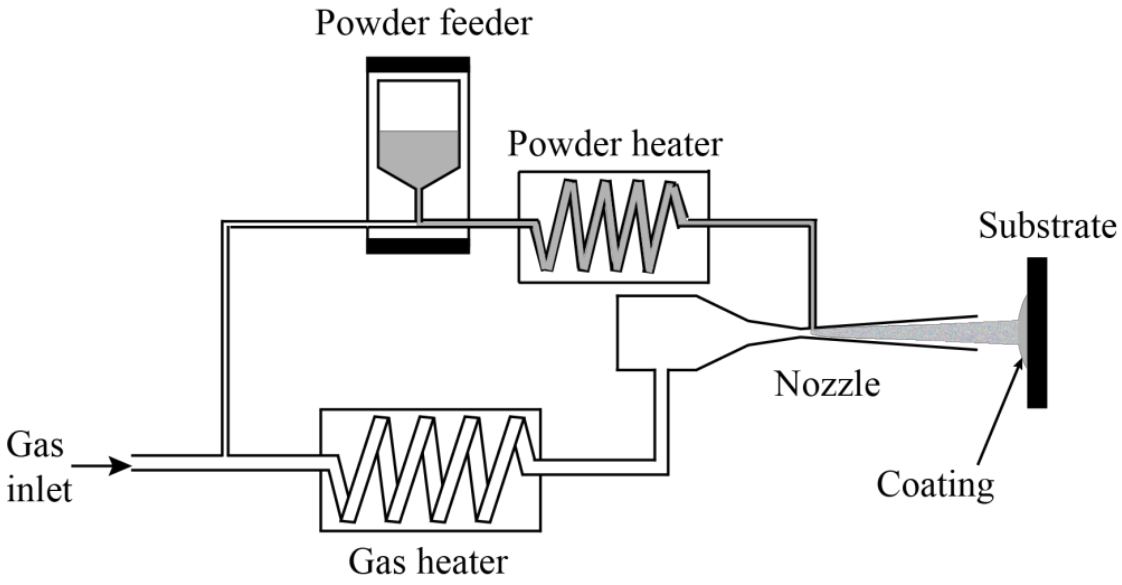

Figure 2.8 Schematic of the LPCS technique

In the HPCS system, the powder is fed under a slightly higher pressure than the operating pressure to create a gas stream that will carry the powder from the feeder to the nozzle assembly. In the LPCS technique, the required pressure inside the powder feeder canister to create the required powder flow is significantly lower than with the HPCS due to its location,

as the gas pressure drops significantly after the throat. The LPCS also has the advantage that the powder does not go through the nozzle throat, which can lead to clogging issues with the HPCS process.

2.2.3. Gas Dynamic Principles in LPCS

Since this work uses the LPCS technique, the fundamental gas dynamic principles involved in the LPCS deposition technique are presented in this section. As the principal characteristic of this process is kinetic energy, the gas dynamics principles governing the creation of a supersonic gas jet are described in the following sections. The acceleration of the particles within the high speed jet will also be explained.

2.2.3.1. Gas Dynamics Assumptions

In order to simplify significantly the complexity of the compressible fluid mechanics involved in the LPCS technique and easily determine the basic working principles, various assumptions are used. First, the gases used in LPCS are typically inert gases such as nitrogen and helium, it is therefore adequate to consider these fluids as calorically perfect gases, with no interactions between the gas particles. Secondly, the flow is assumed to be in a steady-state regime, which means that for a given position within the flow, there is no change in gas properties with respect to time. Thirdly, the flow is considered to be one-dimensional, meaning that the gas properties are uniform throughout a given cross-section of the nozzle. This assumption is acceptable as the change of fluid properties along the main axis varies greatly compared to small variations in the radial direction (considered to be negligible). Finally, it is assumed that there is no heat transfer with the environment (adiabatic flow) and that the flow is reversible, ignoring friction or viscous effect. However, while this assumption may not be valid for this case, since the supersonic flows produced are surely affected by viscous effect and friction, this qualifies the flow as an isentropic flow which will further help the simplifications. Although these assumptions highly simplify the gas dynamic equations describing the flow, each assumption will introduce an error in the final solution compared to the empirical results. However, the resulting equations provide a good first approximation and understanding of the nozzle flow.

2.2.3.2. Compressible Flow

In order to have a good understanding of the fluid flow, it is important to find a baseline that could be applied to any fluid and that would define the limits of what a compressible flow is in respect to the more commonly used incompressible flow. As such, for a flow to be considered compressible, a change in pressure δP must result in a considerable change in fluid density $\delta\rho$. The rate of change of the density in response to a change in pressure depends greatly on the fluid nature. For example, the change of density of water in reaction to a change of pressure is negligible in comparison to the density change of air for the same pressure variation. The speed of sound in a fluid is defined as an infinitesimal pressure wave and is closely related to the change in density with respect to pressure. This pressure wave, travelling in a fluid at the speed of sound c, induces a small increase in pressure dP, density $d\rho$ and velocity du of the fluid. By taking the pressure wave as the control system, the following result is derived from the continuity and conservation of momentum equations [44]:

$$c^2 = \left(\frac{dP}{d\rho}\right)_s \qquad \text{(Eq. 2.1)}$$

As Equation 2.1 indicates, the speed of sound has a direct relationship with the rate of change in pressure with respect to density. Thus, the speed of sound is an important parameter of compressible flows. As described earlier, mediums in which the speed of sound is high, such as water, will have to experience a very high variation of pressure to have an effect on the fluid density. From Equation 2.1, considering a perfect gas in an isentropic evolution ($\frac{P}{\rho^k} = constant$), the speed of sound can be written as:

$$c = \sqrt{kRT} \qquad \text{(Eq. 2.2)}$$

where k is the specific heat ratio (C_P/C_v), R is the specific gas constant and T is the fluid temperature. As such, Equation 2.2 shows that the speed of sound of a perfect gas is determined exclusively by the gas nature and temperature. Therefore, using this equation, the speed of sound in different gases can be calculated. Table 2.1 presents different gases that could be used in CGDS and considered due to their inert nature, high availability or high sound velocity.

Table 2.1 Speed of sound of various fluids at standard pressure and temperature

Fluid	Speed of Sound
Carbon Dioxide	269 m/s
Argon	322 m/s
Air	346 m/s
Nitrogen	351 m/s
Helium	1016 m/s
Hydrogen	1315 m/s

It can be noted that the speeds of sound in helium and hydrogen are very high, in comparison with the other gases. Even though they both represent excellent choices in terms of velocity, hydrogen is usually not used due to its high reactivity. Heavier gases, such as argon and carbon dioxide, were discarded due to their low specific heat ratios and specific gas constants which lead to low speeds of sound.

In compressible flows, the Mach number is a dimensionless quantity used to characterize the flow regime. It is given by the ratio between the flow speed (u) and the speed of sound (c), given by:

$$M = \frac{u}{c} = \frac{u}{\sqrt{kRT}} \qquad \text{(Eq. 2.3)}$$

The Mach number can be used to indicate the level of compressibility effects present in different flows. For a low Mach number (M<0.3), the flow can be considered incompressible, since a pressure change has only a mild effect on its density. When the Mach number is slightly higher (0.3<M<1), the flow is said to be subsonic and the compressibility effects are observed as a change of pressure induces a change of density. The flow is considered sonic when its velocity is equal to its speed of sound (M=1). The supersonic regime (M>1) is defined as a flow with a velocity higher than the speed of sound of the medium. In both subsonic and supersonic regimes, the compressibility effects of the gases must be considered during flow analysis.

2.2.3.3. Flow Through a Variable Cross-Sectional Area

Now that the flows can be sorted based on their Mach number, their behavior and properties as they go through converging or diverging geometry can be investigated. In this section, the

analysis of gas properties, for a flow with various velocities (subsonic and supersonic) through a cross-section of variable area, is carried out. In order to simplify the complex gas dynamics equations, the flow is assumed to be one-dimensional, steady and isentropic. Three governing equations must be considered to analyze the flow behavior: mass conservation, conservation of energy (1st law of thermodynamics) and 2nd law of thermodynamics. Upon simplification and combination of these equations, the following relations are obtained [44]:

$$-\frac{dA}{A} = \frac{du}{u}(1 - M^2) \qquad \text{(Eq. 2.4)}$$

$$\frac{dA}{A} = \frac{dP}{\rho u^2}(1 - M^2) \qquad \text{(Eq. 2.5)}$$

where A is the cross-sectional area. Using these two equations, the effect of the variation of the cross-sectional area can be determined in terms of flow velocity using Equation 2.4 and pressure using Equation 2.5. Different scenarios are possible: the Mach number can be either smaller or greater than 1 and the area change can either be increasing (diverging) or decreasing (converging). Therefore, four different possible scenarios are analyzed. For subsonic flows (M<1), Equation 2.4 shows that the change of flow velocity is inversely proportional to the change in cross-sectional area. Therefore, a subsonic flow experiencing a reduction in area (converging) will accelerate, whereas the flow will decelerate when going through a diverging section. In the case of supersonic flows (M>1), the term $(1-M^2)$ becomes negative in Equations 2.4 and 2.5. Therefore, the fluid behavior passing through different sections will be exactly reverse than for the subsonic flows. An increasing cross-sectionnal area will induce a flow acceleration while a converging section will lead to a flow deceleration. Using Equation 2.5, the variation in pressure to a change in cross-sectionnal area can be found. A graphical representation of the four different scenarios is given in Figure 2.9. Of note, the name nozzle is usually employed when the flow accelerates and diffuser when the flow decelerates.

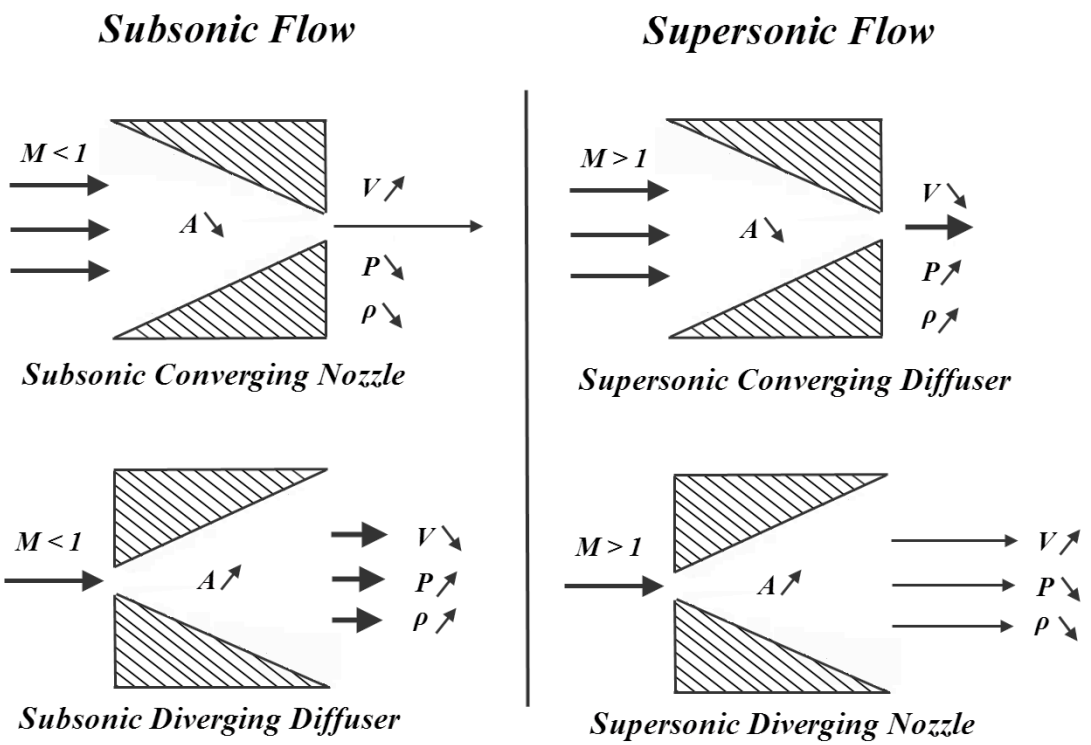

Figure 2.9 Visual representation of the different flow behavior for subsonic and supersonic flows experiencing a converging or diverging section

When the flow Mach number is equal to 1, the area is said to be minimal. From that point, the flow behavior will switch from subsonic to supersonic. Hence the combination of a converging nozzle and a diverging nozzle can be used to accelerate flows from subsonic to supersonic velocities as shown in Figure 2.10. The minimum cross-sectional area between the two sections is called the throat at which the flow Mach number is equal to 1.

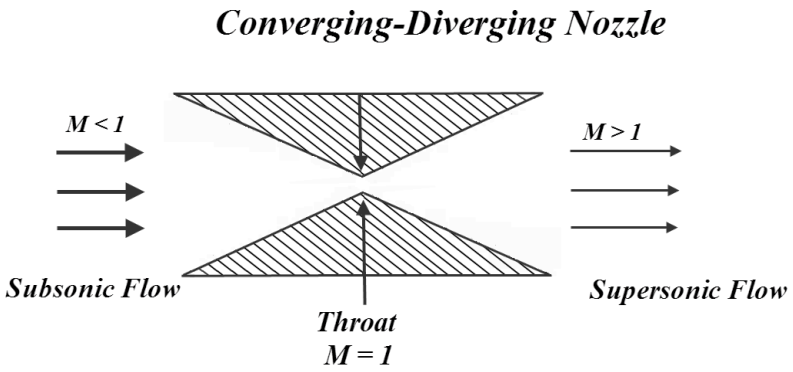

Figure 2.10 Visual representation of the combination of a subsonic converging nozzle with a supersonic diverging nozzle producing a supersonic flow at the exit

However, it is important to note that the flow does not always reach the speed of sound (Mach 1) at the throat. The ability of the flow to accelerate to this velocity depends on the gas stagnation pressure and exhaust back pressure, which will be discussed in Section 2.2.3.5.

2.2.3.4. Fluid Stagnation Properties

The fluid stagnation properties are defined as the properties of a flow decelerated isentropically to zero velocity. For a given flow, the instantaneous properties of the fluid in the CGDS process are subject to change depending on the position whereas the stagnation properties are kept constant. These stagnation properties, such as temperature and pressure can be easily controlled and evaluated for a calorically perfect gas following an isentropic flow [44]:

$$\frac{T_0}{T} = 1 + \frac{k-1}{2}M^2 \qquad \text{(Eq. 2.6)}$$

$$\frac{P_0}{P} = \left(1 + \frac{k-1}{2}M^2\right)^{\frac{k}{k-1}} \qquad \text{(Eq. 2.7)}$$

where the subscript $_0$ designates the stagnation properties. These equations are important to determine flow properties. As such, these relationships can be used to determine the pressure or temperature of a flow knowing its speed (Mach number), if the stagnation properties are known. Conversely, the pressure and temperature ratios required to reach a certain Mach number can also be determined.

2.2.3.5. Compressible Isentropic Flow in a Converging-Diverging Nozzle

The behavior of a flow passing through a converging-diverging nozzle is a key feature of the LPCS technique since it produces the required supersonic flow to accelerate the feedstock particles. In order to analyze the different possible scenarios, the pressure ratio between the stagnation pressure P_0 and the exit chamber pressure or back pressure P_B must be varied. By doing so, it is possible to identify seven different flow behaviors through a converging-diverging nozzle. The pressure change along the nozzle axis for each scenario can be observed in Figure 2.11. Cases a) through g) are obtained by slowly increasing the pressure ratio P_0/ P_B.

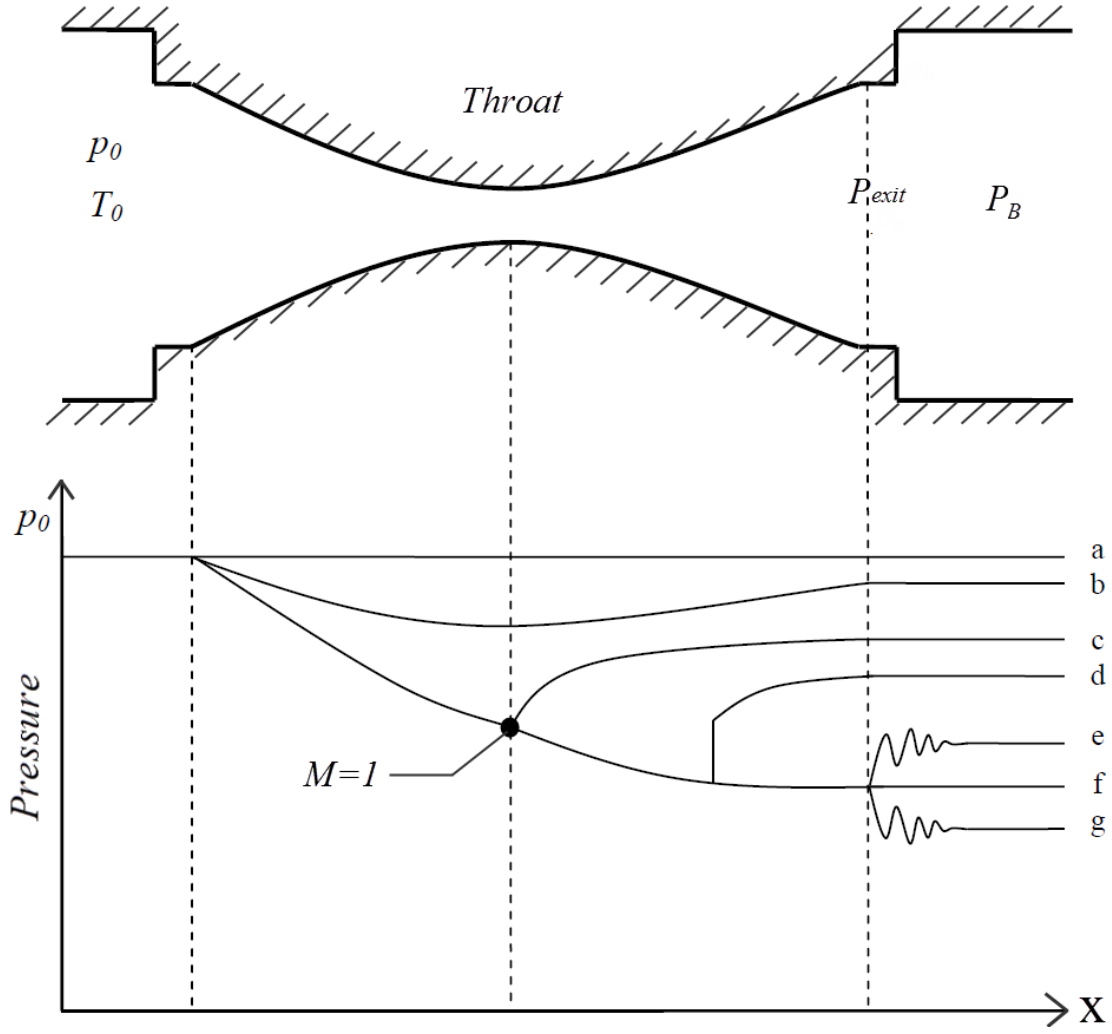

Figure 2.11 Evolution of fluid pressure through a converging-diverging nozzle starting at P_0 (adapted from [45])

Case a) illustrates the case where the back pressure is equal to the stagnation pressure (P_0/ P_B). As expected, as there is no pressure difference to drive the flow, there is no fluid flow in the nozzle. By slightly reducing the back pressure as in case b), the fluid begins to flow in the nozzle. However, the pressure ratio is insufficient to choke the flow at the throat (M<1). Therefore, the flow experiences a subsonic regime in the converging section and since it does not reach Mach 1, the fluid undergoes expansion and decelerates in the diverging section. The gas pressure increases slowly until it reaches the exit of the nozzle, at which the pressure (P_{exit}) equals the back pressure P_B. As the back pressure is further reduced, case c) is achieved. The stagnation pressure is large enough to choke the flow to the speed of sound at the nozzle throat. However, the pressure ratio is not sufficient to sustain the flow acceleration further and the flow switches back to the subsonic regime and decelerates in the

diverging section. The flow then exits the nozzle at a pressure equal to the back pressure P_B. In case d), the flow accelerates to the speed of sound at the throat and supersonic flow is sustained over a certain portion of the diverging section. However, when the flow is expanded too rapidly in the diverging section and the difference between the flow pressure and back pressure becomes too large, a shockwave can occur in the diverging section of the nozzle in order to adapt the flow to the back pressure. Thus, the flow decelerates abruptly as it goes through this shockwave and reverts to the subsonic regime. As in all other cases so far, the flow exits the nozzle at subsonic speed with a pressure equal to the back pressure. By further decreasing the back pressure as for cases e), f) and g), the supersonic flow is maintained throughout the entire diverging section. However, the pressure at which the flow exits the nozzle, for case e), is lower than the back pressure ($P_{exit}<P_B$). Thus, in order to adjust the flow pressure to the gas pressures, a series of oblique expansion waves, reflected on the jet boundary into compression waves are created as shown in Figure 2.12. In this case, the compression waves occur first and the jet is referred as an over-expanded nozzle flow.

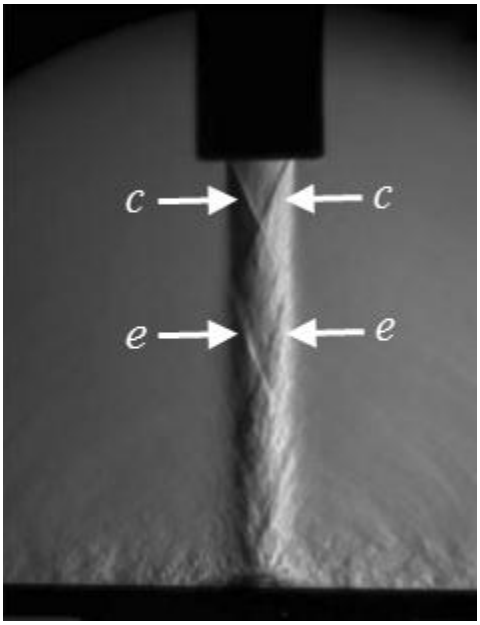

Figure 2.12 Schlieren image of an over-expanded gas at the exit of a converging-diverging nozzle case e), letters "c" identify compression waves and letters "e" identify expansion waves (adapted from [39])

The next case f) is considered to be the ideal isentropic expansion where the supersonic flow exits the nozzle at a pressure equal to the back pressure (P_{exit}=P_B). It is ideal, as no shockwaves are formed at the nozzle exit but is hard to reproduce in reality. Finally in case g), the pressure ratio is sufficient to choke the flow at the throat. The flow becomes supersonic and expands to supersonic speeds inside the diverging nozzle. However, the back pressure is lower than the pressure of the flow exiting the nozzle (P_{exit}>P_B). Thus, expansion waves are created to readjust the gas pressure. However, after going through the expansion waves, the pressure is not perfectly matched and is now even lower than the ambient pressure. Thus, the expansion waves are followed by other compression waves and expansion waves, until the pressure is stabilized to the same level than the back pressure. These waves would form a similar diamond pattern presented in Figure 2.12 but the expansion waves would come first. This type of nozzle flow is identified as an under-expanded flow.

2.2.3.6. Nozzle Design Parameters

So far, the calculation of various flow properties (pressure and temperature) inside the converging-diverging nozzle has been shown in Equations 2.6 and 2.7. Unfortunately, these equations do not provide any details on the dimensions of the nozzle such as the throat area (A^*) and the nozzle exit area (A_e). The relationship between any cross-sectional area (A) and the throat area is found by combining the continuity equation with the stagnation properties ratios [44]:

$$\frac{A}{A^*} = \frac{1}{M}\left[\left(\frac{2}{k+1}\right)\left(1+\frac{k-1}{2}M^2\right)\right]^{\frac{k+1}{2(k-1)}} \qquad \text{(Eq. 2.8)}$$

As seen in Equation 2.8, there are 2 possible scenarios for a given area. The solution can be either subsonic or supersonic. As described in Section 2.2.3.5, it is the pressure ratio P_0/P that determines whether a sustained supersonic flow is possible in the diverging nozzle section or not. Using this relationship, the exit area of the nozzle can be determined for a design Mach number. The design Mach number is the ideal Mach number at which the flow will exit at a pressure equal to the back pressure, minimizing the formation of shockwaves and expansion waves.

In order to calculate the gas flow rate through a converging-diverging nozzle, the continuity equation can be applied at the throat where the throat area is known. As stated previously, the speed of the flow at the throat for a choked flow equals the speed of sound (M=1). Assuming a calorically perfect gas, the continuity equation can be rewritten as [44]:

$$\dot{m} = P_0 A^* \sqrt{\frac{k}{RT_0}\left(\frac{2}{k+1}\right)^{\frac{k+1}{k-1}}} \qquad \text{(Eq. 2.9)}$$

As seen in Equation 2.9, the mass flow rate ($\dot{m}$) of the fluid is related to the stagnation properties (pressure and temperature) as well as the throat area. Therefore, it is possible to calculate the gas consumption and related gas cost of the system knowing the throat area, gas nature, stagnation pressure and temperature. Upon an increase of stagnation pressure or throat area, the flow rate will increase while an increase in temperature reduces the flow rate, due to its reduced density. While selecting the nozzle throat diameter, it is important to consider that lower mass flow rate will also reduce the flow capacity to accelerate the particles. The flow gets saturated at lower feed rates and the potential deposition rate is reduced. In addition, very small throat diameter could lead to machining issues that should be taken into account.

2.2.3.7. Particle Acceleration

The previous sections described in detail how to produce the supersonic flow required to accelerate powder particles to high velocities. This section covers the fundamental equations and relations quantifying the interactions between the particles and the supersonic flow.

Injected at a velocity close to zero inside a high velocity flow, the particles accelerate according to the drag forces they experience. These drag forces depend on different parameters: the flow density (ρ), the projected particle area (A_p), the velocity difference between the particle (u_p) and the local flow speed (u) and the particle drag coefficient (C_D). The drag force on a particle (F_D) is given by [10]:

$$F_D = \frac{1}{2}\rho A_p \left(u - u_p\right)^2 C_D \qquad \text{(Eq. 2.11)}$$

The acceleration of a particle can be obtained by combining Equation 2.11 with Newton's second law. The particle acceleration is therefore given by:

$$a_p = \frac{\frac{1}{2}\rho A_p (u - u_p)^2 C_D}{m_p} \quad \text{(Eq. 2.12)}$$

where m_p is the mass of the particle. Equation 2.12 shows that the acceleration of a particle is closely related to its mass. The projected area of the particle into the flow as well as the drag coefficient are dependent on the powder morphology. The projected area of the particle is also a function of the diameter squared of the particle while the mass of the particle is function of volume, hence proportional to the diameter cubed. Therefore, the ratio of the area over the mass provides that the acceleration of the particles is inversely proportional to the particle diameter [46]. The gas velocity and density, which can greatly affect the particle acceleration, are strongly dependant on the nozzle design. As such, a proper nozzle design without shockwave in the diverging section is extremely important. It is important to note that these equations provide instantaneous measures of the acceleration, which is also function of time. Studies have shown that a longer nozzle would accelerate particles to higher velocities due to a longer exposition to the drag force of the supersonic flow [10,47]. However, friction and boundary layer effects could reduce the flow velocity if the expansion section of the nozzle is too long. The particle deposition can also be affected by another phenomenon, called bow shockwave, appearing near the surface of the substrate created by the flow interaction with the substrate. The bow shockwave is the result of the high-velocity flow adapting to the sudden change in direction caused by the presence of the substrate. The shockwave decreases the flow gas velocity while the temperature and pressure increase. In a study conducted by Jodoin [48], the effect of the exit Mach number on the shockwave created was investigated. It was suggested that the strength of this bow shockwave, for high Mach number flows and small particles, could be sufficient to slow down the particles influencing the deposition process.

2.2.4. LPCS Advantages and Limitations

The LPCS process holds many advantages over other thermal spray processes. The advantages of the low pressure injection point are the elimination of clogging/fouling at the nozzle throat and lower powder feeder pressure compared to HPCS systems, however the LPCS has the disadvantage of not injecting powder into a powder preheating zone like the HPCS [49].

In LPCS, the thermal energy is provided by an electrical heater rather than by the combustion of fuel and oxygen. The advantages of such a heating system are numerous: no hazardous gases involved, no combustion to control, characterize and optimize, no combustion products, possibility to use inert driver gases such as nitrogen and helium, and lower gas temperatures are possible.

The lower spray temperatures used in CGDS (room to 1,000°C) compared to other thermal spray processes and the use of inert propellant gases (helium or nitrogen) in CGDS allows the deposition of heat sensitive materials such as copper, magnesium and titanium [16–21].

Coatings manufactured using LPCS process exhibit high density levels achieved by the severe plastic deformation of the feedstock powder upon impact. Ceramics, being brittle material, have to be sprayed within a ductile matrix in order to be deposited with this process.

The main processing gas used with the LPCS process is helium, when high particle velocities are required. However, helium is costly and a non-renewable gas available in limited quantity. Further process development will eventually lead to higher particle velocities using nitrogen gas, such as specially designed nozzle for specific application. However, when helium gas is required, helium recovery systems could be used to reduce gas consumptions and costs.

2.3. Pulsed Gas Dynamic Spraying

2.3.1. Background

The Pulsed Gas Dynamic Spray (PGDS) process was developed at the University of Ottawa Cold Spray Laboratory in 2005. The first publication presenting a comprehensive description of the process was published in 2007 [22] and a patent was issued shortly after in 2008 [50]. Since then, a partnership with CenterLine Ltd (Windsor, Canada) was made and now, continuous research and development is performed with their collaboration. A commercially available unit is presently available.

In PGDS, as in CGDS, particles reach high velocities and plastically deform upon impact onto the substrate to be coated. Unlike CGDS, where the main gas stream propelling the particles is continuous, the PGDS propels the powder particles using series of pulsed flows. The coalescence of the compression waves, created by a fast opening and closing valve, forms a shockwave capable of accelerating and heating the powder present in the gun to high impact velocities (similar to CGDS) and intermediate temperatures (below melting point) [22]. In CGDS, the use of a converging-diverging nozzle, where the enthalpy is converted to kinetic energy, results in a decrease of propellant gas temperature and consequently particle cooling usually occurs in the diverging section of the nozzle. In PGDS, the particles experience an unsteady flow that ideally exhibits a constant high gas temperature throughout the entire spraying process. Thus, the particles do not experience any cooling and are actually heated while accelerated, leading to a reduction of the critical velocity required for deposition in comparison with CGDS. The intermittent nature of this process could also lead to reduction of gas consumption and operating costs [51].

Although few studies have been published on the PGDS process, it has been shown to produce dense aluminium and copper coatings successfully [22]. The deposition of aluminium alloys mixed with SiC [52] and other harder powders such as stainless steel [53], WC-Co [59, 60] and WC-10Co4Cr [26] and amorphous iron coatings [22] is also possible using the PGDS process.

2.3.2. General Process Overview (PGDS)

The PGDS system has some similarities with the LPCS system. They both require high pressure processing gas, such as nitrogen or helium, to create the main flow propelling the particles. A powder feeder is required to control the amount of powder injected and a powder heater can also be added if required. Furthermore, like the LPCS, the PGDS uses an electrically resistant coil heater to heat the processing gas, capable of reaching 900°C. However, as shown in Figure 2.13, the PGDS process requires a pulsing valve to create the shockwaves; a converging-diverging nozzle is not required in this process.

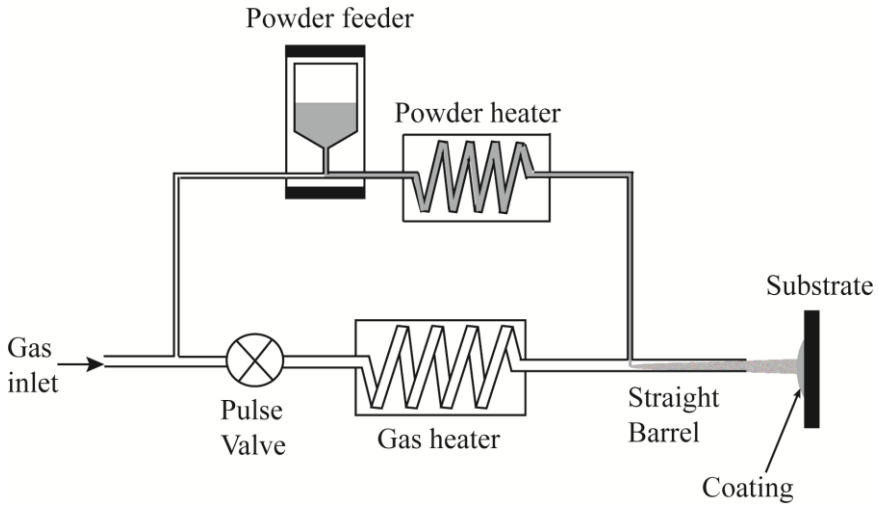

Figure 2.13 Schematic of the PGDS technique

The shockwaves frequency can vary from 1 Hz to 30 Hz. However, the change of frequency, for a given valve, will also change other parameters such as opening and closing times which are crucial for the creation of a shockwave. Slow opening rate would create a regular flow without presence of compression waves and high opening frequencies could lead to a reduced gas density and shockwave strength. The barrel length, where the particles are accelerated, will have an impact on the particle velocities. Simulations have also shown that other parameters, such as gas nature, pressure and temperature will have an impact on the pulsed gas Mach number [23].

2.3.3. Gas Dynamic Principles in PGDS

The main characteristic of this process is the shockwave. In this section, a description of a normal shock is presented as well as its effect on gas properties before and after the shock. Then, the propagation of a shockwave is described, particularly the different zones that develop behind the shock.

2.3.3.1. Gas Properties Across Normal Shocks

The concept of shockwave was introduced to characterize a fluid that experiences a very abrupt, nearly discontinuous change in properties seen in supersonic flows. Fluids can adapt to rapid changes in properties using two different ways: expansion waves or compression waves. Expansion waves are characterized by a pressure reduction while the coalescence of compression waves leads to shockwaves. The properties across a normal shock (90 degrees front versus flow direction) can be derived from continuity, momentum and energy conservation equations and the calorically perfect gas equations. The resulting relationships are presented here based on a supersonic flow, subscript 1, experiencing a stationary shockwave. The resulting properties after the shock are labelled with subscript 2:

$$M_2^2 = \frac{M_1^2 + \frac{2}{k-1}}{\frac{2k}{k-1}M_1^2 - 1} \qquad \text{(Eq. 2.13)}$$

$$\frac{T_2}{T_1} = \frac{1 + \frac{k-1}{2}M_1^2}{1 + \frac{k-1}{2}M_2^2} \qquad \text{(Eq. 2.14)}$$

$$\frac{P_2}{P_1} = \frac{1 + kM_1^2}{1 + kM_2^2} \qquad \text{(Eq. 2.15)}$$

where M is the Mach number, T is the temperature, P is the pressure and k is the specific heat ratio of the gas. The changes of flow properties for a supersonic flow going across a shockwave are: a reduction in speed (Mach number), raises in temperature, pressure and density. These results are for a stationary shockwave as shown in the Figure 2.14.

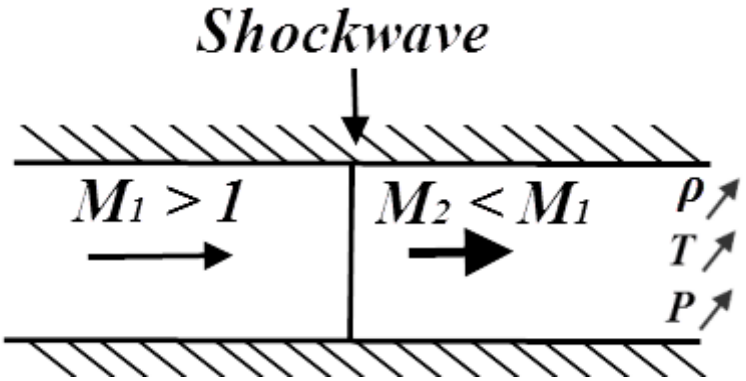

Figure 2.14 Property change across a shockwave

2.3.3.2. Shockwave Propagation

In the PGDS technique, series of shockwave produced at a constant frequency are used to accelerate and heat the powder particles. Therefore, the behavior and characteristics of travelling shockwave have to be understood. For simplification, the gas will not be heated by an external source.

Initially, the system can be modelled as shown in Figure 2.15. Zone 1 is at ambient pressure and temperature and the pressurized section, Zone 4, is contained by the closed valve. The powder has already been injected into the barrel.

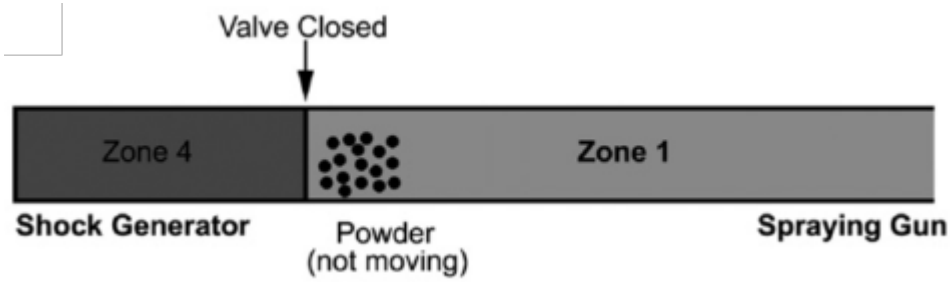

Figure 2.15 Initial PGDS gun state prior to valve opening [22]

By opening and closing the valve quickly, ideally a bursting diaphragm, compression waves are generated and travel towards the exit of the gun. The first compression wave, travelling at the speed of sound, heats up the gas. The subsequent compression wave propagates into a hotter gas at the speed of sound which is faster than the speed of the previous compression wave according to Equation 2.2, which shows that the speed of sound is a function of

temperature. Therefore, the second wave catches up the first one and combine together; the same principle applies to the next compression waves. Ultimately, the compression waves coalesce to form a shock wave (Figure 2.16i) which generates a high speed intermediate temperature flow [44]. The feedstock powder is accelerated and heated by the flow induced inside the barrel, as it moves towards the exit of the spraying gun (Figure 2.16ii and iii). The particles impact the substrate at high velocities and plastically deform and bond to the substrate similarly to the LPCS process. However, in contrast with the LPCS where particles experience cooling in the nozzle [49], the intermediate gas temperature created by the shockwave heats up the particles to intermediate temperatures remaining below their melting point. The temperature gain decreases the critical velocity required to deposit the material due to the increased ductility. The process can be repeated multiple times per second with the use of a special device specially built for this application: a rotating valve with a slotted disk. As the disk turns on the valve seat, it simulates a bursting diaphragm and provides very quick opening and closing, enough to induce compression waves and form a shockwave.

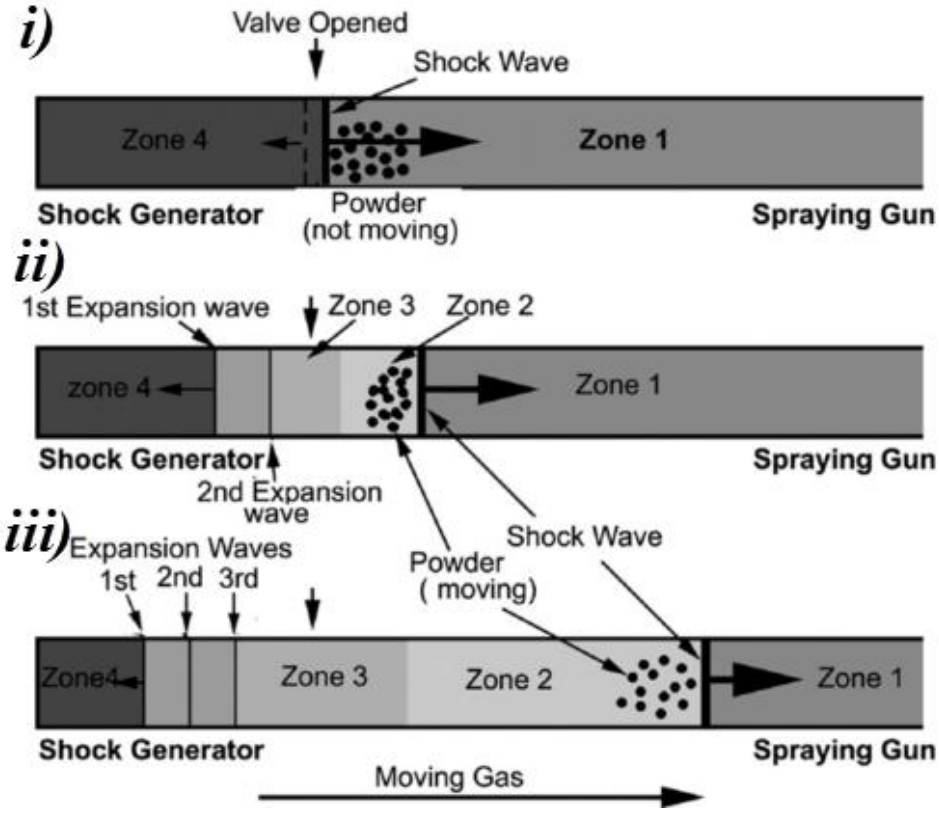

Figure 2.16 Schematic of the propagation of one shockwave inside the gun [22]

The shockwave travels in the spraying gun at a velocity that is a function of the initial pressure ratio between Zone 1 and Zone 4 and initial temperatures of these zones. The induced flow created by the passage of the shockwave (Zone 2) is at higher pressure and temperature than the stagnant gas located in Zone 1. Zone 3 is the zone that was originally within Zone 4, which experienced an expansion, thus cooler than Zone 2. This zone expands and moves at a lower velocities than Zone 2. Hence, in order to achieve optimal particle velocities and temperatures, the particles should be injected and remain in the Zone 2 throughout their acceleration. Further modelling was performed and supported the existence of a high heat, high velocity zone formed behind the travelling shockwave [23,50,54].

2.3.4. PGDS Advantages and Limitations

The advantages and limitations are very similar to those of the LPCS process. The low temperatures of the processing gases and their inert nature can lead to coatings having the same microstructure than the feedstock powders. However, gas consumptions of the PGDS process may be reduced with a proper design of the shock wave generator. It is also believed that the higher particles impact temperatures could be beneficial for the coating properties.

2.4. Critical Velocity

Particle "critical velocity" is a widely used term in the CGDS field. It refers to a particle velocity at which a given material in the powder form starts to deform sufficiently to deposit and create a coating on a substrate. Multiple studies were performed in order to determine the minimum velocity required to get adhesion of various feedstock materials [35,43,47,55–60]. The critical velocity has been defined as the threshold velocity at which a noticeable increase in deposition efficiency (DE) is observed. The DE of a material is calculated as the ratio of the deposited mass on the substrate over the total mass of the powder sprayed. Recent studies introduced the existence of an erosion velocity above which the particles, experiencing too much deformation, start eroding the substrate. Figure 2.17 illustrates the different deformation regimes of a copper ball impacting the substrate at different velocities.

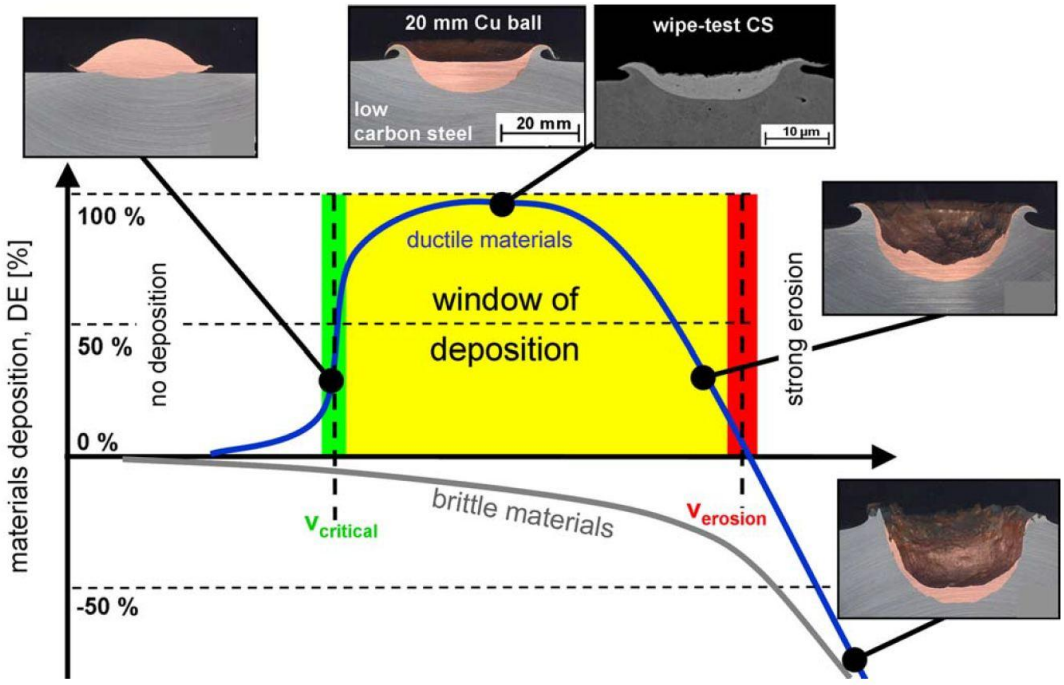

Figure 2.17 Deposition efficiency with respect to particle velocity and corresponding cross-sectional images for large-scale kinetic processes [35]

As seen in Figure 2.17, the deposition efficiency is low until the critical velocity is reached and the DE increases significantly. At this point, the ball produces significant deformation in the substrate and also presents signs of important deformation. The outer edges form what is commonly referred to as jetting that occurs when a particle experiences significant deformation. In addition, due to the high stresses induced within the particles during a very short period of time, the atomic structure of the ball experiences high levels of shear and it can be supposed that no heat transfer is made with the environment during impact. These adiabatic shear instabilities, further described in Section 2.4, create a temperature concentration on the particle edges, enhancing bonding. Further increase of particle velocity leads to a slowly rising DE until it reaches a maximum. Then, theoretically, increasing the velocity beyond this point will lead to a reduction in DE and as the strong erosion image suggests, only a part of the incoming particle is bonded. As the particle velocity increases even more, only erosion occurs and the impact of the particle leaves a hole in the substrate. This point is identified as the erosion velocity.

The critical velocity of different materials follows this general trend of DE against particle velocity. However, the order of magnitude of the critical velocity is known to vary depending on particle size [43,57], substrate material [61,62], powder oxide content [63,64], particle impact temperature [47,56] and especially on powder material [35,60]. Thus, the critical velocities are usually given with respect to the nature of the powder. Typical critical velocity values of various feedstock materials are reported in Figure 2.18; the hatched areas represent critical velocity variations due to powder size distributions of the feedstock powders.

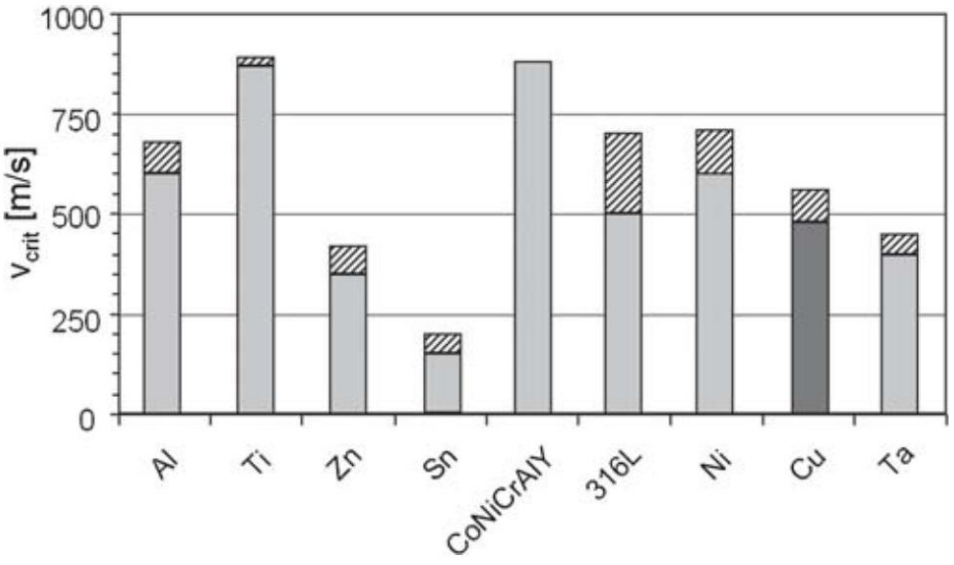

Figure 2.18 Experimentally determined critical velocities of various materials [60]

From Figure 2.18, a wide range of critical velocities can be observed depending on the material nature. This variation is attributed to differences in crystallographic structures, stiffness, melting temperature and mechanical strength [60]. Furthermore, any other properties susceptible of influencing the energy required to create plastic deformation will also affect the critical velocity, as the kinetic energy will be used towards deformation. titanium has one of the highest critical velocities due to its high strength and melting point.

As previously stated, the critical velocity can be affected by the powder impact temperature. Modelling studies conducted by Schmidt *et al*. [43] showed that higher powder impact temperature reduces the critical velocity. As shown in Figure 2.19, the left part of the diagram, in gray, indicates that no deposition is possible due to the lack of substrate deformation and brittle material behavior of the substrate. As the substrate temperature increases, a window of sprayability of a powder appears and lies in between the critical velocity V_{crit} and the erosion velocity $V_{erosion}$. At velocities lower than V_{crit}, the velocity is too low and erosion occurs like with sand blasting. Then, when the particle velocity reaches $V_{erosion}$ no deposition occurs until the materials start eroding significantly.

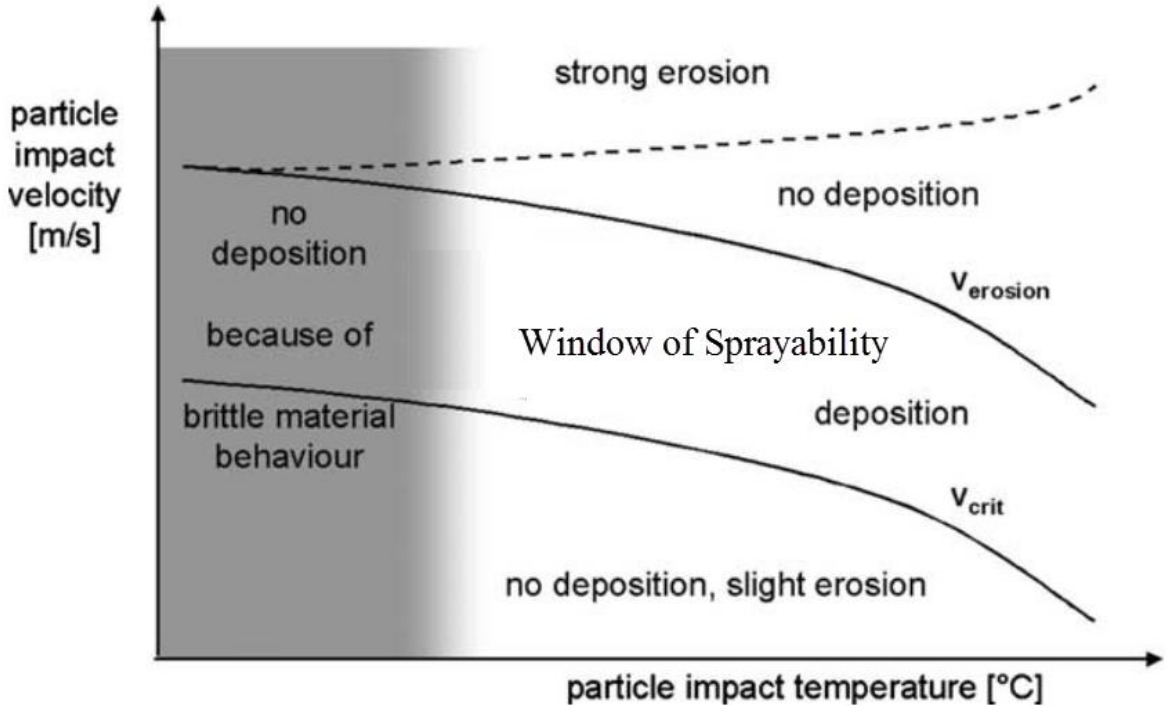

Figure 2.19 Particle velocity over particle temperature with window of sprayability and the regime of particle impact conditions chosen by the author (adapted from[43])

However, increasing particle temperatures is a challenge for CGDS processes. The use of a converging-diverging nozzle converts the gas thermal energy into kinetic energy; thus, as the flow velocity increases, the gas experiences cooling and so do the particles in flight. In HPCS, the particles have the advantage of being injected into a high temperature zone where the particle temperatures rise before the throat as shown in Figure 2.20. In this figure, the two arrows represent two different injection points of copper particles; close to the throat (gray) and far before the throat (black). Due to lower heating and cooling rates of coarser particles, the impact temperature is higher for the particle that was exposed for a longer period to the high temperature gas before the throat. The high particle temperature resulting from the far injection increases particle ductility and deformation.

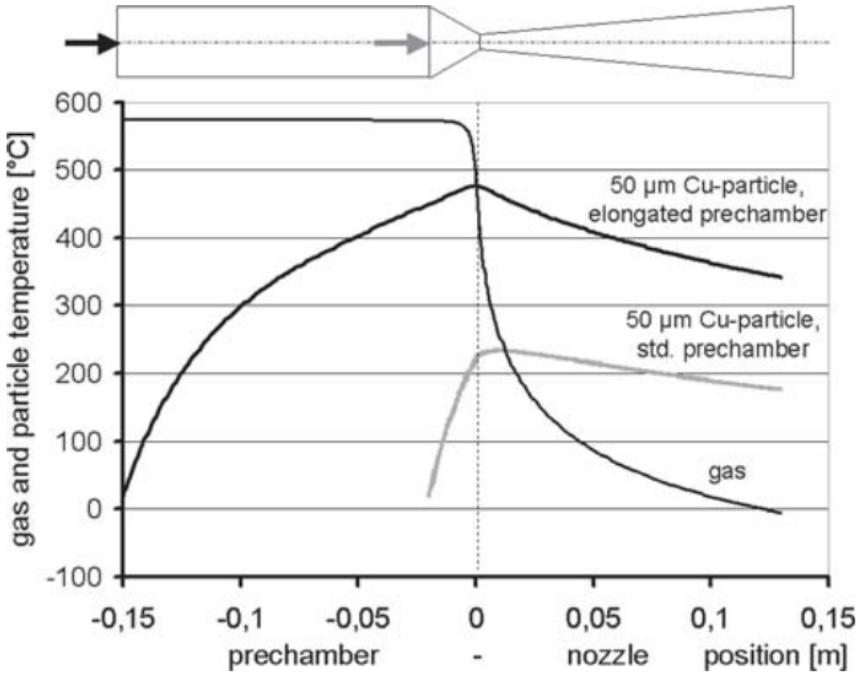

Figure 2.20 Thermal history of a 50 μm copper particle, passing through the prechamber and the nozzle starting from two different position on the high pressure and temperature side [49]

The powder injection in a longer prechamber of a HPCS nozzle is beneficial in terms of particle temperature at the nozzle exit. However, this can create nozzle clogging issues at the throat. In the case of the LPCS system, the powder is injected directly into the cooler gas located after the nozzle throat. A powder preheating apparatus might be convenient to spray high critical velocity materials such as titanium. In LPCS, due to the location of the powder injection point, there are no disadvantages related to the injection of hot powder. For the PGDS system, even though the process itself has a high temperature zone, powder preheating may be beneficial as well in order to preheat the whole powder distribution and enhanced powder ductility.

For the LPCS and PGDS to form a coating properly, the particles must accelerate above their critical velocity which may vary depending on material composition, particle size, particle temperature and oxide content. However, the bonding mechanisms remain the same for these processes and the next section will aim at explaining the different bonding mechanisms found in kinetic spraying (HPCS, LPCS and PGDS).

2.5. Bonding Mechanisms

So far, the gas dynamic principles of the LPCS and PGDS processes have been presented. In order to form a coating, it was defined that the particle had to accelerate and reach critical velocity. At this velocity, significant increase in deposition efficiency is observed and a coating is produced. In this section, the bonding mechanisms involved in the adhesion of the particles with the substrate will be described. Despite the differences between LPCS and PGDS, the bonding mechanisms of a high velocity particle are expected to be the same regardless of the powder acceleration method.

Over the years, the phenomena involved in the particle-substrate and particle-particle bonding mechanisms have been the focus of numerous CGDS studies [18,57–59,65–67]. The determination of the bonding mechanisms is a challenge due to their complex and fast nature. In addition, they may also be material dependant, increasing the difficulty of this investigation. To date, a few possible theories are commonly discussed but there is no consensus on a single dominant bonding mechanism. However, most researchers recognize that particles, impacting the substrate at high velocities, deform plastically as well as the substrate in addition to dissipation of heat [18,57–59,65–67]. Some researchers argue that the heat dissipated could cause local melting of the particle which would influence the bonding mechanisms [59]. Others claim that the particles remain in solid state throughout the whole deposition process [57,58]. Based on the two different points of view, various theories have been formulated for the bonding mechanisms present in kinetic deposition processes.

Dykhuizen *et al*. [66] proposed a theory related to the bonding mechanism involved in cold spraying. They suggested that the bonding process in CGDS was very similar to the bonding mechanisms observed in explosive welding. In this process, an explosion is used to impact two metal sheets at high velocity which causes localized softening at the impact point due to heat dissipation. This results into the formation of solid state jetting at the impact interface and is believed to be responsible for breaking up the surface oxides, resulting in a clean and intimate contact between the two surfaces enhancing bonding. According to the modeling and experimental work conducted by Dykhuizen *et al*. [66], the formation of a material jet

created by the impact of a particle can be observed in Figure 2.21 which supports their theory.

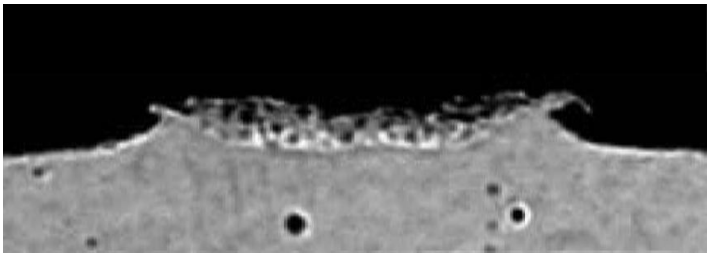

Figure 2.21 Cross-section of crater formed with HPCS process by the impact of a 700 m/s copper particle onto stainless steel substrate showing evidence of material jetting [66]

In addition, their work revealed that jetting occurred for the substrate and also the particle, resulting in good bonding even though the particle remained unmolten. Since then, the jetting phenomenon has been observed by many other researchers [39,67–70]. Some of them also believe that the local heating near the jetting zone could result in local melting of the material [39,67,68,70]. Further studies revealed that substrate jetting is not required in order to achieve adhesion. For example, aluminium particles successfully bonded to a ceramic substrate which showed no signs of deformation, as seen in Figure 2.22.

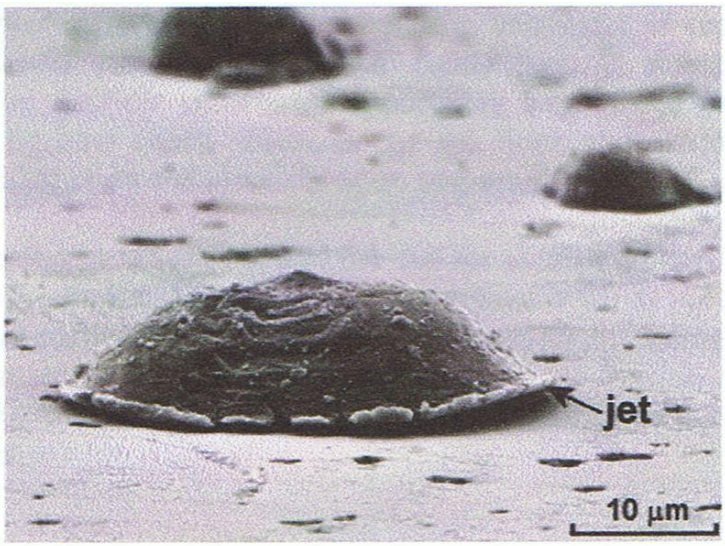

Figure 2.22 Aluminium splat showing jetting bonded to a ceramic substrate [71]

One last possible bonding mechanism theory in kinetic spraying is commonly referred to as adiabatic shear instability. The original detailed description of this mechanism was given by

Wright [72] and was later used by Assadi *et al*. [58] and Grujicic *et al*. [18] to explain the deformation mechanism of particle to particle and particle to substrate bonding observed in the CGDS process. Adiabatic shear instability is associated with the rapid localized heating and shearing phenomenon experienced by the particles upon impact with the substrate. The principal assumption is that the local temperature increases adiabatically to a point where localized thermal softening occurs. This location is usually the contact interface upon particle impact. When the high velocity particle impacts the substrate, a strong pressure field is created inside the particle from the impact point. The high strain rates resulting from it lead to shearing instabilities where thermal softening is locally dominant over work strain and strain rate hardening, thus changing the material deformation behavior from plastic to viscous flow. Heat transfer being time dependant, the assumption of adiabatic evolution during the deformation of a particle is adequate considering the short period of time required for the particle to contact and deform upon impact.

In their numerical simulations, Assadi *et al*. [58] evaluated the impact behavior of copper particles at different impact velocities and found that the material deformation is governed by adiabatic shear instability for particle with sufficient kinetic energy (high strain rates). Assadi compiled the evolution of strain, temperature and stress as a function of time of copper particles impacting a substrate which are presented in Figure 2.23. From these figures, one can observe that the particle velocity increase, from 550 m/s to 580 m/s, has a significant effect on the strain, temperature and stress of the particle. Based on this, the required velocity of a copper particle to experience adiabatic shear instability at the particle interface should be around 580 m/s which is close to the critical velocity of copper presented in Section 2.4, thereby supporting the results obtained by Assadi *et al*. [58]. Therefore, adiabatic shear instability is an important phenomenon affecting the bonding in kinetic spraying and can be closely related to the critical velocity of a material.

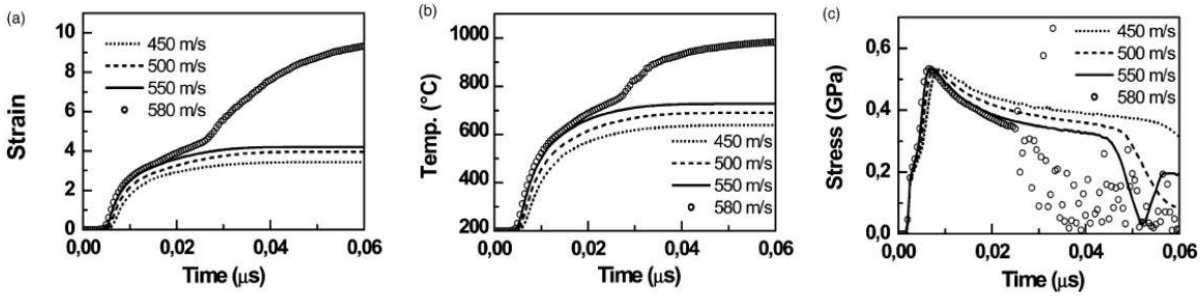

Figure 2.23 Evolution of (a) strain, (b) temperature and (c) stress with respect to time in the interface region of a impacting particle at various velocities [58]

The adiabatic shear instability has been known to form shear bands, highly deformed regions. Many CGDS studies observed the presence of these shear bands supporting the theory of adiabatic shear instability as an important bonding mechanism in CGDS [43,73,74]. Jetting and shear band formation caused by adiabatic shear instability can be observed in Figure 2.24 and Figure 2.25 respectively. It is believed that these shear bands can create intimate contact and promote metallurgical bonding.

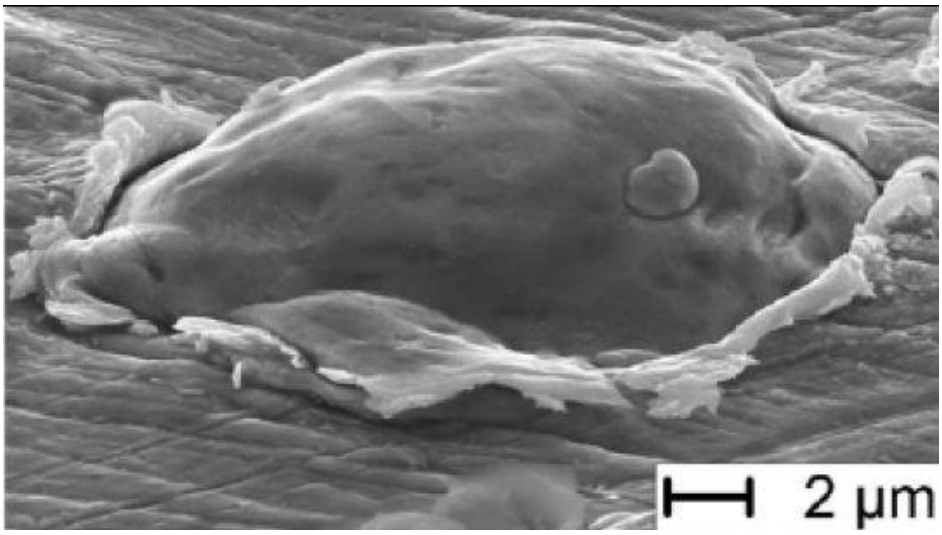

Figure 2.24 Copper particle splat showing presence of jets around the impact surfaces (adapted from [58])

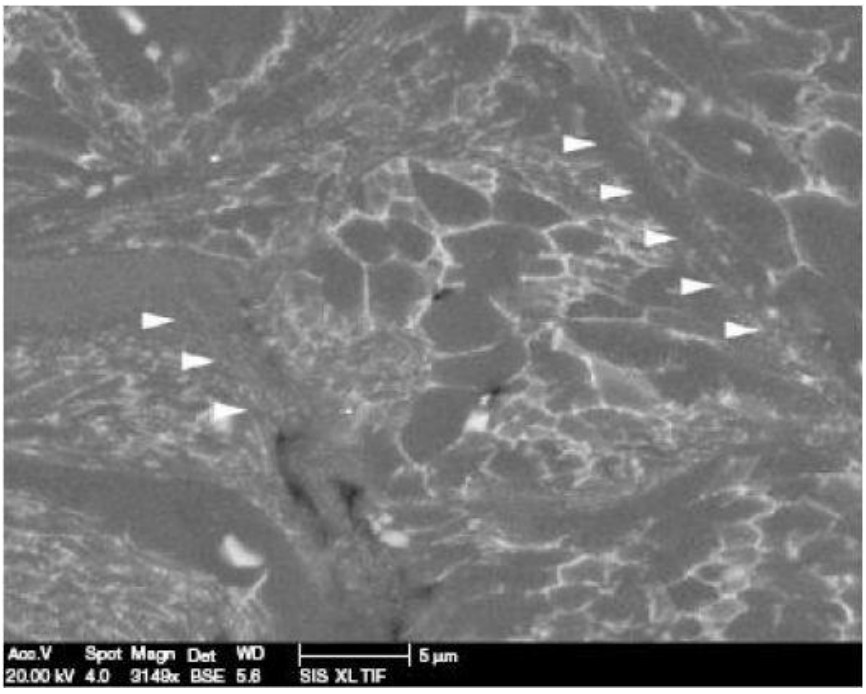

Figure 2.25 Evidence of shear bands (indicated by the white arrows) in the microstructure of an Al-alloy coating produced by CGDS [73]

The presence of metallurgical bonding in the coatings has been observed in a large number of studies [65,67,75]. The presence of such bonding is usually associated with adiabatic shear instability phenomena. The localized hot region of the particle promotes metallurgical bonding, particularly when the activation energy for a chemical reaction is low, as in the case of titanium. Metallurgical bonding can be observed in fractured surfaces as cup and cone ductile-like fracture at high magnification, as shown in Figure 2.26.

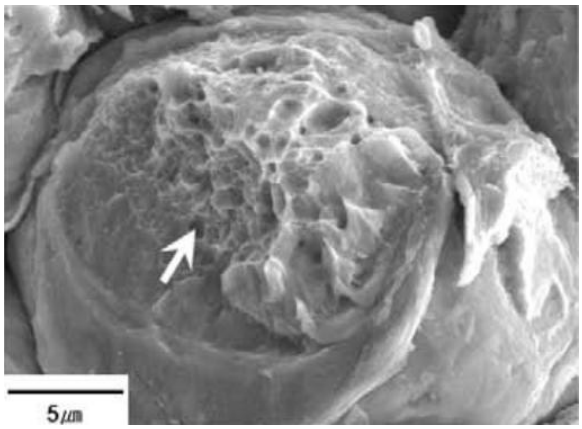

Figure 2.26 Fracture surface morphology of a CP titanium coating produced by CGDS showing a ductile fracture surface [67]

2.6. Influence of Powder Morphology

In most thermal spray processes, the feedstock material used to produce coatings is in powder form. The powder characteristics, such as morphology and size distribution, are known to have an impact on the critical velocity, therefore on the coatings quality.

Powder morphology is known to have an impact on the coatings properties. However, it is still unclear if a spherical morphology is better than non-spherical powders as they both have their advantages. On the one hand, a spherical morphology can be desired as the particle velocities are more predictable and build a more uniform structure. On the other hand, angular morphology powders can reach higher particle velocities due to their higher drag coefficient. The rotation of the non-spherical particle induces a constantly changing projected area. Over time, the average projected area will be higher for an angular particle than a spherical particle, for a given volume, resulting in a higher impact velocity. This increase of particle velocity could lead to enhanced coating properties.

In the CGDS and PGDS processes, the powder size must be relatively small with low oxide content. The smaller particles are beneficial for the coatings properties as they are more likely to reach the required critical velocity. However, particles with a very low mass will not be able to carry enough momentum to go through the bow shock and retain critical velocity. Particles with a very large diameter will also have problems to accelerate due to their high mass and the small acceleration time period before impacting the substrate. This phenomenon has been demonstrated by Gilmore [20] and is shown in Figure 2.27. The particles of 1 μm diameter experiences more deceleration going through the bow shock (around 0.5 mm away from substrate) than the 5 and 22 μm copper particles, despite its larger velocity at the nozzle exit.

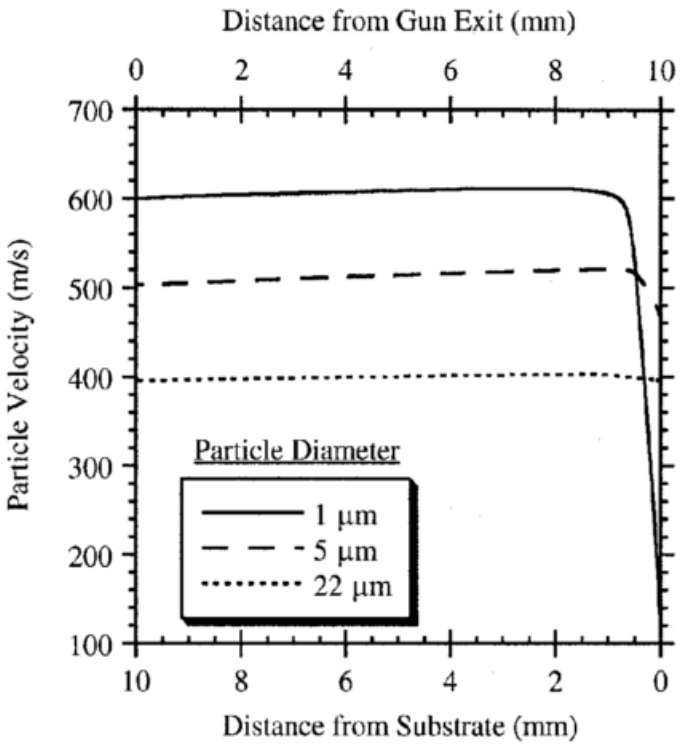

Figure 2.27 Theoretical calculations of particle deceleration for different diameters [20]

2.7. Powders Manufacturing Processes

A variety of manufacturing processes can be used to produce the feedstock powders. This section presents the different powder manufacturing processes currently used in the industry.

2.7.1. Atomized Powders

Powder atomization can be performed using different methods for melting the powder (induction, plasma), while the atomizing medium can be gases (air or inert gas) or water. Three of these techniques are: gas atomization, water atomization, and plasma atomization.

Gas and water atomization are usually performed using an induction heater under vacuum to reduce contamination and corrosion. The molten metal then flows inside the atomization nozzle where water, air or inert gases can be injected. The powder can be collected using a pump to gather the finest particles while the larger particles are accumulated at the bottom in a collection chamber. A schematic of the gas or water atomization process is presented in Figure 2.28.

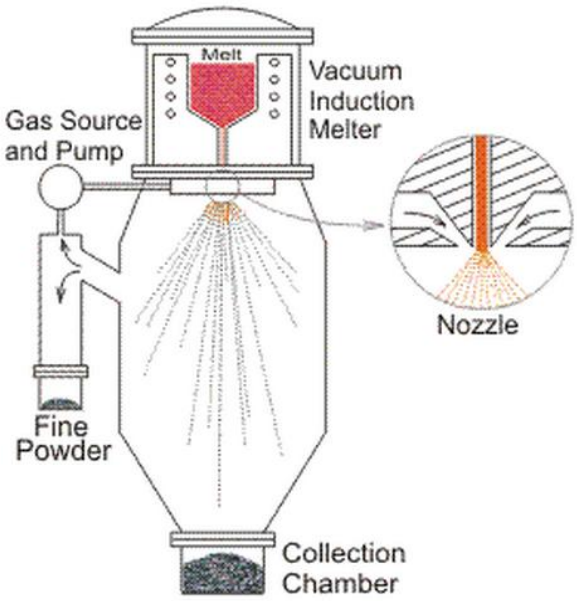

Figure 2.28 Schematic of a gas or water atomizer [76]

Depending on the atomizing medium used, different powder morphologies are achieved. As shown in Figure 2.29, the use of inert gases will produce spherical powders, while water atomized powders show an irregular morphology. In general, water atomization of highly reactive metals such as titanium and other superalloys is not performed due to oxide formation [76]. The use of inert gases is required for such materials. Powders produced by this method have a typical size distribution between 6 and 125 μm.

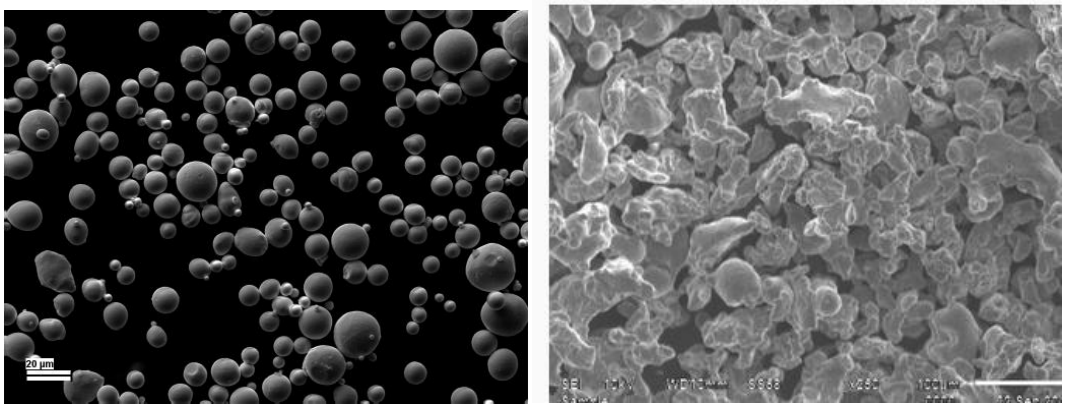

Figure 2.29 SEM images showing the morphology of spherical gas atomized CoNiCrAlY powder (left) [46] **and irregular water atomized aluminum powder (right)** [77]

Plasma atomization is similar to gas or water atomization processes, but uses a different feedstock heating device. This process consists of pulverizing a metal wire by melting and pulverizing it through a plasma torch, atomizing the material into micron size droplets.

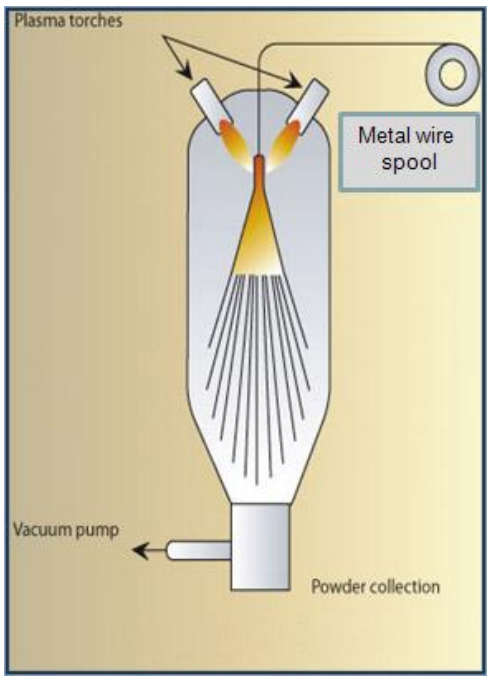

Figure 2.30 Schematic of the plasma atomization process [78]

Upon solidification, spherical shape powder is usually obtained. When performed in a vacuum chamber, this process can be used to create heat sensitive powders such as titanium. The resulting powder is collected at the bottom of the apparatus. This process is presented in Figure 2.30 and the typical powder morphology can be observed in Figure 2.31.

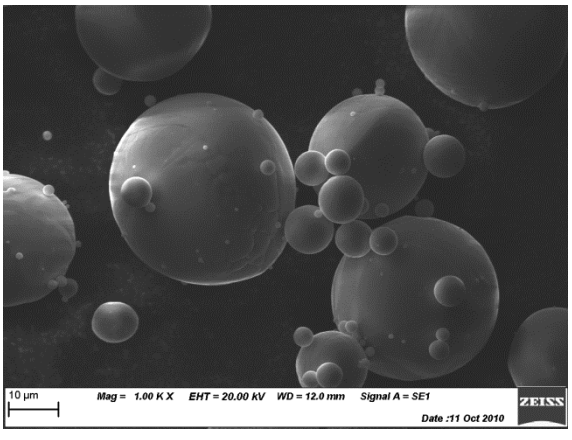

Figure 2.31 Typical spherical morphology of a plasma atomized CP titanium powder

2.7.2. Hydride-Dehydride Powders

Powders of the transition materials of the periodic table can also be manufactured using the hydride/dehydride (HDH) process consisting in a reversible chemical reaction with hydrogen. This process is illustrated in Figure 2.32 where the red circles are the hydrogen atoms and the gray circles are the metal atoms.

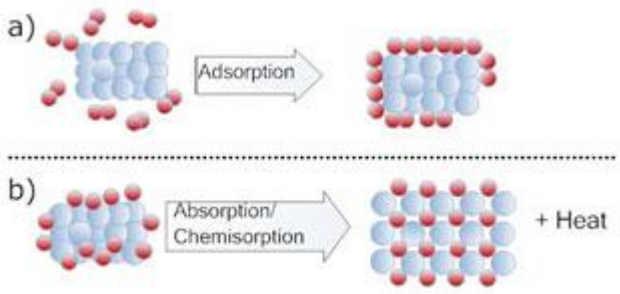

Figure 2.32 Atomic representation of the hydriding step of the hydride/dehydride process [79]

During the hydriding process, the metal absorbs hydrogen leading to an expansion of its lattice promoting cracking and embrittlement. The brittle material is then crushed under argon in a vibratory mill, until the desired particle size is achieved. The reverse process removing the hydrogen, called dehydriding, is done under vacuum and heating helps the hydrogen to diffuse more quickly and efficiently leaving higher purity titanium behind. The resulting irregular morphology of the powder manufactured with this process is depicted in Figure 2.33.

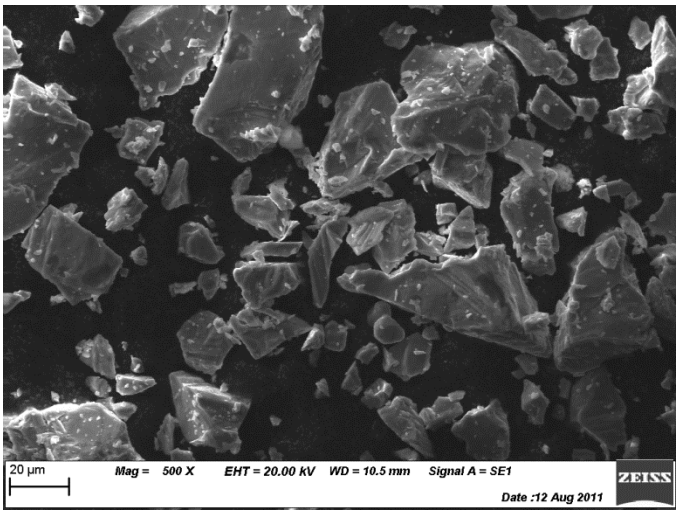

Figure 2.33 Typical angular morphology of a hydride-dehydride titanium powder

Chapter 3. Description of the Research Objectives

In previous chapters, the research topic and the different thermal spray processes were introduced and a detailed description of the two deposition processes used in this work was provided. The present chapter presents the specific description of the research, the objectives and the procedure followed to completed this work.

3.1. General Objectives

The general purpose of this study is to develop a repair process for the rapidly growing aerospace titanium parts market. This work is the first step towards a complete repair procedure. As introduced in Chapter 1, titanium has notable advantages over other materials, such as its very high specific strength and corrosion resistance, that has created an increasing demand for titanium parts in the last decade [28] across different industry sectors. This increase is particularly obvious in the aerospace sector, which is continuously seeking improvements in terms of weight reduction and energy efficiency [27]. However, the increasing price of titanium aerospace components amplifies the need of repairing damaged/worn parts to increase their useful life and reduce operating costs. While no current repair alternatives exist, the aerospace industry is particularly interested in developing a low cost and time effective reparation technique. Current material deposition methods are either not able to build coatings thick enough for part repair purposes or do not have the capacity of spraying heat sensitive materials such as titanium without major defects. As discussed previously, LPCS and PGDS could potentially provide suitable solutions for titanium coating deposition and repair of aerospace parts. **The aim of this research project consists in demonstrating the potential to deposit thick commercially pure titanium coatings for repair purposes using the new commercially available technologies, LPCS and PGDS.** With this study, the Technology Readiness Level of LPCS and PGDS should be such that these technologies may be applied to repair realistic components and tested to characterize their behavior under realistic conditions. A flowchart, demonstrating the different phases of the present work, is illustrated in Figure 3.1.

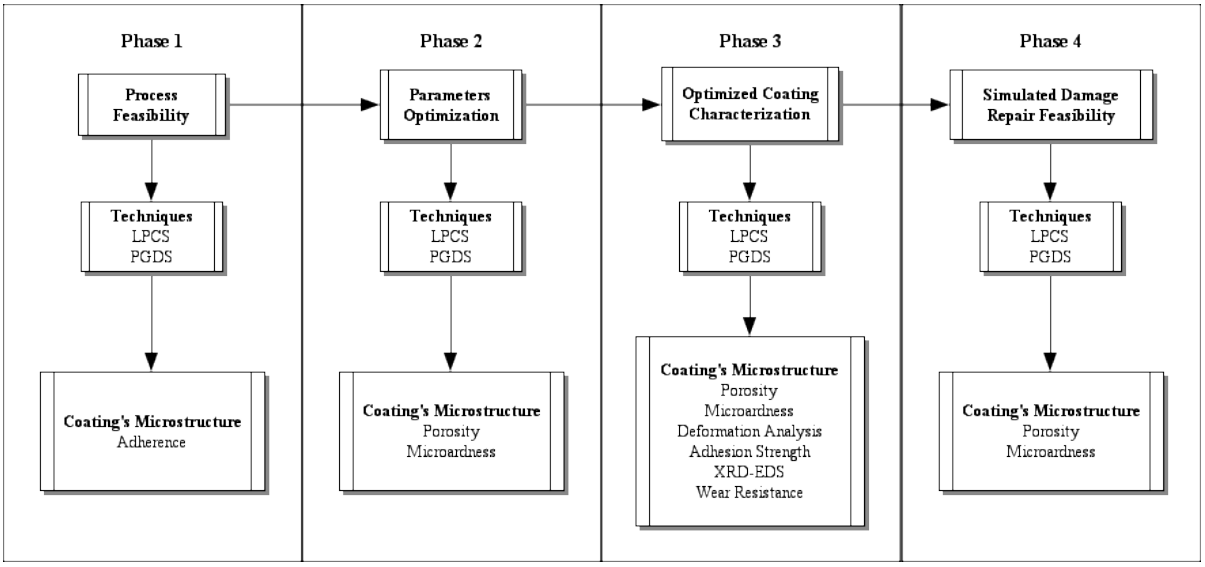

Figure 3.1 Overall test plan of the research work

3.2. Feasibility of CP Titanium Coatings

As discussed in Chapter 2, deposition of thick (about 1,500 μm) titanium coatings for repair using conventional thermal spray techniques such as plasma spraying and HVOF typically results in in-flight powder oxidation with minimal to no coating build-up. Therefore, **the first objective (Phase 1) of this research work is to demonstrate the ability of LPCS and PGDS to deposit thick titanium coatings**. As stated in Chapter 2, other spraying techniques such as HPCS and WS have produced titanium coatings on different types of substrates. From a technical point of view, the LPCS technique is based on the same physical principles with a different injection point. The advantages of the low pressure injection point (illustrated in Figure 2.8) are the elimination of clogging/fouling at the nozzle throat and lower powder feeder pressure compared to HPCS systems. However, as discussed in Chapter 2, the LPCS has the disadvantage of not injecting powder into a powder preheating zone like the HPCS [49]. Therefore, in order to increase powder ductility upon impact, a separate powder heater capable of reaching 1000°C has been added to the system. For the PGDS, the shockwave provides a high heat zone behind the shockwave that keeps the particles warm throughout the spraying process. Nevertheless, a powder preheater is used to maximize the powder impact temperature.

In addition, it has been shown that the powder size distribution and morphology can lead to different coating properties. For example, smaller particles will tend to reach higher velocities than larger particles. Also, spherical powder can lead to uniform coatings while the higher drag generated by angular shape powders could result into higher particle velocity, hence better properties. As such, **the effect of the particle shape and particle size distributions will be studied**.

3.2.1. Optimization of LPCS and PGDS Parameters

Once feasibility of producing thick titanium coatings has been demonstrated, this study will aim at **optimizing the spraying parameters in order to achieve the highest possible coating quality (Phase 2)**. As described in Chapter 2, coatings with high porosity are undesirable as they exhibit compromised mechanical properties. In addition, the voids could create potential crack initiation points with stress concentrations; hence porosity level is a critical aspect for repair applications. The coating microhardness is also an important coating feature to evaluate since this measure can indicate the presence of voids inside the coating (denser coatings will have higher microhardness). In summary, the present work will aim at optimizing the LPCS and PGDS parameters and powder in order to obtain low porosity levels and high microhardness coatings.

3.2.2. Optimized Coatings Characterization

In order to use these techniques for repair in the industry, it is necessary to understand the mechanical behavior of the sprayed coatings compared to the bulk material and also how these materials interact with each other. As such, a **thorough microstructural characterization of the optimized coatings will be performed (Phase 3)**. The adhesion strength between the coating and the substrate will be evaluated and the adhesion mechanisms characterized using different techniques such as fracture surface observation and wipe tests analysis. Furthermore, the oxidation/nitridation levels of the sprayed coatings will be investigated as the brittle phases (alpha case) associated with oxides/nitrides create inclusions that are susceptible to creating stress concentration points and crack initiation sites. X-Ray Diffraction analysis (XRD) and Energy Dispersive Spectroscopy (EDS) will be performed. In summary, this study will aim to produce highly bonded coatings and minimal oxide levels.

3.3. Feasibility of Parts Repair

Ultimately, this study will test the deposition on an angled substrate to reproduce the repair procedure (Phase 4). This step is necessary to ensure that the porosity and microhardness of the coating show no major differences with coatings produced on flat substrates.

Chapter 4. Equipment and Procedures

This chapter introduces the equipment and procedures that were used to achieve the objectives stated in the Chapter 3. Specifically, this chapter will provide details about the feedstock material used throughout the study as well as the spray equipment used for depositing the coatings. Finally, the equipment and procedures used for coating characterization will be discussed.

4.1. Feedstock Material

4.1.1. Feedstock Powder

CP titanium was selected as the feedstock powder , being of the same nature as the substrate used throughout this research (Ti-6Al-4V). The feedstock powders used in this study are commercially available plasma atomized pure titanium powder (grade 1 CP titanium, Raymor Industries, Montréal, QC, Canada) and hydride/dehydride commercially available pure titanium powder (CP titanium, Centerline Ltd., Windsor, ON, Canada).

Laser scattering particle size analysis (Beckman Coulter LS200) was used to determine the particle size distributions of the feedstock powders. In this technique, several grams of powder are mixed into a dispersing agent that scatters the agglomerations of powder particles. The powder solution is then pumped into the analysis device where the particles are exposed to a laser. The scattered light resulting from the interaction of the laser with the particle is collected and the different particle sizes are calculated based on the angular intensity distribution.

4.1.1.1. Feedstock Powder Material Storage

As part of safety regulations, all feedstock powders used are stored in an environmentally controlled fireproof cabinet. The cabinet has been equipped with a controlled electrical heater to ensure that the temperature is kept constant and warm (50°C) to avoid moisture in the powders. A dehumidifier has been installed in the cabinet room to keep the humidity level as low as possible (below 30%). This controlled environment ensures longer shelf life of the powders. To limit the contamination between different types of powder, the

containers are well labelled and never re-used. Figure 4.1 shows an image of the powder storage cabinet.

Figure 4.1 View of environmentally controlled powder storage cabinet

4.1.1.2. Feedstock Powder Material Processing

In order to investigate the effect of the powder size distribution on the coatings quality, the as-received powder is sieved using an automated sieving machine (W.S. Tyler model RX-29) shown in Figure 4.2. Multiples drum sieves of proper mesh size (CE Tyler) presented in Figure 4.3 have been used.

Figure 4.2 Photograph of the sieving machine (W.S. Tyler model RX-29)

Figure 4.3 Photograph of three stacked sieve drums (CE Tyler)

The drum sieves are stacked from fine (bottom) to coarser (top) mesh size. With the agitation and vibration of the machine, the small particles go through the mesh until the mesh size is smaller than the particles diameter. At the end of the process, each drum has gathered the particles larger than its specific size and smaller than the mesh size of the sieve above it.

Different powder morphologies were achieved by mechanical ball milling of the as-received powder. A small quantity of the as-received powder is placed into a container filled with 3 mm diameter steel balls. The mixing container is then filled with ethanol to avoid contact with air which could result in powder oxidation. A stainless agitator is operated at a constant rpm (260 rpm) for an hour, which is typical for CP titanium, to mill the powder until the desired morphology is achieved. A water cooling unit is used to maintain the mixture temperature below 50°C during the milling process. The powder milling machine and accessories are presented in Figure 4.4 and Figure 4.5.

Figure 4.4 Photograph of powder milling machine

Figure 4.5 Photograph of powder milling agitator, balls and container

4.1.2. Feedstock Substrate Material Processing

Titanium alloy Ti-6Al-4V 3 mm thick sheets were cut into small coupons (3 cm by 8 cm) using a horizontal band saw. These coupons were used for deposition of the CP Ti coatings for the parameter optimization process. The adhesion test samples were machined by a professional machinist using the CNC mill and lathe in the mechanical engineering machine shop of the University of Ottawa, shown in Figure 4.6.

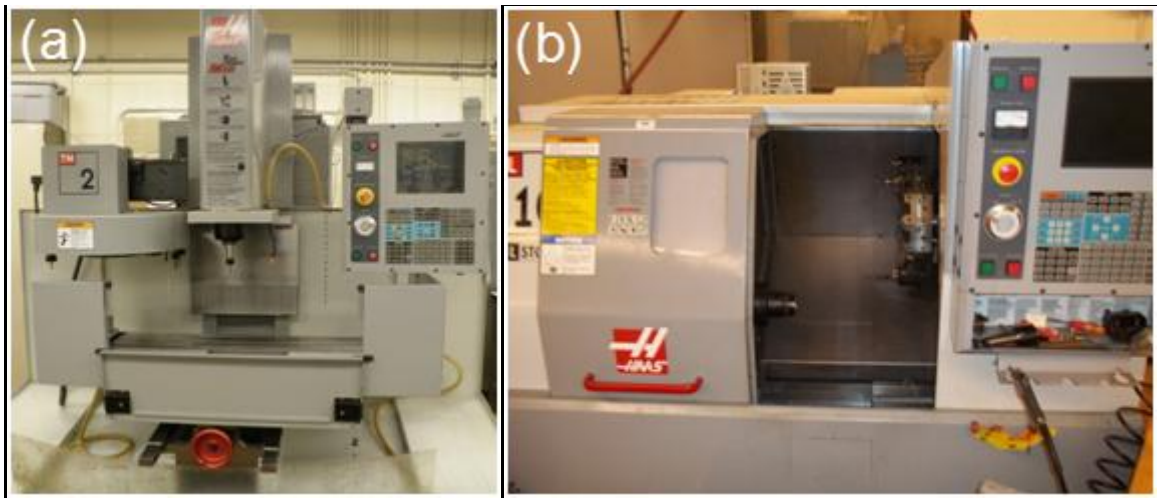

Figure 4.6 Photograph of (a) CNC Mill (Haas model TM-2) and (b) CNC Lathe (Haas model SL-10)

Due to high costs of machining Ti-6Al-4V, the adhesion samples were machined according to ASTM C633-01 alternative substrate and fixture apparatus as their geometry is much simpler. Instead of machining threads inside the samples, the bond plugs are pierced with a single hole allowing a shear pin to link them to the sample holders. Technical drawings of the samples can be found in Appendix A.

The simulated damage samples were machined on the CNC mill to form a 1.5 mm deep gouge with a 10 to 1 slope as shown in Figure 4.7. The depth of the gouge was chosen to be 1.5 mm as it is sufficient to completely remove completely any small damages or cracks on the surface of the parts. The minimum slope angle used in the aerospace industry for a proper stress distribution is typically a 20 to 1 slope. However, these samples are typically large, therefore the cost of spraying these samples was reduced by proving the feasibility on a 10 to 1 slope. Furthermore, research has shown that a small spray angle variation (lower than 10 degrees) from 90 degrees does not affect deposition efficiency significantly [80].

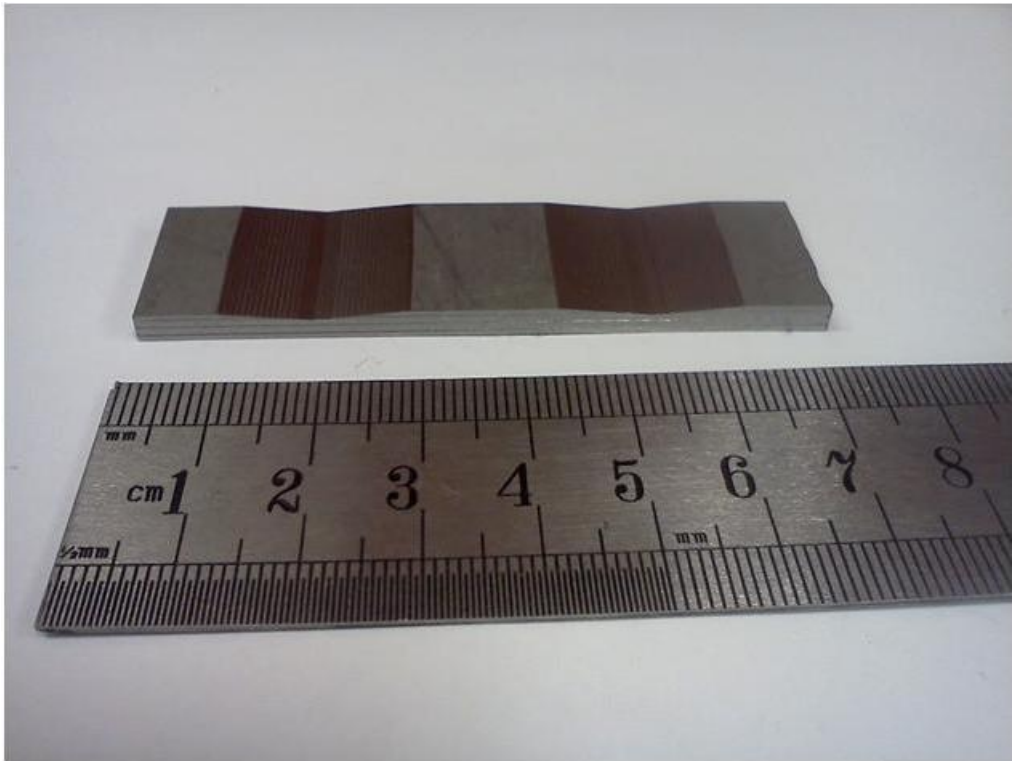

Figure 4.7 Simulated damage samples with a 10 to 1 machined slope

4.1.3. Substrate Material Processing

The powders were sprayed onto 3 mm thick Ti-6Al-4V substrates. Prior to the coating process, the substrates were cleaned/degreased and air dried to remove any contaminants that could negatively affect the coating quality. The substrates were not grit blasted prior to spraying as it is often the practice in Cold Spray, as this has shown to reduce fatigue endurance [81] and bond strength [82]. Coatings for adhesion strength tests were produced according to ASTM C633-01 standard onto Ti-6Al-4V acetone cleaned/degreased standard test samples having a 25.4 mm diameter and an overall length of 60 mm. A single pass using different steps size was required to spray the whole sample to the required coating thickness.

4.2. Coating Deposition and Characterization Equipment

The spray and characterization equipment and procedures used throughout this study are outlined in this section.

4.2.1. Low Pressure Cold Gas Dynamic Spray (LPCS) Facility

The following sub-sections present a detailed description of the LPCS facility developed at the University of Ottawa Cold Spray Laboratory. This system is custom built equipment to be used as a research platform for the commercially available LPCS 10kW EP system manufactured by Centerline (Windsor) Ltd. A picture of this spraying process is shown in Figure 4.8.

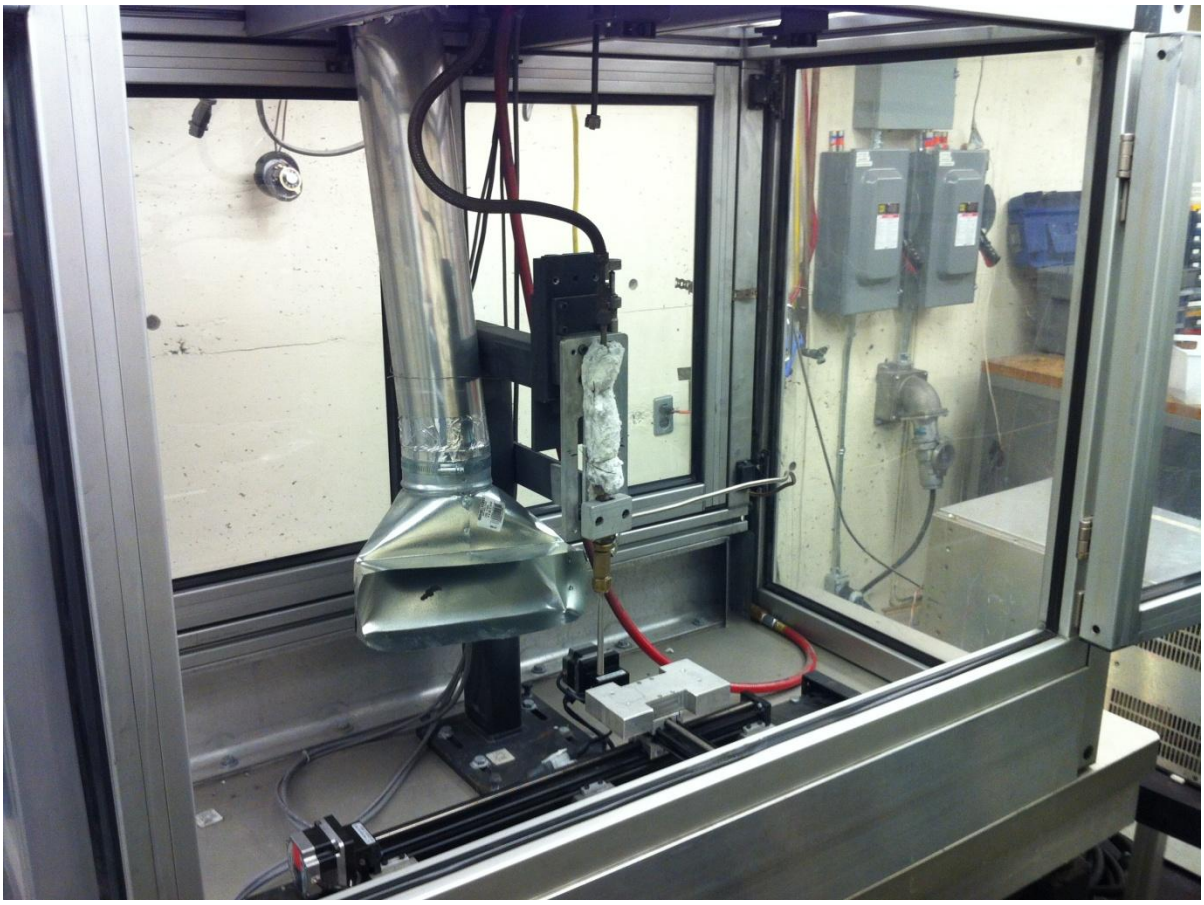

Figure 4.8 University of Ottawa 10 kW LPCS system

4.2.1.1. Driving Gas Supply

As described in Chapter 2, different driving gases such as nitrogen and helium can be used with the LPCS system. Although nitrogen offers an economical advantage, helium is commonly used with feedstock powder materials requiring large critical velocities such as titanium. Due to its high specific heat ratio and low molecular weight, speed of sound in helium is considerably higher (1015 m/s at room temperature) than in nitrogen (346 m/s at room temperature) and produces faster gas velocities to accelerate particles above their critical velocities. Mixtures of these two gases might have seemed to be an interesting solution due to the low cost of nitrogen and high speed of helium, however research has shown that no major economic benefits are observed using helium and nitrogen mixtures [83]. In this research, the CP titanium coatings were produced using helium as the driver gas and few coatings were also deposited using nitrogen. In addition to the lower particle velocities encountered when using nitrogen, the CP titanium powder could potentially react chemically creating undesirable nitrides inside the coating, hence helium was preferred.

In the uOttawa Cold Spray Laboratory, four nitrogen bottles are joined to a manifold providing gas to the gas regulator. Nitrogen is used to warm up the entire system up to roughly 80% of the desired spraying temperature which can take several minutes. This operation substantially reduces the gas-related operating costs, since helium is 6 times more expensive than nitrogen. Upon reaching 100°C below spraying temperature, the driving gas is switched to helium using a 3 way ball valve (Figure 4.10). Six helium bottles are connected together via another manifold to ensure minimal pressure variation and long duration sprays at high pressures (Figure 4.9). The driver gas pressure is adjusted by hand with the pressure display of the screen (Figure 4.10). The data shown on the screen is more reliable as it measures the pressure just before the nozzle after the expansion due to gas heating. The maximum operating pressure of this system is limited by the section that will withstand the lowest maximal pressure; with the LPCS, the weakest section is the throat/nozzle assembly rated at 1.7 MPa, hence the maximal operating pressure of this system is 1.7 MPa.

Figure 4.9 Photograph of nitrogen and helium gas supply

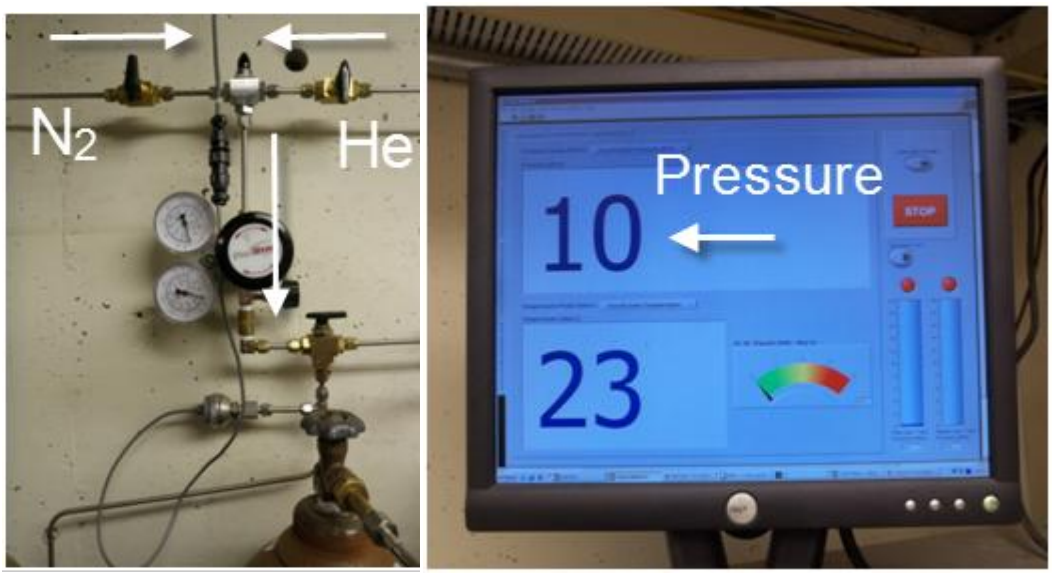

Figure 4.10 Photograph of three-way ball valve and gas regulator (left) and live pressure display (right)

4.2.1.2. Gas Heater and Power Supply

The pressurized gas coming from the regulator is heated using a coil-shaped stainless-steel tube with an outside diameter of 5/8" connected to a 30kW DC power supply shown in Figure 4.11(a). The coil acts as an electrical resistance and dissipates the power into heat producing inlet gas temperatures of up to 1,000°C. The heat is transferred by convection as the gas flows through the coil heater. The power delivered to the heater can be adjusted manually with a variac control, thus controlling the working gas temperature. To reduce heat losses to the environment, the coil heater is insulated with ceramic wool as shown in Figure 4.11(b).

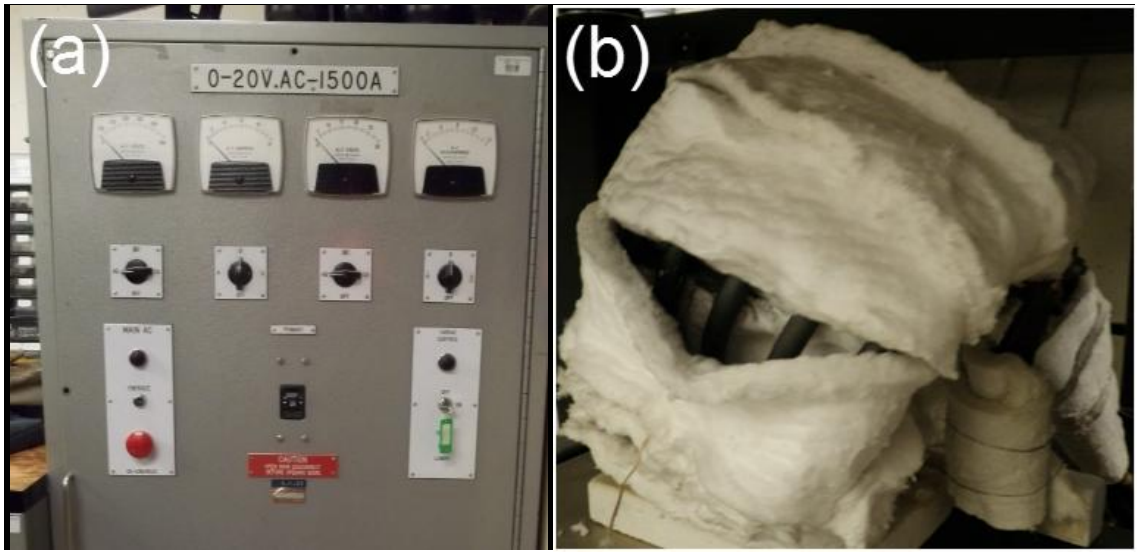

Figure 4.11 Photograph of (a) DC 30 kW power supply and (b) Electric coil heater

4.2.1.3. Spraying Chamber and Accessories

The CGDS equipment is mounted inside an air-tight chamber with 4 clear acrylic doors and acrylic walls providing accessibility and visibility from all sides. A ventilation unit is attached to the spraying chamber to collect gases and powder particles. It consists of a 1.5 hp fan combined with a 0.4 μm particulate filtration unit. A photograph of the spray chamber is presented in Figure 4.12.

Figure 4.12 Photograph of the CGDS spray chamber

The spray booth is also equipped with a two axes traverse system (Velmex Inc., China) to ensure substrate displacement during the spraying process. The stepper motors are controlled using a computer interface and have a straight line inaccuracy of 0.01%. The software uses simple line commands to control the motors. Programs to spray multiple passes and different step size can be written by the user. The nozzle stand-off distance is adjusted accurately with a micrometer on a linear stage holding the nozzle. The final adjustment is done at operating temperature to compensate for the thermal expansion of the nozzle. The accessories inside the spray chamber are shown in Figure 4.13.

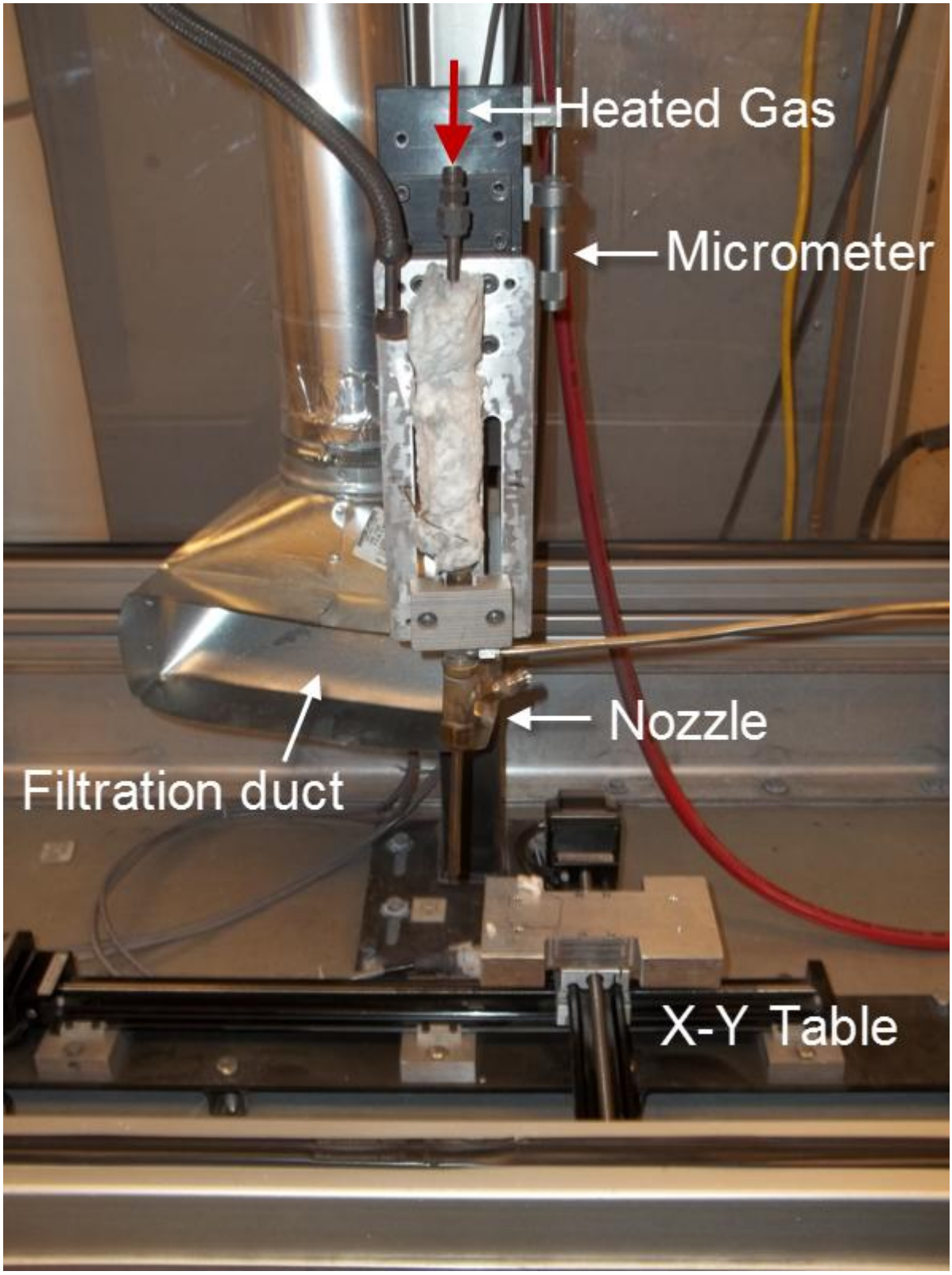

Figure 4.13 Photograph of spray chamber equipment

In order to record all the spraying conditions and parameters, a Labview program was developed. This program displays in real time the gas pressure and temperature. It also records the variation of driving gas pressure and temperature versus time as well as the gas supply pressure which will be required for gas consumption measurements. The two different displays of the program are shown in Figure 4.14.

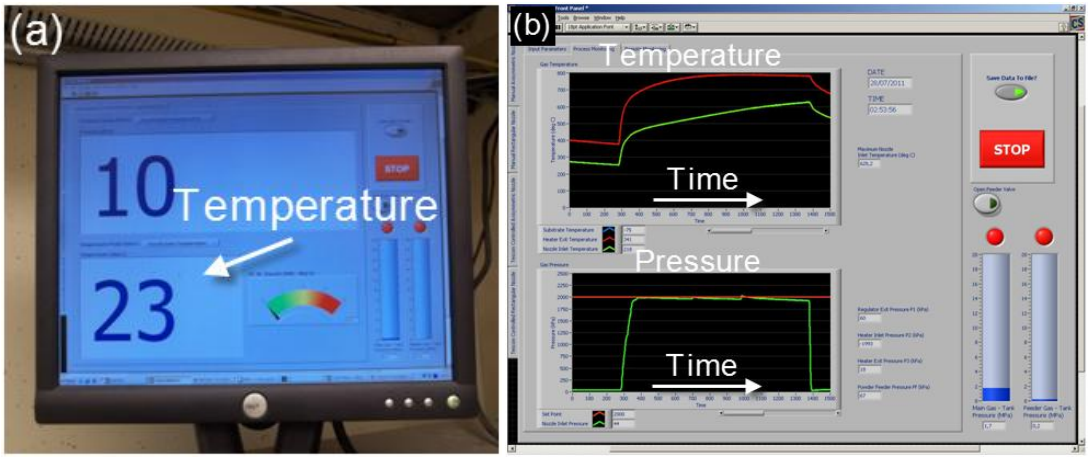

Figure 4.14 Photograph of (a) the Labview live temperature display and (b) the temperature and pressure versus time

4.2.1.4. Low Pressure CGDS Nozzle

For the current study, the CGDS system was equipped with a standard commercially available low pressure throat/nozzle assembly. It has been designed to be low cost and quickly interchangeable as seen in Figure 4.15. The nozzles are manufactured by hydroforming to produce a smooth and straight diverging nozzle. The throat orifice diameter has been set at 2.0 mm as a larger throat would lead to a higher flow rate and a lower maximal gas temperature. The nozzle exit diameter is 6.5 mm thus the exit to throat area ratio is 10.

Figure 4.15 Commercially available throat and nozzle assembly

4.2.2. Pulsed Gas Dynamic Spray (PGDS) Facility

In this section, the main components of the PGDS system are presented; the driving gas supply, the gas heater, the rotary valve, the barrel, the spraying chamber and the PGDS control screens. The equipment presented in this section is the commercial system manufactured by Centerline Ltd (Windsor, Canada). It has been built based on the patent and development carried out at the uOttawa Cold Spray Laboratory. Some of the process development can be found in Appendix A. A detailed drawing of the PGDS spraying technique and a picture of the PGDS gun are presented in Figure 4.16 and Figure 4.17.

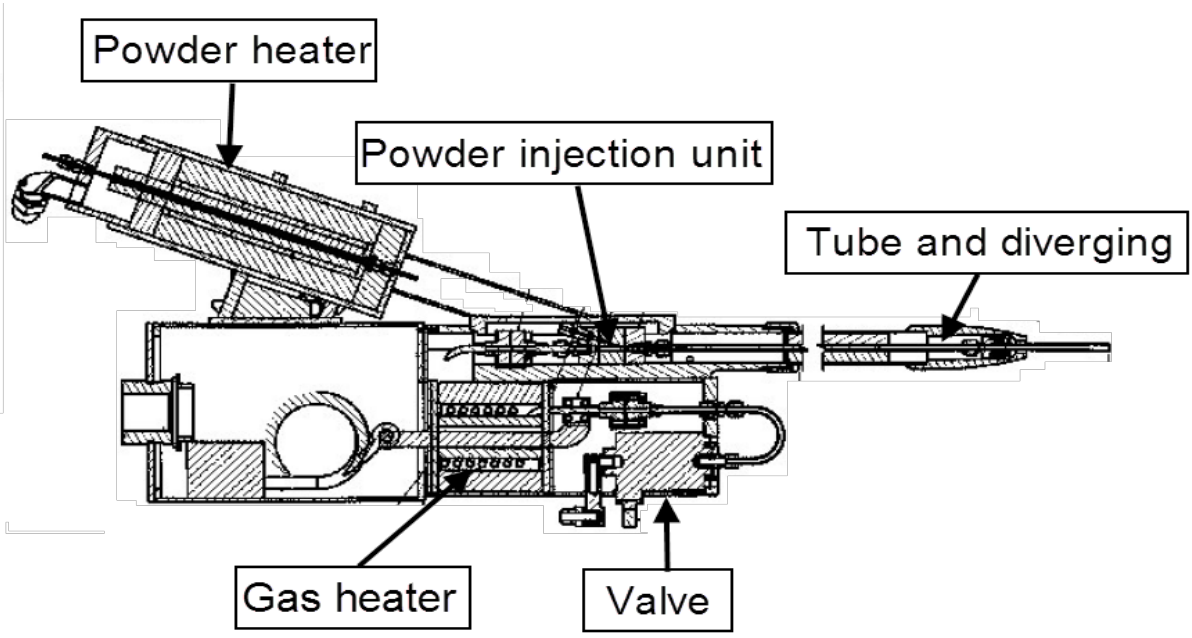

Figure 4.16 Detailed drawing of the PGDS gun [84]

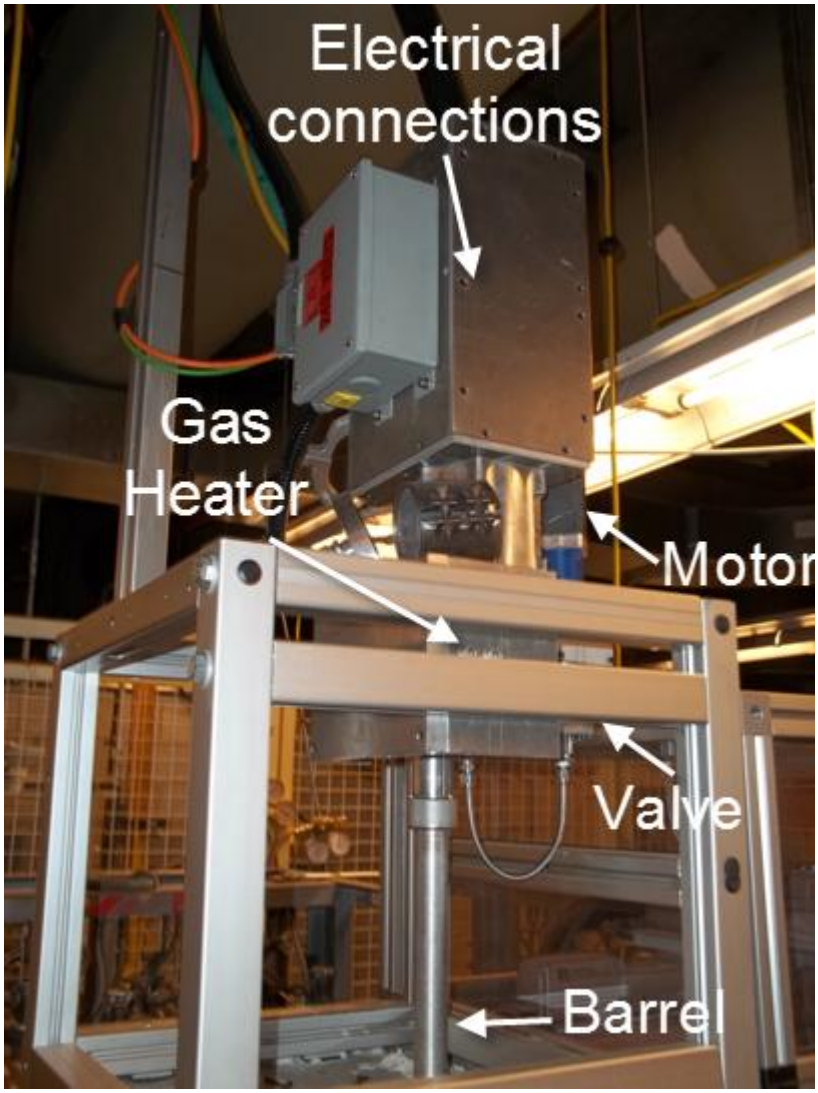

Figure 4.17 PGDS gun

4.2.2.1. Driving Gas Supply

As previously discussed in Section 4.2.1.1, helium will be used as the main driving gas and few tests will be conducted using nitrogen.

The PGDS system is installed in a less confined space than the CGDS equipment and the use of 11 gas cylinders contained in bottle packs is therefore possible. These commercial bottle packs are available for both helium and nitrogen gases as shown in Figure 4.18.

Figure 4.18 Nitrogen and helium bottles packs

The first pressure reduction stage is done using a gas regulator connected to the bottle pack. The pressure is set to the maximum rated pressure of the PGDS system, 5 MPa. A three way ball valve, located on the side of the control desk, allows the operator to switch from pressurized air while preheating the system to the driving gas once ready to spray (Figure 4.19). Pressurized air is also used for cooling down the system to 100°C; the temperature at which it is safe to turn off the equipment. A 3/8" diameter heated flexible hose supplies the gas from the ball valve up to the rotary valve.

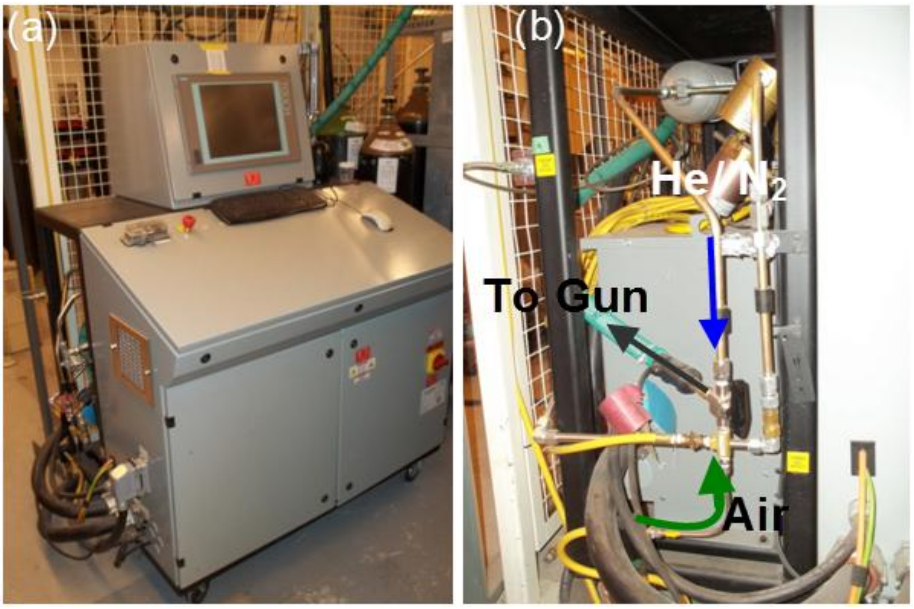

Figure 4.19 Photograph of (a) operator control station and (b) three-way ball valve to switch from driving gas to pressurized air

4.2.2.2. Power Supply and Gas Heater

The PGDS system is powered by a 14kW 600V 3 phase transformer. The gas heater is similar to the CGDS system; however its coil is made of a 1/4" diameter 1.4 m long Inconel tube. The gas heater has been thoroughly insulated with ceramic wool to reduce heat losses and can reach steady gas temperatures of up to 800°C. The electrical connections for the gas heater are cooled down with pressurized air for safety reasons. The gas heater assembly can be seen in Figure 4.20.

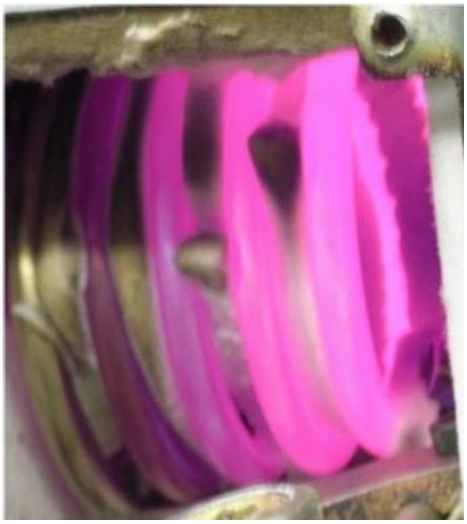

Figure 4.20 PGDS gas heater glowing at high temperature [50]

4.2.2.3. Valve and Barrel Assemblies

A rotary valve has been developed specially for the PGDS system. Previously, a solenoid valve was opened and closed quickly to create the shockwave. However, the valve lifetime in this operating condition was only several hours. The new valve is a slotted rotating disk turning on a seal with exit ports. As the disk turns, it aligns with the open ports creating a strong gas pulse. The pulsation speed is controlled by the motor rpm. The opening angle of the disk and the seat are critical as well since they change the valve opening time and total open area, hence gas flow. Most of these parameters are dependent on each other as changing one will also affect the others. The different components of the rotating valve are shown in Figure 4.21.

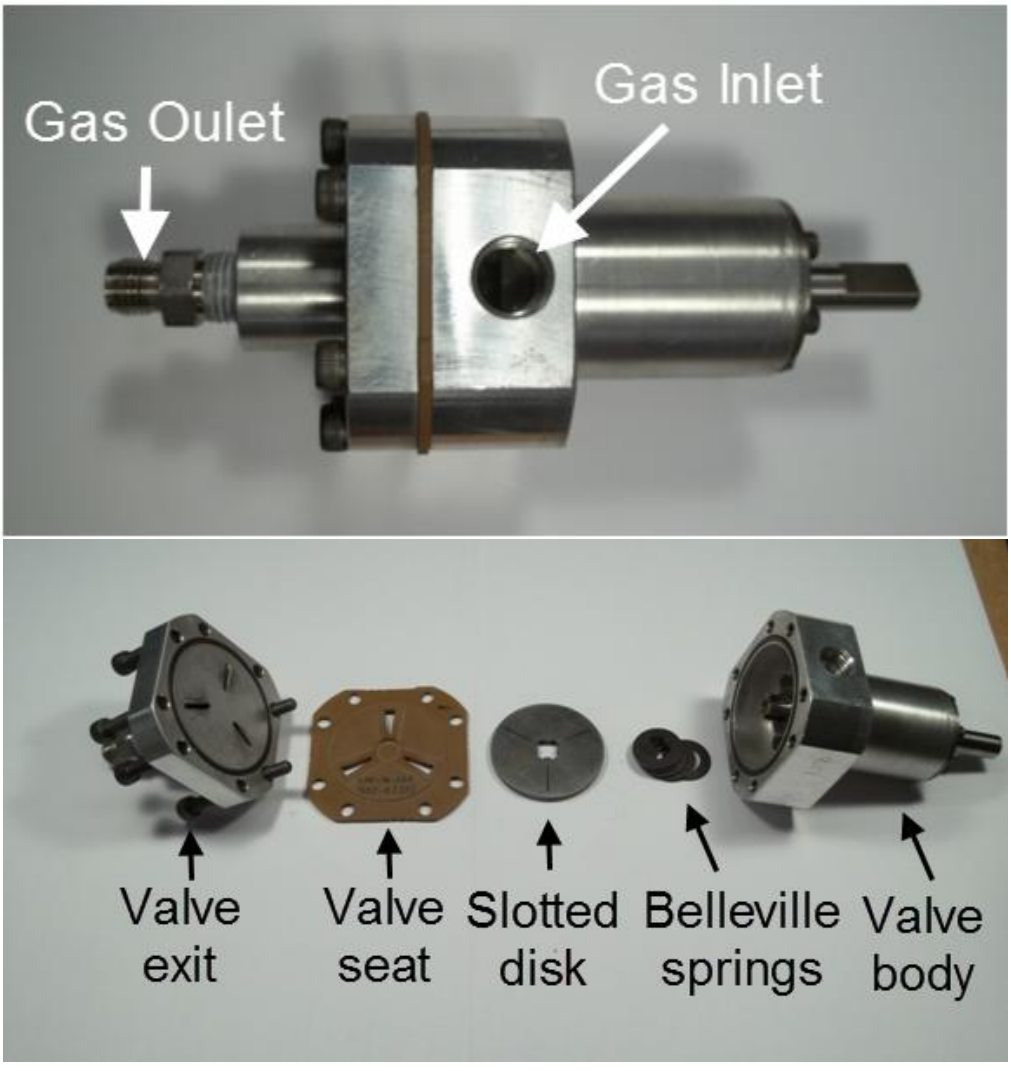

Figure 4.21 Rotary pulsing valve assembly (top) and components (bottom)

Upon creation of the shockwave, the gas pulse travels through the driving gas heater, then collects powder at the injection point. The particles caught by the shockwave travel through the barrel of the PGDS system before exiting the nozzle. A tapered tip is placed at the end of the barrel to increase the spraying pattern area and to further increase the gas velocity [23]. The barrel and nozzle assembly is presented in Figure 4.22.

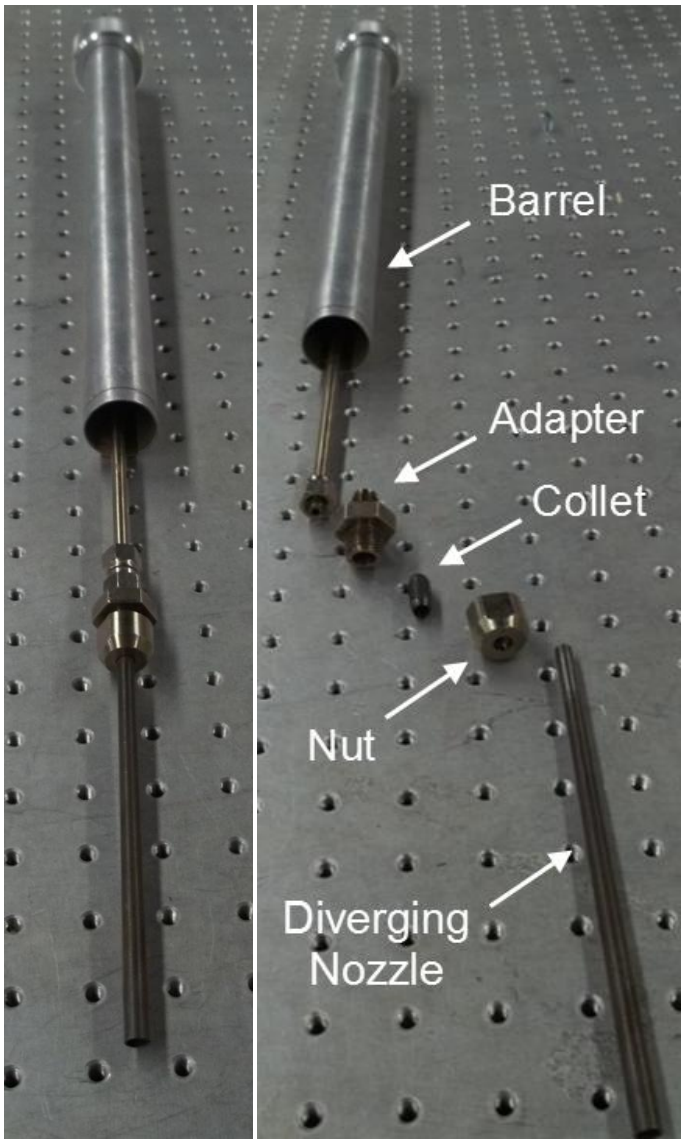

Figure 4.22 Barrel and nozzle assembly (left) and associated parts (right)

4.2.2.4. Spraying Chamber and Accessories

The PGDS gun is mounted at the top of the spraying booth. The gun was chosen to be fixed rather than mounted on a robot for costs and space considerations. A two axes traverse system (Velmex Inc., China), enclosed in an air-tight shell, is composed of two electronically controlled stepper motors with a straight line inaccuracy of 0.01%. It is used to move the substrate under the spray gun. They are controlled using the same software and control system as the CGDS system. The sample holder is placed on a small adjustable table lift in order to adjust the stand-off distance. For health and safety reasons, the air inside the spraying chamber is filtered using a water filtration unit to remove particles that did not adhere during the process. This unit is connected with a duct to the spray chamber. The accessories inside the spray chamber and an overall view of the PGDS system are shown in Figure 4.23.

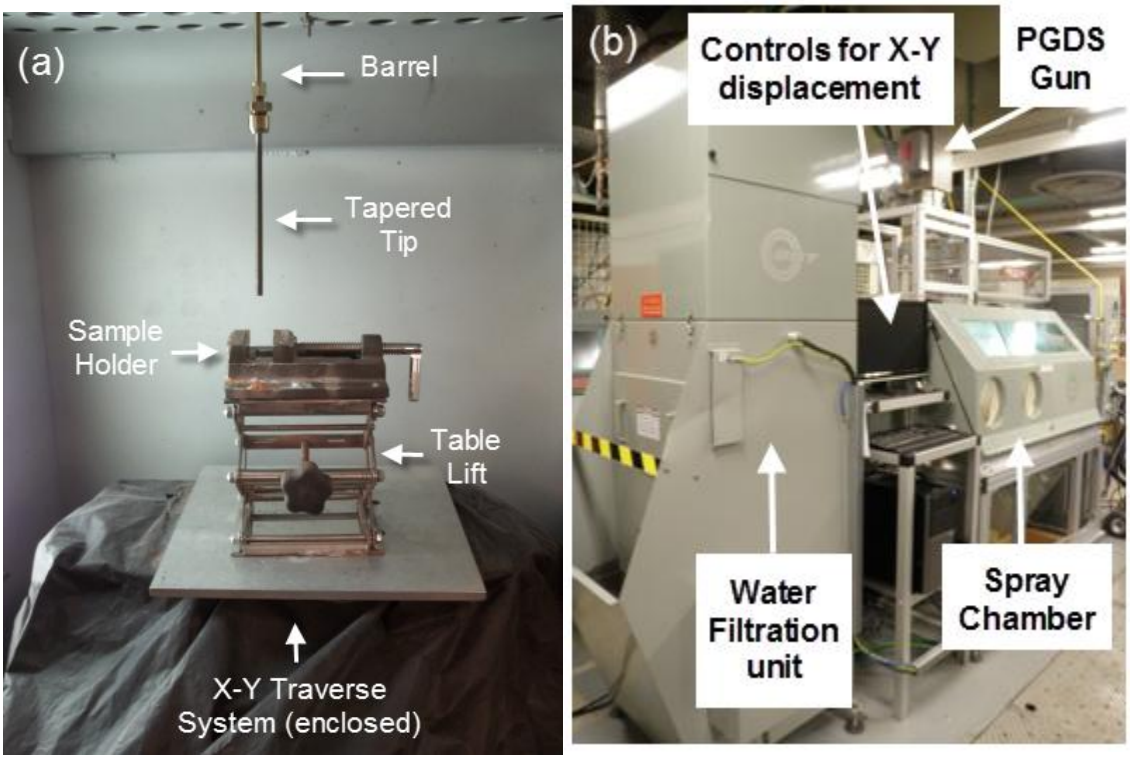

Figure 4.23 Photograph of (a) PGDS spray chamber and (b) overall view of PGDS system

4.2.2.5. PGDS Controller Screen

The driving gas pressure, temperature and pulse frequency are controlled from the main operator screen. The computer regulates the second pressure reduction step using a gas pressure regulator. The driving gas heater can be turned on and off from the same operation window as seen in Figure 4.24. Using a different user window, the valve frequency of the pulsing valve can be changed from 1 Hz to 30 Hz. The program automatically calculates the required motor speed, taking into account the reduction unit, to provide the desired pulse frequency. On this screen (Figure 4.25), the valve can also be turned on and off as desired.

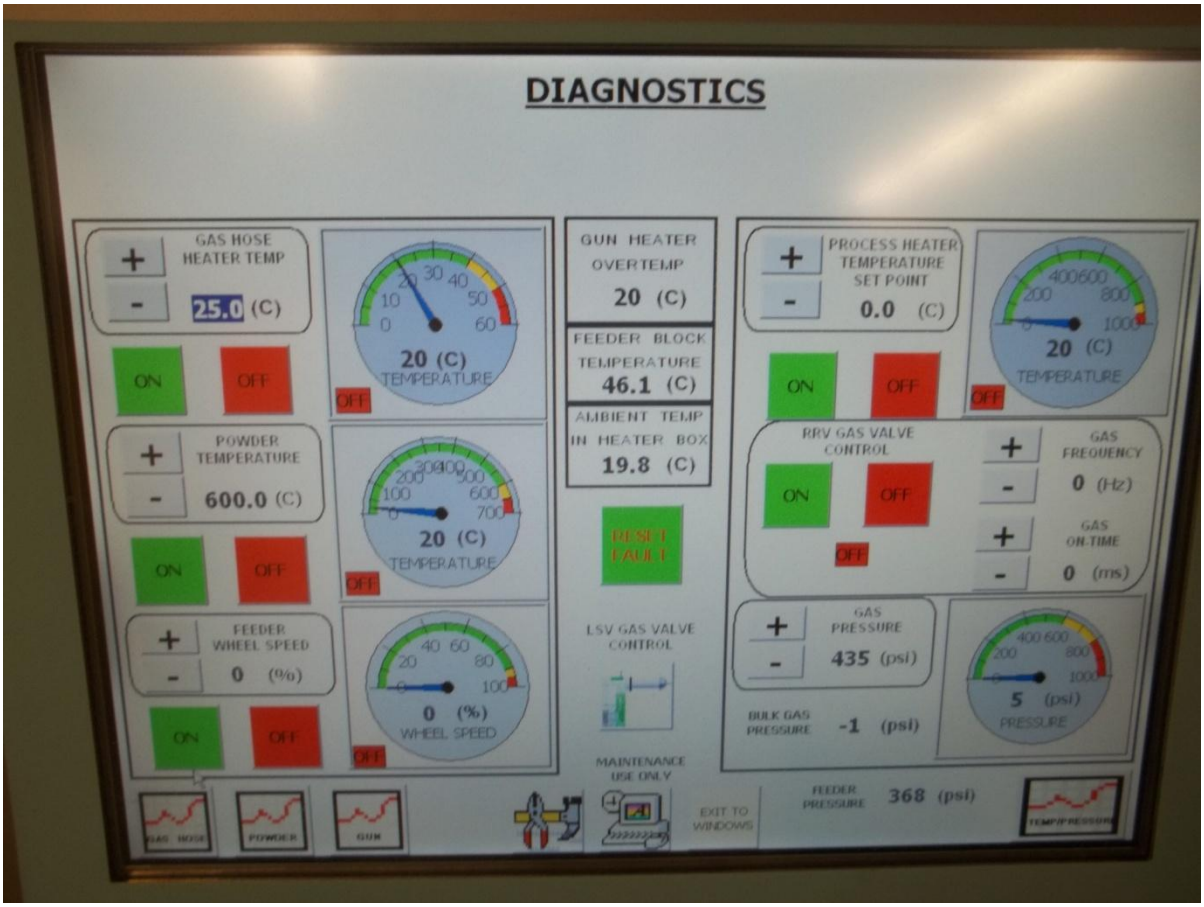

Figure 4.24 PGDS main controller screen

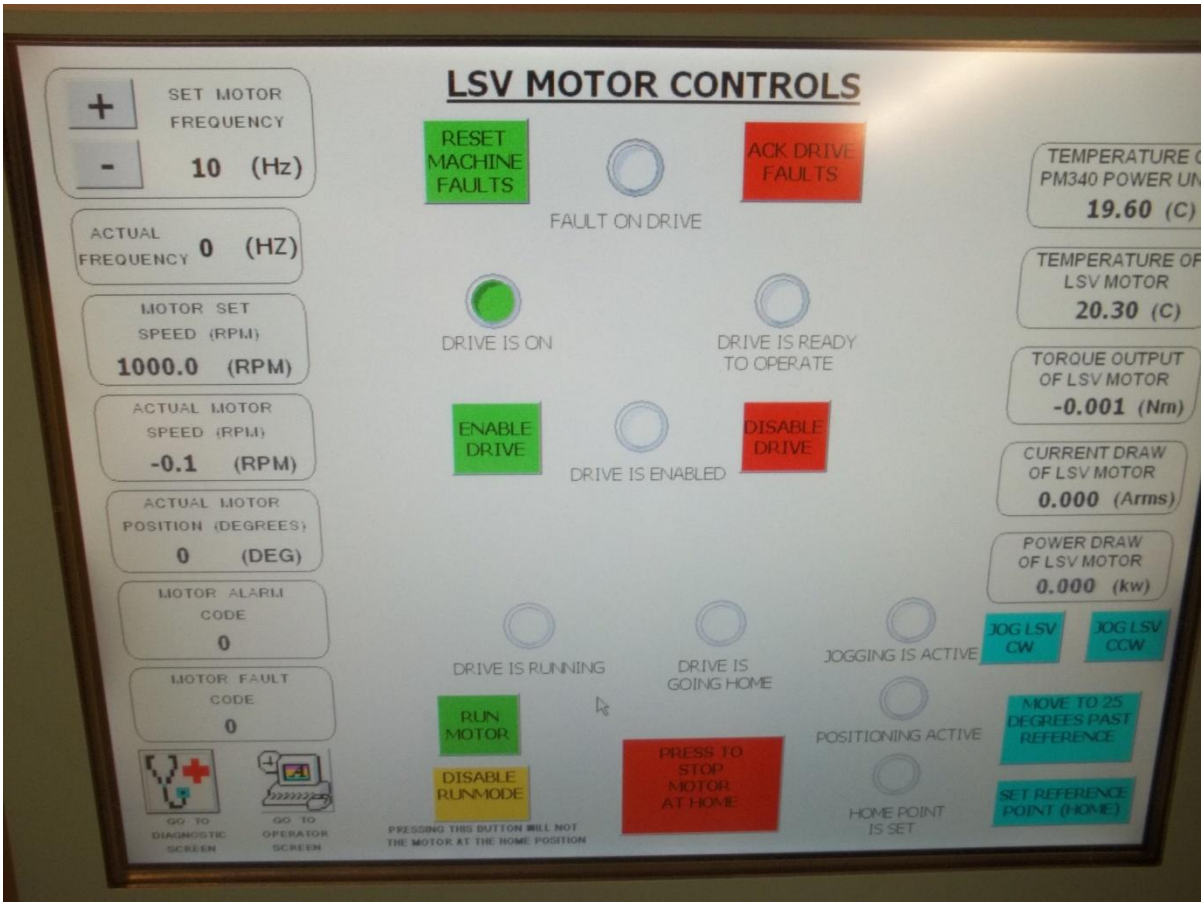

Figure 4.25 PGDS pulsing valve control screen

4.2.3. Powder Supply and Control

The following section describes the powder management and control for the two spraying systems.

4.2.3.1. Powder Feeder and Accessories

The powder is delivered to the spraying unit by means of a commercially available powder feeder (Model 1264, Praxair Surface Technologies, Concord, NH, USA) presented in Figure 4.26. The powder is slowly delivered by a rotating powder carrier disk and a tamper assembly is used to help the powder fill the holes. The powder feed rate can be adjusted by changing the feeder rpm and the gas carrier flow rate. In this work, the smallest feeder disk (320 holes) was chosen to achieve low powder feed rates based on preliminary experiments. The feeder rpm and gas carrier flow rate will be optimized by experimentation. The gas powder carrier is adjusted using a flow meter connected to a gas regulator set at the maximum rated pressure (1.7 MPa) of the feeder canister. During operation, the disk rotates and the carrier gas fluidizes the powder as it passes past an exit port. The mix of gas and powder then flows into the powder heater before being injected into the main driving gas stream.

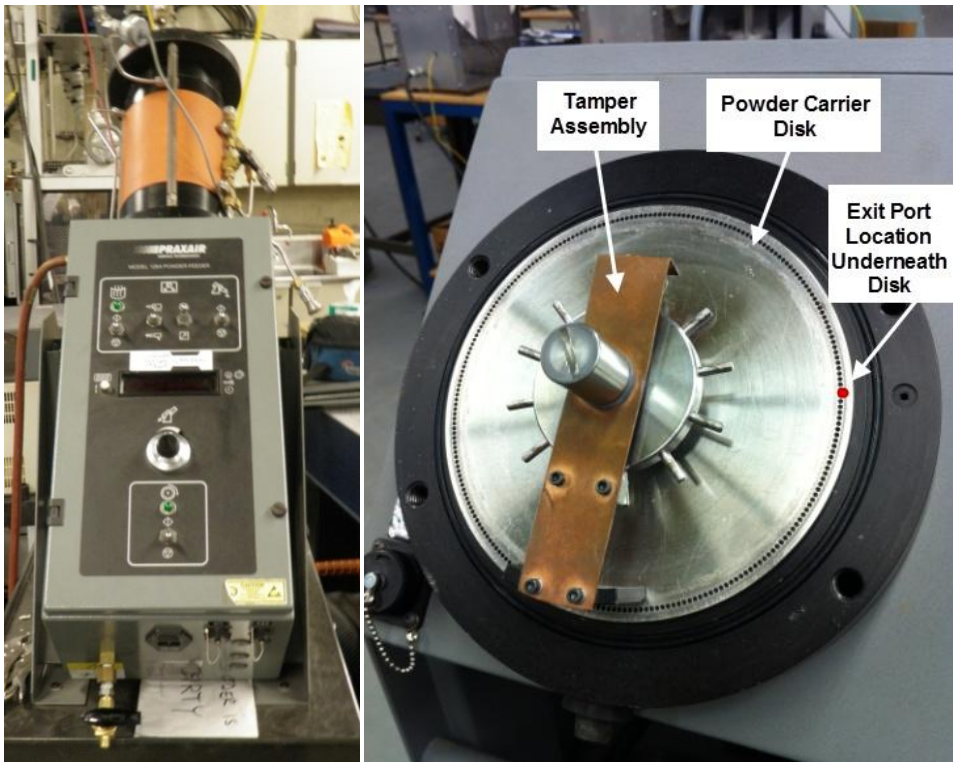

Figure 4.26 Photograph of powder feeder (left) and with container removed (right)

Figure 4.27 Gas pressure regulator and flow meter of the powder carrier gas

4.2.3.2. Powder Heater, Power Supply and Control

The powder heater is constructed following the same principle as the driving gas heaters. A 6 foot long 1/4" diameter 316 stainless steel tube with a 0.035" thick wall is coiled. It acts as an electrical resistance for the 8 kW powder supply to transfer heat through convection to the powder carrier gas; it can reach up to 1100°C. The coil has been plasma sprayed with alumina to reduce oxidation due to high temperature cycles and enhance its longevity. The coil is thermally insulated with ceramic wool and enclosed in a 3" diameter alumina tube. The coil temperature is read from a thermocouple placed at the middle section of the coil and displayed on a thermocouple reader shown in Figure 4.28. The coil temperature is controlled by a variac that changes the current from the power supply.

Figure 4.28 (a) Stainless steel powder heater coil alumina coated, (b) Temperature reader and (c) Power supply

4.2.3.3. Powder Feed Rate Measurements

Live powder feed rate measurements are difficult to perform. In LPCS and PGDS, the feed rates are usually only few grams per minute and therefore require a scale that is able to detect very low mass changes. However, such scales also have a maximum mass rating that is much less than the total mass of the powder feeder. Thus, a specialized scale has to be incorporated to the powder feeder and different models are now commercially available. Unfortunately, this equipment was not available in the laboratory and an alternative was developed to measure the powder feed rates.

Powder feed rate measurements were done using the same gas carrier flow rate and feeder wheel rpm used during the spraying processes. This replicates exactly the spraying conditions as the same pressure differential between the gun and the feeder canister. Using a 0.5 μm particle filter bag, the powder is collected at the powder feeder exit for 2 minutes. The filter weight difference divided by the spray time gives the powder feed rate in grams per minute. This process was repeated 6 times for each spraying system conditions to determine a reliable rate and statistical error.

4.3. Material Characterization

This section describes the material characterization approach employed in order to complete the objectives of this study. More specifically, the procedures and equipment of the University of Ottawa Material Characterization Laboratory used to characterize the coating properties are presented.

4.3.1. Sample Preparation

Once the coatings have been produced, they have to be prepared prior to microstructural investigation of the cross-sections. First, the coatings are sectioned at different locations using a precision wet saw (Struers Secotom-10). The resulting cross-sections are then mounted in a thermosetting epoxy resin (Struers LaboPress-3). Samples are polished according to CP titanium Struers polishing method using an automated polisher (Struers Tegrapol with TegraForce-5 and TegraDoser-5 attachments). Samples are gold sputtered (Denton Vacuum Desk IV) prior to SEM observations for electrical conductivity. Photographs of this equipment are presented in Figure 4.29.

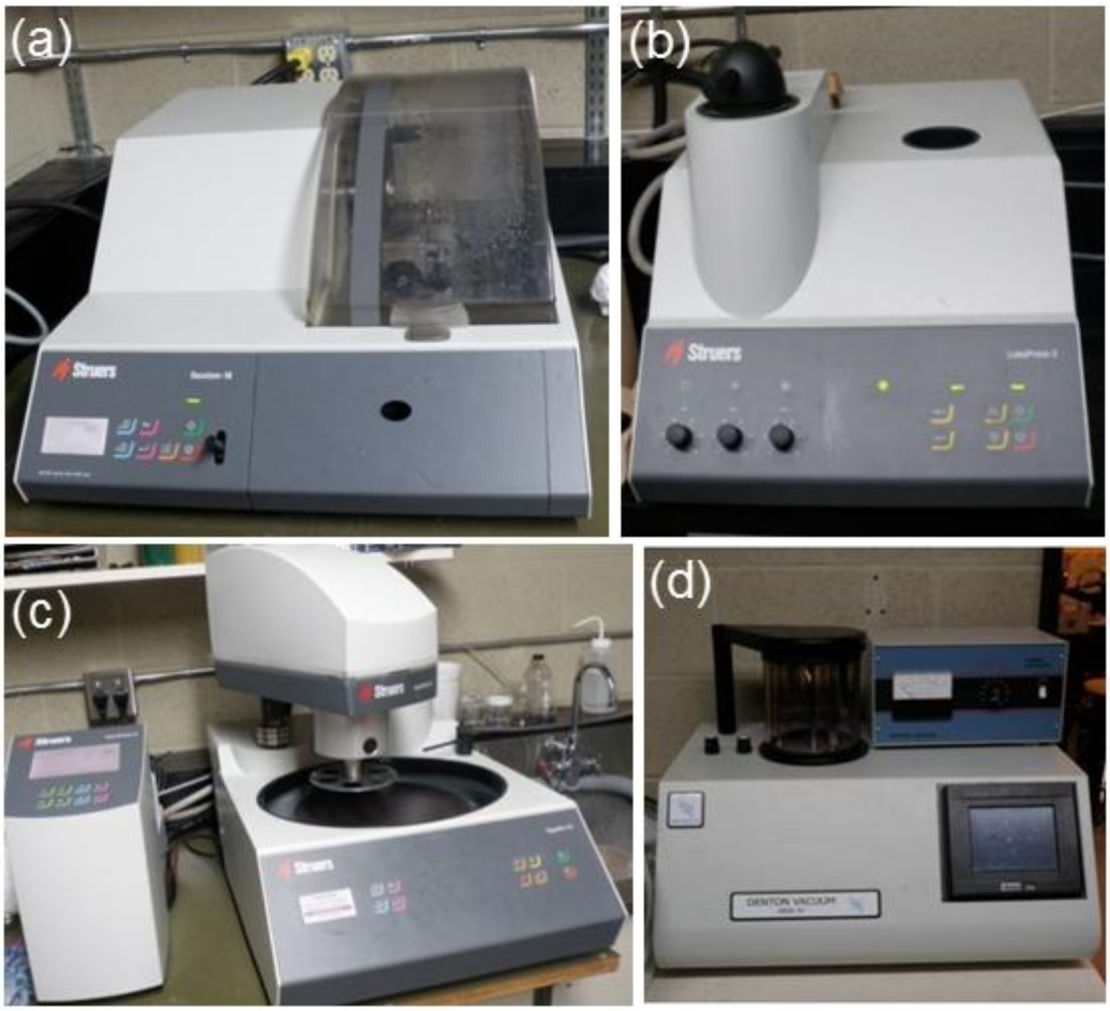

Figure 4.29 Sample preparation equipment prior to optical microscope and SEM microstructural investigation:
(a) Precision wet saw with aluminium oxide blade (Struers Secotom-10)
(b) Thermosetting resin mounting chamber (Struers LaboPress-3)
(c) Sample polisher (Struers Tegrapol, TegraForce-5 and TegraDoser-5)
(d) Gold sputtering (Denton Vacuum Desk IV)

4.3.2. Microstructure Characterization

Qualitative and quantitative characterizations of the CP titanium coatings were performed using various methods. The coatings microstructure was assessed by examining the cross-sections using optical microscopy (OM, Kingdak NMM-800TRF) and scanning electron microscopy (SEM, EVO-MA10, Zeiss, UK). The SEM is equipped with secondary electron (SE), back-scattered electron (BSE), energy dispersive spectroscopy (EDS), electron backscatter diffraction (EBSD) and X-ray computed tomography (CT) detectors. These instruments are shown in Figure 4.30 and Figure 4.31.

Figure 4.30 Photograph of optical microscope (Kingdak NMM-800TRF)

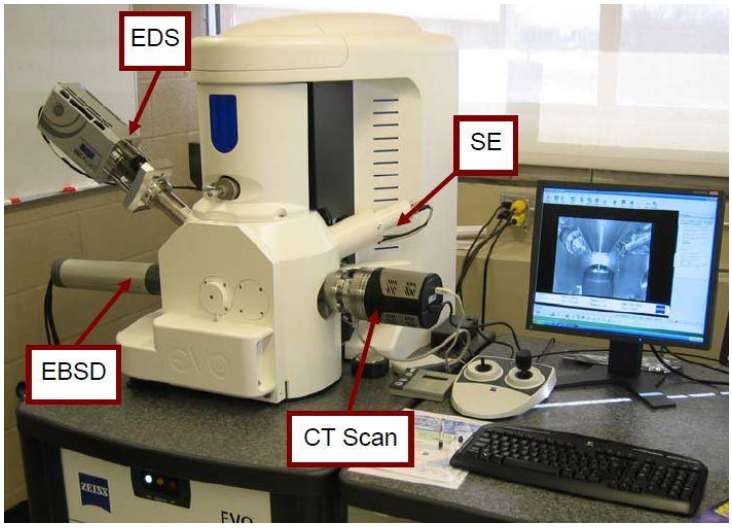

Figure 4.31 Photograph of scanning electron microscope (Zeiss Evo10) with SE, BSE, EDS, EBSD and CT scan detectors (adapted from [46])

The quantification of nitrogen and oxygen level in the coatings was done through EDS (X-Act Analytical Silicon Drift Detector, Oxford instruments). A total of nine measurements were done on each sample; three near the substrate-coating interface, three in the middle of the coating and three in the top region of the coating.

Porosity measurements and particles deformation analysis were done on cross-sectioned and polished coatings surfaces using the optical microscope equipped with commercial image analysis software (Vision-Lite, Clemex, Montreal, Canada). Five measurements were taken per cross-section using 200x magnification images, while the intensity range and thresholds were standardized on reference materials. Each porosity value reported represents the average of at least 15 porosity measurements over 3 different cross-sections.

Particle deformation analyzes were performed by compiling the average flattening ratio of the particles inside the coating. This ratio was calculated using multiple methods presented in the literature. Goldbaum calculated the ratio of the width and height of singular splats [85]. Moy defined the flattening ratio as the splat main length over the initial mean diameter of the feedstock powder [86]. Champagne used the ratio of the splat main length over the initial diameter calculated using the equivalent volume of a deformed ellipse (splat) and a sphere ($d_0^3 = d_a^2\, d_b$) where d_0 is the initial diameter, d_a the splat main length and d_b the splat main height [87]. In the current work, the flattening ratio (L/D_o) represents the ratio between the particle main length (L) as deformed in the coating and the mathematically retransformed spherical diameter (D_o) based on the cross-sectional splat area. A schematic representation of different flattening ratios is presented in Figure 4.32. This technique is applied to coating cross-sections; therefore it was impossible to determine if the particles were cut in the vicinity of the splat center. Thus, the values recorded do not represent the absolute flattening ratios but rather qualitative measurements used for coatings comparison. Applying the same technique to all coatings can provide useful data for coating characterization produced with the two cold spray systems. Prior to the measurements, the coatings were etched using Keller's reagent (10 ml HF, 15 ml HNO_3, 75 ml distilled water) to clearly distinguish the particles interfaces. The deformed particle characteristics (area, main length, etc.) were then recorded by image analysis at a magnification of 1,000x on the optical microscope. The average flattening ratio reported cumulates over 350 particles for each powder/process

combination taken at random locations within the coating cross-section. The values used were also compiled to find the powder size distribution inside the coating based on the area measured.

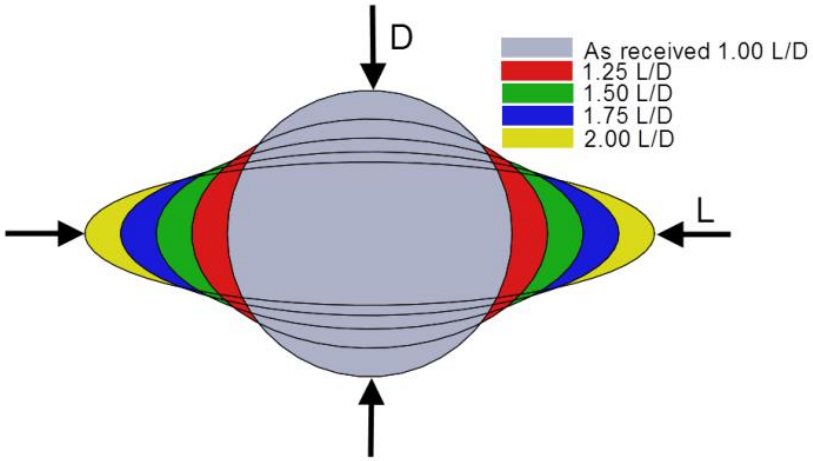

Figure 4.32 Schematic of different flattening ratios

4.3.3. Microhardness

Microhardness measurements were performed to assess the quality of CP Ti coatings for parameter optimization of the LPCS and PGDS processes as well as determining the feasibility of using these coatings for repairs. Microhardness is highly dependent on the coating microstructure, namely the coating's porosity and particle deformation. Porosity inside the coating will lead to weak support of the tested region, increasing the indentation size and resulting in a lower hardness. In addition, cracks between particles can be observed after the indentation was performed, indicating the lack of support underneath the tested region. Furthermore, microhardness measurements provide an impression of the deformation level of the particles since harder coatings are indicative of more deformation and cold-working. Therefore, microhardness testing is a way to assess coatings quality and can be used as an indication of parameter optimization.

The microhardness tests were conducted on polished samples cross-sections using a Vickers microhardness tester (Struers Duramin-1). A 300 g load ($HV_{0.3}$) was used for a duration of 10 seconds while a load of 50 g was applied for powder microhardness measurements. The distance between indentations was at least three times indentation diagonal dimension in order to avoid stress field effects induced by other indentations [88]. Ten measurements were made at various positions on each sample to determine the average values. A photograph of the hardness testing machine is displayed in Figure 4.33.

Figure 4.33 Photogram of Vickers microhardness tester (Struers Duramin-1)

4.3.4. XRD Analysis

X-Ray Diffraction (XRD) was used to identify the crystal structure of the as received materials and sprayed coatings. The XRD analysis were done using a Philip X-Pert model PW 1830 X-ray diffractometer equipped with a monochromator using Cu Kα radiation shown in Figure 4.34. High precision scans were performed for diffraction angles (2θ) ranging from 20° to 90° at 50 steps per degree and acquisition time of two seconds per step. Prior to performing XRD analysis, the substrates were removed from the coatings by slowly grinding down the substrate on the polishing machine.

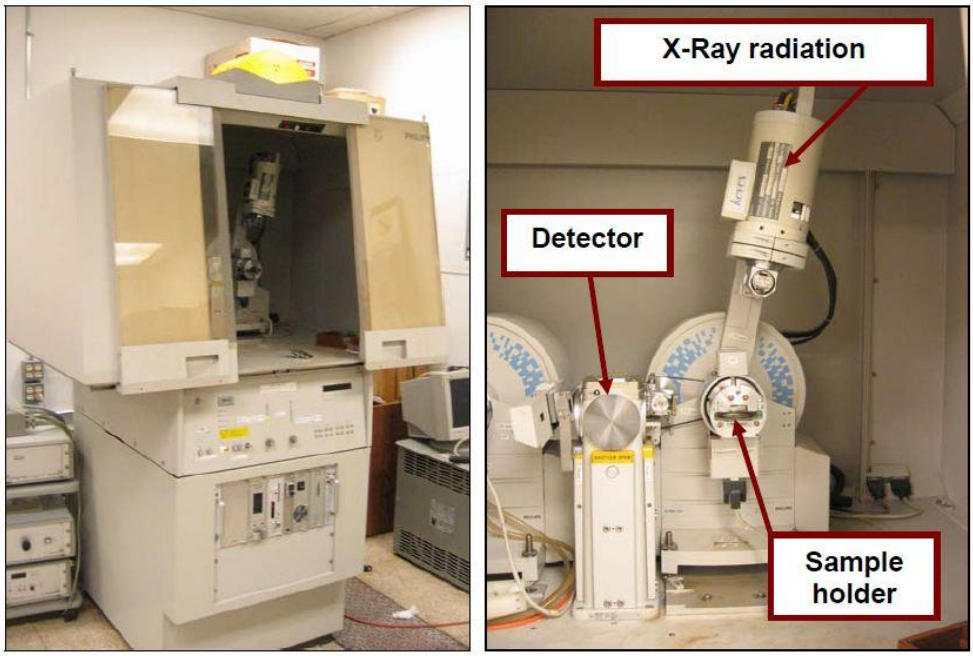

Figure 4.34 XRD equipment used for phase identification of coatings and powders (adapted from [46])

4.3.5. Bond Strength Evaluation

Bond strength evaluations were conducted according to the ASTM Standard C633-01 (Appendix B) [89]. Coatings were deposited on Ti-6Al-4V samples described in Section 4.1.2 using both spraying techniques. A multiple sample hold was designed and built in order to hold the samples during the spray (Appendix C) The coated samples were then carefully aligned and glued to an uncoated sample using a special apparatus shown in Figure 4.35. The technical drawings of this apparatus are included in Appendix D. The adhesive used to bond the test specimens together was an epoxy based film (FM1000, Cytec Engineered Materials, Maryland, USA). The bonding apparatus was placed in a programmable oven at 190°C for 2 hours in order to cure the glue. The adhesion test samples were loaded in tension with a universal tensile machine (Instron model 4482). Before testing the coatings, the bonding agent was tested separately on four uncoated test samples, and failed at 89 ± 2 MPa, which conforms to the product specifications. The average adhesion strength was calculated based on four different test samples for each powder/process combination. The photographs of the different procedures and apparatus to perform this test are presented in Figure 4.35.

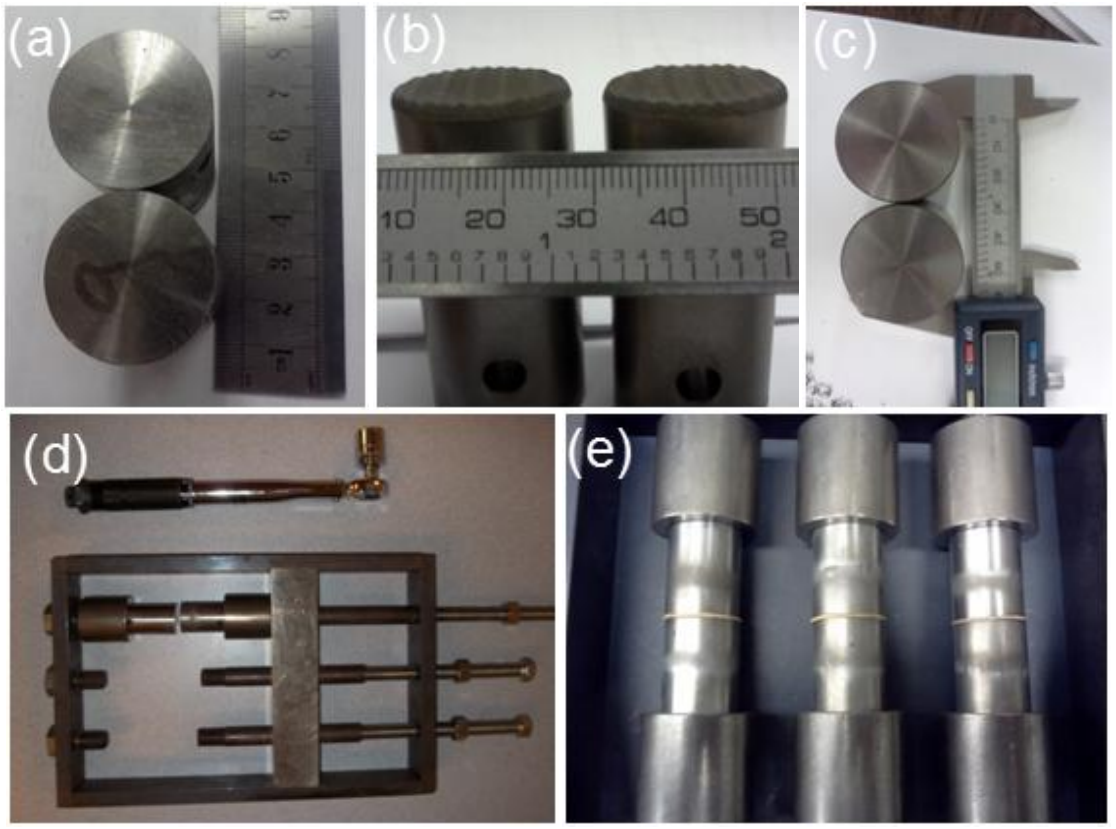

Figure 4.35 Photograph of the adhesion test procedure and apparatus:
(a) Uncoated samples, (b) As-sprayed samples, (c) Machined samples, (d) Gluing device and (d) Glued samples

Figure 4.36 shows an alternative set-up for the ASTM C633-01 standard where shear pins are used to link the samples to the sample holders instead of threads. This set-up reduces costs as titanium is very hard and expensive to machine. The figure also presents the Instron tensile test machine with a usual threaded sample ready to be tested.

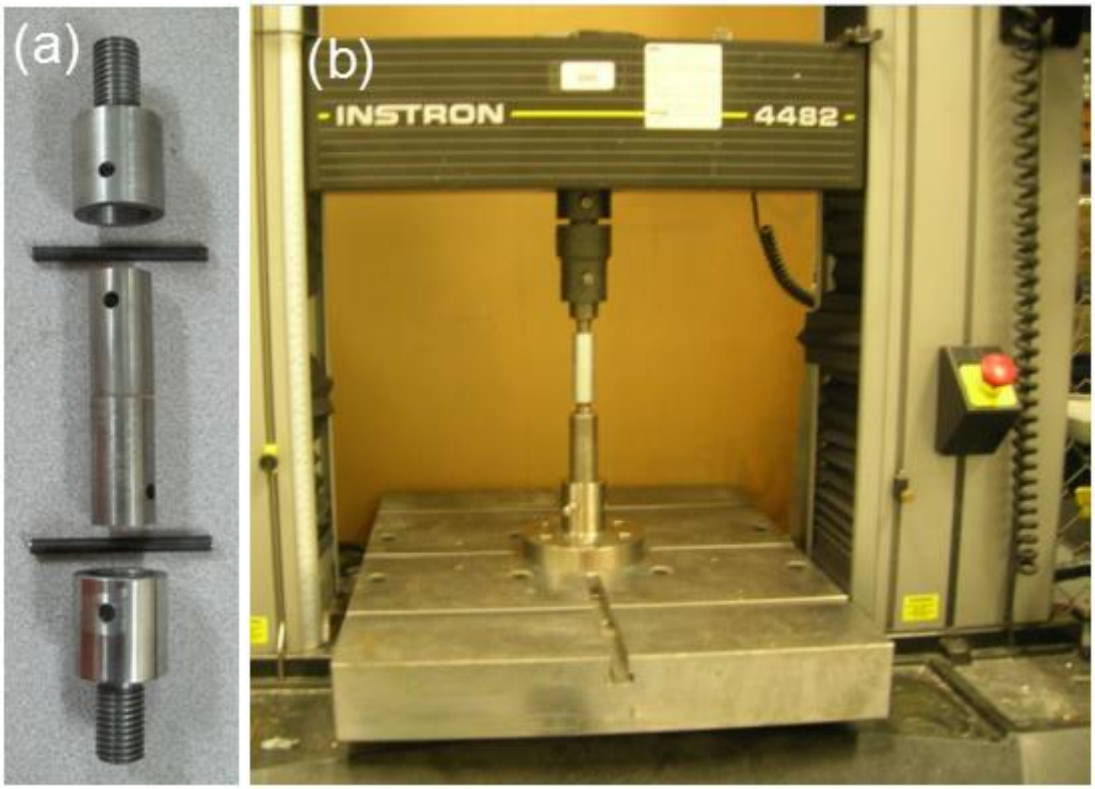

Figure 4.36 Photograph of (a) Adapters, pins and glued samples and (b) Instron machine model 4482

4.3.6. Wear Characterization

Wear tests were performed according to ASTM Standard G133 [90]. Prior to the tests, some parts of the equipment were redesigned and replaced (see Appendix E). The coatings were machined flat to obtain a smooth surface and then ground and polished with 320, 500 and 1200 SiC papers. A load was applied vertically onto the coating surface with a 3/8" diameter ball on the sample at a constant force of 10 N. This test was done without lubrication to represent the actual application environment. The specimens were mounted on an x-axis robot and moved linearly over a distance of 10 mm at a speed of 5 mm/s. The photographs of the wear testing equipment are presented in Figure 4.37.

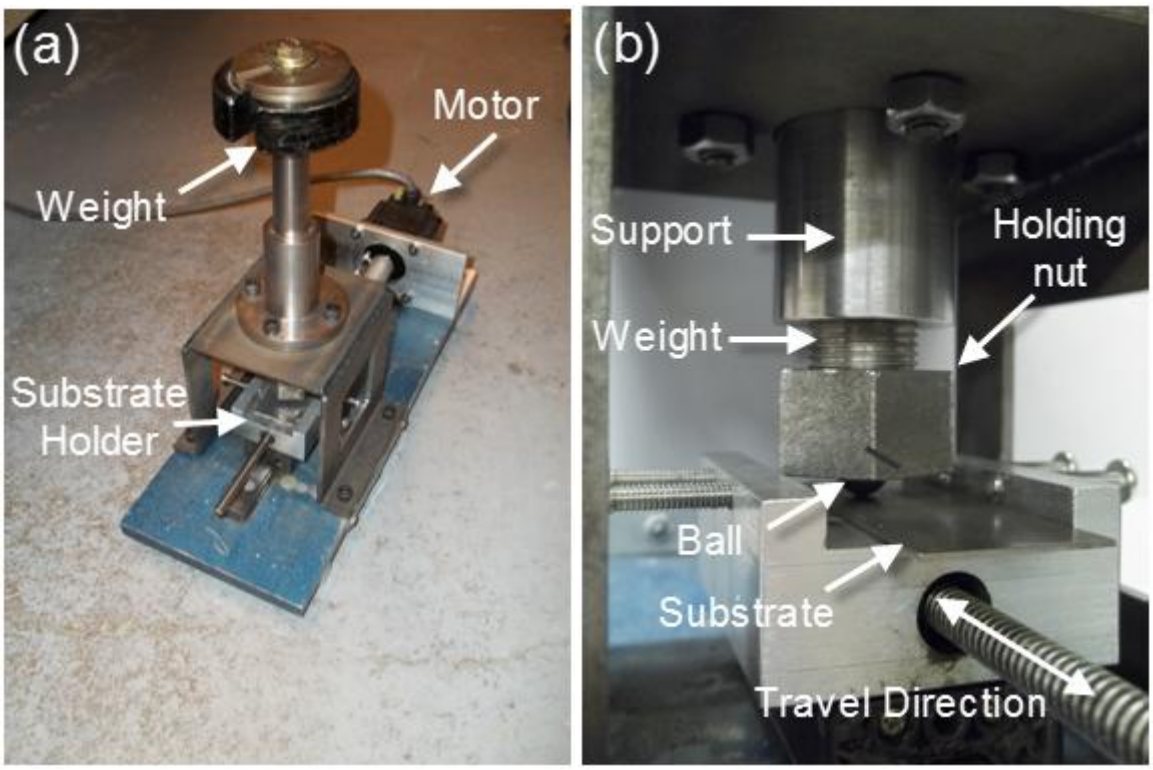

Figure 4.37 Photograph of the wear equipment: (a) Overview and (b) Substrate holder close-up

Four distances were completed for each powder/process combination, 50 m, 100 m, 200 m and 400 m. The averages values reported were calculated from three different wear specimens for each distance. Each specimen was cleaned using acetone and ethanol in an ultrasonic bath and air dried prior to the wear test. Mass losses were evaluated using an analytical balance (Sartorius ED124S) with a precision of 0.1 mg shown in Figure 4.38.

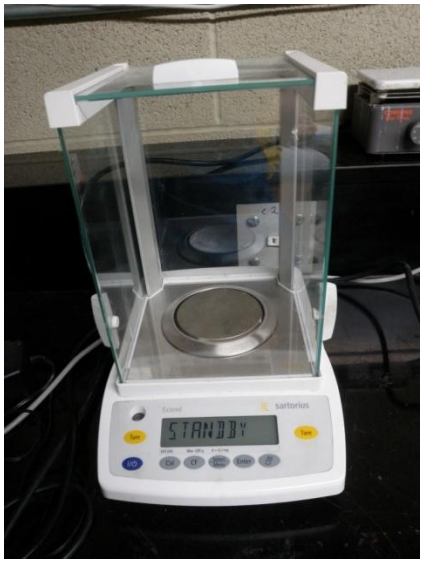

Figure 4.38 Photograph of digital scale (Sartorius Extend – model ED124S)

Wear tracks were analyzed with the optical microscope equipped with commercial image analysis software (Clemex, Vision-Lite 6.0) and observed under SEM.

Chapter 5. Powders Characterization

This chapter will describe the particle diameter distributions and morphology of the different powders used throughout this study.. The powder size distribution was characterized with a laser scattering particle size analyzer while the powder morphology was observed using SEM.

5.1. As-received CP Titanium Powder (Raymor)

Figure 5.1 presents an SEM image of the as-received CP titanium feedstock powder. The powder exhibits a spherical morphology, as expected for plasma atomized powder.

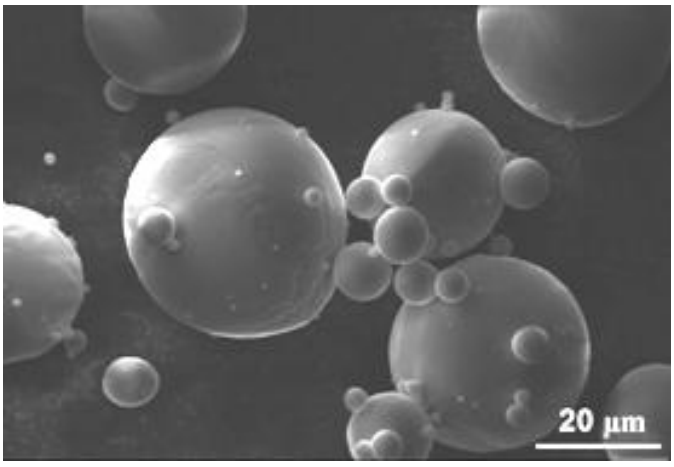

Figure 5.1 SEM image illustrating the spherical morphology of the CP titanium powder (Raymor)

This powder's chemical composition, provided by the manufacturer, is presented in Table 5.1. As previously discussed, the powder composition shows impurities in very low concentrations which is acceptable for thermal spray deposition. Higher purity levels could be achieved but the high cost related cost of the powder would not be justified in light of the little to no impact on the deposition process. The oxygen level present in the powder is due to the passive oxide layer covering titanium particles which are usually within the range of 10-20 nm thick.

Table 5.1 Chemical composition of CP titanium powder (Raymor)

Element	O	N	C	H	Fe	Others	Titanium
CP titanium Raymor[w%]	0.13	0.01	0.02	0.03	0.05	< 0.5	Balance ~99,3%

The CP titanium feedstock powder's microhardness was measured to be 144 ± 6 $HV_{0.05}$. The particle size distribution is presented in Figure 5.2. It presents the following size distribution: 90% of the total volume of the powder is between 14 μm (d_{10}) and 50 μm (d_{90}) with an average particle size of 34 ± 15 μm. The particle size used in Cold Spray is typically between 5 and 50 μm. Such small particles are preferable as they are more likely to reach the required critical velocity due to their lower mass compared to larger particles. The relatively wide distribution of this feedstock powder could be detrimental for coating properties as the larger particles (≥ 35 μm) are more difficult to accelerate, heat and deform than the smaller particles. Undeformed particles could lead to the creation of coating defects such as voids.

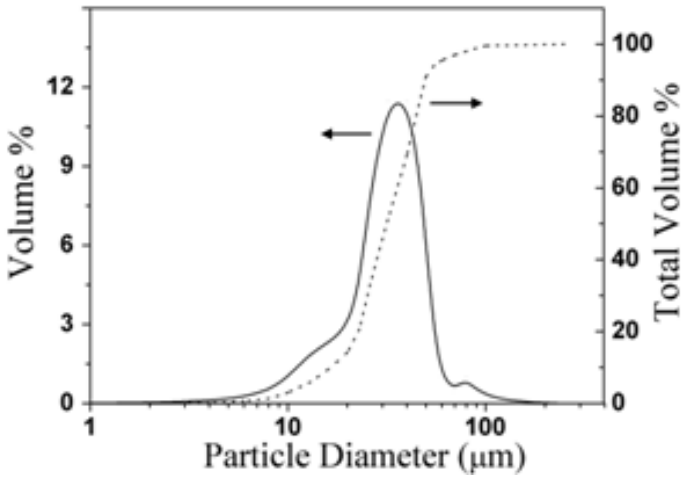

Figure 5.2 Particle size distribution of CP titanium powder Raymor)

XRD analysis of the feedstock powder was performed as a comparison baseline for the sprayed coatings. The XRD reveals a typical hexagonal closed-packed α phase pure titanium.

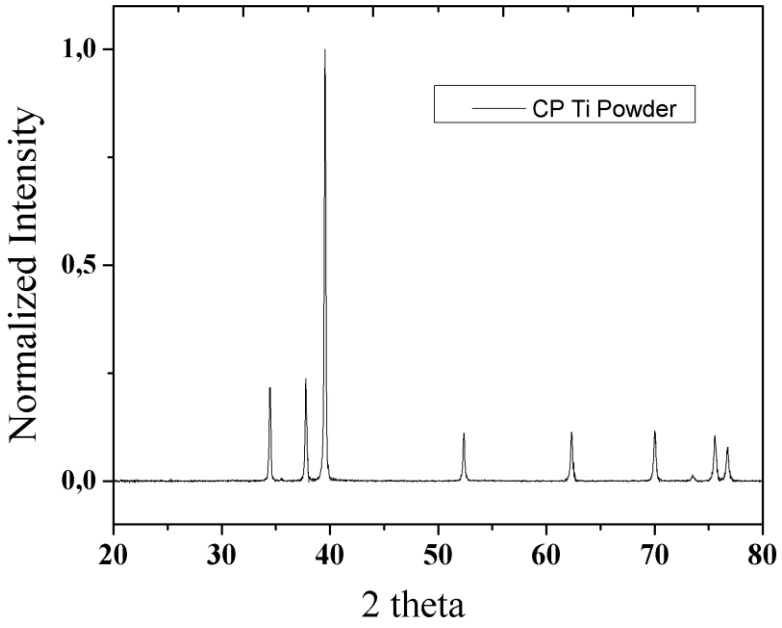

Figure 5.3 XRD spectrum of as-received 0-50μm powder (Raymor)

5.1.1. Powder Sieving

The powder size distribution has a strong influence on the coatings microstructure. Therefore, two powder size distributions were achieved by sieving the spherical powder 0-50 µm (Raymor) to investigate the effect. The first sieved powder referred to as "Sieved 0-20 µm" contained only particles with diameters lower than 20 microns obtained by sieving the original powder with a 625 mesh sieve. The second powder is the "Sieved 20-50 µm" which contains the rest of the original powder. Based on Figure 5.2, the sieving process should result into 20% of the original powder sieved to 0-20 µm powder and 80% of the original powder sieved to 20-50µm powder.

5.1.2. Milled (Raymor)

Powder morphology is also known to have an effect on coatings microstructure [91,92]. Higher impact velocities are reached by irregularly shaped particles, as a result of their higher drag coefficient, and can result in better coating microstructural properties. Hence, the original powder was mechanically milled to obtain an irregular morphology. The resulting powder morphology is shown in Figure 5.4. The milled powder presents a different morphology to the original powder, in the form of small disks, typical of milled materials.

Laser scattering results, presented in Figure 5.5, also show that the average size diameter has increased upon deformation during the milling process, also typical of mechanical milling. Assuming that the particles do not break into multiple smaller pieces during milling and using conservation of mass, the particles deform from a sphere into a disk, hence the diameter of the disk has to increase. It is important to note that this powder size distribution is biased due to the non-spherical powder morphology; however the comparison with the original powder provides a qualitative view of the increasing particles diameter upon deformation.

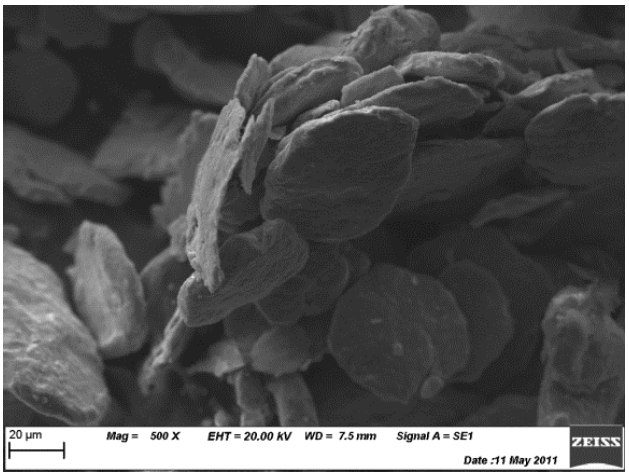

Figure 5.4 SEM micrograph illustrating the morphology of the milled CP titanium powder (Raymor)

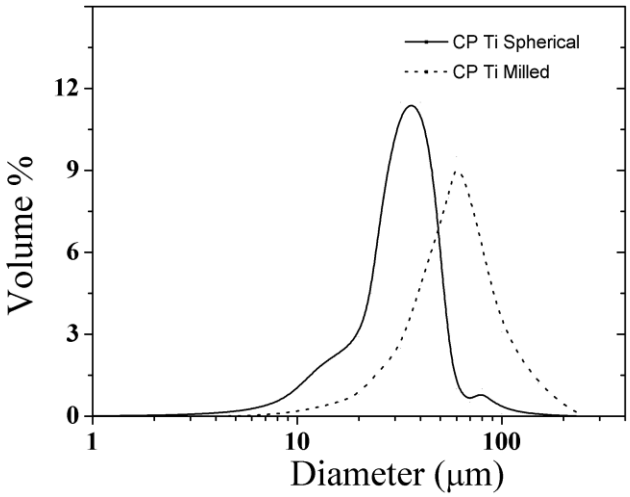

Figure 5.5 Powder size distribution of the milled powder and original as-received powder (Raymor)

5.2. As-received CP Titanium Powder (Centerline)

A second titanium powder, produced by HDH process, was used (CenterLine Ltd, Windsor, Canada). SEM investigation results, presented in Figure 5.6, reveal the angular morphology of this powder. In this case, since the powder is not spherical, a particle size distribution would not be representative of the actual powder size. The values would be an average of the projected diameter of the particles and would not be very representative of the shape depicted in Figure 5.6. Therefore, it was considered that SEM observations would be sufficient at this point and no laser analysis was performed. SEM observations indicate that the particles sizes are generally below 50 μm, which is suitable for Cold Spray techniques.

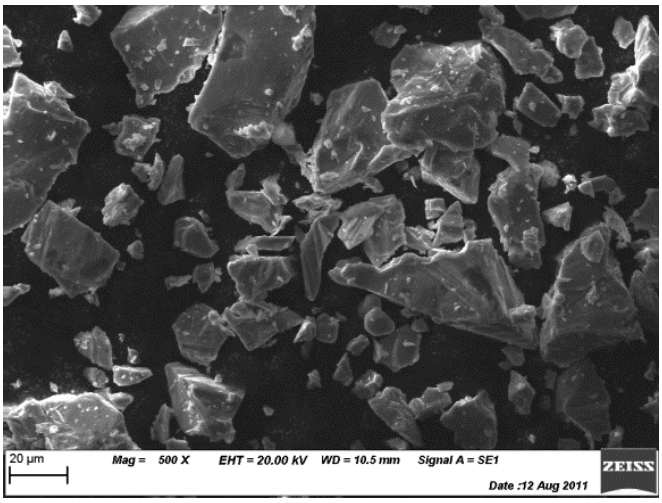

Figure 5.6 SEM micrograph illustrating the angular morphology of the CP titanium powder (CenterLine)

Chapter 6. CP Titanium Coatings - Feasibility Study and Spray Parameter Optimization of LPCS and PGDS Systems

In this chapter, the methodology used for feasibility study (**Phase 1**) and spray parameter optimization phase (**Phase 2**) is presented. The process parameters for each spray system were determined and classified into different categories. The important parameters influencing the coatings microstructure were determined based on previous studies of the literature. The optimized parameters refers to the best parameters that were achieved in this study and are not considered the be fully optimized since some parameters were not investigated. The parameter optimization of each process, LPCS and PGDS, was performed based on the produced coatings porosity level and microhardness. A table detailing the optimized spray parameters found in this work and used throughout the rest of this work is presented at the end of each process section.

It should be noted that the results presented in this section were chosen as the most representative data for each test. For example, the effect of pressure was tested at various temperature, however only one series of results was reported as similar observations were made for the two temperatures. The exploration of the parameters required multiple iterations in order to achieve high density coatings using both spraying techniques and the tests plans are shown in Appendix F. In order to simplify the large amount of information regarding the study of the variation of the parameters, the parameters were compiled and presented in order of appearance in Appendix G (LPCS) and Appendix H (PGDS).

The effect of the various parameters was evaluated based on coatings porosity and microhardness. Once an optimal parameter was determined, the value was used throughout the rest of the optimization phase.

6.1. Low Pressure Cold Spray (LPCS)

6.1.1. LPCS Parameters Description

The LPCS process has over 15 different parameters that can have an influence on the final LPCS coating properties. For clarity, these parameters are listed and classified under 4 main categories: Gas, Powder, Substrate and Nozzle. The classification of all LPCS process parameters is presented in Figure 6.1.

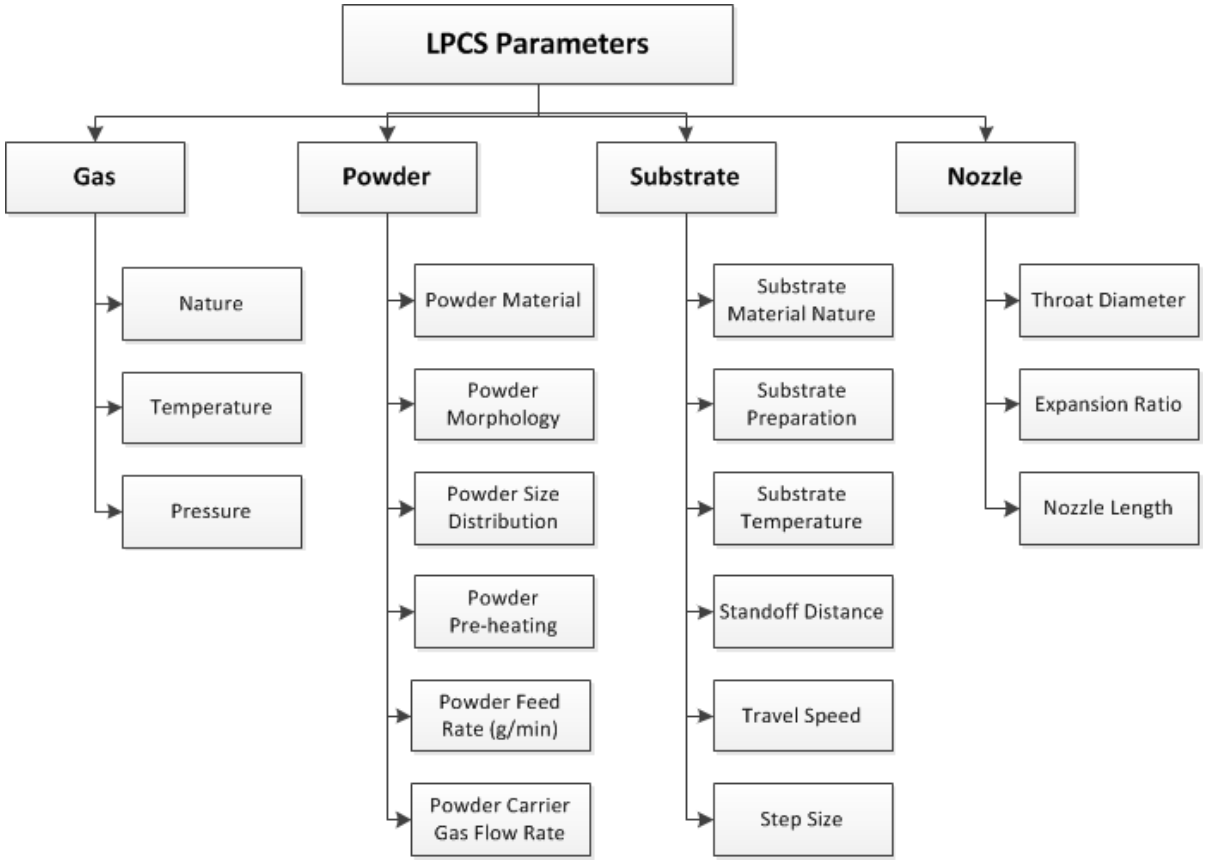

Figure 6.1 LPCS Process Parameters

6.1.1.1. Gas-related Parameters

As previously discussed, the formation of a coating using the CGDS techniques strongly depends on the particles impact velocity. Therefore, the gas velocity should be maximized by using helium [93] rather than nitrogen and by increasing the gas stagnation temperature. The gas pressure will affect the gas density throughout the flow and will have an impact on particle drag based on Equation 2.11, thus stagnation pressure should be maximized.

6.1.1.2. Powder-related Parameters

Material dependant properties such as crystallographic structures, stiffness melting temperature and mechanical strength are usually attributed to the wide critical velocity range for powder deposition [60]. However, in the present study, the effect of the nature of the powder will not be studied as the goal of this project is to deposit a specific material, CP titanium.

As discussed in Chapter 2, both spherical and non-spherical powder morphologies have benefits. Spherical powders are easier to use and lead to more uniform coating microstructure, whereas the non-spherical powder particles experience higher drag forces, potentially leading to higher deformation rates and better coating properties. Unfortunately, due to time constraints, the powder morphology was not investigated.

Powder size distribution is known to have an impact on coating properties [43,57,91]. Large particles experience high drag forces but due to their larger mass, their final velocities are lower than smaller particles [13]. The effect of lower particle velocity translates directly into less particle deformation upon impact, thus decreasing coating quality. Powders, such as the ones used in this study, with a size distribution between 0 and 50 μm are usually desired for LPCS.

Powder preheating could be used to increase the powder ductility by thermal softening. This reduces the required critical velocity and ensure proper deformation of the particles upon impact [49].

Powder feed rate should be kept low enough to ensure that the gas is not saturated and decelerated [20]. However, it should be optimized for maximum deposition rate such that the capacity of the jet is fully used to reduce spray time and gas costs.

The carrier gas should be of the same nature than the main gas, to ensure uniform fluid properties. The carrier gas flow rate should be minimal to ensure a proper powder feeding without disturbing the main gas flow.

6.1.1.3. Substrate-related Parameters

As introduced in Chapter 2, the substrate material nature can have an influence on the critical velocity. Substrate hardness can affect the deformation mechanisms related to particle bonding. However, once the first material layer is deposited, the second layer builds up only on the powder material and the effect of substrate hardness is negligible [61].

Substrate preparation must be able to remove any foreign substances such as grease or debris from the substrate surface. Usually with other thermal spray processes, grit blasting is performed on the substrate to increase the roughness. This typically leads to higher adhesion strength [94] but can also lead to grit contamination of the substrate [95]. Studies have also shown that for Ti-6Al-4V substrates, there is a decrease in bond strength [81] and fatigue life associated with grit-blasting [82], hence, the substrates used in this study will be acetone cleaned only.

The travel speed of the substrate with respect to the gun affects the amount of impingement effect applied to the coating. As the powder is deposited, a portion of the particles, mainly the larger ones, do not carry enough energy to successfully deform upon impact and adhere to the substrate. However, their large mass induce high deformation to the adhered particles at impact and further deform them, similarly to what is seen with shot peening. This effect is increased when particles are warm and ductile. The use of lower travel speeds could induce higher local temperature than higher travel speeds at the deposition area. Hence, lower travel speeds could be beneficial by increasing the substrate temperature locally and enhancing the impingement; resulting into better coating properties.

Finally, the standoff distance between the nozzle and the substrate had to be optimized for particle speed. Studies have shown that low standoff distances (10 mm) are desirable and that higher standoff distances results into reduction of deposition efficiency [96].

6.1.1.4. Nozzle-related Parameters

In Chapter 2, the effect of various parameters concerning the converging-diverging nozzle has been discussed.

First, the expansion ratio should be large enough to provide the highest gas Mach number at the nozzle exit but designed to reach the back pressure in order to reduce the formation of compression/expansion waves.

Secondly, the nozzle has to be of adequate length to provide a long particle dwell time for acceleration but also short enough to minimize the effects of friction.

Thirdly, the throat diameter is preferred to be small to reduce gas consumption for research purpose, whereas larger throat diameter could be used in industrial application to increase the powder deposition rate. In this work, a commercially available nozzle of 120 mm in length and an expansion ratio of 10 will be used. The choice of the throat diameter was made to be 2.0 mm rather than 2.5 mm to minimize gas consumption.

6.1.1.5. Summary of LPCS Parameters

The following table summarizes the influence of the LPCS process parameters on the coatings properties, mainly the effect on porosity based on the knowledge of the laboratory group as well as from the literature. The parameters that were kept constant throughout this study are placed in the constant column. The other parameters were classified based on their capacity to have an effect on the coating porosity. As such, gas nature, temperature and pressure have a strong influence on the coating properties as they can change the final porosity level by several percent due to their direct effect on particle velocity. The parameters classified as having a medium effect are parameters that are important, but that do not severely affect the particle velocity. The small influence category was based upon factors that would be more likely to have effects on adhesion strength or other properties but not on porosity level, or that were chosen based on literature (e.g. the substrate standoff distance and substrate preparation).

Table 6.1 Evaluation of the influence of LPCS process parameters on coating porosity

Strong Influence	Medium Influence	Small Influence	Constant
Gas Nature	Substrate Travel Speed	Substrate Temperature	Substrate Nature
Gas Temperature	Powder Morphology	Substrate Step Size	Nozzle Expansion Ratio
Gas Pressure	Powder Size Distribution	Substrate Standoff Distance	Nozzle Length
	Powder Preheating	Powder Carrier Gas Flow Rate	Nozzle Throat Diameter
	Powder Feed Rate	Substrate Preparation	Powder Material

6.1.2. CP Titanium Coating Production - LPCS Feasibility

As the first step of this study, preliminary testing was performed to assess the feasibility of depositing CP titanium powder using the LPCS process. The parameters used for this trial were based on literature HPCS CP titanium studies [39,67,75,97–99] and uOttawa laboratory knowledge. As Table 6.1 suggests, the gas parameters are the first ones to explore when depositing a new powder.

The first trial was performed using nitrogen gas and was unable to produce a coating. The parameters used in this preliminary test can be found in Appendix I. As a first trial using helium, the driver gas at a stagnation pressure of 1.0 MPa was preheated at 350°C and helium was preferred to nitrogen as the driving gas to achieve higher particle velocities due to its high specific heat ratio and low molecular weight. The default powder used to start this study is the spherical 0-50 μm powder. The powder carrier gas was helium to match the driver gas nature with a flow rate of 12.5 standard cubic feet per hour (scfh) and the powder feed rate was set at 2.0 grams per minute. Stand-off distance and travel speed were set at 10 mm and 1 mm/s respectively. Ti-6Al-4V substrates were acetone cleaned/degreased prior to coating deposition. A complete list of the process parameters used for preliminary testing is provided in Table 6.2.

Table 6.2 Preliminary parameters for CP titanium deposition using LPCS technique

Category	Parameters Description	Preliminary Value
Gas	Nature	Helium
	Temperature	350°C
	Pressure	1.0 MPa
Powder	Material Nature	CP titanium
	Morphology	Spherical
	Size Distribution	0-50 μm
	Preheating Temperature	None
	Powder Feed Rate	2.0 g/min
	Powder Carrier Gas Nature	Helium
	Powder Carrier Gas Flow Rate	12.5 scfh
Substrate	Substrate Material Nature	Ti-6Al-4V
	Substrate Preparation	Acetone Cleaned/Degreased
	Substrate Temperature	Room Temperature
	Substrate Travel Speed	1 mm/s
	Gun Step Size	3 mm
	Substrate Stand-Off Distance	10 mm
Nozzle	Throat Diameter	2 mm
	Nozzle Geometry	Straight hydro formed
	Expansion/Area Ratio	10
	Nozzle Expansion Length	120 mm

As seen in Figure 6.2, LPCS process successfully deposited CP titanium powder and the resulting coating was promising for this research. It can also be observed that the coating shows more porosity as well as undistorted particles at the top than deeper in the coating. Due to a very high porosity level (greater than 15%), the spraying parameters had to be optimized to get a denser coating.

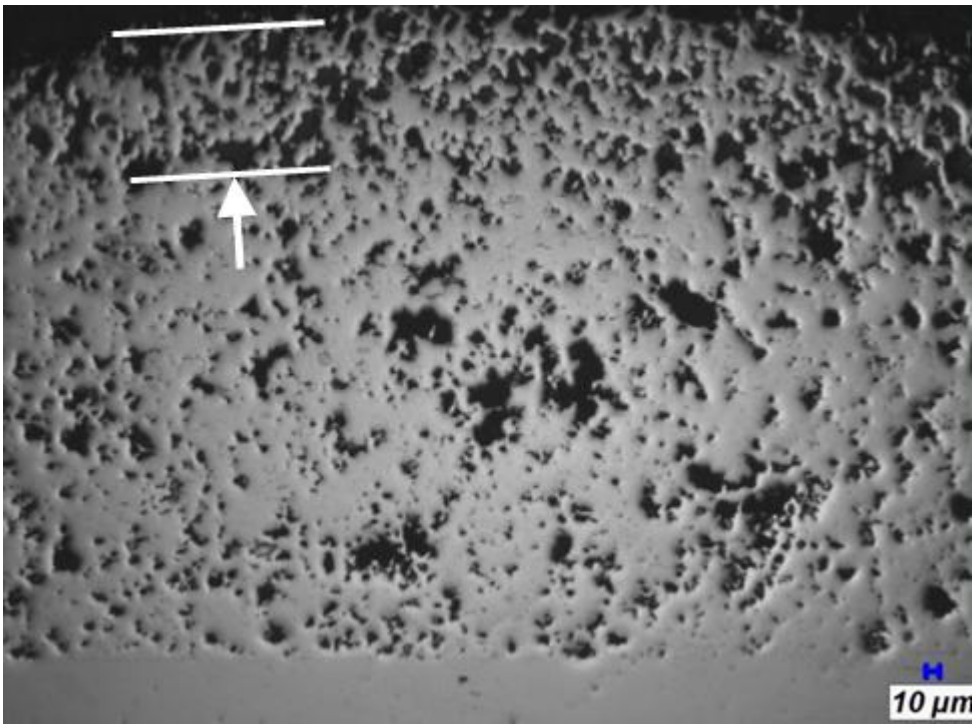

Figure 6.2 Micrograph of LPCS CP titanium coating feasibility, arrows showing the porous top layer

6.1.3. LPCS Parameter Optimization

In this section, each of the LPCS parameters category are in different sub-sections.

6.1.3.1. Gas-related Parameter Optimization

As previously stated, no coatings were successfully produced using nitrogen gas. This is due to the low gas jet velocity that was unsuccessful at accelerating particles beyond their critical velocity. In addition, the powder preheater was not available at that time. Hence, the utilization of nitrogen should be investigated again in the future as it would represent an important reduction in gas costs. Further investigation, based on the knowledge acquired during this work, should be done to create CP titanium coatings using nitrogen.

The use of helium as the main driving gas leads to the deposition of particles and the formation of a coating. The optimization of the gas temperature and pressure was performed. The nozzle inlet gas pressure was tested at two different pressures, at 1 MPa and at the maximum operating pressure of the system, 1.7 MPa (250psi). It is expected that the coating porosity will decrease as the pressure is increased. Therefore intermediate pressures experiments would be performed only if a fully dense coating was achieved at 1.7 MPa. Similarly to the pressure, the literature has shown that increasing the gas temperature will lead to lower porosity, hence only 2 values were chosen to be analyzed. The nozzle inlet gas temperature was tested at 450°C and 650°C, the latter being the maximum temperature that the system can reach. The coatings porosity results are presented in Table 6.3 and Table 6.4. The complete list of the parameters used can be found in Appendix G.

Table 6.3 Effect of nozzle inlet pressure on LPCS coating porosity

Nozzle Inlet Gas Pressure	Coating Porosity
1.0 MPa	18 ± 5%
1.7 MPa	8 ± 3%

Table 6.4 Effect of nozzle inlet temperature on LPCS coating porosity

Nozzle Inlet Temperature	Coating Porosity
450 °C	8 ± 3%
650 °C	2 ± 1%

As seen in Table 6.3, the coating porosity decreased drastically when the gas inlet pressure was increased from 1.0 MPa to 1.7 MPa. As discussed previously, higher nozzle inlet pressure leads to higher gas density which also increases particles drag force. Thus higher particle impact velocities were reached, which resulted into more particle deformation and denser coatings. Increasing in nozzle inlet temperature from 450°C to 650°C reduced the porosity level from 8% to 2%. According to these results, higher gas temperature could be desirable to reduce the porosity level.

For a given geometry, the Mach number of the gas stream at the nozzle exit is fixed but the speed of sound is a function of the gas temperature. Consequently, a higher nozzle inlet gas temperature leads to higher gas velocity to accelerate the powder. Unfortunately, it is not possible to reach higher temperature with the present system and it is believed that coating could start oxidizing, lowering its final mechanical properties. In summary, the optimized gas pressure and temperature were 1.7 MPa and 650°C respectively. Higher gas pressure could enhance particle velocity and coating properties but the system limit was attained at 1.7 MPa.

6.1.3.2. Powder-related Parameter Optimization

In this section, the different parameters related to the deposition of CP titanium powder are described. Due to time limitation, only one powder morphology and powder size distribution was sprayed (spherical, 0-50 μm from Raymor). The powder feed rate was kept low, at 2.0 grams per minutes. Although a higher powder flow rate would increase the deposition rate and induce a thicker coating built-up, this would result in a reduced deposition efficiency for subsequent passes due to the high angle change between the particle stream and the previous pass. The powder gas carrier was chosen to be of the same nature as the processing gas to

avoid gas mixtures having different properties. The powder gas carrier flow rate was fixed at 12.5 scfh which is a very light gas stream; lower flow rate might not be enough to create a flow of particles. Increasing the powder carrier gas flow rate could potentially disturb the main gas jet and as the lower setting provided sufficient powder feeding, higher flow rates were not tested. Powder preheating was introduced to this system to increase the powder impact temperature and thus ductility at impact and potentially lead to denser coatings. The different parameters and resulting coatings porosity, microhardness and thickness are presented in Table 6.5. The complete list of the parameters used can be found in Appendix G.

Table 6.5 Effect of powder preheating temperature on LPCS coating porosity, microhardness and thickness

Powder Preheating Temperature	Coating Porosity	Coating Microhardness	Coating Thickness
500 °C	1.5 ± 1.3%	160 ± 26 $HV_{0.3}$	1.98 mm
600 °C	0.7 ± 0.4%	189 ± 10 $HV_{0.3}$	1.55 mm
650 °C	0.3 ± 0.3%	192 ± 19 $HV_{0.3}$	1.43 mm
700 °C	0.2 ± 0.2%	206 ± 23 $HV_{0.3}$	1.44 mm
750 °C	0.1 ± 0.1%	235 ± 19 $HV_{0.3}$	0.60 mm
800 °C	0.7 ± 0.3%	274 ± 39 $HV_{0.3}$	0.20 mm

Powder preheating was performed to increase the ductility of the powder at impact. Table 6.5 shows that the coating porosity decreased with powder preheating temperature. The coatings microhardness values slowly increased with the increasing preheating temperature. Particles experienced more deformation (cold work) upon impact as they were softer at higher powder preheating temperatures which led to an increasing coating microhardness. However, a major reduction of coatings thickness was also observed above preheating temperature of 700°C which was attributed to in-flight oxidation of the powder. As reported in another study [100], temperatures above 700°C lead to oxidation of titanium particles. Due to the high hardness and brittle behavior of oxides, less particles adhere to the substrate, resulting in an increasing microhardness along with a reduction of coating thickness. Furthermore, the coating created was far from uniform in thickness and shape and therefore it would be impossible to apply this coating on a part. Figure 6.3 shows an example of the

resulting coating exhibiting blue oxide coloration and poor uniformity. It was therefore determined that the optimal powder preheating temperature is 700°C.

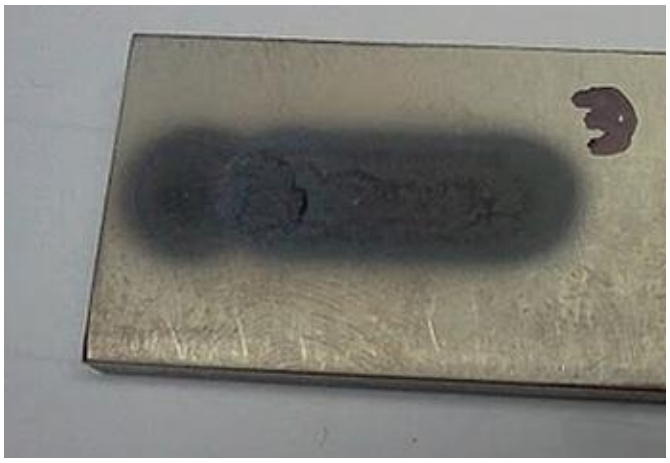

Figure 6.3 LPCS coating example using powder preheating temperature above 700°C

6.1.3.3. Substrate-related Parameter Optimization

The substrate material used is always Ti-6Al-4V, as required for this research. As described in Chapter 4, the substrates were acetone cleaned only since sandblasting could lead to reduced adhesion strength and reduce fatigue life of Ti-6Al-4V substrates.

The nozzle standoff distance was chosen to be 10 mm [99]. Research has shown that increasing standoff distances can result in a reduction of deposition efficiency for titanium [99] and aluminum [13] powders. The gas jet reaches its maximum velocity at the nozzle exit and then starts to slow down due to the surrounding steady environment inducing resistance and friction. The particles experience the same phenomenon and decelerate which causes the particles to lose kinetic energy. The effect is greater as the distance between the nozzle and substrate increases. Standoff distances (below 10 mm) are not desirable as the nozzle could interfere with the coating as it builds up during the spraying process.

The effect of the substrate travel speed was investigated and the results are shown in Table 6.6. The detailed list of the parameters used can be found in Appendix G.

Table 6.6 Effect of travel speed on LPCS coating porosity

Travel Speed	Coating Porosity
1 mm/s	1.2 ± 0.8%
5 mm/s	2.4 ± 1.9%

It was observed that the coatings porosity level increased when using a higher travel speed. Lower travel speeds had the advantage of creating a shot peening effect from the impact of impinging particles. The particles that did not reach critical velocity to properly deform and adhere to the coating impacted and deformed the already deposited particles before bouncing off the coating. This was confirmed by the observation that the top layer of the coating which was more porous than the bottom section of the coatings, shown in the LPCS feasibility test in Figure 6.2. The top layer, consisting of deformed particles upon impact, had not been exposed yet to the impingement of the other incoming particles which further compacted the coating and reduces porosity. As such, the increase of particles velocity did not only enhance the particle deformation but also intensified the impingement effect compacting the coating.

Substrate preheating was performed in order to soften the substrate allowing more substrate deformation and enhancing coating adhesion. The substrate was slowly moved under the nozzle over the entire area to be sprayed. The detailed characterization of the substrate temperature was not performed due to time limitation. However, due to the relatively long exposure time to elevated processing temperature, the substrate microhardness should be monitored in future experimentations. Long exposition time to elevated temperatures can induce annealing effect, changing the microstructure of the heat-treated Ti-6Al-4V substrate. During the adhesion strength testing, the effect of the spray pattern was studied for two different spraying patterns shown in Figure 6.4, and the results are presented in Table 6.7. The step size was chosen in order to obtain a coating thickness of about 1.5 mm, as required for the repair process. The rest of the parameters values can be found in Appendix G.

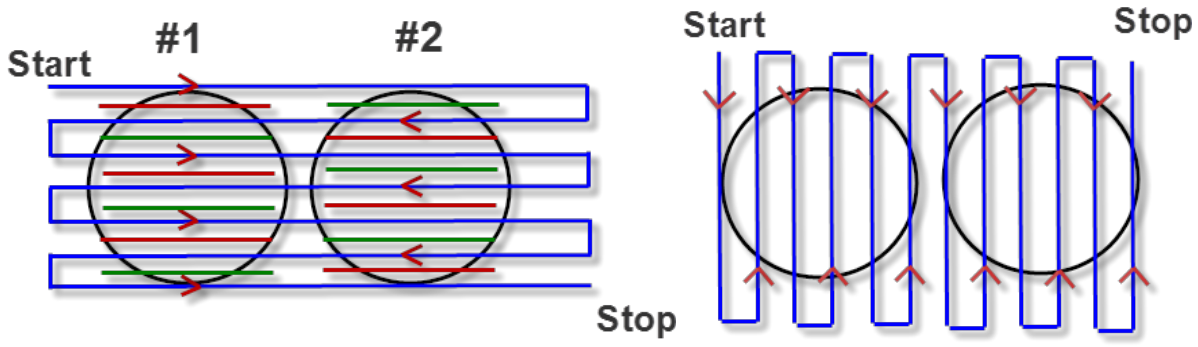

Figure 6.4 Different spraying patterns for bond plugs, old spray pattern (left) and new spray pattern (right)

Table 6.7 Effect of spray pattern on LPCS coating adhesion strength

Spray Pattern	Adhesion Strength
Old	25 ± 3 MPa
New	47 ± 7 MPa

As shown in Figure 6.4 and Table 6.7, the second spray pattern (new) used produced a higher adhesion strength with the Ti-6Al-4V substrate (47 vs 25 MPa). The new pattern provided a steadier and warmer substrate temperature throughout the deposition process. A warmer substrate sees its ductility increased and is more favorable to form bonding, either mechanical or metallurgical which increases adhesion strength. As seen in Figure 6.4, the first spray pattern (old) led to a larger difference in substrate temperature indicated in green for high temperature zone and in red for low temperature zones as the substrate had time to cool down between the subsequent deposition pass. The new spray pattern was determined to be a better choice to deposit CP titanium.

6.1.3.4. Nozzle-related Parameter Optimization

As previously stated, the nozzle used in this study was the standard commercially available nozzle. Even though the nozzle design plays a significant role during the powder acceleration, the scope of this study did not include the investigation of different nozzle parameters or design but should be performed in further studies.

6.1.3.5. Summary of LPCS Optimized Parameters

This sub-section concludes the parameter optimization phase for the LPCS system. The following table summarizes the optimal conditions for CP titanium deposition using the LPCS technique. These will be used to create the coatings analyzed in Chapter 7. As introduced at the beginning of the section, parameters shown in bold in Table 6.8 were optimized only to a certain extent for different reasons. Specifically, the gas pressure had been limited to 1.7 MPa due to the maximum system capacity of 1.7MPa. The morphology and size distribution of the powder were not investigated but could have had a substantial impact on the particle velocities, thus coating quality. The substrate preheating was performed in a qualitative manner and could be fully characterized. Finally, as no clogging issues were observed during CP titanium powder deposition, a better designed nozzle could be used and would have a significant impact on the final particle velocities [39].

Table 6.8 Optimized parameters for CP titanium deposition using LPCS technique

Category	Parameter Description	Optimized Value
Gas	Nature	Helium
	Temperature	650°C
	Pressure	**1.7 MPa**
Powder	Material Nature	CP titanium
	Morphology	**Spherical**
	Size Distribution	**0-50 μm**
	Preheating Temperature	700°C
	Powder Feed Rate	2.0 g/min
	Powder Carrier Gas Nature	Helium
	Powder Carrier Gas Flow Rate	12.5 scfh
Substrate	Substrate Material Nature	Ti-6Al-4V
	Substrate Preparation	Acetone Cleaned/Degreased
	Substrate Temperature	**Preheating before spray**
	Substrate Travel Speed	1 mm/s
	Gun Step Size	3 mm
	Substrate Stand-Off Distance	10 mm
Nozzle	**Throat Diameter**	**2 mm**
	Nozzle Geometry	**Straight hydro formed**
	Expansion/Area Ratio	**10**
	Nozzle Expansion Length	**120 mm**

6.2. Pulsed Gas Dynamic Spray (PGDS)

Similarly to the LPCS, the PGDS parameters were divided into 4 different categories. However, instead of a converging-diverging nozzle, the PGDS has a valve to create a shockwave and a barrel that can be considered as the powder acceleration zone. The different parameters involved in PGDS are presented in Figure 6.5.

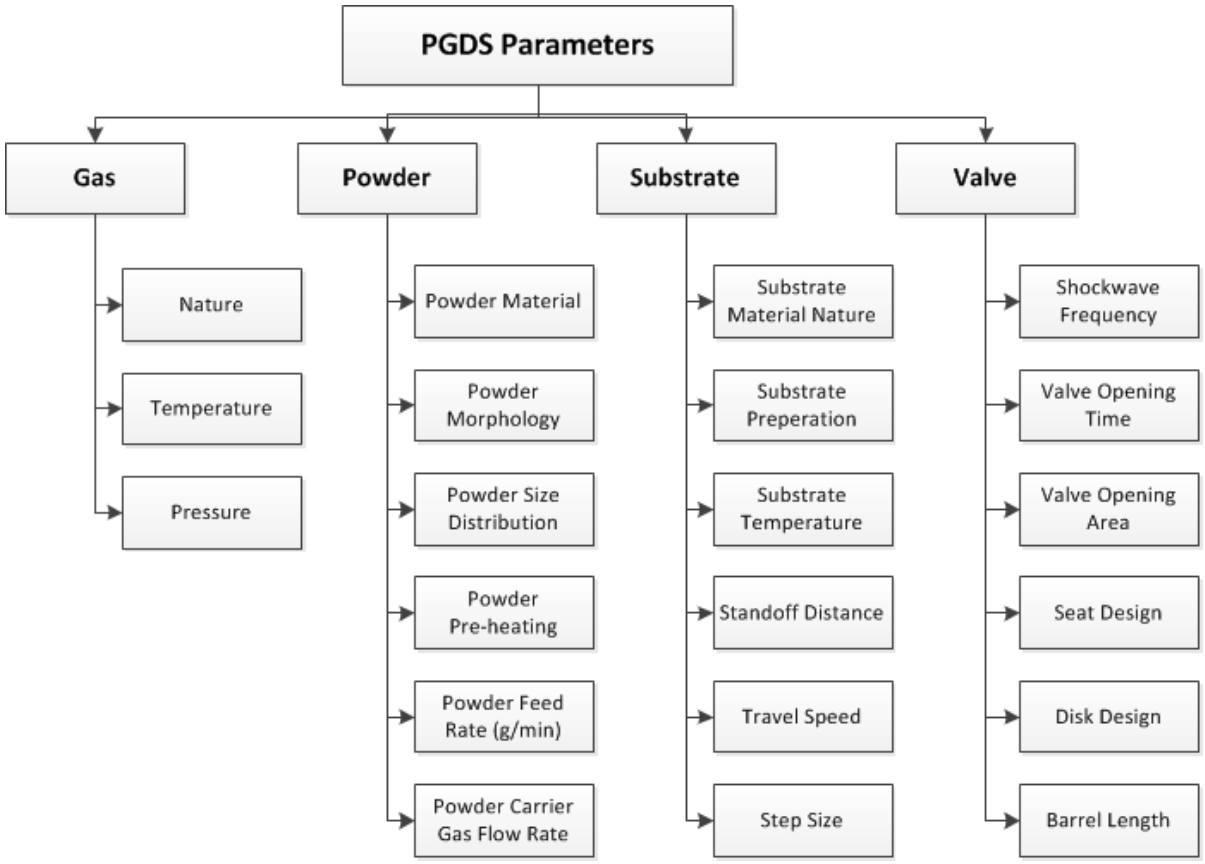

Figure 6.5 PGDS process parameters

Even though the PGDS process is based on slightly different principles to accelerate and heat the particles than LPCS, the effect of most parameters is similar and the main purpose of the flow is to accelerate the particles above the critical velocity to obtain adhesion to the substrate. As described in Section 2.3.3, the shockwave properties depend strongly on the gas nature, temperature and pressure. Similarly to the LPCS process, higher gas speed of sound will produce higher flow velocity. The shockwave velocity also increases with temperature and pressure as seen in Equation 2.14 and 2.15. At the same time, the density of the flow accelerating the powder is increased [23]. These factors contribute positively to the

acceleration of the powder through drag due to its dependency on the gas velocity and gas density (Equation 2.12).

Once accelerated, the particles impacting the substrate experience deformation, as in the LPCS process. As such, the powder characteristics affecting the particle velocity prior to impact will influence the final coating properties; particularly the powder morphology and powder size. As discussed for the LPCS, higher powder impact temperature could also lead to increased powder ductility and an increase in particle deformation. The high heat zone provided by the shockwave could, additionally to powder preheating, lead to better coating properties than LPCS where the particles experience cooling in the diverging section. The amount of powder injected in the gas pulses has to be controlled such that the shockwave does not slow down as it accelerates the powder. In order to promote adhesion, the substrate is cleaned from debris and degreased using acetone. The nature of the substrate material can also affect the coating properties. Variation of the substrate temperature could affect the adhesion mechanisms as it will change the deformation behavior of the substrate, thus affecting the bonding mechanisms. Lower travel speeds will most likely enhance the impingement effect by increasing the local temperature of the substrate. High substrate standoff distance will most likely have a negative impact on the particle velocity as the shockwave dissipates in atmosphere. Therefore, the standoff distance was based on LPCS studies and limited to short distances.

Various parameters of the valve can affect the formation of the shockwave. The valve opening time and the valve opening area will affect the amount of gas going through it during each pulse. The amount of gas let through should be enough to sustain the formation of a shockwave and provide enough gas and energy to accelerate the powder. The frequency of the pulses will have an effect on multiple parameters if the same components are used, which increases the complexity of the valve study. It will change how quickly the valve opens and closes leading to the formation of compression waves, or not if the valve opens too slowly. Changing the frequency will also affect the amount of gas per pulse by changing the valve opening time. The design of the seat and disk is based upon the number of openings and the shape of the opening used. In the present study, the openings in the disk were slots to have an abrupt flow and create the required compression wave, rather than a

round opening which will gradually open until its full opening is attained. The number of slots was set to 3, multiplying the number of shockwaves per rotation of the valve. This was done to reduce the required motor speed in order to reduce friction and wear of the seat. Finally, the length of the barrel should have an optimal value where the acceleration time of the powder is balanced against the dissipation of the shockwave as it is travelling.

6.2.1. CP Titanium PGDS Coating Feasibility

Preliminary testing was performed to assess the feasibility of depositing CP titanium powder using the PGDS process. The spraying conditions for CP titanium deposition were based on previous successful studies performed at the University of Ottawa Cold Spray Laboratory, particularly on the deposition of stainless steel [53]. In this previous study, dense stainless steel coatings were produced using the PGDS technique. Stainless steel, having high mechanical properties, requires high particles velocity (700 m/s) in order to deform and create a coating. The critical velocity of CP titanium powder is higher (850 m/s) than that of stainless steel but the procedure used to get denser coating may be inferred from this study. However, in order to understand the effects of the different parameters, the first experiments were performed using nitrogen and low gas temperatures and pressures. The preliminary parameters used for the feasibility study are presented in Table 6.9.

Table 6.9 Preliminary parameters for CP titanium deposition using PGDS technique

Category	Parameter Description	Preliminary Value
Gas	Nature	Nitrogen
	Temperature	350°C
	Pressure	2.5 MPa
Powder	Material Nature	CP titanium
	Morphology	Spherical
	Size Distribution	0-50µm
	Preheating Temperature	350°C
	Powder Feed Rate	7.0 g/min
	Powder Carrier Gas Nature	Nitrogen
	Powder Carrier Gas Flow Rate	20 scfh
Substrate	Substrate Material Nature	Ti-6Al-4V
	Substrate Preparation	Acetone Cleaned/Degreased
	Substrate Temperature	Room Temperature
	Substrate Travel Speed	1 mm/s
	Step Size	2 mm
	Gun Stand-Off Distance	10 mm
Valve	Valve Frequency	10 Hz
	Barrel Length	75 cm
	Valve Opening Time	13 ms
	# Slots in disk	3

Unfortunately, these first trials did not produce any coatings. The propellant gas was then switched to helium, with the hope that the higher shockwave strength would help the particles reach critical velocity. This change had a strong impact on powder deposition and a coating (depicted in Figure 6.6) was successfully produced. Coating porosity (10%) being higher than requirements, a spray parameter optimization phase was required.

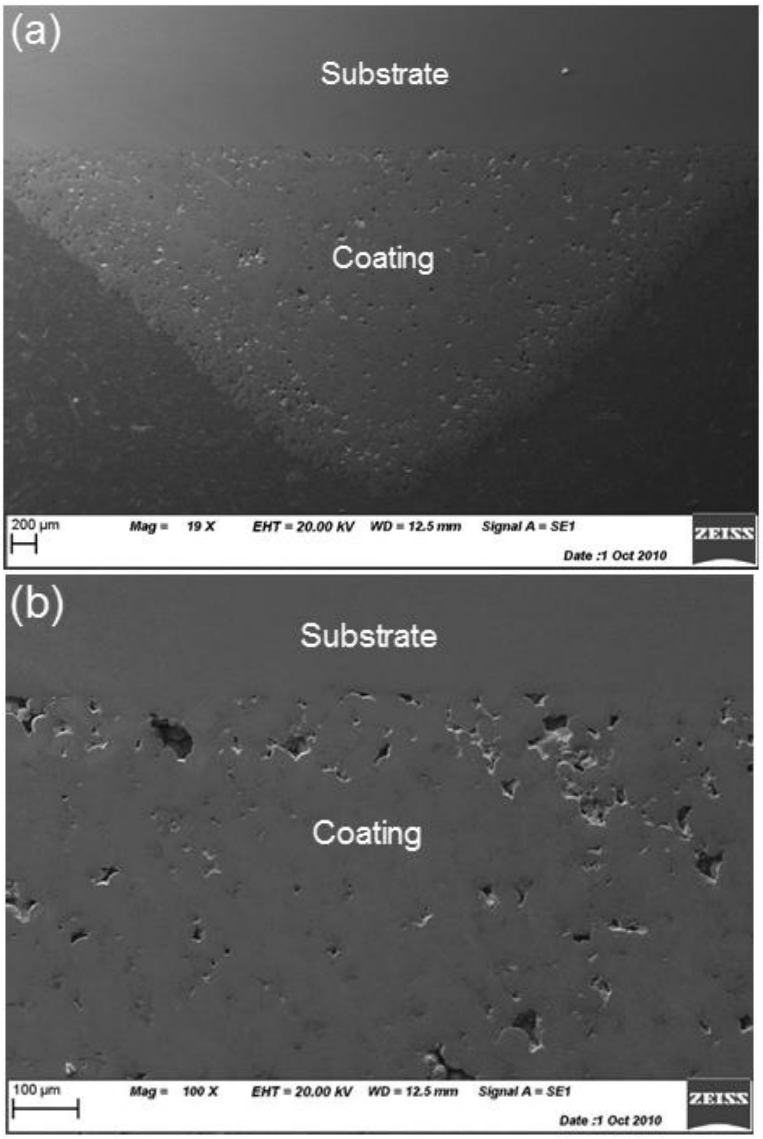

Figure 6.6 Micrograph of PGDS CP titanium coating feasibility: (a) Overview and (b) Magnified view 100x

6.2.2. PGDS Parameter Optimization

In this section, the optimization process for each of the PGDS parameters is described in the different sub-sections.

6.2.2.1. Gas-related Parameter Optimization

As stated previously, the first trials performed using nitrogen were not successful and helium was then used as the main propelling gas. Different gas stagnation pressures and gas heater temperatures were tested. The resulting coatings properties are presented in Table 6.10 and Table 6.11. The sprayed parameters used to perform these experiments are shown in Appendix H.

Table 6.10 Effect of gas stagnation pressure on PGDS coating porosity

Gas Stagnation Pressure	Coating Porosity
2.5 MPa	>15 %
3.5 MPa	>10 %
4.5 MPa	6 ± 2 %

Table 6.11 Effect of gas heater temperature on PGDS coating porosity and microhardness

Gas Heater Temperature	Coating Porosity	Coating Microhardness
350 °C	>10 %	n/a
550 °C	0.3 ± 0.3 %	190 ± 20 $HV_{0.3}$
600 °C	0.2 ± 0.2 %	200 ± 15 $HV_{0.3}$
700 °C	0.2 ± 0.2 %	198 ± 20 $HV_{0.3}$

As seen in Table 6.10, the gas stagnation pressure used to induce the shockwave has a strong effect on the quality of the coatings. By increasing it from 2.5 MPa to 4.5 MPa, the coatings porosity level decreased from over 15% down to 6%. The increased gas pressure led to a more powerful shockwave in terms of higher density, higher velocity and higher temperature. These characteristics enhance the particles acceleration and maximum velocity as they increased the drag forces seen by each particle. The increased pressure also led to

higher particle temperatures due to the increased flow temperature. The highest pressure setting (4.5 MPa), which is also the limit of the current system, will be used as the optimal spraying pressure.

In Table 6.11, it is possible to observe that the PGDS coatings quality increases drastically when a gas temperature of 550°C or higher is used. Beyond a gas temperature of 550°C, there is no reduction of porosity since the coatings can be considered fully dense. Very little gain, in terms of microhardness, is observed which is attributed to a similar level of deformation. It could be possible that the particle speed and temperature have leveled off and any increases in temperature lead to very small variation in particle deformation. A longer barrel length might be necessary to give more acceleration and heating time for the powder before hitting the substrate. Based on these results and as higher gas temperatures can also lead to in-flight oxidation of the powder, the optimized gas temperature for the PGDS process is set at 550°C.

6.2.2.2. Powder-related Parameter Optimization

Numerous parameters relating to the feedstock powder can influence the coating quality. The influence of the powder feed rate, powder carrier gas flow rate, preheating temperature and powders morphology were investigated.

Similarly to the LPCS process, it is important to limit the powder feed rate to a level which will not result in a deceleration of the propellant gas. However, too low feed rate would increase the coating costs as a longer spray time would be required to build a specific thickness. Three different feed rates were tested and the results are shown in Table 6.12. The feed rate was set to 7.0 grams per minute, given that lower feed rates lead to insufficient deposition rates to be economically viable. The sprayed parameters used to deposit these experiments are shown in Appendix H.

Table 6.12 Effect of powder feed rate on PGDS coating porosity, microhardness and thickness

Powder Feed Rate	Coating Porosity	Coating Microhardness	Coating Thickness per pass
7.0 g/min	0.4 ± 0.2%	193 ± 16 $HV_{0.3}$	670 µm
8.3 g/min	0.4 ± 0.2%	187 ± 28 $HV_{0.3}$	960 µm
9.6 g/min	0.4 ± 0.2%	169 ± 34 $HV_{0.3}$	1370 µm

As seen in Table 6.12, increasing the powder feed rate did not affect the coating porosity. However, the coating microhardness decreases with the increasing powder feed rate. Even though particles experience enough deformation to reach low porosity level, the microhardness difference could be associated to a reduced deformation level of the particles forming the coating. As the feed rate is increased, it is possible that the flow gets saturated with particles and decelerates, not enough to increase the porosity but enough to decrease the particle velocity and reduce the cold working effect by the impinging particles. The powder feed rate optimized value is 7.0 grams per minute which shows high microhardness with minimal variation.

The powder carrier gas flow rate was tested at two different values and the results are presented in Table 6.13. Low porosity levels have been observed for both cases while the microhardness was higher for the 20 scfh than 10 scfh (193 vs 172 $HV_{0.3}$). In this case, due to the pulsing nature of the PGDS, a moderate gas flow rate (20 scfh) was required to obtain a sufficient amount of particles inside the main stream. It can be hypothesized that the higher gas carrier flow rate of 20 scfh versus 10 scfh was able to inject more powder at the proper location, into the high temperature and high velocity zone of the shockwave. The lower gas flow rate did not produce a pressure differential high enough to resist the gas pulsation and would inject most of the powder in the wrong zone, behind the shockwave. The extra powder introduced in the proper zone using 20 scfh resulted in higher microhardness which can be explained by a higher amount of impingement effect and cold working. No tests were performed at higher flow rates since it could disturb the main gas flow and 20 scfh was sufficient to obtain a continuous and sustained powder feeding. The complete list of the parameters for these tests can be found in Appendix H.

Table 6.13 Effect of powder carrier gas flow rate on PGDS coating porosity and microhardness

Powder Carrier Gas Flow Rate	Coating Porosity	Coating Microhardness
10 scfh	0.4 ± 0.2%	172 ± 30 $HV_{0.3}$
20 scfh	0.4 ± 0.2%	193 ± 16 $HV_{0.3}$

The effect of powder preheating temperature was studied from 350°C up to 950°C. These temperatures were recorded using a thermocouple on the outer surface of the coil. The alumina coating was removed locally at the middle of the coil for the measurements. The results are reported in Table 6.14 and the spraying conditions are described in Appendix H.

Table 6.14 Effect of powder preheating temperature on PGDS coating porosity, microhardness and thickness

Powder Preheating Temperature	Coating Porosity	Coating Microhardness
350 °C	6.5 ± 1.3%	130 ± 20 $HV_{0.3}$
400 °C	6.2 ± 1.5%	136 ± 27 $HV_{0.3}$
550 °C	2.8 ± 1.0%	160 ± 25 $HV_{0.3}$
650 °C	1.1 ± 0.6%	180 ± 32 $HV_{0.3}$
700 °C	0.2 ± 0.1%	202 ± 23 $HV_{0.3}$
800 °C	0.3 ± 0.3%	217 ± 25 $HV_{0.3}$
950 °C	0.4 ± 0.3%	270 ± 20 $HV_{0.3}$

The powder preheating temperature mainly affects the particles temperature, and thus their ductility, as it is a function of temperature. As long as no oxidation occurs in-flight, increasing the preheating temperature will enhance particle ductility and deformation upon impact. If oxidation occurs, the coating microhardness will increase due to the presence of hard oxides and might lead to an increase of coating porosity. As seen in Table 6.14, the porosity level of the coating reduces up to 700°C most likely due to the increased powder ductility. The coating porosity stabilises close to zero above this point whereas the coating microhardness increases up to 270 $HV_{0.3}$ potentially caused by oxide formation. The coatings deposited above 700°C had a very irregular thickness and were considered unusable. The optimal powder preheating for the PGDS system is therefore 700°C.

Different titanium particle morphologies were tested using the PGDS technique and the parameters provided in Appendix H. Overall, five different powders described in Chapter 5 were sprayed: spherical 0-50 μm, spherical 20-50 μm, spherical 0-20 μm, milled and non-spherical powders. The coating properties resulting from the deposition of these powders are presented in Figure 6.7.

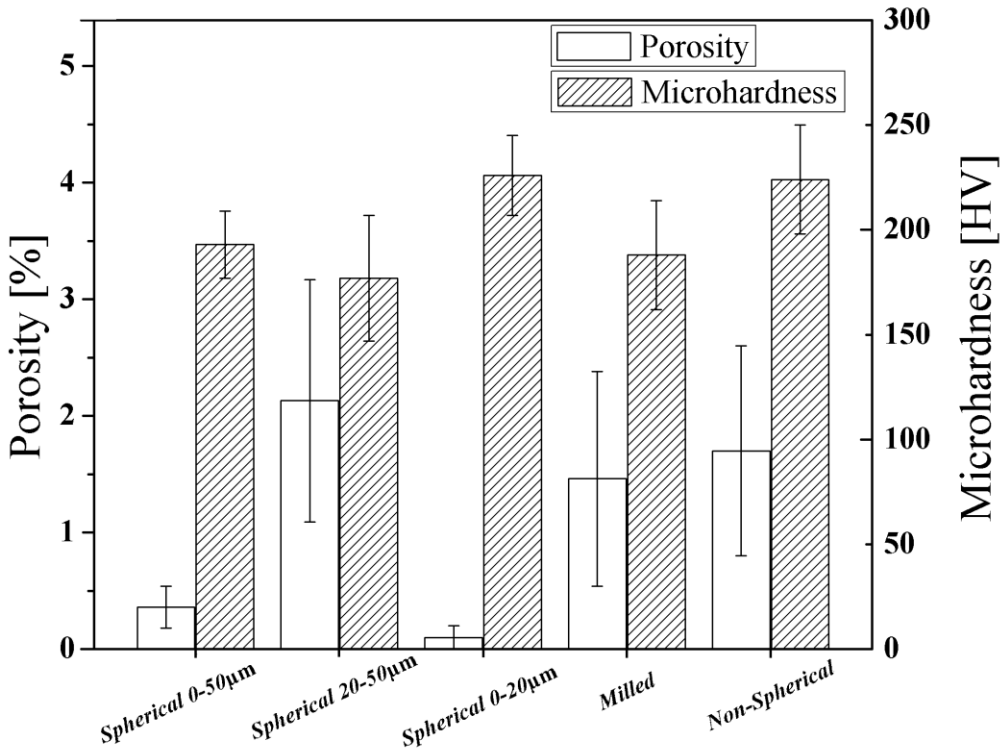

Figure 6.7 Effect of powder morphology on PGDS coating porosity and microhardness

As expected, the powder morphology has a direct impact on the coatings properties. First, the spherical 20-50 µm feedstock powder stands out with a high porosity level of 2.1%, which can be seen in Figure 6.8.

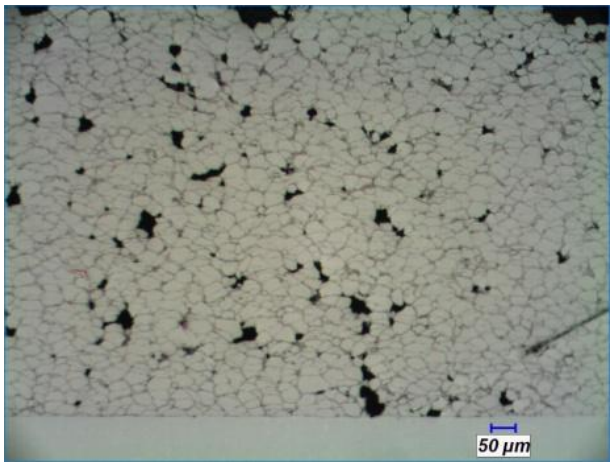

Figure 6.8 Micrograph of PGDS coating using spherical 20-50 μm powder at 100x

Due to their larger diameter, the probability for the particles to stack unevenly and leave larger holes was greater. In addition, it can be hypothesized that the particles were too large to achieve high velocities and experience high deformation to close the voids. Furthermore, the microhardness of the coating is also the lowest one at 177 $HV_{0.3}$, thus low level of deformation was experienced which could also be related to lower particle velocities. The two non-spherical powders present high porosity levels; 1.5% and 1.7% for milled and non-spherical, respectively. The particles within each coating seem to be well deformed based on Figure 6.9 and Figure 6.10; however both powders were already non-spherical before spraying, it is therefore impossible to say whether they are deformed or not based on cross-section observations.

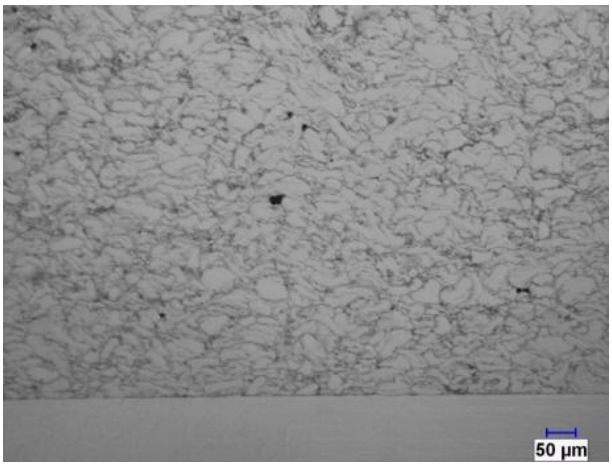

Figure 6.9 Micrograph of PGDS coating using milled powder at 100x

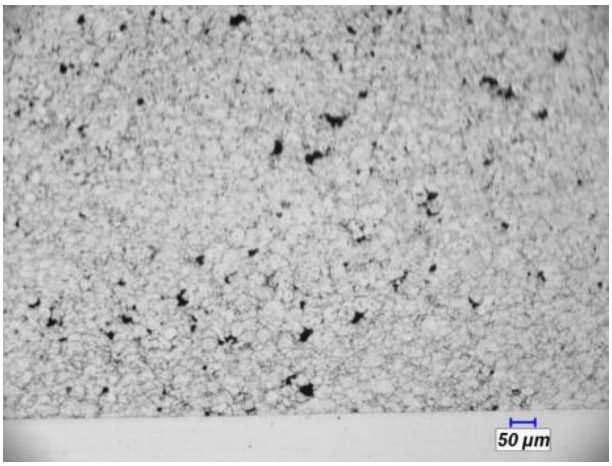

Figure 6.10 Micrograph of PGDS coating using non-spherical powder at 100x

Their microhardness values are very close to the coatings produced using spherical powder, which indicates that the total level of deformation of the particles is similar. However, their non-spherical shape has promoted the formation of voids. Even though higher particle velocities are supposed to be achieved compared to spherical powders, the non-spherical morphology of the powder can result into uneven particle stacking. The deformation that would be required to successfully close the voids was too extensive and voids were created.

Finally, the two remaining powder morphologies, namely spherical 0-50 µm and spherical 0-20 µm, have both low porosity levels (below 0.5%) and seem to be deformed to the same level according to OM at higher magnification. Low magnification cross-section views of these coatings are shown in Figure 6.11 and Figure 6.12.

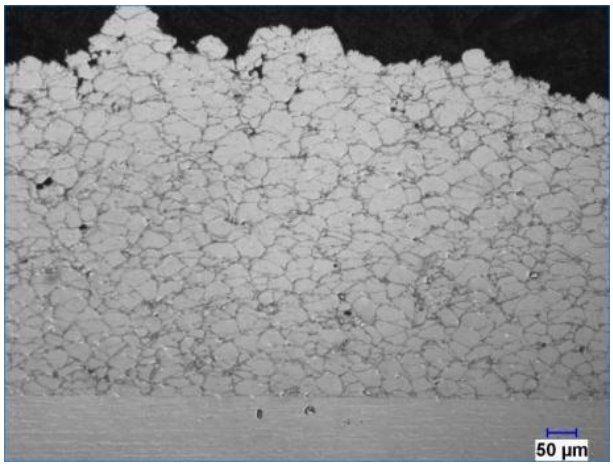

Figure 6.11 Micrograph of PGDS coating using spherical 0-50 μm powder at 100x

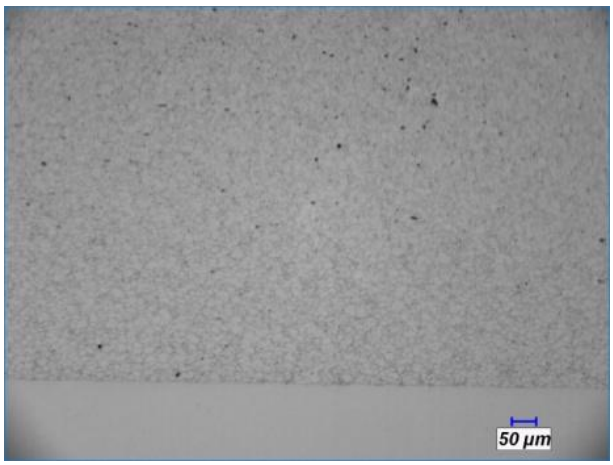

Figure 6.12 Micrograph of PGDS coating using spherical 0-20 μm powder at 100x

The microhardness of these coatings confirms that the level of deformation is similar for these coatings but the 0-20 μm coating microhardness is slightly higher (195 ± 16 and 226 ± 19 $HV_{0.3}$). The average particles of the 0-20 μm powder reached higher velocities prior to impact than the average 0-50 μm particle due to a lower size distribution. These higher velocities resulted into higher deformation, hence higher microhardness measurements. The 0-50 μm powder was chosen due to the very low quantity of 0-20 μm available (20% volume) from the original feedstock powder acquired from the manufacturer.

6.2.2.3. Substrate-related Parameter Optimization

The substrate material is Ti-6Al-4V as required for this research. As described in Chapter 4, the substrates were acetone cleaned only since sandblasting could lead to reduced adhesion strength and reduce fatigue life of Ti-6Al-4V substrates. The substrate standoff distance was investigated and chosen to be 10 mm [99], for the same reasons as with the LPCS technique. The spray pattern found during the LPCS optimization was used to spray the PGDS samples to maximize the local temperature and promote impingement by the increased ductility caused by the higher local temperature. Substrate preheating was performed in a similar manner as the LPCS sprays to increase substrate ductility and increase the deformation upon particle impact, and potentially promote adhesion. At operating temperature, the area of interest was sprayed by the jet only, without powder. Once preheated, the powder was fed to the specified feed rate to create a coating. Unfortunately, due to time restraints, the full characterization of the effect of substrate temperature on coating properties was not performed. The substrate is therefore said to be preheated to an undetermined temperature. The microhardness of the substrate should be monitored since the prolonged exposure to high temperature could induce annealing effect and therefore, reduce the microhardness. The substrate displacement speed was optimized at 1 mm/s. Any increase of travel speed resulted in porous coatings due to a reduced impingement effect compacting the coating. The step size (2 mm) was determined based on the thickness of a single layer and the overlapping required to obtain a coating thickness of about 1.5 mm. For instance, the deposited material trace of the PGDS is about 6 mm wide. If the deposited layer has a thickness of 0.5 mm, the PGDS gun will overlap 3 passes using a 2 mm step and result into a 1.5 mm thick coating.

6.2.2.4. Valve-related Parameter Optimization

In the PGDS technique, a rotary valve is used to create a shockwave that propels the particles towards the substrate while heating them. The formation of this shockwave is critical and a poor valve design could result into a simple pulsing flow of gas, rather than creating a shockwave. As such, valve opening time must be kept short and the total opening area large enough to let through enough gas to accelerate the powder. With the possible change in frequency, disk slot design and seat opening angle, the valve is a complex system whose parameters are interrelated. A single change, such as changing the frequency from 5 Hz to 10 Hz, will have an effect on other parameters like opening time if the internal components are not changed. Due to time constraints, the full optimization of the valve was not completed. However, it was determined that the valve frequency should be 10 Hz for the 13.5 degrees valve seat with a 3 slots disk. These values were based on previous studies performed in the University of Ottawa Cold Spray Laboratory [53].

The effect of the barrel length has been studied as it affects the powder acceleration. A barrel of inadequate length will lead to lower particle velocities due to reduced dwell time. A barrel that is too long will also give lower particle velocities potentially caused by boundary effect or the cooling temperature gradient created by the lack of heating after the gas coil up to the tapered tip exit. The reduction in temperature would result into slower shockwave velocity, thus slower particle velocity. Furthermore, the energy of a shockwave dissipates as it is propagating. Velocity measurements could be performed to characterize the effect of the barrel length on particle velocity. In this work, three different lengths (50, 75 and 100 cm) were tested using a gas temperature of 550°C, a gas pressure of 3.5 MPa and a powder preheating temperature of 350°C; results are reported in Table 6.15. The remaining spraying conditions are presented in Appendix H.

Table 6.15 Effect of barrel length on PGDS coating porosity

Barrel Length	Coating Porosity
50 cm	>15 %
75 cm	>10 %
100 cm	>15 %

Based on the porosity results given in Table 6.15, the barrel of 75 cm produced denser coatings than the other two. This length seems to be a trade-off between particle acceleration and negative effects due to longer barrel.

6.2.2.5. Summary of PGDS Optimized Parameters

This sub-section concludes the parameter optimization phase for the PGDS system. The following table summarizes the optimal conditions for CP titanium deposition using the PGDS technique. These will be used to create the coatings analyzed in Chapter 7.

For the deposition of CP titanium using PGDS, most of the parameters were fully optimized and tested using different values. The parameters that would need more investigation are the valve and the substrate temperature as shown in bold in Table 6.16. The creation of a proper shockwave is the key feature of this system. A full characterization of the different parameters of the valve could lead to major improvements of this system. Furthermore, the powder injection should be carefully controlled in order to inject it into the proper zone behind the shockwave where particles can be accelerated and heated prior to impacting the substrate. The effect of a turning coil in which the shockwave travels should be investigated and compared to a straight tube. The substrate temperature should also be controlled and measured to fully characterize its effect on coating properties. Finally, particle velocity measurements could be used to verify the effect of different barrel length on particle velocities and could provide useful information for the valve optimization as well.

Table 6.16 Optimized parameters for CP titanium deposition using PGDS technique

Category	Parameters Description	Optimized Value
Gas	Nature	Helium
	Temperature	550°C
	Pressure	4.5 MPa
Powder	Material Nature	CP titanium
	Morphology	Spherical
	Size Distribution	0-50µm
	Preheating Temperature	700°C
	Powder Feed Rate	7.0 g/min
	Powder Carrier Gas Nature	Helium
	Powder Carrier Gas Flow Rate	20 scfh
Substrate	Substrate Material Nature	Ti-6Al-4V
	Substrate Preparation	Acetone Cleaned/Degreased
	Substrate Temperature	**Preheating before spray**
	Substrate Travel Speed	1 mm/s
	Step Size	2 mm
	Gun Stand-Off Distance	10 mm
Valve	**Valve Frequency**	**10 Hz**
	Barrel Length	**75 cm**
	Valve Opening Time	**13 ms**
	# Slots in disk	**3**

Chapter 7. Characterization of Optimized CP Titanium Coatings

7.1. Introduction

In this chapter, investigation of the CP titanium coatings produced with LPCS and PGDS processes onto Ti-6Al-4V substrates is presented (**Phase 3**). These coatings were produced using the optimized parameters described at the end of Chapter 6. Microstructural and mechanical properties such as porosity, hardness, deformation level, adhesion strength, single splat analysis, surface fracture analysis, element content analysis and wear performances of the coatings are presented. The feasibility of repairing a simulated damaged part is also demonstrated and the microstructural evaluation of the repair is performed (**Phase 4**). This chapter concludes with a brief summary of the CP titanium coating properties for the LPCS and PGDS systems.

7.2. Coatings Microstructure

Porosity measurements for the coatings produced using the two spray processes are shown in Table 7.1 while SEM images are presented in Figure 7.1.

Table 7.1 Optimized CP titanium coatings porosity level

Experiment	Porosity (%)
CP titanium LPCS	<0.5
CP titanium PGDS	<0.5

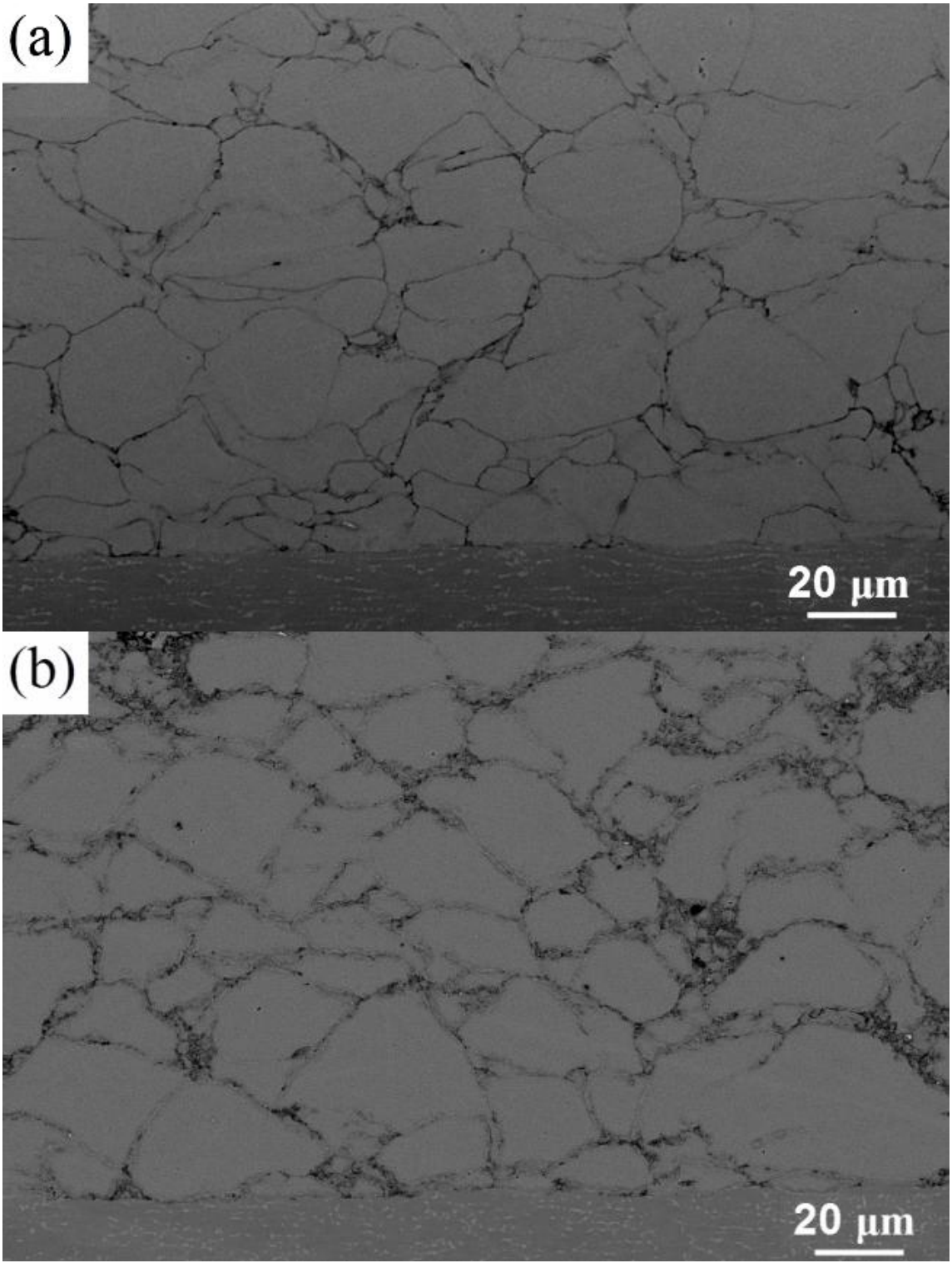

Figure 7.1 Back-scattered (BS) images (a) CP titanium coating using LPCS, (b) CP titanium coating using PGDS

One can observe that porosity levels are similar for both coatings regardless of the spraying method. It has been possible to get close to fully dense coatings (< 0.5%) using both LPCS and PGDS techniques. Other studies, using HPCS, have reported similar porosity level results (< 1%) for CP titanium coatings using helium [75] as the driving gas while typically higher porosity levels (2%-8%) have been reported when using nitrogen [39] as the driving gas. Figure 7.1 reveals that individual particles are still discernible in the coatings, but shows a certain level of deformation as they are not spherical anymore. The particle interfaces are clear and well defined for the coating produced using the LPCS system which is typically seen in cold sprayed coatings. In contrast, the particle interfaces in the PGDS coating seems irregular and broader than in the LPCS coatings. The presence of agglomerations of very small particles (below 5 microns) between larger particles can be observed in the PGDS coatings at higher magnification in Figure 7.2. Small particles were also observed in other studies using HPCS systems [39,67]. It was hypothesized that the high temperatures created by the adiabatic shear instabilities induce local melting in the jetting region upon impact of the particles. Some of the molten material is propelled, splashes and solidifies to form nano-size particles similar to what can be found in VPS [4]. In this work, the particle dimensions observed in the PGDS coatings are larger than what is found in VPS and would indicate a different formation mechanism. In addition, the morphology of these particles is not perfectly spherical, as they would be in the case of solidifying droplets. These small particles are not observed within the CP titanium LPCS coatings.

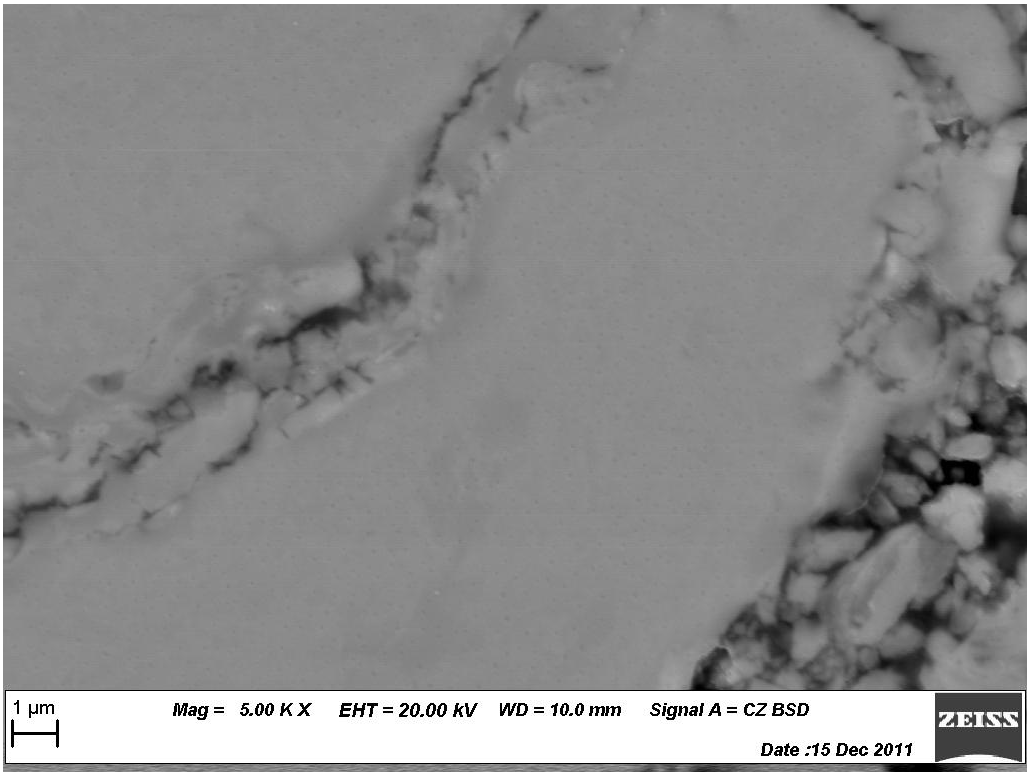

Figure 7.2 Higher magnification of BS images of CP titanium using the PGDS technique

7.2.1. Deformation Analysis

To further investigate coatings features produced using the two spray processes, detailed particle deformation analyzes were performed on the etched coatings cross-sections. In particular, the particle flattening ratios (Fr) were computed for each of the two coating types in Table 7.2.

Table 7.2 Optimized CP titanium coatings flattening ratios

Experiment	Flattening Ratio L/D_0
CP titanium LPCS	1.5 ± 0.3
CP titanium PGDS	1.5 ± 0.2

It was observed that the particle flattening ratios within the coatings were identical using the two systems. LPCS and PGDS flattening ratios are 1.5 for CP titanium coatings. These deformation levels are lower than what is typically observed in aluminum or copper cold spray coatings [101]. The main difference is that titanium has higher strength than aluminium and copper and therefore a higher critical velocity, which leads to lower deformation rate [102]. The deformation level of every powder/spraying technique is even throughout the coating thickness except in the top portion of the coatings where there was less impingement to compact and reduce coating porosity. Other studies [98,103] also reported this porous region in titanium coatings. Figure 7.3 presents the region described in a coating produced with LPCS.

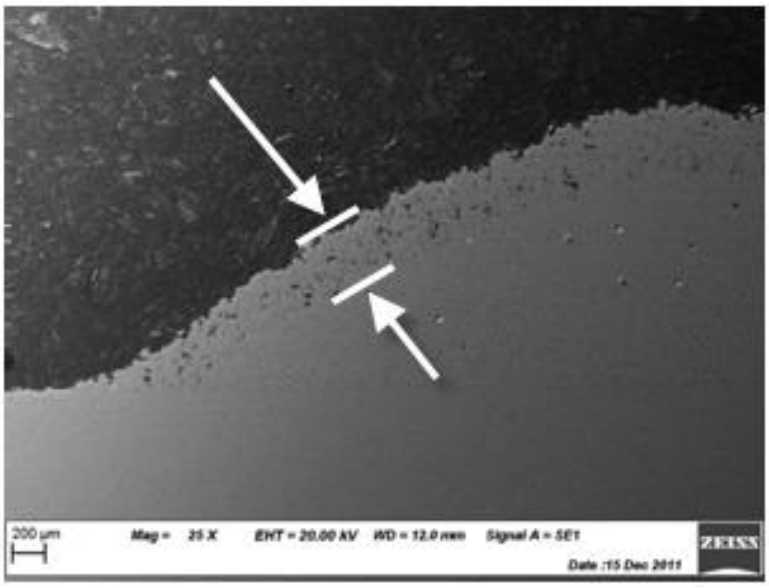

Figure 7.3 Example of the porous region typically observed in titanium coatings

7.2.2. Powder Distribution Inside Coating

Powder size distribution measurements inside the coating have been performed. The area of the deformed particles were measured and their equivalent spherical diameter are reported in Table 7.3 and Figure 7.4.

Table 7.3 Optimized CP titanium coatings average particle diameter

Experiment	Mean diameter (μm)
CP titanium Powder (spherical)	34
CP titanium LPCS	30
CP titanium PGDS	30

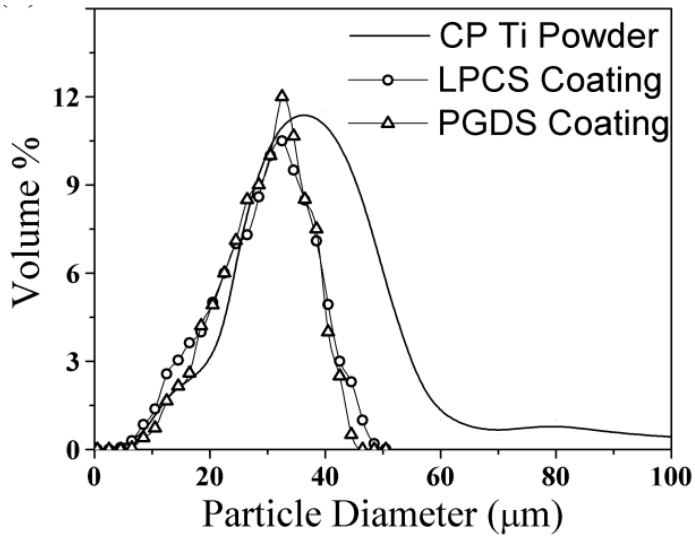

Figure 7.4 Particle size distribution of CP titanium powder and coatings produced with each system

The first observation that can be made is that the average particles diameter within the coatings is smaller than the feedstock powder using either spray process. The average diameter decreased from 34 μm in the CP titanium feedstock powder to 30 μm inside both LPCS and PGDS coatings. In another study, the smaller particles tend to adhere more with

HPCS due to their higher velocities while larger particles accelerate slowly and do not reach critical velocity to adhere to the substrate [43]. However, it is hypothesized that the larger particles play a significant role in the coating process providing deposited particles further deformation through impingement effect. Studies supporting this concept reported an increase in porosity with higher nozzle traverse speeds, where less impingement takes place [39]. This phenomenon is observed in the powder distributions inside the CP titanium coatings in Figure 7.4 where the particles larger than 40 μm did not adhere and bounced off while all the smaller particles deposited to form coatings using either LPCS or PGDS processes.

7.2.3. Microhardness

The coating microhardness results are presented in Table 4. CP titanium coating microhardness was evaluated at 180 ± 20 $HV_{0.3}$ and 190 ± 20 $HV_{0.3}$ for the LPCS and PGDS respectively. This represents an increase compared to the original CP titanium powder microhardness evaluated at 144 ± 6 $HV_{0.05}$. The LPCS and PGDS processes produce CP titanium coatings with the same hardness than what has been found in other studies using the HPCS process (193 ± 5 $HV_{0.1}$) with similar porosity levels and using helium as the driving gas [97].

Table 7.4 Optimized CP titanium coating microhardness

Experiment	Microhardness
CP titanium Powder (spherical)	144 ± 6 $HV_{0.05}$
Ti-6Al-4V Substrate	355 ± 17 $HV_{0.3}$
CP titanium LPCS	180 ± 20 $HV_{0.3}$
CP titanium PGDS	190 ± 20 $HV_{0.3}$

The increased microhardness observed for both spray processes is explained by severe plastic deformation during impact also known as strain-hardening and cold work. This phenomenon occurs due to the solid state of the particles hitting the substrate and the non-recovery of the dislocations created upon impact inducing strain hardening that increases with the degree of particle deformation. As seen in all coatings produced in this study [87], further particle deformation is achieved by the impingement effect of the subsequent larger particles closing the voids usually seen in titanium coatings (Figure 7.3).

7.2.4. Adhesion Strength

Adhesion tests were performed according to the ATSM C633 standard and results are displayed in Figure 7.5. The adhesion strength of CP titanium LPCS coatings to the Ti-6Al-4V substrate was 47 ± 7MPa. In the literature, bond strength of CP titanium HPCS coatings onto Ti-6Al-4V with porosity of 15% yielded 20 MPa [82] while bond strengths of 80 MPa were reported for dense CP titanium coatings on mild steel [104]. Bae was able to achieve 85 MPa adhesion strength for a sieved (16 μm) CP titanium powder on aluminium using a HPCS unit [67]. The lower bond strength obtained in this study is attributed to lower deformation levels for both powders and to the difference in substrate material. In other studies, materials softer than titanium alloy were used resulting into more substrate deformation and roughness which is known to enhance the adhesion strength due to the increased particle-substrate interlocking. For the PGDS process, the bond strength was 61 ± 2 MPa for CP titanium coating, thus considerably higher than the LPCS coating, even though both processes have produced similar microstructures.

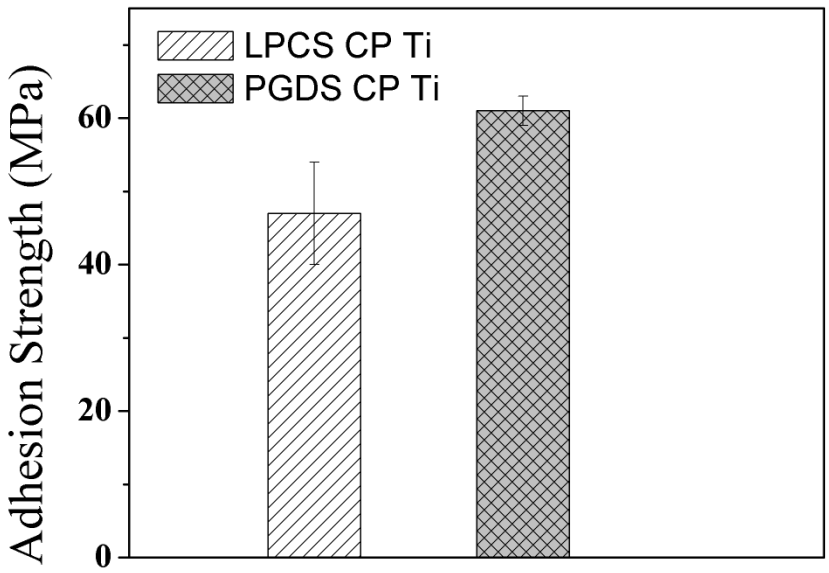

Figure 7.5 Adhesion test results of titanium coatings produced by LPCS and PGDS processes

The coating failure mode is also important to characterize the coating behavior. Two failure modes are possible: cohesive failure and adhesive failure. A coating is said to have failed in cohesion when the coating breaks within its thickness, such that the weakest point was the cohesion between the particles that form the coating. Adhesive failure happens when the coating separates at the coating-substrate interface, usually referred to as peeled off, thus the adhesion strength is less than particle cohesion within the coating. The highest adhesion strength is preferable, but when the coating fails due to high applied stresses, a cohesive failure is preferable as part of the coating is still protecting the part underneath. As seen in Figure 7.6, the failure mode of the LPCS coatings was different from the PGDS coatings. Adhesion failure occurred for LPCS coatings while the failure mode of coatings produced with PGDS system was mainly cohesive. The large difference in bond strength and failure mechanism variation cannot be attributed to a difference in particle deformation as they were measured as equal for both processes. In order to determine the origin of the increased bond

strength using the PGDS process, single splat analysis was done to evaluate how particles deform on the substrate upon impact for each spraying system.

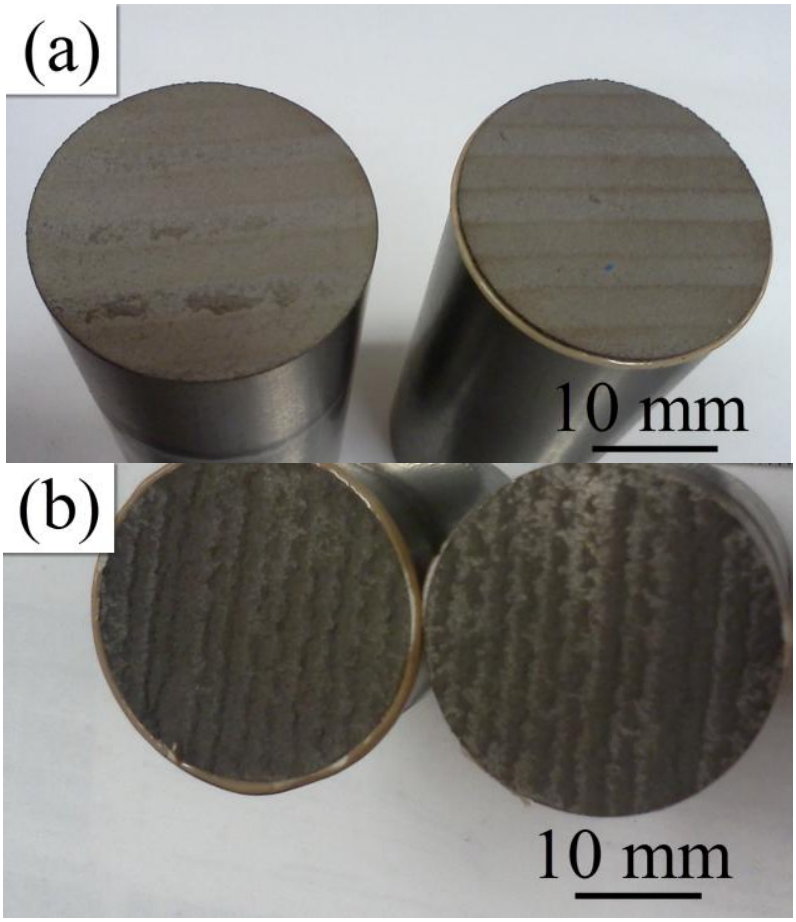

Figure 7.6 Adhesion tests pulled samples of (a) CP titanium coating using LPCS and (b) CP titanium coating using PGDS

7.3.Single Splat Analysis

Single splats were analyzed for each spray process to investigate why the two processes led to in considerably different adhesion strengths. Figure 7.7 (a, c) illustrates top-view SEM images of the resulting splats for each spray process. The samples were then processed for SEM observations on the etched splat cross-sections illustrated in Figure 7.7 (b, d).

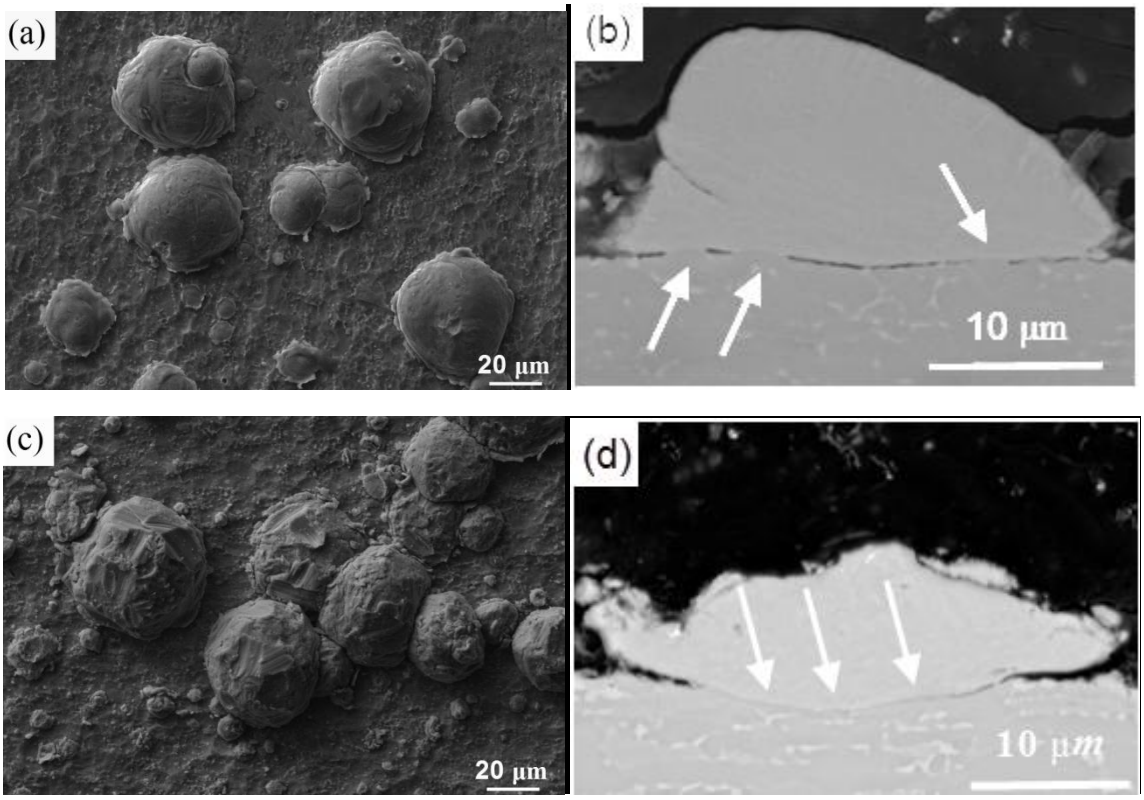

Figure 7.7 Wipe test SEM micrographs of (a) CP titanium LPCS top view, (b) etched CP titanium LPCS cross-section BS view, (c) CP titanium PGDS top view, (d) etched CP titanium PGDS cross-section view

CP titanium splats present a high level of deformation at the particle edges, especially for LPCS (Figure 7.7(a)). This phenomenon, jetting, is created by the high shear loads at the particle point of impact generated from the high pressures of the particles impacting the substrate. The high shear loading creating adiabatic shear instabilities induces local thermal softening due to the lack of heat transfer, creating a flow of material in the transverse

direction identified in Figure 7.7(b). It is also observed that the adhered particle surfaces for PGDS coatings present rough and smeared surfaces compared to the original feedstock powders (Figure 7.7(c)). This would correspond to the observations made previously in the PGDS coating cross-sections of Figure 7.2 where the interfaces between particles were observed to be broad and irregular. It is hypothesized that the sharp edges of the particles are created in flight from particle-particle interactions within the barrel. Every shockwave travelling inside the barrel accelerates the injected particles. However, the driving gas is pulsed at a certain frequency while the powder is feed in the barrel at a constant powder feed rate. Hence, the portion of particles injected between two shockwaves travels in the barrel at lower velocities. These slower particles are then hit by faster particles coming down the barrel from subsequent shock waves. It is also plausible that the particles could impact each other within the high heat zone of the shockwave, due to the radial injection of the powder providing the particles a radial velocity. It is hypothesized that the high temperature particles in the heated zone have their surfaces easily sheared off upon particle-particle impact which creates a high amount of micron size particles and smeared surfaces visible in Figure 7.7(c) and in Figure 7.2, between the larger particles. This hypothesis was preferred to particle-barrel interactions based on the spherical concave erosion sites found on the particles smeared surfaces. This observation also indicates high temperature and ductility of the powder prior to impacting the substrate. Considering that the impact point of the rough particles might be multiple and that material flow outward of the impact region (as seen in jetting), new high temperature sites could be created and promote local metallurgical bonding where the particle temperature approaches melting point. For spherical particles, the high deformation rate at particle impact results into adiabatic shear instabilities which leads to a high temperature rise at the equator of the particle. For the roughen particles, it is

possible that this phenomenon occurs locally around each new impact point as shown in Figure 7.8. In this figure, the green arrows represent the material flow and the red circles represent high temperature sites while the black arrow shows the new high temperature location created by the rough particle shape.

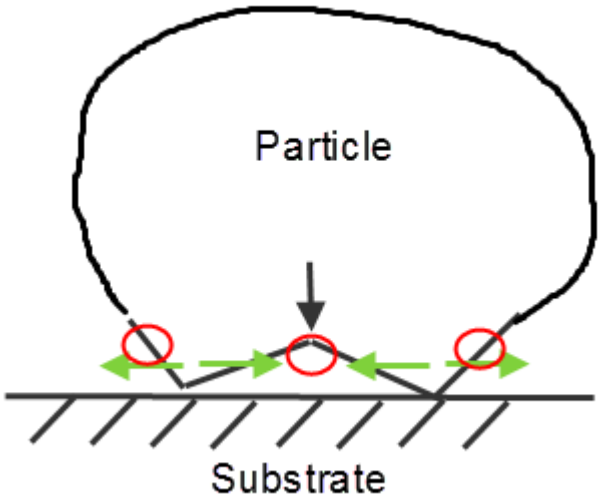

Figure 7.8 Schematic of a rough particle impacting the substrate

In the etched cross-sections shown in Figure 7.7 (b, d), moderate jetting can be identified. It is also observed that some particles are partially metallurgically bonded to the substrate, with bridges between particles and the substrate. This can be observed for the LPCS and PGDS systems pointed by arrows in Figure 7.7(b, d). A higher amount of metallurgical bonding could explain the increased adhesion strength of the PGDS coatings. Fracture surface analysis was carried out to try to confirm this theory.

7.4. Surface Fracture Analysis

Surface fracture investigation of the adhesion test samples was performed to examine qualitatively the possible metallurgical bonding, as it was observed in other studies [65,67,75]. Formations of dimples and cup-cones regions, identified as metallurgical bond sites by other authors [67,69], were observed for CP titanium coatings produced by LPCS and PGDS systems as seen in Figure 7.9. Overall, the CP titanium PGDS coatings presented a higher concentration of these bonded regions compared to the LPCS, which would explain the higher adhesion strength. Larger metallurgical bonding areas were created with the PGDS process due to the higher powder temperature coming from the high heat zone located behind the shockwave [22,23]. As indicated by Papyrin [105], low activation energy is required to initiate the chemical reaction necessary for titanium to form metallurgical bonding. In addition, titanium, with its low thermal conductivity (21.9 $Wm^{-1}K^{-1}$), is more likely to create a highly localised temperature rise upon impact due to adiabatic shear instabilities, enhancing the metallurgical bonding. Also, this temperature rise increases with sharp edges seen in PGDS splats contributing the bonding mechanism. The combination of the high temperature and irregular shape particles explains the higher formation of metallurgical bonding.

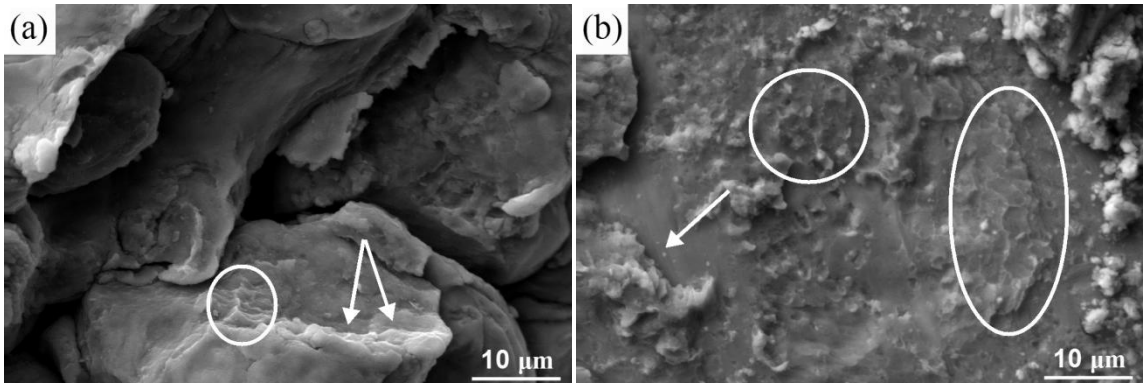

Figure 7.9 Surface fracture of bond plugs showing presence of dimples circled or pointed by arrows: (a) CP titanium LPCS, (b) CP titanium PGDS

7.5. EDS and XRD Analysis

Titanium is usually subjected to oxidation or nitridation during thermal spray processes due to the high temperature involved and the oxygen/nitrogen exposition. Oxides and nitrides are generally identified as structural defects that can cause premature failure or corrosion of coatings. Presence of such elements in the coating was therefore investigated. Figure 7.10 shows X-ray diffraction spectra of the spherical 0-50 µm powder and of the sprayed coatings for each process. The main crystal structure identified in the XRD spectrum of the powder is hexagonal close packed alpha phase titanium.

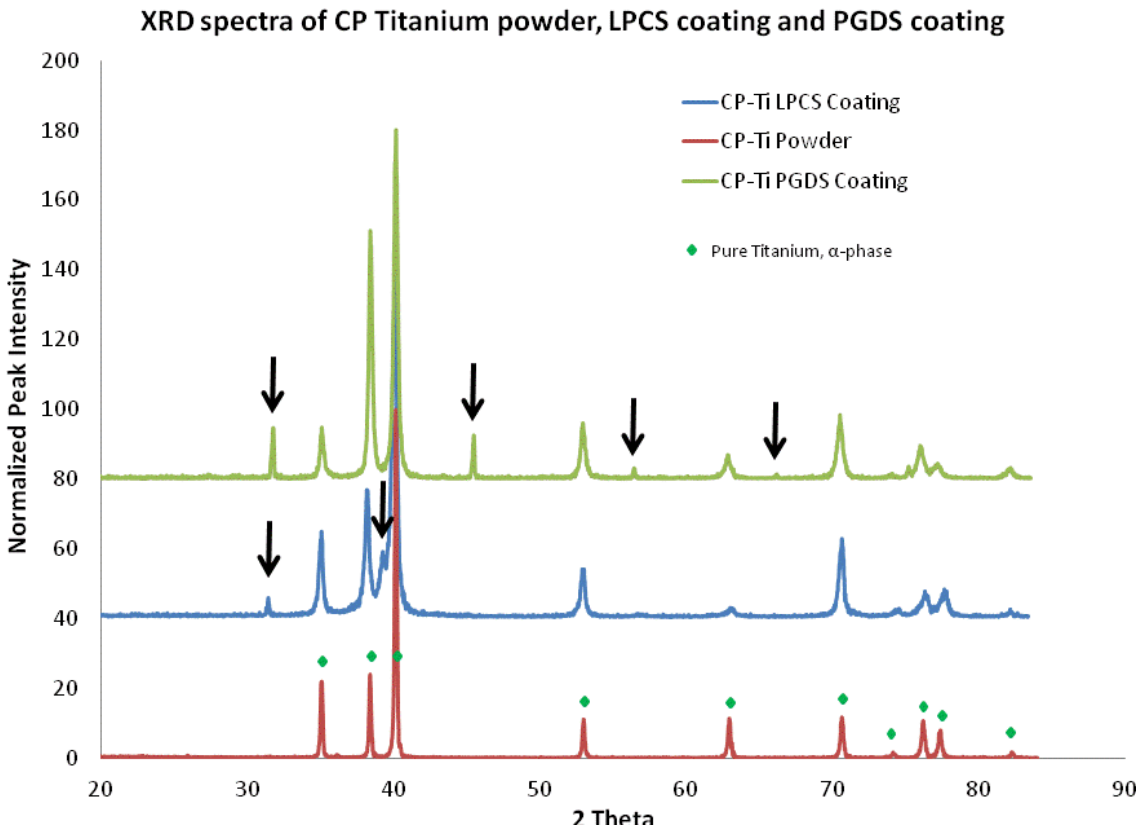

Figure 7.10 XRD spectrum of CP titanium powder, LPCS CP titanium coating and PGDS CP titanium coating, the green diamonds identify the pure titanium alpha phase while the black arrows shows additional peaks present in the coatings

As seen in the Figure 7.10, unidentified peaks, indicated with arrows, appeared in the XRD of the coatings produced with LPCS and PGDS. Due to the elevated processing temperatures involved, the investigation was focused on identifying a possible phase combining titanium with either oxygen and/or nitrogen. Thorough comparisons with the information available in XRD libraries indicates that no oxide/nitride phases fully correspond to the new peaks observed upon deposition of the powder using either technique. Some phases had peaks aligning with the unidentified peaks, but the lack of presence of other main peaks eliminated those possibilities. In Warm Spray, traces of oxygen were found within CP titanium coating [37], while oxide and nitride were identified within a CP titanium coating produced by HPCS [38].

The presence of metallic contaminant phases could be the explanation for these new peaks within the XRD spectra after the deposition process. However, due to the unknown nature of these contaminants and the possibility of superimposed intensity peaks it has not been possible to identify the exact nature of the contaminants. Based on the deposition apparatus materials, the contaminants in the LPCS coating could be derived from brass (orifice material) or stainless steel (nozzle material) and in the PGDS coating, the main material used throughout the process is stainless steel.

EDS analysis was performed throughout the coatings at three different heights to identify the presence of single elements within the coating not detected by the XRD which is based on crystallographic microstructures. At each height, three measurements were made to quantify elements in the coatings and the results are summarized in Table 7.5.

Table 7.5 Optimized CP titanium coatings oxygen and nitrogen content

Experiment	Oxygen Content (wt.%)	Nitrogen Content (wt.%)
CP titanium LPCS	0	0
CP titanium PGDS	0	0

Oxide and nitride were quantified with a value of 0% in weight in each coating for both processes. No evolution of oxide and nitride throughout the spray is observed since no trace of oxygen of nitrogen was observed throughout the entire coatings thicknesses. Element mapping was performed to assess these results. Figure 7.11 shows an element mapping of LPCS coating and Figure 7.12, an element mapping of PGDS coating. The light coloration seen for oxygen and nitrogen was due to system noise.

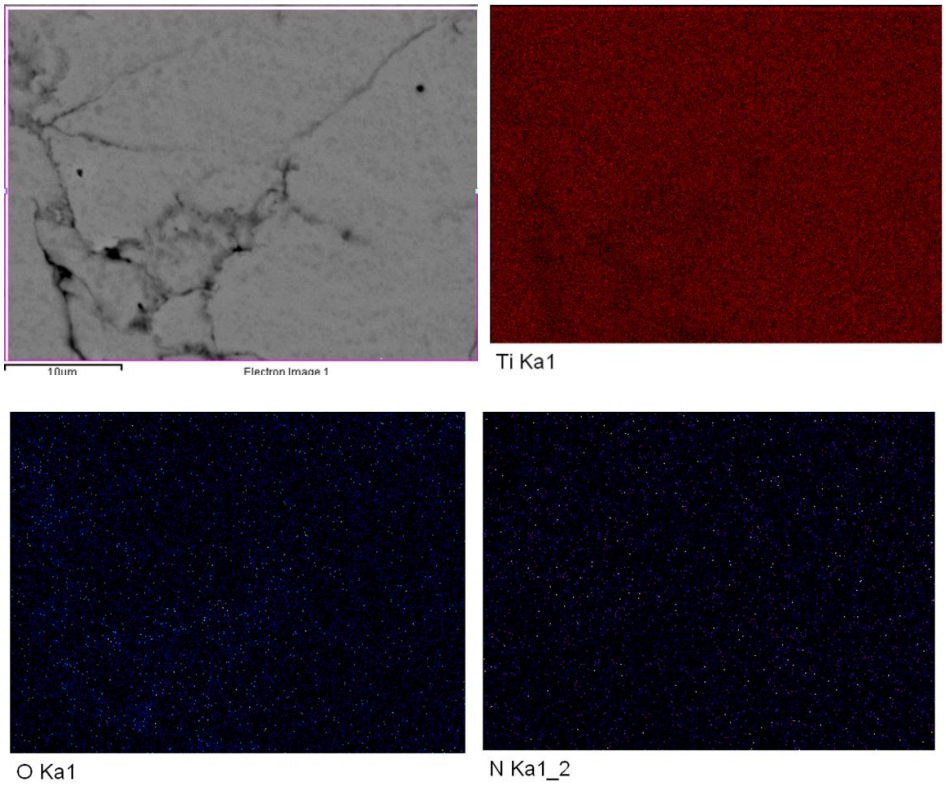

Figure 7.11 SEM element mapping of CP titanium coating produced using LPCS process

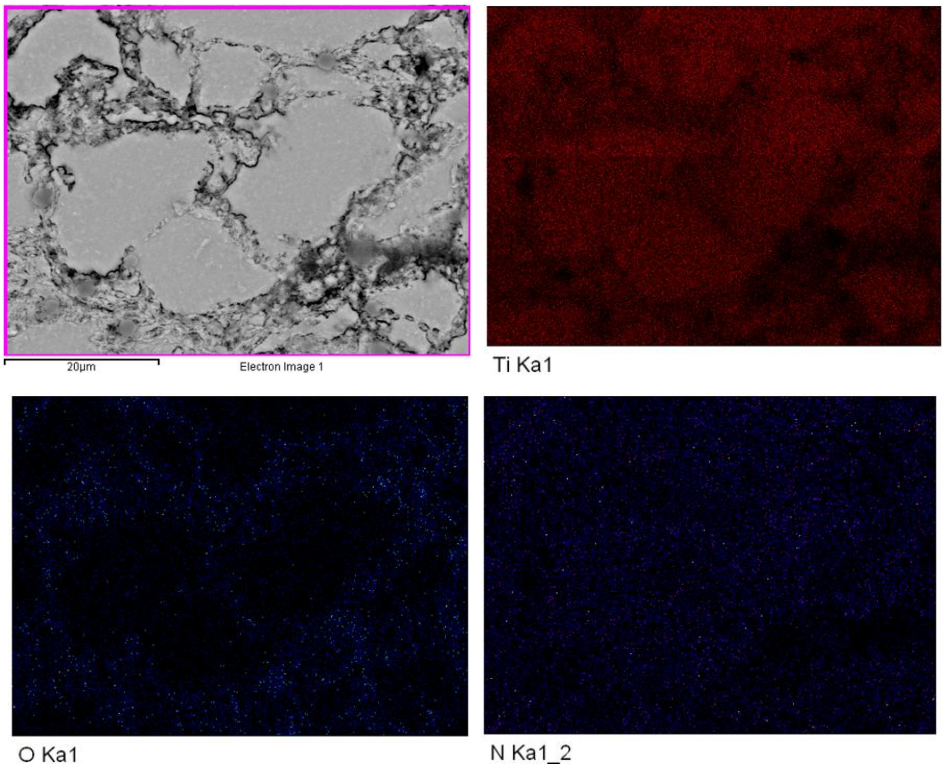

Figure 7.12 SEM element mapping of CP titanium coating produced using PGDS process

7.6. Sliding Wear Resistance

As introduced in Chapter 1, coatings can be used as a protective layer for the substrate. In the present work, the substrate material presents higher microhardness than the coatings (325 $HV_{0.3}$ vs ~190 $HV_{0.3}$). Therefore, it is expected that the substrate will present higher wear resistance than the coatings. However, it is important to know the wear behavior of the coatings to ensure that it is a gradual process and that the coatings do not catastrophically degrade under normal wear circumstances. Figure 7.13 shows the coatings mass losses after different sliding distances for each coating as well as the as-received substrate. LPCS and PGDS coatings for CP titanium have similar mass losses for each sliding distance up to 400 m due to their similar coating microstructures and properties, principally microhardness. The Ti-6Al-4V substrate mass losses were about half the mass losses of the CP titanium coatings. This could be explained by the higher hardness of Ti-6Al-4V substrate (355 $HV_{0.3}$) compared to CP titanium coatings (~185 $HV_{0.3}$) which will present much more resistance to the penetration of the ball under the same loading condition, thus reducing the erosion.

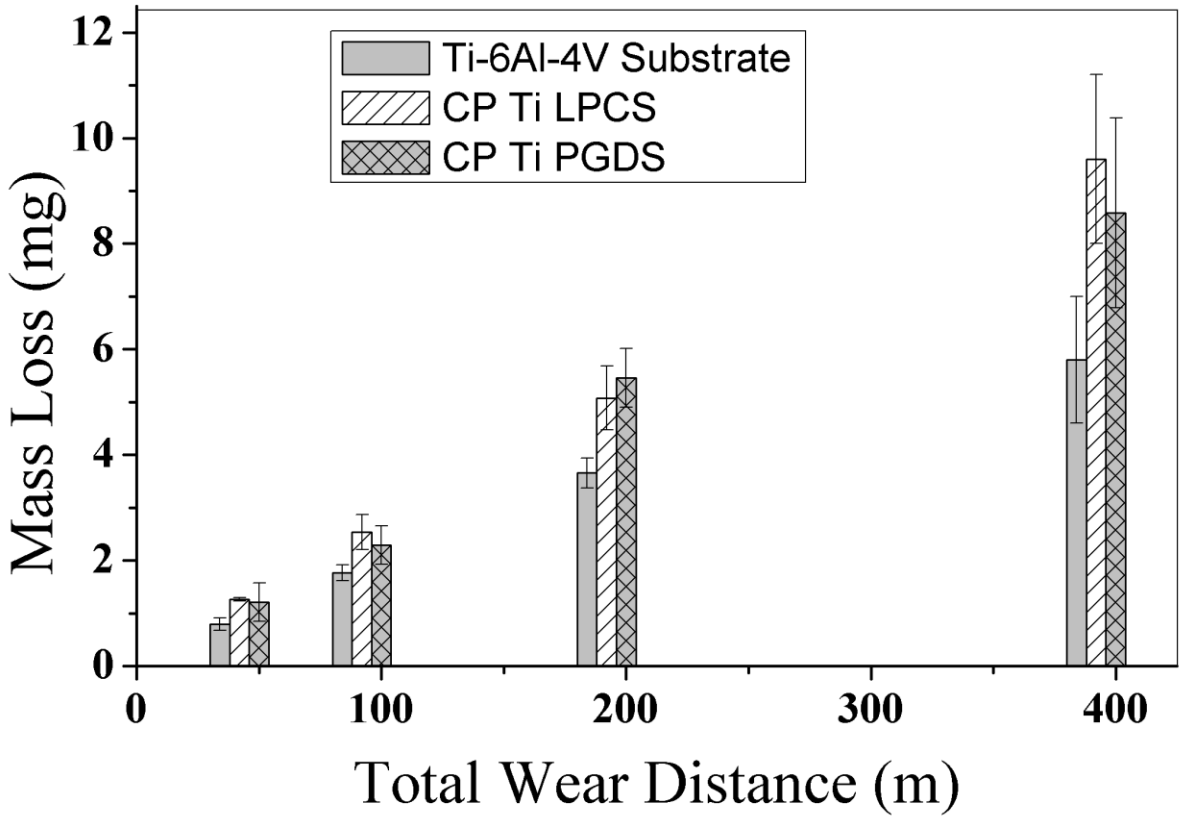

Figure 7.13 Mass losses upon wear test at different distances for CP titanium and Ti-6Al-4V substrate

For the two CP titanium coatings and the Ti-6Al-4V substrate, wear surfaces were observed and presented plastic deformation as seen in Figure 7.14. Wear debris could be observed in the track along the sliding direction in all coatings. Titanium, like aluminium, always builds a passive protective oxide layer on its surface. However, the oxide layer formed in air at room temperature is very thin, about 5–10 nm thick, and weak [106]. Under the action of a ball, this thin and weak oxide layer would be easily broken off exposing the unprotected material to the erosion effect of the ball. The wear debris created were found to accumulate and adhere in the tracks especially for the higher ductility CP titanium coatings versus the Ti-

6Al-4V substrate which presents cleaner tracks. The wear evolution of the coatings produced by LPCS and PGDS was gradual and no cracking/premature delamination was observed throughout wear testing.

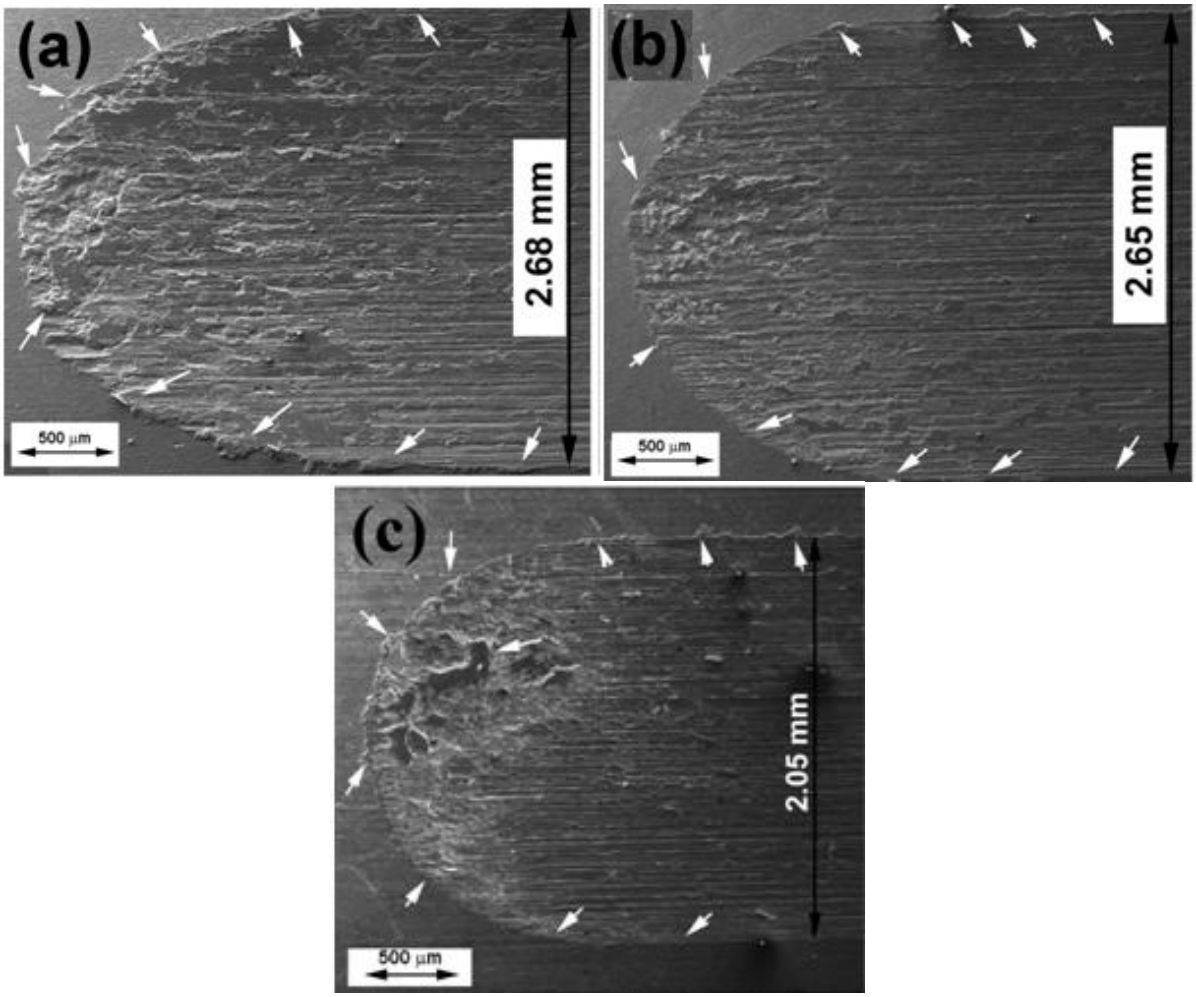

Figure 7.14 Wear morphology of the track showing plastic deformation left by a silicon nitride ball under 10 N at 5 mm s^{-1} after 400m on, (a) CP titanium LPCS coating, (b) CP titanium PGDS coating and (c) Ti-6Al-4V substrate

7.7. Simulated Damage Repair Feasibility

In order to emulate the restoration of a damaged Ti-6Al-4V part, repairs of simulated damages were performed. Gouges were milled into the substrates at a depth of 1.5 mm, at a 10:1 slope. These damages were then filled with CP titanium coatings. The repairs were sprayed using both the LPCS and PGDS processes using the optimized parameters described earlier. The repairs were then machined to restore the part to its original dimensions and polished; an example is shown in Figure 7.15. The coating characteristics are reported in Table 7.6.

Table 7.6 Simulated damage repair microstructure properties

Experiment	Porosity	Microhardness
CP titanium LPCS	< 1 %	186 ± 20 $HV_{0.3}$
CP titanium PGDS	< 1 %	196 ± 20 $HV_{0.3}$

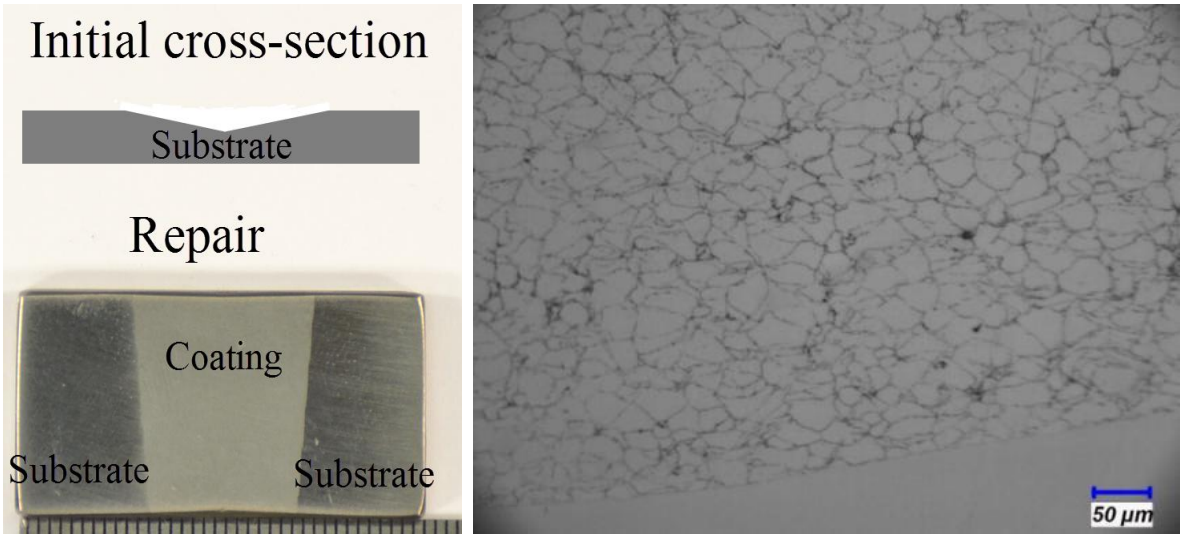

Figure 7.15 Example of simulated damage repair of Ti-6Al-4V substrate with a CP titanium coating using LPCS (left) and the resulting repair microstructure using optical microscope (right)

In cold spray, the angle between the gas jet and the surface, knows as impact angle, should be approximately 90 degrees. This ensures that the normal velocity component of the incoming particles is maximized, transferring all of their kinetic energy into deformation. Research has shown that deviating more than 10 degrees from this angle will have a detrimental effect on both copper particles [20] and pure titanium particles [107] deposition efficiencies. Any deviation from 90 degrees with the substrate leads to a lower normal velocity component, while the tangential component increases. Upon impact at an angle, the tangential velocity remains the same, minus friction, and do not contribute to any deformation, hence the normal component has to be maximal to ensure maximum particle deformation. However, a slight angle change, such as spraying on a 10 to 1 slope (6 degrees), still produces high quality titanium coatings (< 1% porosity for CP-Ti). In this work, a slight increase in CP titanium coatings porosity was observed in the cross-sections of Figure 7.15. The coatings porosity and microhardness results are reported in Table 5. The microhardness values of CP titanium repairs are similar than CP titanium coatings sprayed on flat substrates; LPCS 180 ± 20 $HV_{0.3}$ (flat) versus 186 ± 20 $HV_{0.3}$ (repair) and PGDS 190 ± 20 $HV_{0.3}$ (flat) versus 196 ± 20 $HV_{0.3}$ (repair). In summary, titanium alloy Ti-6Al-4V parts could be repaired by producing a CP titanium coating on a machined surface flat surface or with a 10 to 1 slope (6 degrees) or less. Furthermore, the properties of the CP titanium coatings produced using either LPCS or PGDS were not significantly affected by the particle impact angle. Further studies would be required to assess the mechanical properties and behavior of such repairs before applying either spraying techniques to commercial applications.

7.8. Summary

Coatings of CP titanium onto Ti-6Al-4V alloy substrates were successfully produced using both spraying processes. The coatings characteristics are summarized in Table 7.7.

Table 7.7 Summary of CP titanium coatings characteristics

Characteristic/ Spraying System	LPCS	PGDS
Porosity (%)	<0.5	<0.5
Microhardness ($HV_{0.3}$)	180 ± 20	190 ± 20
Flattening Ratio L/D_0	1.5 ± 0.3	1.5 ± 0.2
Adhesion Strength (MPa)	47 ± 7	61 ± 2
Oxide Content (wt.%)	0	0
Nitride Content (wt.%)	0	0
Wear Performance - Mass Loss for 400 m (mg)	9.6 ± 1.6 mg	8.6 ± 1.8 mg
Repair - Porosity (%)	< 1	< 1
Repair - Microhardness ($HV_{0.3}$)	186 ± 20	196 ± 20

In summary, coatings produced with LPCS and PGDS present a dense microstructure (<0.5% porosity). The microhardness of the coatings are higher than the original feedstock powder which is attributed to plastic deformation. No differences between the two coatings produced by the different spraying process were found in terms of hardness, deformation within the coating, oxide or nitride level and wear performance. However, the adhesion strength was 30% higher than LPCS using the PGDS process. Metallurgical bounding was observed in the wipe test as well as in the fracture interface. SEM observations revealed higher amounts of metallurgical bonding within the PGDS coating than in the LPCS coating. This difference has been attributed to the higher PGDS particles temperature induced by the shockwave heat zone and to the multiple impact points created by the rough shape of the

particles impacting the substrate. Thus, the 30% increase of the adhesion strength of the PGDS versus the LPCS can be attributed to the higher metallurgical bonding concentration.

In summary, the coatings produced by LPCS and PGDS present competitive microstructure (density, microhardness, oxide content) and mechanical properties compared with HPCS coatings.

Conclusions

The purpose of this research was to investigate the deposition of CP titanium using commercially available LPCS and PGDS processes. This project was a first step towards the implementation of these processes as repair techniques in the aerospace industry. As such, the parameters of the two processes were optimized in order to achieve dense and hard coatings. Then, coatings were produced using these optimal parameters for each system and thorough coating characterization was performed.

The feasibility of deposition CP titanium coating using LPCS and PGDS processes was demonstrated in Phase 1 of this project. However, the coatings exhibited high porosity levels indicating that the process parameters should be optimized to produce high performance coatings.

During Phase 2, the parameters of each process were optimized. Both processes required helium gas as the propellant gas due to its higher speed of sound compared with nitrogen. For both systems, increasing gas stagnation temperatures (650°C for LPCS and 550°C for PGDS) led to better coating properties, as a result of its direct effect on the speed of sound. High gas pressures (1.7 MPa for LPCS and 4.5 MPa for PGDS) were used to achieve high particle velocities. The higher gas pressures increased gas density (LPCS and PGDS) and also temperature (PGDS), resulting in higher drags forces on the particles, hence higher particle velocity. Powder preheating was performed with LPCS and PGDS in order to increase the powder ductility, thus decreasing the critical particle velocity required to deposit CP titanium. Consequently, lower porosity levels were achieved. The substrate travel speed in respect to the nozzle was optimized at 1 mm/s for both spraying techniques, at which the impingement was maximized and enhanced by higher local temperature during the deposition processes.

In Phase 3, optimized coatings were produced using LPCS and PGDS which were then fully characterized. Both processes produced coatings with a very low porosity level (lower than 0.5%) and high microhardness (~190 $HV_{0.3}$), showing that the powder experienced substantial cold working effect compared to the original powder hardness (144 $HV_{0.05}$). Even though coatings deposited using the two different systems exhibited similar porosity,

microhardness and flattening ratios, the adhesion strength of PGDS coatings was 30% higher than the LPCS coating (61 vs 47 MPa). This difference was attributed to a higher amount of metallurgical bonding in the PGDS coating due to higher particle temperature caused by the heat zone of the shockwave. Upon XRD and EDS analysis, it was determined that the coatings contain some contamination, but were not a product of the reaction of titanium with oxygen or nitrogen elements. It was therefore concluded that the coatings were oxide/nitride free.

In Phase 4, the feasibility of repairing a damaged part was demonstrated. Due to the slope of the repair site, a small increase of porosity was observed for the LPCS and PGDS coatings, however the porosity was still below 1%. The microhardness remained similar to the coatings produced on flat plates.

In summary, this work has shown that both LPCS and PGDS systems are capable of producing high quality CP titanium coatings on Ti-6Al-4V substrates. Furthermore, the coatings produced exhibit high adhesion strength and the relatively low processing temperatures involved in these processes lead to oxide-free coatings. Therefore, LPCS and PGDS are promising techniques for the production of high performance CP titanium coatings.

Future Work

Following the work accomplished in this thesis, numerous topics could be of interest in subsequent studies. The following sections present some possible avenues in terms of process improvement and coating characterization for further advancement of this project.

Coating Deposition Techniques

LPCS Development

1. As mentioned during the parameter optimization phase of the LPCS process, the gas stagnation pressure was limited to 1.7MPa. However, the use of higher gas pressures would increase the density of the flow, leading to higher drag forces and higher particle velocity.
2. The optimization of particle morphology and size distribution could be performed using the LPCS process. Lower particle size distribution such as 0-20µm particles could result in higher mean particle velocity and better coating properties.
3. Throughout this work, the nozzle used for the deposition of CP titanium was a commercially available nozzle. The development of a specialised nozzle for this powder type and a specific powder size distribution should be performed to maximize the potential of the flow and accelerate the powder particles to higher velocities.
4. Following the parameters exploration and optimization that was conducted, a multifunctional optimization could be performed to verify the results obtained in this work and optimize the parameters that were not investigated.

PGDS Development

5. The PGDS relies on the formation of a strong shockwave to accelerate the particles. Ideally, the shockwave would be formed using a bursting diaphragm. However, the process requires series of shockwave to work efficiently and a different shockwave formation mechanism had to be built. Throughout this work, a rotary valve was used to produce the shocks but other principles could also be investigated since this feature is critical for this system. For example, the mechanism could consist of a metal ball sitting on a seat, lifted by a magnetic field produced by a solenoid.

6. The valve used consisted of a disk and seat with 3 openings positioned 120 degrees apart such that the opening is done with perfect timing. In theory, these three sets of compression waves would coalesce to form the main shockwave. However, the effect of such practice over the formation of a single shockwave should be investigated.
7. One of the characteristics of a shockwave is that it dissipates slowly as it is travelling. Due to the high temperatures involved, the pulsing valve has been placed behind the gas heater but this practice extended the total distance traveled by the shockwave, reducing its strength. In addition, the effect of the curvature of the coil heater on the shockwave properties has not been investigated. Thus, new valve development should take into consideration the positioning of the valve relative to the coil heater.
8. PGDS powder injection has been performed continuously during the deposition. However, the flow used in this process is pulsed with a specific zone in which the particles are accelerated and heated. As such, the powder injection process should be meticulously timed to coincide with the proper zone behind the shockwave.

LPCS and PGDS Development

9. The main characteristic of the thermal spray processes used throughout this study is high particle velocity. Unfortunately, no velocity measurements were performed. These data would improve further parameter optimization efforts for both systems as the quality of the coatings increases with higher particle velocities.
10. A powder preheating unit was used for the two systems to increase the powder temperature. There are currently no methods of measuring the temperature of micron-size particles travelling at such high velocities (> 600 m/s). Powder temperature measurements could further explain the differences between the LPCS and the PGDS processes.
11. The processing gas used for both spraying devices was helium due to its higher speed of sound than nitrogen. Conversely, as shown in Section 2.2.3.2, hydrogen has the highest speed of sound and could provide higher particle velocities. Helium is also an expensive and non-renewable resource, whereas hydrogen is more affordable and also renewable. However, the use of hydrogen would require significant safety considerations due to its volatile and highly flammable nature. Along with safety

concerns, the use of hydrogen gas could cause hydrogen embrittlement of some materials. With all those concerns addressed, the use of hydrogen as the main processing gas could lead to lower LPCS and PGDS costs and increased coating quality.

Coating Characterization

12. Substrate temperature measurements and its effect on substrate heat treatment should be investigated. For these coatings to be used in an industrial application, it is necessary to understand the effect of the coating deposition on the mechanical properties of the parts. Other coating characterization tests such as fatigue tests, corrosion tests and wear at the repair interface could also be performed.
13. The next step of this project would be to apply the repair technique to real damaged parts and investigate the performance of the repairs.

References

[1] Harris D. H., Selected Applications: A Lesson from Thermal Spray Technology, ASM International, 1992.

[2] Davis J. R., Handbook of Thermal Spray Technology, ASM International, 2004.

[3] Chraska T., and King A. H., "Effect of different substrate conditions upon interface with plasma sprayed zirconia — a TEM study," *Surface and Coatings Technology*, vol. 157, pp. 238-246, 2002.

[4] Salimijazi H. R., Raessi M., Mostaghimi J., and Coyle T. W., "Study of solidification behavior and splat morphology of vacuum plasma sprayed Ti alloy by computational modeling and experimental results," *Surface and Coatings Technology*, vol. 201(18), pp. 7924-7931, 2007.

[5] H. Voggenreiter, H. Huber, S. Beyer, and H.J. Spies, "Thermal Spray: Science and Technology", C.C. Berndt and S. Sampath, eds., *ASM International*, Materials Park, OH, p. 303-08., 1995.

[6] Davis J. R., Introduction to Thermal Spray Processing, 2004.

[7] Kawakita J., Katanoda H., Watanabe M., Yokoyama K., and Kuroda S., "Warm Spraying: An improved spray process to deposit novel coatings," *Surface and Coatings Technology*, vol. 202(18), pp. 4369-4373, 2008.

[8] Alkhimov A., Papyrin A., and Kosarev V., "Gas-dynamic spraying method for applying a coating," US Patent 5,302,414, p. 13, 1994.

[9] Rolland G., Guetta S., Christoulis D. K., Guipont V., and Jeandin M., "Mise en oeuvre et caractéristiques de dépôts par projection thermique Cold Spray: vers la maîtrise de la porosité," *37e Congrès du Traitement Thermique et de l'Ingénierie des Surfaces*, 2009.

[10] Dykhuizen R. C., and Smith M. F., "Gas Dynamic Principles of Cold Spray," *Journal of Thermal Spray Technology*, vol. 7(September 1997), pp. 205-212, 1998.

[11] Wu J., Fang H., Yoon S., Kim H., and Lee C., "Measurement of particle velocity and characterization of deposition in aluminum alloy kinetic spraying process," *Applied Surface Science,* vol. 252, pp. 1368-1377, 2005.

[12] Li W.-ya, Li C.-jiu, Wang H.-tao, Li C.-xin, and Bang H.-seon, "Measurement and Numerical Simulation of Particle Velocity in Cold Spraying," *Journal of Thermal Spray Technology,* vol. 15(December), pp. 559-562, 2006.

[13] Steenkiste T. H. V., Smith J. R., Teets R. E., Moleski J. J., Gorkiewicz D. W., Tison R. P., Marantz D. R., Kowalsky K. A., Riggs W. L., Zajchowski P. H., Pilsner B., Mccune R. C., and Barnett K. J., "Kinetic spray coatings," *Surface and Coating Technology*, vol 111, pp. 62-71, 1999.

[14] Li W.-ya, Liao H., Douchy G., and Coddet C., "Materials & Design Optimal design of a cold spray nozzle by numerical analysis of particle velocity and experimental validation with 316L stainless steel powder," *Materials & Design*, vol. 28, pp. 2129-2137, 2007.

[15] Grujicic M., Zhao C. L., Tong C., Derosset W. S., and Helfritch D., "Analysis of the impact velocity of powder particles in the cold-gas dynamic-spray process," *Materials Science and Engineering*, vol. 368, pp. 222-230, 2004.

[16] Suo X., Guo X., Li W., Planche M.-P., Bolot R., Liao H., and Coddet C., "Preparation and characterization of magnesium coating deposited by cold spraying," *Journal of Materials Processing Technology*, vol. 212(1), pp. 100-105, 2012.

[17] Karthikeyan J., "Cold spray," (March), *Advanced Material Processes*, pp. 33-36, 2005.

[18] Grujicic M., Zhao C. L., Derosset W. S., and Helfritch D., "Adiabatic shear instability based mechanism for particles / substrate bonding in the cold-gas dynamic-spray process," *Materials & Design*, vol. 25, pp. 681-688, 2004.

[19] Gärtner F., Schmidt T., Stoltenhoff T., and Kreye H., "Recent Developments and Potential Applications of Cold Spraying ," *Advanced Engineering Materials*, vol. 8(7), pp. 611-618, 2006.

[20] Gilmore D. L., Dykhuizen R. C., Neiser R. A., Roemer T. J., and Smith M. F., "Particle Velocity and Deposition Efficiency in the Cold Spray Process," *Journal of Thermal Spray Technology*, vol. 8(December), pp. 576-582, 1999.

[21] Bu H., Yandouzi M., Lu C., and Jodoin B., "Effect of heat treatment on the intermetallic layer of cold sprayed aluminum coatings on magnesium alloy," *Surface and Coatings Technology*, 205(19), pp. 4665-4671, 2011.

[22] Jodoin B., Richer P., Bérubé G., Ajdelsztajn L., Erdi-Betchi A., and Yandouzi M., "Pulsed-Gas Dynamic Spraying: Process analysis, development and selected coating examples," *Surface and Coatings Technology*, 201(16-17), pp. 7544-7551, 2007.

[23] Karimi M., Jodoin B., and Rankin G., "Shock-Wave-Induced Spraying: Modeling and Physics of a New Spray Process," *Journal of Thermal Spray Technology*, 20(4), pp. 866-881, 2011.

[24] Goyal T., Walia R. S., and Sidhu T. S., "Surface roughness optimization of cold-sprayed coatings using Taguchi method," *The International Journal of Advanced Manufacturing Technology*, vol. 60(5-8), pp. 611-623, 2011.

[25] Yandouzi M., Ajdelsztajn L., and Jodoin B., "WC-based composite coatings prepared by the pulsed gas dynamic spraying process: Effect of the feedstock powders," *Surface and Coatings Technology*, vol. 202(16), pp. 3866-3877, 2008.

[26] Yandouzi M., Sansoucy E., Ajdelsztajn L., and Jodoin B., "WC-based cermet coatings produced by cold gas dynamic and pulsed gas dynamic spraying processes," *Surface and Coatings Technology*, vol. 202(2), pp. 382-390, 2007.

[27] Irissou E., Legoux J.-G., Ryabinin A. N., Jodoin B., and Moreau C., "Review on Cold Spray Process and Technology: Part I—Intellectual Property," *Journal of Thermal Spray Technology*, vol. 17(4), pp. vol. 495-516, 2008.

[28] Cui C., Hu B., Zhao L., and Liu S., "Titanium alloy production technology, market prospects and industry development," *Materials & Design*, vol. 32(3), pp. 1684-1691, 2011.

[29] Pattison J. Ã., Celotto S., Morgan R., Bray M., and Neill W. O., "Cold gas dynamic manufacturing : A non-thermal approach to freeform fabrication," *International Journal of Machine Tools and Manufacture*, vol. 47, pp. 627-634, 2007.

[30] Herman H., Sampath S., and Mccune R., "Thermal Spray : Current Status and Future Trends," *Materials Research Society Bulletin*, vol. 25(July), pp. 17-25, 2000.

[31] Fauchais P., "Understanding plasma spraying," *Journal of Physics D: Applied Physics*, vol. 37(9), p. R86-R108, 2004.

[32] Baik J.-S., and Kim Y.-J., "Effect of nozzle shape on the performance of high velocity oxygen-fuel thermal spray system," *Surface and Coatings Technology*, vol. 202(22-23), pp. 5457-5462, 2008.

[33] Thorpe M. L., "A Pragmatic Analysis and Comparison of HVOF Processes," *Journal of Thermal Spray Technology*, vol. 1(June), pp. 169-178, 1992.

[34] Kuroda S., Kawakita J., Watanabe M., and Katanoda H., "Warm spraying—a novel coating process based on high-velocity impact of solid particles," *Science and Technology of Advanced Materials*, vol. 9(3), p. 033002, 2008.

[35] Schmidt T., Assadi H., Gärtner F., Richter H., Stoltenhoff T., Kreye H., and Klassen T., "From Particle Acceleration to Impact and Bonding in Cold Spraying," *Journal of Thermal Spray Technology*, vol. 18(5-6), pp. 794-808, 2009.

[36] Bray M., Cockburn A., and O'Neill W., "The Laser-assisted Cold Spray process and deposit characterisation," *Surface and Coatings Technology*, vol. 203(19), pp. 2851-2857, 2009.

[37] W. Tillmann et al., Manufacturing Diamond Impregnated Tools for Stone Machining through Thermal Spraying, *International Thermal Spray Conference*, 2004.

[38] Kim K., Watanabe M., Kawakita J., and Kuroda S., "Effects of Temperature of In-flight Particles on Bonding and Microstructure in Warm-Sprayed Titanium Deposits," *Journal of Thermal Spray Technology*, vol. 18(3), pp. 392-400, 2009.

[39] Wong W., Irissou E., Ryabinin A. N., Legoux J.-G., and Yue S., "Influence of Helium and Nitrogen Gases on the Properties of Cold Gas Dynamic Sprayed Pure Titanium Coatings," *Journal of Thermal Spray Technology*, vol. 20(1-2), pp. 213-226, 2010.

[40] Champagne V., "The cold spray materials deposition process," Cambridge, England: Woodhead Publishing Limited, 2007.

[41] Alkhimov A., Papyrin A., Kosarev V., Nesterovich N., and Shushpanov M., "Method and device for coating," European Patent No. 0 484 533, January 25, 1995.

[42] Kashirin A., Klvuev O. F., and Buzdygar T. M., "Apparatus for Gas-Dynamic Coating," US6402050; WO9822639; EP0951583; RU2100474; CN1137003C; CA2270260, year of priority (issued): 1996 (2002).

[43] Schmidt T., Gärtner F., Assadi H., and Kreye H., "Development of a generalized parameter window for cold spray deposition," *Acta Materialia*, vol. 54(3), pp. 729-742, 2006.

[44] Shapiro A. H., "The Dynamics and Thermodynamics of Compressible Fluid Flow," 1953.

[45] Sansoucy E., "Development of Aluminum-Based Coatings Produced by Cold Gas Dynamic Spraying," University of Ottawa, 2008.

[46] Richer P., "Development of Conventional and Nanocrystalline Bond Coats by Cold Gas Dynamic Spraying for Aerospace Thermal Barrier Coatings," University of Ottawa, 2010.

[47] Stoltenhoff T., Kreye H., and Richter H. J., "An Analysis of the Cold Spray Process and Its Coatings," *Journal of Thermal Spray Technology*, vol. 11(December), pp. 542-550, 2002.

[48] Jodoin B., "Cold Spray Nozzle Mach Number Limitation," *Journal of Thermal Spray Technology*, vol. 11(December), pp. 496-507, 2002.

[49] Schmidt T., Gaertner F., and Kreye H., "New Developments in Cold Spray Based on Higher Gas and Particle Temperatures," *Journal of Thermal Spray Technology*, vol. 15(4), pp. 488-494, 2006.

[50] Karimi M., Rankin G. W., and Jodoin B., "Shock-wave induced spraying: Gas and particle flow and coating analysis," *Surface and Coatings Technology*, 2012.

[51] Villafuerte J., Vanderzwet D., Yandouzi M., and Jodoin B., "Shockwave Induced Spraying," *Advanced Materials and Processes*, vol. (March), pp. 32-34, 2009.

[52] Yandouzi M., Richer P., and Jodoin B., "SiC particulate reinforced Al–12Si alloy composite coatings produced by the pulsed gas dynamic spray process: Microstructure and properties," *Surface and Coatings Technology*, vol. 203(20-21), pp. 3260-3270, 2009.

[53] Assaad J., Corbeil A., Richer P. F., and Jodoin B., "Novel Stacked Wire Mesh Compact Heat Exchangers Produced Using Cold Spray," *Journal of Thermal Spray Technology*, vol. 20(6), pp. 1192-1200, 2011.

[54] Karimi M., Fartaj a., Rankin G., Vanderzwet D., Birtch W., and Villafuerte J., "Numerical Simulation of the Cold Gas Dynamic Spray Process," *Journal of Thermal Spray Technology*, vol. 15(4), pp. 518-523, 2006.

[55] Raletz F., Vardelle M., and Ezo's G., "Critical particle velocity under cold spray conditions," *Surface and Coatings Technology*, vol. 201, pp. 1942-1947, 2006.

[56] Li C.-J., Li W.-Y., and Liao H., "Examination of the Critical Velocity for Deposition of Particles in Cold Spraying," *Journal of Thermal Spray Technology*, vol. 15(2), pp. 212-222, 2006.

[57] Steenkiste T. H. V., Smith J. R., and Teets R. E., "Aluminum coatings via kinetic spray with relatively large powder particles," *Surface and Coatings Technology*, vol. 154, pp. 237-252, 2002.

[58] Assadi H., "Bonding mechanism in cold gas spraying," *Acta Materialia*, vol. 51(15), pp. 4379-4394, 2003.

[59] Grujicic M., Saylor J. R., Beasley D. E., Derosset W. S., and Helfritch D., "Computational analysis of the interfacial bonding between feed-powder particles and the substrate in the cold-gas dynamic-spray process," *Applied Surface Science,* vol. 219, pp. 211-227, 2003.

[60] Gärtner F., Stoltenhoff T., Schmidt T., and Kreye H., "The Cold Spray Process and Its Potential for Industrial Applications," *Journal of Thermal Spray Technology*, vol. 15(2), pp. 223-232, 2006.

[61] Yin S., Wang X.-fang, Li W. Y., and Jie H.-en, "Effect of substrate hardness on the deformation behavior of subsequently incident particles in cold spraying," *Applied Surface Science*, vol. 257(17), pp. 7560-7565, 2011.

[62] King P. C., Zahiri S. H., and Jahedi M., "Focused ion beam micro-dissection of coldsprayed particles," *Acta Materialia*, vol. 56, pp. 5617-5626, 2008.

[63] C.-J. L. et al, "Influence of Spray Materials and Their Surface Oxidation on the Critical Velocity in Cold Spraying," *Journal of Thermal Spray Technology*, vol. 19 (1-2), pp. 95-101, 2010.

[64] Li W.-Y., Li C.-J., and Liao H., "Significant influence of particle surface oxidation on deposition efficiency, interface microstructure and adhesive strength of cold-sprayed 251 copper coatings," *Applied Surface Science*, vol. 256, pp. 4953-4958, 2010.

[65] Hussain T., McCartney D. G., Shipway P. H., and Zhang D., "Bonding Mechanisms in Cold Spraying: The Contributions of Metallurgical and Mechanical Components," *Journal of Thermal Spray Technology*, vol. 18(3), pp. 364-379, 2009.

[66] Dykhuizen R. C., Smith M. F., Gilmore D. L., Neiser R. A., Jiang X., and Sampath S., "Impact of High Velocity Cold Spray Particles," *Journal of Thermal Spray Technology*, vol. 8(May), pp. 559-564, 1999.

[67] Bae G., Kumar S., Yoon S., Kang K., Na H., Kim H.-J., and Lee C., "Bonding features and associated mechanisms in kinetic sprayed titanium coatings," *Acta Materialia*, vol. 57(19), pp. 5654-5666, 2009.

[68] Hussain T., McCartney D. G., and Shipway P. H., "Impact phenomena in cold-spraying of titanium onto various ferrous alloys," *Surface and Coatings Technology*, vol. 205(21-22), pp. 5021-5027, 2011.

[69] Goldbaum D., Shockley J. M., Chromik R. R., Rezaeian A., Yue S., Legoux J.-G., and Irissou E., "The Effect of Deposition Conditions on Adhesion Strength of Ti and Ti6Al4V Cold Spray Splats," *Journal of Thermal Spray Technology*, vol. 21(2), pp. 288-303, 2011.

[70] Li C.-J., Li W.-Y., and Wang Y.-Y., "Formation of metastable phases in cold-sprayed soft metallic deposit," *Surface and Coatings Technology*, vol. 198, pp. 469-473, 2005.

[71] King P. C., and Jahedi M., "Relationship between particle size and deformation in the cold spray process," *Applied Surface Science*, vol. 256(6), pp. 1735-1738, 2010.

[72] Wright T. W., "Shear band susceptibility: work hardening materials," *International Journal of Plasticity*, vol. 8 (5), pp. 583-602, 1992.

[73] Ajdelsztajn L., Zúñiga a., Jodoin B., and Lavernia E. J., "Cold gas dynamic spraying of a high temperature Al alloy," *Surface and Coatings Technology,* vol. 201(6), pp. 2109-2116, 2006.

[74] Ajdelsztajn L., Jodoin B., Richer P., Sansoucy E., and Lavernia E. J., "Cold Gas Dynamic Spraying of Iron-Base Amorphous Alloy," *Journal of Thermal Spray Technology,* vol. 15(December), pp. 495-500, 2006.

[75] Zahiri S. H., Antonio C. I., and Jahedi M., "Elimination of porosity in directly fabricated titanium via cold gas dynamic spraying," *Journal of Materials Processing Technology*, vol. 209(2), pp. 922-929, 2009.

[76] German R. M., "Powder Metallurgy Science," 2nd edition, MPIF, Princeton, 1994.

[77] MPI, "Aluminium Atomized Powders," http://mpi-eg.com/MPI/aluminum-powder.html, visited sept. 2012.

[78] Raymor Industries I., "Plasma Atomization Process," http://www.raymor.com/apc/processes/plasma/,visited sept. 2012.

[79] Solar Atmospheres O., "HDH Processing," http://www.solaratm.com/vacuum-furnace-services/raw-materials/hdh-processing, visited sept. 2012.

[80] Li C., Li W., and Wang Y., "Effect of Spray Angle on Deposition Characteristics in Cold Spraying," *Thermal Spray 2003 : Advancing the Science and Applying the Technology,* pp. 91-96, 2003.

[81] Price T. S., Shipway P. H., and McCartney D. G., "Effect of Cold Spray Deposition of a Titanium Coating on Fatigue Behavior of a Titanium Alloy," *Journal of Thermal Spray Technology*, vol. 15(4), pp. 507-512, 2006.

[82] Marrocco T., McCartney D. G., Shipway P. H., and Sturgeon a. J., "Production of Titanium Deposits by Cold-Gas Dynamic Spray: Numerical Modeling and Experimental Characterization," *Journal of Thermal Spray Technology*, vol. 15(2), pp. 263-272, 2006.

[83] Irissou E., Ilinca F., Wong W., Legoux J. G., and Yue S., "Investigation on the effect of helium-to-nitrogen ratio as propellant gas mixture on the processing of titanium coating using cold gas dynamic spray," *International Thermal Spray Conference* 2011.

[84] CenterLine Ltd., "Pulsed Gas Dynamic Spray (WaveRider) Operator Manual," Windsor, Ontario, 2010.

[85] Goldbaum D., Chromik R. R., Yue S., Irissou E., and Legoux J.-G., "Mechanical Property Mapping of Cold Sprayed Ti Splats and Coatings," *Journal of Thermal Spray Technology*, vol. 20(3), pp. 486-496, 2010.

[86] Moy C. K. S., Cairney J., Ranzi G., Jahedi M., and Ringer S. P., "Investigating the microstructure and composition of cold gas-dynamic spray (CGDS) Ti powder deposited on Al 6063 substrate," *Surface and Coatings Technology*, vol. 204(23), pp. 3739-3749, 2010.

[87] Champagne V. K., Helfritch D. J., Trexler M. D., and Gabriel B. M., "The effect of cold spray impact velocity on deposit hardness," *Modelling and Simulation in Materials Science and Engineering*, vol. 18(6), p. 065011, 2010.

[88] "Standard Test Method for Knoop and Vickers Hardness of Materials 1," E384-11, Annual Book of ASTM Standards, Vol. 03.01, ASTM.

[89] "Standard Test Method for Adhesion or Cohesion Strength of Thermal Spray Coatings," C 633-01, Annual Book of ASTM Standards, Vol. 02.05, ASTM, 2008.

[90] "Standard Test Method for Linearly Reciprocating Ball-on-Flat Sliding Wear 1," G133-05, Annual Book of ASTM Standards, Vol. 03.02, ASTM, 2010.

[91] Jodoin B., Ajdelsztajn L., Sansoucy E., Zúñiga a., Richer P., and Lavernia E. J., "Effect of particle size, morphology, and hardness on cold gas dynamic sprayed aluminum alloy coatings," *Surface and Coatings Technology*, vol. 201(6), pp. 3422-3429, 2006.

[92] Blose R. E., "Spray forming titanium alloys using the cold spray process," *Proceedings International Cold Spray Conference*, ITSC, 2005.

[93] Christoulis D. K., Guetta S., Guipont V., and Jeandin M., "The Influence of the Substrate on the Deposition of Cold-Sprayed Titanium: An Experimental and Numerical Study," *Journal of Thermal Spray Technology*, vol. 20(3), pp. 523-533, 2010.

[94] Varacalle D. J., Guillen D. P., Deason D. M., Rhodaberger W., and Sampson E., "Effect of Grit-Blasting on Substrate Roughness and Coating Adhesion," *Journal of Thermal Spray Technology*, vol. 15(September), pp. 348-355, 2006.

[95] Day J., Huang X., and Richards N. L., "Examination of a Grit-Blasting Process for Thermal Spraying Using Statistical Methods," *Journal of Thermal Spray Technology*, vol. 14(December), pp. 471-479, 2005.

[96] Pattison J., Celotto S., Khan A., and Neill W. O., "Standoff distance and bow shock phenomena in the Cold Spray process,"*Surface and Coating Technology,* vol. 202, pp. 1443-1454, 2008.

[97] Wong W., Rezaeian A., and Yue S., "Effects of Gas Temperature , Gas Pressure , and Particle Characteristics on Cold Sprayed Pure Titanium Coatings," *Proceedings International Cold Spray Conference*, 2009.

[98] Li C.-jiu, and Li W.-ya, "Deposition characteristics of titanium coating in cold spraying," *Surface and Coating Technology*, vol. 167, pp. 278-283, 2003.

[99] Li W., and Zhang C., "Materials & Design Effect of standoff distance on coating deposition characteristics in cold spraying," *Materials & Design*, vol. 29, pp. 297-304, 2008.

[100] Schulz O., Eisenreich N., Kelzenberg S., Schuppler H., Neutz J., and Kondratenko E., "Non-isothermal and isothermal kinetics of high temperature oxidation of micrometer-sized titanium particles in air," *Thermochimica Acta*, vol. 517 (1-2), pp. 98-104, 2011.

[101] Li W.-ya, and Li C.-jiu, "Optimal Design of a Novel Cold Spray Gun Nozzle at a Limited Space," *Journal of Thermal Spray Technology,* vol. 14(September), pp. 391-396, 2005.

[102] Li W.-ya, Liao H., Wang H.-tao, and Li C.-jiu, "Optimal design of a convergent-barrel cold spray nozzle by numerical method," *Applied Surface Science*, vol. 253, pp. 708-713, 2006.

[103] Cinca N., Barbosa M., Dosta S., and Guilemany J. M., "Study of Ti deposition onto Al alloy by cold gas spraying," *Surface and Coatings Technology*, vol. 205(4), pp. 1096-1102, 2010.

[104] Wong W., Rezaeian A., Irissou E., Legoux J.-G., and Yue S., "Cold Spray Characteristics of Commercially Pure Ti and Ti-6Al-4V," *Advanced Materials Research*, vol. 89-91(January), pp. 639-644, 2010.

[105] Papyrin A., Klinkov S., and Kosarev V., "Thermal spray 2003: advancing the science and applying the technology," Materials Park, OH: ASM International, p. 27–35, 2003.

[106] Lacombe P., "Titanium and Titanium Alloys," Vol. 2, Plenum, London, pp. 847–863,1982.

[107] Li W.-Y., Yin S., and Wang X.-F., "Numerical investigations of the effect of oblique impact on particle deformation in cold spraying by the SPH method," *Applied Surface Science*, vol. 256(12), pp. 3725-3734, 2010.

Appendix A - PGDS Development

When this project started, the first prototype of the PGDS system was replaced with prototype specially built by CenterLine Ltd (Windsor, Canada) for the University of Ottawa Cold Spray Laboratory. This prototype had a 6 KW electric gas heater and could reach a maximum of 550°C with a gas pressure of 4.5 MPa (helium). This system was used during the first year of this work before being replaced by the commercial version described in Section 4.2.2.

Powder Feeder and Preheater

The powder feeder of the prototype was originally a closed container and a valve was used to restrain the amount of powder going into the flow. Unfortunately, this powder feeder was not continuous and could contain only a limited amount of powder. Therefore, the powder feeder was switched to a continuous commercial powder feeder from Praxair. However, the old powder preheater, made of a band heater attached to the container, could not be used. A new powder preheating system was required for the continuous powder feeding. The designed that was chosen was similar to the gas heater; it consisted of a resistive coil heater. The length of the coil had to be long enough to provide maximum heat transfer to the flow and particles. After few tests, it was determined that 2 meters of 1/4" diameter tubing would be enough for this application. However, in order to reduce the dimension of the powder preheater, it was shaped into a coil and wrapped in ceramic insulation. The first prototype, made of brake line chosen for its low cost and high flexibility, corroded very quickly after only a few cycles at high temperatures. Stainless steel tubing was used for the second prototype. This version was able to reach temperatures above 1000°C. In order to limit oxidation but also reduce the heat losses with the environment, the powder preheater was sent to be coated with an alumina coating. The coil was then wrapped into ceramic insulation before being place into a 4" diameter alumina tube to electrically and thermally insulate the coil. Overall, the powder preheater reached the expectations and performed as required.

Valve Improvement

The prototype of the PGDS system built by CenterLine was originally equipped with an ASCO valve shown in Figure A.1. This valve was designed for pressurized gases with few opening and closing per minute. However, the PGDS system required a frequency of about 10 Hz which greatly reduced the lifetime of the valve. CenterLine eventually designed a new valve based on the rotation of a slotted disk. The performances of this valve was similar to the ASCO valve, when the 13.5 degree opening seat was employed. When aligned with the opening of the seal, the valve would open and close very quickly depending on the rotation speed of the disk. The slots were made long and thin such that the partial opening and closing times were as short as possible with the maximum fully opened time. Their design is composed of a disk with three slots shown in Figure A.2. Even though the disk and seat are machined to have a perfect timing (120 degrees between each opening), the effect of having three coalescing shockwave to form one at the exit of the valve is unknown. Therefore, a new valve prototype was designed with a single exit port aligned with the disk opening, minimizing the change of direction of the shockwave. The 3D model of this valve and the technical drawings are shown in Figures A.3 through A.6.

Figure A.1 Original ASCO Vakve

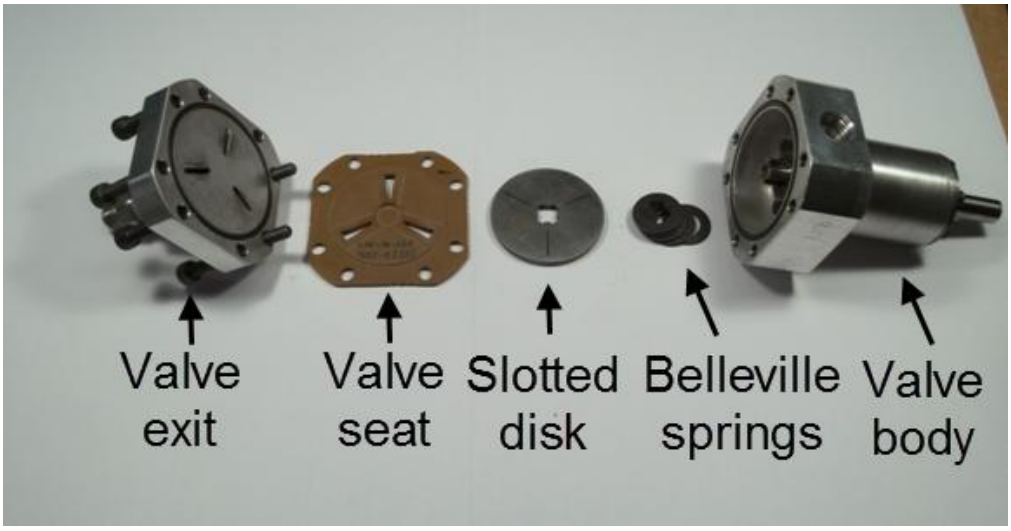

Figure A.2 New rotating disk design

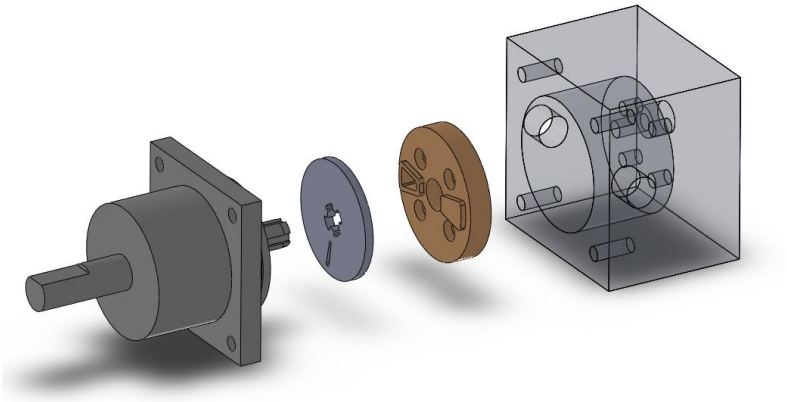

Figure A.3 Single exit design (3D model)

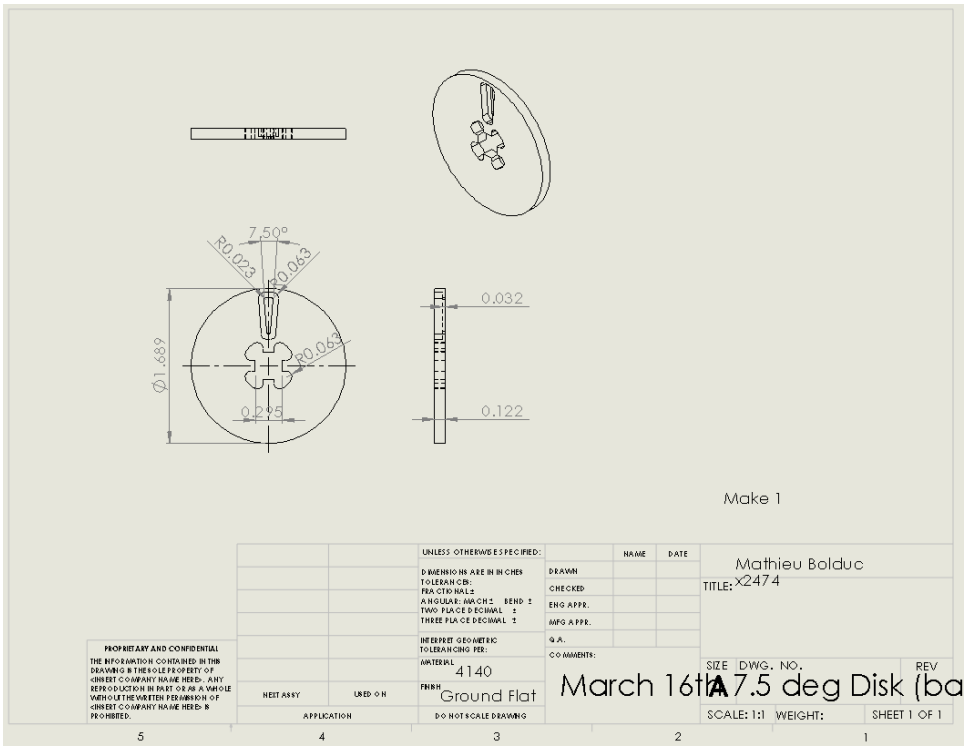

Figure A.4 Single exit design (3D model)

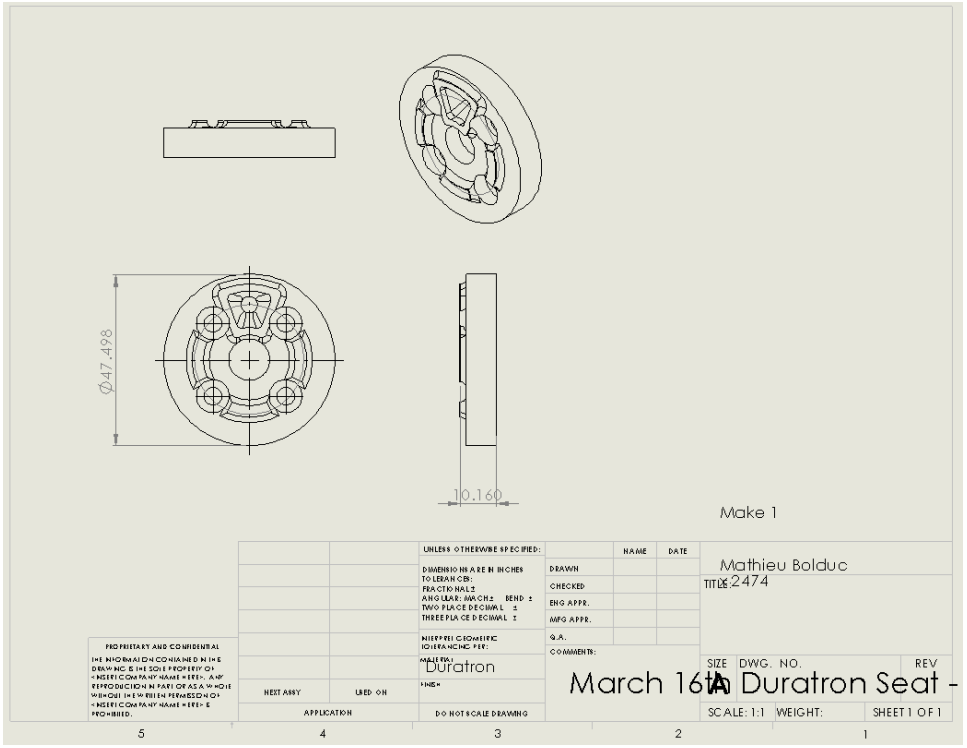

Figure A.5 Single exit design (3D model)

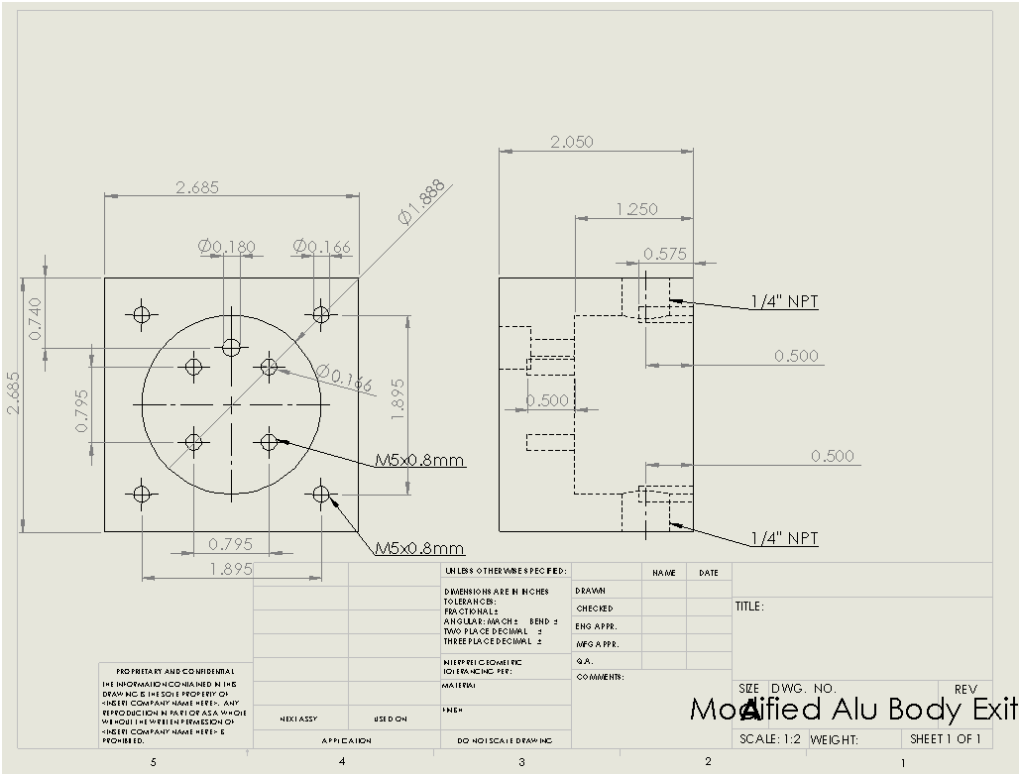

Figure A.6 Single exit design (3D model)

The material used to build the single opening seat was the same then the one used by CenterLine (Rulon). However, in order to obtain the same pulse frequency, the disk had to rotate three times faster than the three slotted disk. The extra friction produced enough heat at this speed to deform the seat until it started to leak (see Figure A.7).

Figure A.7 Deformed rulon seat

A new material specially designed to make valve seats was sourced (Duraton®). This material can withstand high temperature and has a high wear resistance. The new seat is shown in Figure A.8 installed in the valve. Note that o-rings were required under the outer section of the seat as well as under each bolt, in order to have a proper seal.

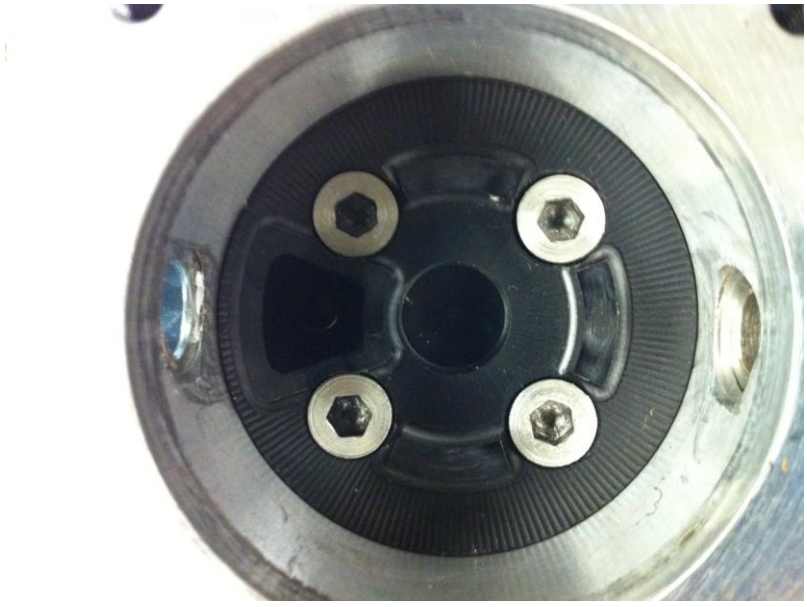

Figure A.8 New Duratron valve seat

In order to evaluate and compare the two valve designs (three and single opening valves), pressures measurements were performed using very sensitive pressure sensors (PCB 113B24) and recorded using a LabView. The pressure measurements were also made to verify that the pressure reaches the regulator pressure before the next pulse. These tests were performed using helium gas at various pressures and at three different pulse frequencies (1, 6 and 10 Hz). In addition, two feed gas line (1/4" diameter and 3/8" diameter) were tested. Results are shown in Figures A.9, A.10 and A.11. Similar results were observed for each pressure tested and therefore, only one set of results is presented below. Note that the time, expressed in ticks, is a time unit very close to 1 millisecond.

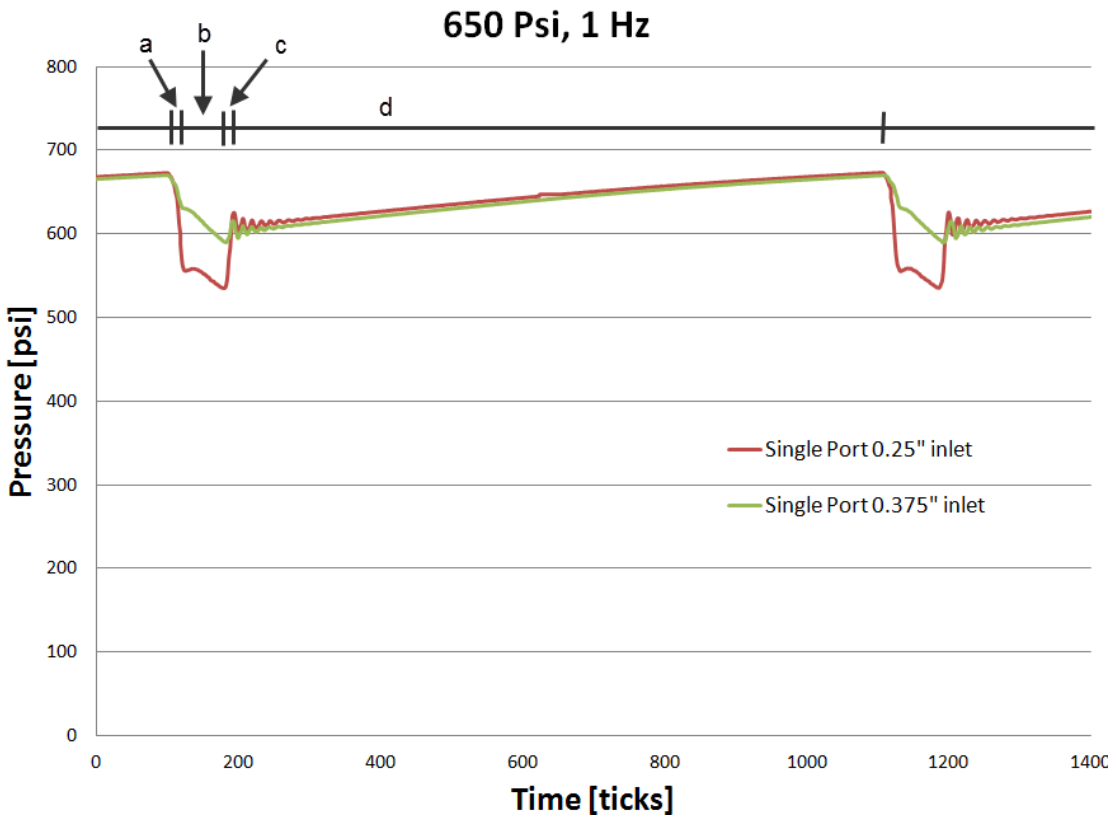

Figure A.9 Single Port Valve showing ; (a) Valve Opening time, (b) Fully Open time, (c) Closing time and (d) fully closed time

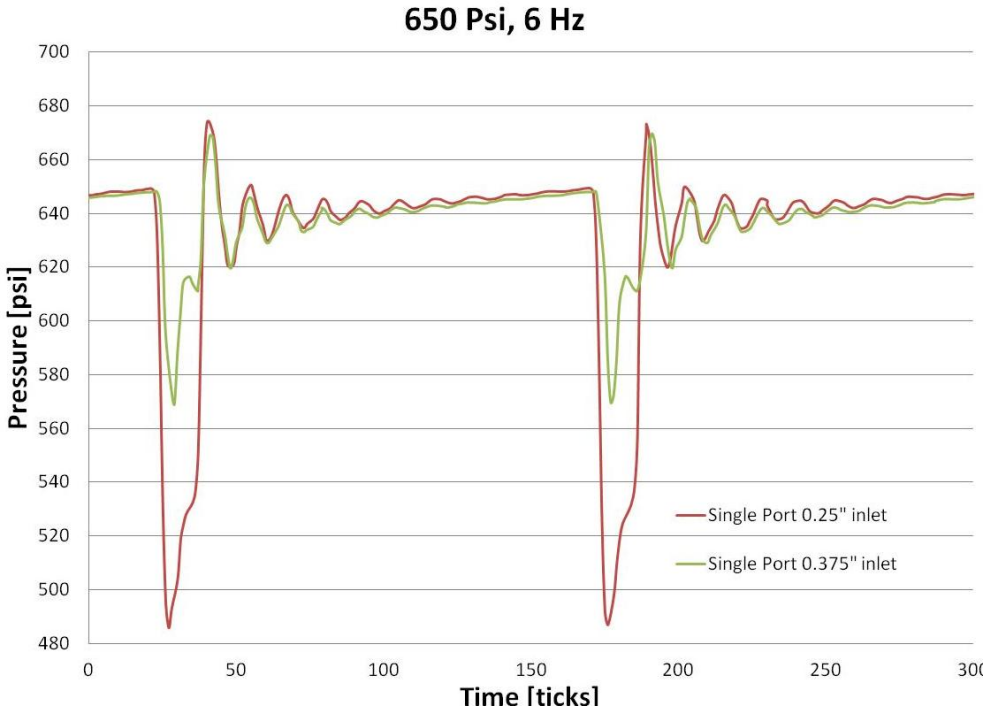

Figure A.10 Single port valve using 2 different gas inlet diameters

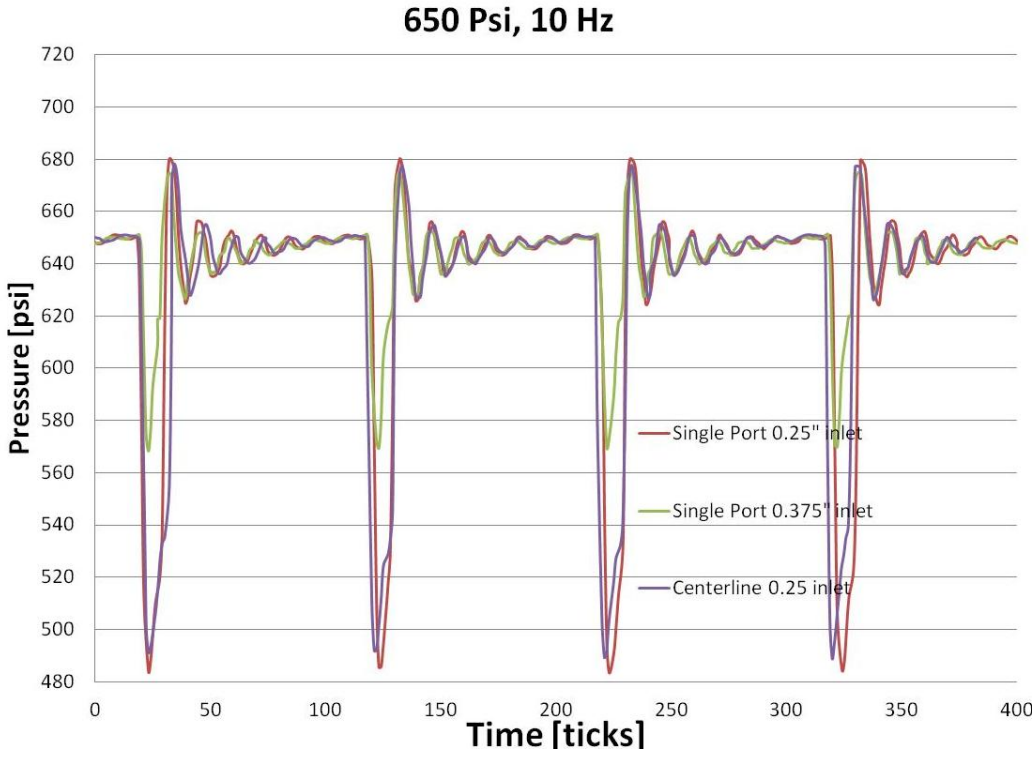

Figure A.11 Three and single opening valve comparison

As seen in Figure A.9, A.10 and A.11, the gas pressure has time to get back to the regulated pressure before each new pulse. In Figure A.9, the pressure recovery is much lower and the pressure never spikes over the regulated pressure. However, at higher frequencies (6 and 10 Hz), it is possible to see that the pressure attains a maximum when the valve closes. This phenomenon is called water hammer effect and happens when a flow is stopped abruptly. The pressure difference is related to the speed of sound of the fluid, its density, and the change in velocity. In addition, it can be noted that the overall pressure during the open time of the valve is higher for the valve having a 3/8" diameter inlet port. This higher pressure could contribute to form a stronger shockwave to propel the particles. In Figure A.11, one can see that the variation of pressure is very similar for the two valves. The deposition of CP titanium was also performed using the single opening valve and no major improvements in coating porosity or microhardness were observed in comparison to the three opening valve.

Appendix B - ASTM C633-01 Standard

Designation: C 633 – 01

Standard Test Method for Adhesion or Cohesion Strength of Thermal Spray Coatings[1]

This standard is issued under the fixed designation C 633; the number immediately following the designation indicates the year of original adoption or, in the case of revision, the year of last revision. A number in parentheses indicates the year of last reapproval. A superscript epsilon (ε) indicates an editorial change since the last revision or reapproval.

This standard has been approved for use by agencies of the Department of Defense.

1. Scope

1.1 This test method covers the determination of the degree of adhesion (bonding strength) of a coating to a substrate or the cohesion strength of the coating in a tension normal to the surface. The test consists of coating one face of a substrate fixture, bonding this coating to the face of a loading fixture, and subjecting this assembly of coating and fixtures to a tensile load normal to the plane of the coating. It is adapted particularly for testing coatings applied by thermal spray, which is defined to include the combustion flame, plasma arc, two-wire arc, high-velocity oxygen fuel, and detonation processes for spraying feedstock, which may be in the form of, wire, rod, or powder.

NOTE 1—Thermal spray coating materials include ceramics, such as metal oxides or carbides, and metals. In some cases, a coating is formed of different spray materials, such as an oxide layer sprayed onto a sprayed metal-bonding layer. The substrate generally is a metal, but may be a ceramic, such as an oxide or graphite.

1.2 Usually this test method is performed at ambient temperature. Higher temperature testing is restricted by the need for a suitable adhesive bonding agent. For certain fundamental investigations, it is suggested that very low (cryogenic) temperature be used.

1.3 This test method is limited to testing thermal spray coatings that can be applied in thickness greater than 0.015 in. (0.38 mm). The limitation is imposed because an adhesive bonding agent is used in the test. Those bonding agents established so far for this method tend to penetrate thermal spray coatings and may invalidate results unless the coatings are thick enough to prevent penetration through the coating. Further development may establish that thin layers of certain types of especially dense coatings may be tested satisfactorily. Alternatively, new adhesive bonding agents that would allow reduction of the minimum thickness limitation may become available.

1.4 *This standard does not purport to address all of the safety concerns, if any, associated with its use. It is the responsibility of the user of this standard to establish appropriate safety and health limitations prior to use.*

2. Referenced Documents

2.1 *ASTM Standards:*

E 4 Practices for Force Verification of Testing Machines[2]

3. Significance and Use

3.1 This test method is recommended for quality control, acceptance testing; or it may help to develop or qualify a thermal spray operator's equipment and procedure or to aid in developing thermal spray coatings with improved adhesion and integrity.

3.2 This test method is useful for comparing adhesion or cohesion strengths of coatings of similar types of thermal spray materials. The test should not be considered to provide an intrinsic value for direct use in making calculations, such as to determine if a coating will withstand specific environmental stresses. Because of residual stresses in thermal spray coatings, actual strength depends upon the shape of the particular coated part. Also, in use, a coating may be stressed in a more complex manner than is practical for a standard test.

4. Apparatus

4.1 A tension testing machine shall conform to the requirements of Practices E 4. The loads used in determining the adhesion or tensile strength shall be within the loading range of the testing machine, as defined in Practices E 4. Permissible variation shall be less than 1.0 %. It shall be possible to apply increasing tensile load at a constant rate of cross-head travel between 0.030 in./min (0.013 mm/s) and 0.050 in./min (0.021 mm/s). The machine shall include a load-indicating device that registers the maximum load applied before rupture occurs.

4.2 Self-aligning devices, for applying the tensile load to the assembly of the coating and fixtures, shall not permit eccentric load or bending moment to the specimen. Self-alignment is often provided by the manufacturer as an integral part of the testing machine. An alternative, satisfactory apparatus is shown in Fig. 1, which also shows methods of connecting the self-aligning apparatus to an assembled test specimen.

5. Material

5.1 *Adhesive Bonding Agent*—A suitable adhesive bonding

[1] This test method is under the jurisdiction of ASTM Committee B08 on Metallic and Inorganic Coatingsand is the direct responsibility of Subcommittee B08.12 on Materials for Porcelain Enamel and Ceramic-Metal Systems.

Current edition approved March 10, 2001. Published July 2001. Originally published as C 633 – 69. Last previous edition C 633 – 79 (1999).

[2] *Annual Book of ASTM Standards*, Vol 03.01.

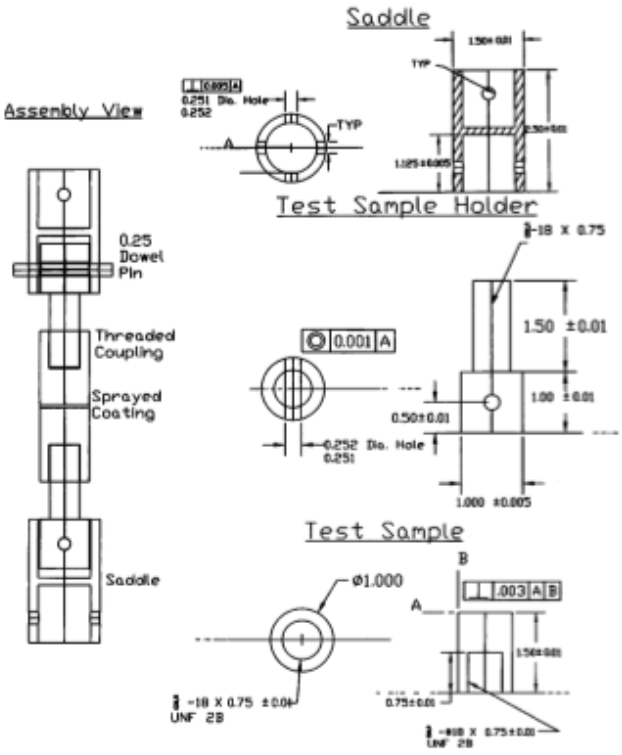

FIG. 1 Self-Aligning Device

agent shall be agreed between the purchaser and manufacturer of the coating and shall meet the following requirements.[3]

5.1.1 The bonding agent shall be capable of bonding the coating to the loading fixture with a tensile strength that is at least as great as the minimum required adhesion and cohesion strength of the coating.

5.1.2 The bonding agent shall be sufficiently viscous not to penetrate through a 0.015-in. (0.38-mm) thickness of the coating. Certain commercial resins that cure or harden at room temperature by means of a curing agent have been proven satisfactory. If any other bonding agent is to be used, it shall first be compared with a proven bonding agent using this test method with the desired thermal spray coating.

NOTE 2—Thermal spray coatings may have an inherent porosity. Excessive penetration of the adhesive bonding agent into this porosity may affect the results determined by this test method. Unless proved satisfactory by comparison testing, any agent requiring elevated temperature for curing should be avoided because viscosity may decrease at high temperature, allowing penetration.

NOTE 3—When liquid epoxy bonding agents are used, there should be a procedure in place to ensure relatively consistent thickness on every sample.

5.1.3 The adhesion strength of the bonding agent shall be determined each time this test method is performed. This shall be done by using the bonding agent to attach a loading fixture to a second loading fixture, in accordance with 6.5, except that the coated substrate fixture of 6.5 is replaced with the second loading fixture.

NOTE 4—One reason for testing the bonding agent each time is to detect improper preparation of the agent if it is a two-part mix. Another reason is that adhesion strength generally decreases with age of the unused agent. If strength is lower than required, more adhesive bonding agent shall be prepared and tested, or the agent shall be discarded and replaced.

6. Test Specimens

6.1 *Substrate and Loading Fixtures*—Each test specimen is an assembly comprising a substrate fixture, to which the

[3] A list of satisfactory bonding agents is provided in the annex which follows this standard.

coating is applied, and a loading fixture. The substrate and loading fixtures shall each be circular, solid cylinders of no less than 1.5 in. in length, or as agreed upon by the manufacturer and customer. A suggested detail for either fixture is shown in Fig. 2. One end of each fixture shall be adapted for attachment to the self-aligning loading devices of the tension testing machine. Both ends of each fixture shall have faces parallel to each other and normal to the loading axis. The facing diameters shall be not less than 0.9 in. (23 mm), nor more than 1.0 in. (25 mm). The diameters of the two fixtures shall be the same and shall be measured so that the error is no greater than 0.5 %.

NOTE 5—In Appendix X1, an alternative substrate and fixture arrangement is provided that has proved cost effective and simple.

6.1.1 *Material for Substrate Fixture*—The substrate fixture shall be constructed of metal, preferably metal intended for use as the substrate for the coating. If no such substrate material is specified, the substrate fixture shall be SAE 1018 or 1020 steel.

NOTE 6—If desired because of cost or ease of fabrication, it may be suitable to attach or bond a layer of the specified substrate material to a fixture formed of any convenient metal. Such a layer of substrate material need not be metal. The layer must be substantially thicker than the possible depth of effects on the substrate, such as recrystallization or diffusion zones, that may result from applying the coating. A layer greater than 0.1 in. (2.5 mm) thick should be sufficient.

6.1.2 *Material for Loading Fixture*—The loading fixture shall be constructed of metal, but material is otherwise optional. It is usually convenient to make the loading fixture of the same material as the substrate fixture; thus, the fixtures may be interchangeable until a coating is applied to one.

6.2 *Coating Application*—The front facing of the substrate fixture shall be prepared in the manner required by the specification for the coating. (Roughening by grit blasting or surface grinding may be typical preparations.) The coating shall be thermal sprayed onto this prepared surface.

6.3 *Coating Thickness*—The coating thickness shall be measured with a micrometer by measuring the total length of the coating fixture before and after the coating is applied. (Care must be taken to avoid contaminating the prepared surface before coating.) The final coating thickness shall be more than 0.015 in. (0.38 mm). If the coating is to be ground or machined, the as-sprayed coating shall be approximately 0.005 in. (0.13 mm) thicker to allow for removal of material. The coating thickness shall not vary across the surface by more than 0.001 in. (0.025 mm). (This thickness variation, as measured from the

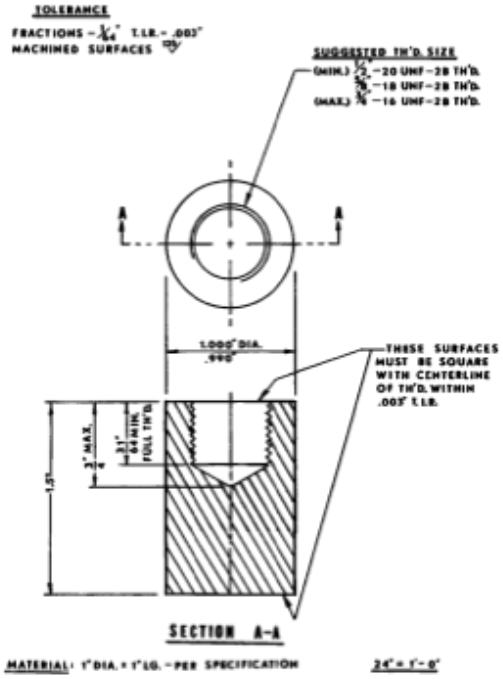

U.S.	0.003 in.	1/64 in.	31/64 in.	1/2 in.	5/8 in.	
Metric	(0.08 mm)	(0.39 mm)	(12.3 mm)	(12.7 mm)	(15.9 mm)	
U.S.	3/4 in.	0.990 in.	1 in.	1.000 in.	1 ft.	24 in.
Metric	(19 mm)	(25.15 mm)	(25.4 mm)	(25.4 mm)	(0.3 m)	(610 mm)

FIG. 2 Substrate and Loading Fixture

rear face, does not refer to the ordinary surface texture or roughness typical of thermal spray coatings.) If, upon completion of the thermal spraying, the coating thickness varies in excess of this limit, this shall be corrected by removing the coating and respraying or by grinding or machining the coating surface.

6.4 *Grinding or Machining the Coating Surface*—The surface of the coating may be finished by grinding or machining when the thickness variation is excessive. If the thickness variation is not excessive, it shall be optional to finish the surface of the coating as a useful and convenient aid in holding the fixtures together parallel and aligned as required for the next step. No specific grinding or machining procedure can be recommended, as this depends on the type of coating material. Usually manufacturers of the coatings have recommendations published or available. Only a rough grinding or machining step is needed, to provide a final coating thickness that does not vary by more than 0.001 in. (0.025 mm). Removal rate shall be insufficient to damage the coating or bond. A recommended method is to use a surface grinder with a magnetic chuck, positioning the rear face of the coated fixture on this magnetic chuck. No other treatment, such as grit blasting, shall be done to the surface of the coating.

6.5 *Attachment of Fixtures*—The facing of the loading fixture shall be free of oil, grease, or grinding or cutting fluids. The facing shall be mechanically cleaned by such means as machining, grinding, light grit blasting, or rubbing with emory cloth. This facing shall be attached to the surface of the coating, using the adhesive bonding agent according to its manufacturer's instructions. Excessive adhesive shall be wiped from the assembly with soft paper or cloth. The two fixtures shall be held together parallel and aligned until the bonding agent is cured or hardened. A suitable holding device such as a "V-block" shall be used for the purpose, except such a device is not necessary if the surface of the coating has been ground or machined smooth.

6.6 *Number of Test Specimens*—The number of test specimens chosen depends upon the purpose of the particular tests under consideration. However, if specimens are to be used for acceptance tests, not less than five specimens of a type shall be tested.

7. Procedure

7.1 Prepare the chosen number of substrate fixtures, and apply a thermal spray coating to each. Finish the coating surface if required.

7.2 Prepare the adhesive bonding agent. Attach cleaned loading fixtures to all the coated substrate fixtures at essentially the same time. In addition, prepare one set of uncoated fixtures for measurement of the adhesion strength of the bonding agent.

7.3 Apply a tensile load to each test specimen at a constant rate of cross-head travel between 0.030 in./min (0.013 mm/s) and 0.050 in./min (0.021 mm/s) until rupture occurs. Record the maximum load applied.

NOTE 7—Loading fixtures may be gravity or pressure devices. The design of the loading fixtures should enable the correct alignment of the specimen.

8. Calculation

8.1 Calculate the degree of adhesion or cohesion strength as follows:

$$\text{Adhesion or cohesion strength} = \text{maximum load/cross-sectional area} \quad (1)$$

9. Interpretation of Results

9.1 Any interpretation of results depends on the purpose of using this test method and on the description of failure. The adhesion or cohesion strength value measured represents the weakest part of the system, whether in the coating or at an interface. A low-power microscope with a magnification range up to 100× is suggested for determining location of failure (also termed as the "locus" of failure).

9.2 The adhesion strength of the coating is given if failure is entirely at the coating-substrate interface.

9.3 The cohesion strength of the coating is given if rupture is only within the coating. Failure in the bonding agent may be a satisfactory result for a quality control assurance test or for a qualification test, if the strength of the bonding agent is greater than the minimum required adhesion or cohesion strength of the coating.

9.4 If failure occurs in a combination of these locations in one specimen, generally no interpretation of the initial cause can be provided. Fig. 3 diagrams the possible modes of failure.

9.5 For a multicomponent system; for example, a bond coat with a ceramic overlay, then failure at the interface between two coatings is described as "internal adhesive."

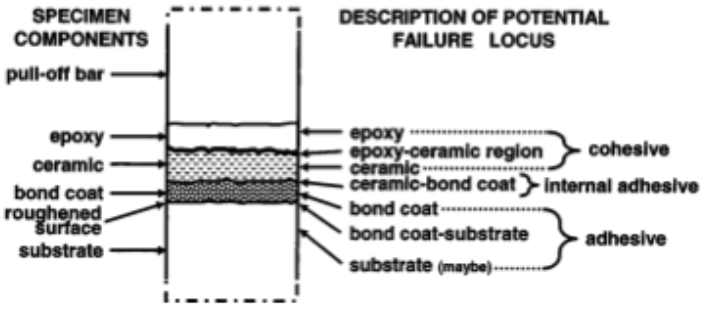

FIG. 3 Nomenclature of Specimen Components and Classification of Failure Locii

10. Report

10.1 The report shall include the following:

10.1.1 Coating material or manufacturer's designation technique used to apply the coating, including type of thermal spray equipment, and spray parameters.

10.1.2 Final coating thickness and statement of whether surface is finished or as-sprayed.

10.1.3 Substrate material.

10.1.4 Description of surface preparation of substrate.

10.1.5 Name or description of bonding agent and details of bonding procedure if different from manufacturer's instructions.

10.1.6 Number of thermal spray specimens and number of specimens tested.

10.1.7 The adhesion or cohesion strength of each specimen tested.

10.1.8 Average adhesion and cohesion strength, and the maximum and minimum values, in pounds per square inch (or pascals).

10.1.9 Description of failure, including statement of whether failure occurred at the coating-substrate interface, in the coating, in the bonding agent, or a combination of these. For multilayered coatings, an internal adhesion failure also must be indicated if it is present. Fig. 3 diagrams the possible modes of failure.

10.1.10 Adhesion strength of the bonding agent in the test specimen without a thermal spray coating.

11. Precision and Bias

11.1 No justifiable statements can be made regarding the precision and bias of this test method because it evaluates coatings that exhibit brittle fracture, an unpredictable characteristic.

11.2 This test method is applicable to a wide variety of materials with different characteristics.

11.3 Since design, base metal composition, fabrication, and processing, as well as thermal spraying the coating, will give rise to variables in adherence, each application of this test method should have tolerances and interpretation of adherence set and agreed upon between the purchaser and the manufacturer.

12. Keywords

12.1 adhesion strength; cohesion strength; fracture locus; thermal spray coatings

ANNEX

(Mandatory Information)

A1. ADHESIVE BONDING AGENTS FOR ATTACHMENT OF LOADING FIXTURE TO THERMAL SPRAY COATINGS

A1.1 The following adhesive is recommended for attaching the loading fixture to thermal spray coatings that are primarily metallic or that have a metal matrix. It is not recommended for thermal spray oxide or other porous ceramic coatings because of the possibility of excessive penetration into the coating. This is a two-part mix that is cured at 300°F (149°C) for 1 h. When the adhesive is new, typical adherence strength to thermal spray coatings may range up to approximately 8000 psi (55 MPa) depending on the coating material.

A1.1.1 CONAP 1222, manufactured by CONAP Inc., 184 E. Union St., Allegheny, NY 14706.

A1.2 The following adhesives are recommended for attaching the loading fixture to thermal spray coatings of any type, ceramic or metallic. These are two-part mixes that should be cured at room temperature when used for this test method. When the adhesive is new, typical adherence strength to thermal spray coatings may range up to approximately 4000 psi (28 MPa) depending on the coating material.

A1.2.1 Bondmaster M666 or M777, manufactured by Pittsburgh Plate Glass Co., Adhesive Products Div., 225 Belleville Ave., Bloomfield, NJ 07003 (M777 may be easier to use as it may be more viscous than M666).

A1.2.2 Epon 911F, manufactured by Shell Chemical Co., Adhesives Dept., P.O. Box 831, Pittsburgh, CA 94565.

A1.2.3 Armstrong A-12, manufactured by Armstrong Products Co., Argonne Rd., Warsaw, IN 46580.

A1.2.4 Hysol XA7-H368 Grey, manufactured by Hysol Inc., Olean, NY 14760.

APPENDIX

X1. ALTERNATIVE SUBSTRATE AND FIXTURE ARRANGEMENT

X1.1 See Fig. X1.1 for an alternative substrate and fixture arrangement that has proved cost effective and simple.

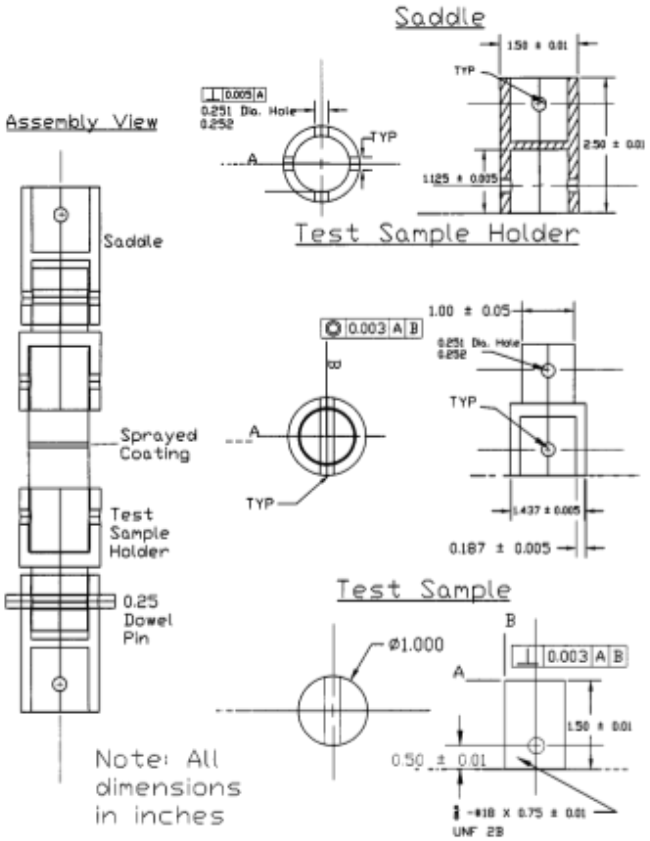

FIG. X1.1 Alternative Load Train Geometry for Test Assembly

BIBLIOGRAPHY

(1) F. J. Hermanek, "Determining the Adhesive and Cohesive Strengths of Thin Thermally Sprayed Coatings," *Welding J.*, Vol 57, 1978, pp. 31–35.

(2) P. Ostojic and C. C. Berndt, "Variability in Strength of Thermally Sprayed Coatings," *J. Surf. Coat. Tech.*, Vol 34, 1988, pp. 43–50.

(3) C. C. Berndt, "Tensile Adhesion Testing Methodology for Thermally Sprayed Coatings," *ASM J.Mater.Eng.*, Vol. 12, No. 2, 1990, pp. 151–160.

(4) W. Han, E. F. Rybicki, and J. R. Shadley, "An Improved Specimen Geometry for ASTM C 633–79 to Estimate Bonds Strengths of Thermal Spray Coatings," *J. Thermal Spray Technology*, Vol. 2, No. 2, 1993, pp. 145–150.

(5) C. K. Lin and C. C. Berndt, "Measurement and Analysis of Adhesion Strength for Thermally Sprayed Coatings," *J. Thermal Spray Technology*, Vol. 3, No. 1, 1994, pp. 75–104.

(6) D. J. Greving, J. R. Shadley, and E. F. Rybicki, "Effects of Coating Thickness and Residual Stresses on the Bond Strength of ASTM C 633–79 Thermal Spray Coating Test Specimens," *J. Thermal Spray Technology*, Vol. 3, No. 4, 1994, pp. 371–378.

Appendix C - Adhesion Test Sample Holder

In order to spray multiple samples, a custom made holder was designed and built. The technical drawing is shown in Figure C.1. The device is machined from a solid aluminium block with a capacity of 5 samples. Each sample is held in position by the round holes at the bottom of the block. The samples are locked in position by passing a 1/4" diameter rod through all of them which is forced down by two 3/8" diameter screws located at each end of the block.

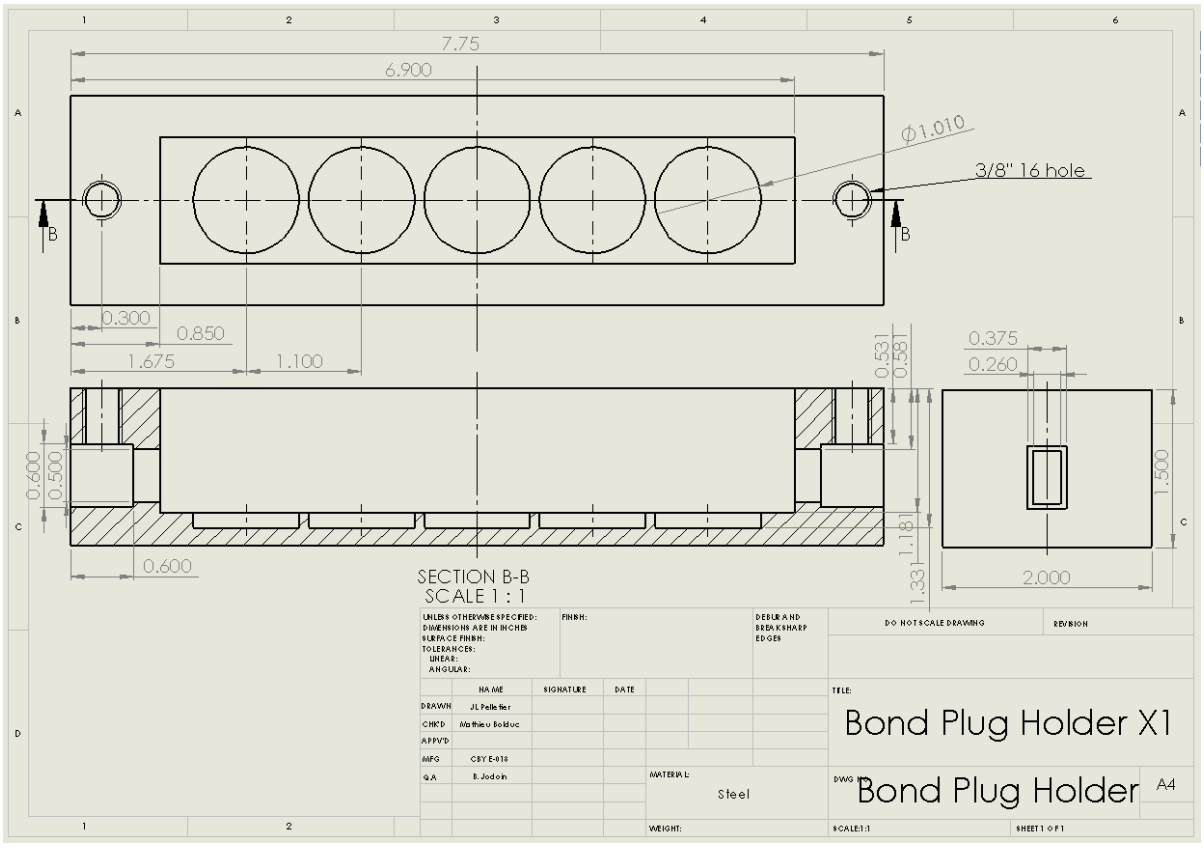

Figure C.1 Technical drawing of the adhesion test sample holder

Appendix D - Technical Drawings of Gluing Device

This apparatus has been specially design to glue adhesion test samples. The main consideration about this device is that the samples have to be perfectly aligned. Overlooking the alignment between the two samples will have an effect on the adhesion values. Hence, to ensure minimal movement during the manipulations, the device was made from thick steel plates, 1/2" rods and bolts. In addition, the device was build with an alignment block rather than just bolts, reducing the misalignment that could have been caused by the tolerances of the threads. Extra nuts are used to ensure the bold stay tightened at the specific torque (3 Nm). The overview of the 3D model made using Solidworks and final result are shown in Figure D.1. The technical drawings of the major components are shown in the Figures D.2 through D.6.

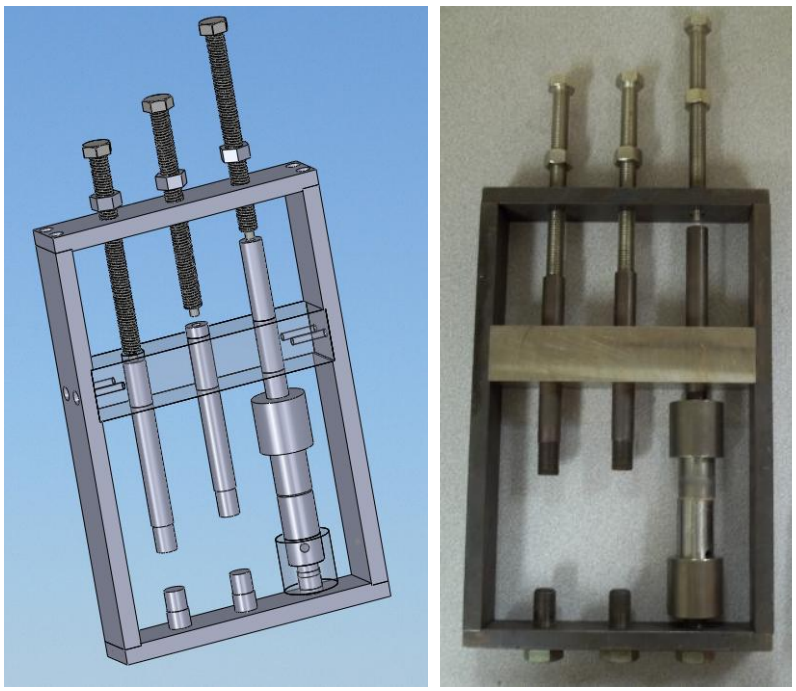

Figure D.1 (a) 3D model of the gluing device and (b) machined and assembled device

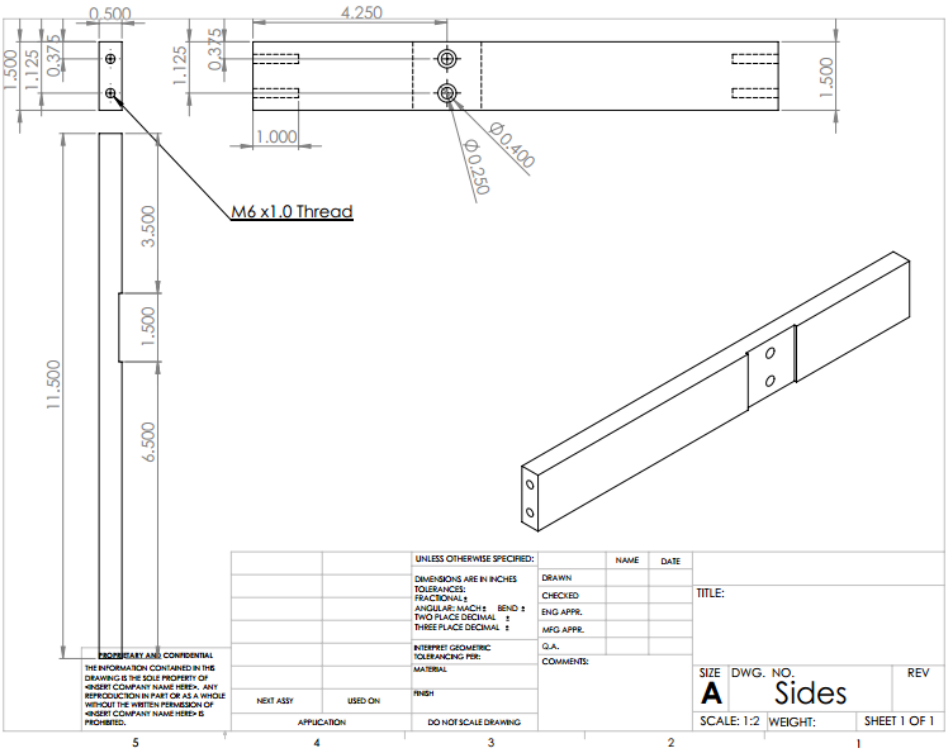

Figure D.2 Side plates

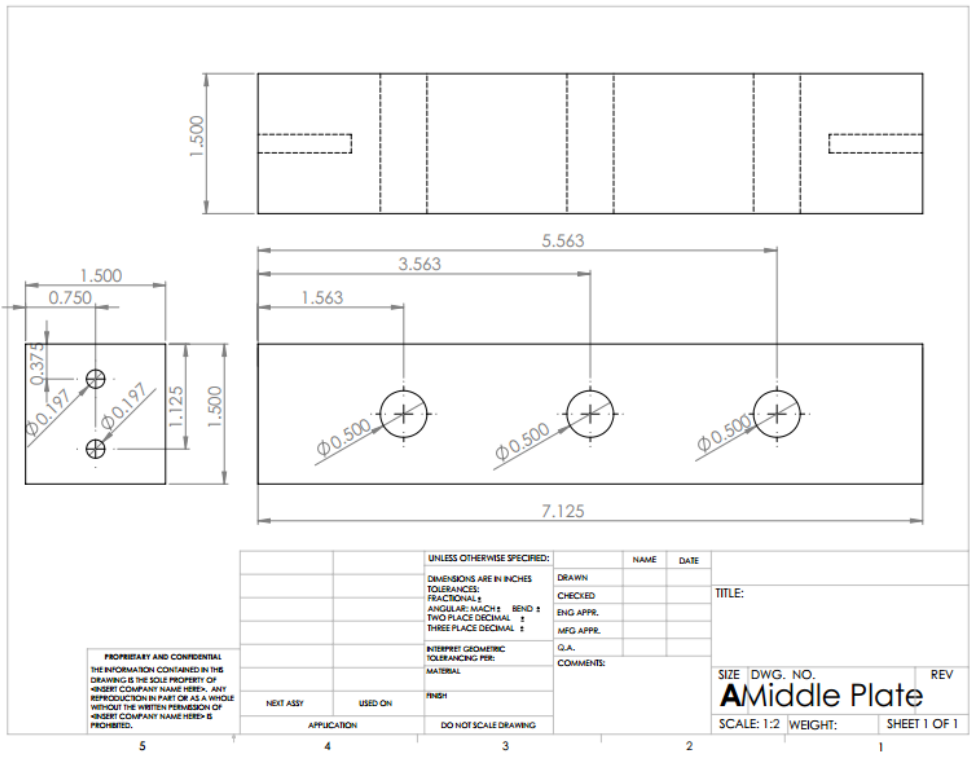

Figure D.3 Middle alignment block

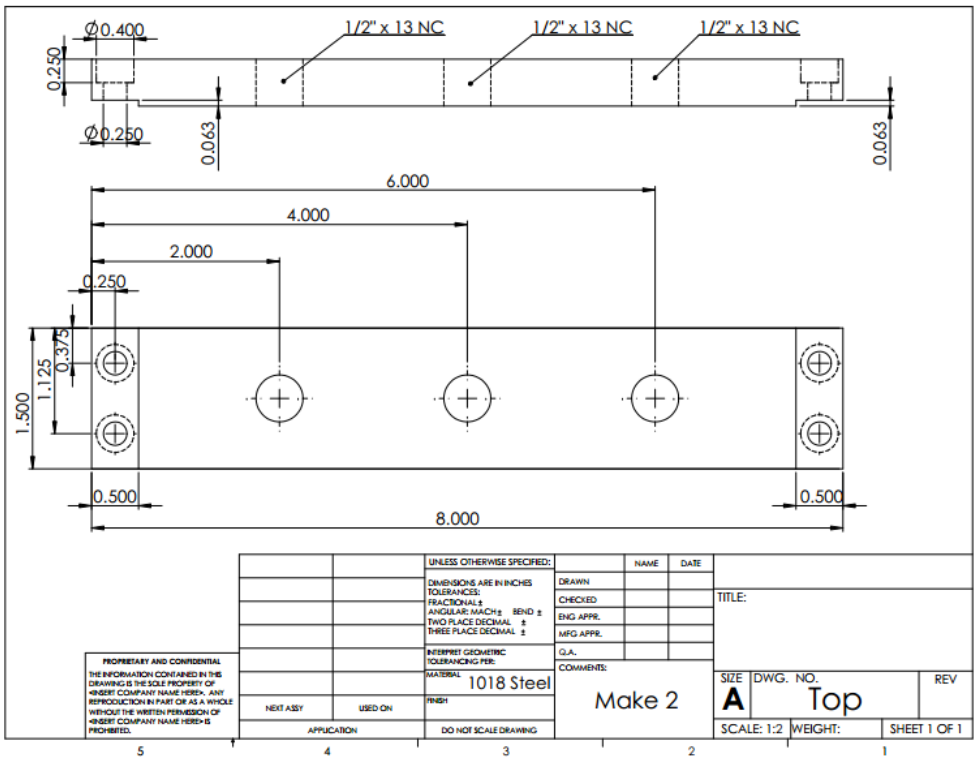

Figure D.4 Top and bottom plates

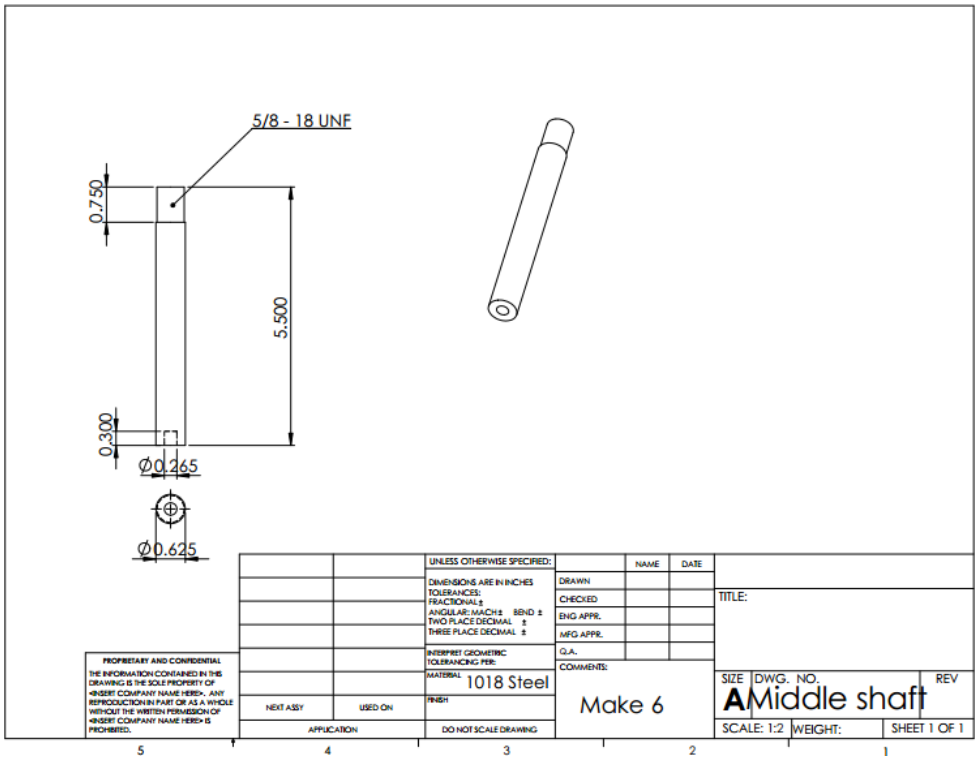

Figure D.5 Center rods

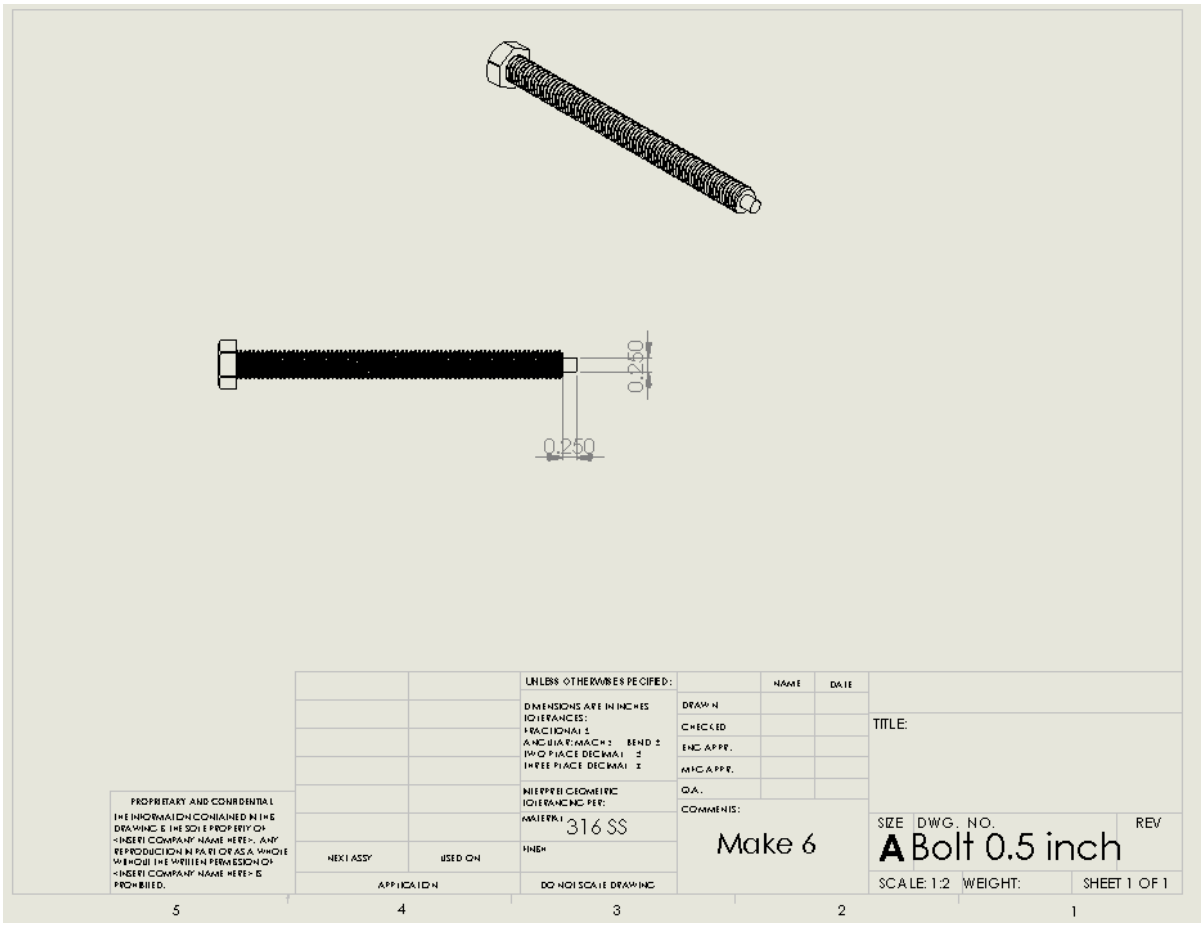

Figure D.6 Bolts

Appendix E - Wear Equipment

The wear equipment used throughout this study was build previously by other students and the research assistant. Over many years of utilisation, some parts of the equipment (weight rod and its holder) started to wear and to a point that they needed replacement. The considerations for replacement were the following: low machining costs, low material costs, high wear resistance, minimum tolerances allowable.

During wear tests, the substrate is displaced over a short distance in one direction before being stopped and displaced in the other direction. Due to this alternating motion, friction and tolerances between the parts, the ball will tend to stay at the same position until the shaft reaches the maximal position in the other direction. The difference between these two positions, called play, can be minimized by: increasing the length of the support and reducing the distance between the support and the substrate. A schematic of the different cases is shown in Figure E.1.

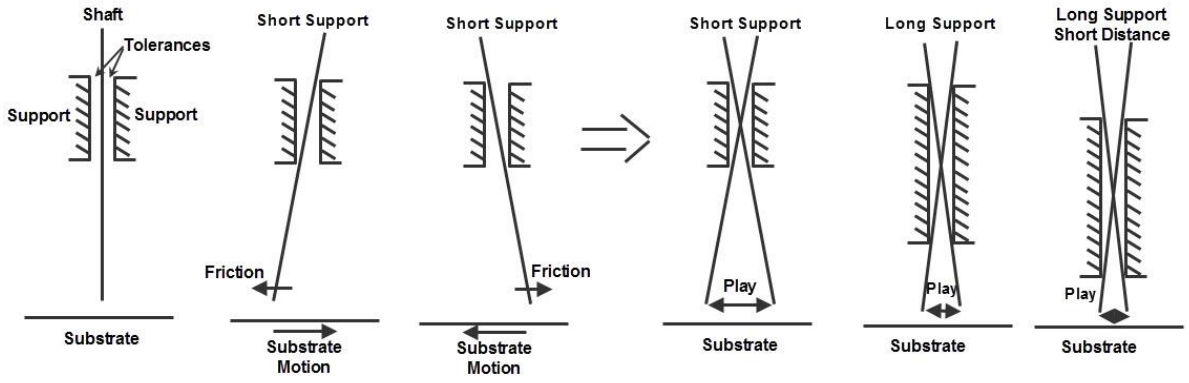

Figure E.1 Schematic of the different cases showing the effect of support length and distance between substrate and support on the play

Increasing the length of the support reduces and angle of the shaft for the same tolerance, which leads to lower play. The play is also reduced by decreasing the distance between the end of the support and the substrate. In the latter case, the angle of the shaft is constant and the play becomes a function of the distance with the part.

Therefore, it was determined that the shaft support had to be extended to be closer to the substrate and also longer to minimized the angle created by tolerances between the parts.

The design was also optimized to require a minimum machining, number of parts and have easy access for ball replacement. The design had to be able to prohibit the ball from turning on itself, as required in the ASTM G133 standard. The final concept, is shown in Figure E.2.

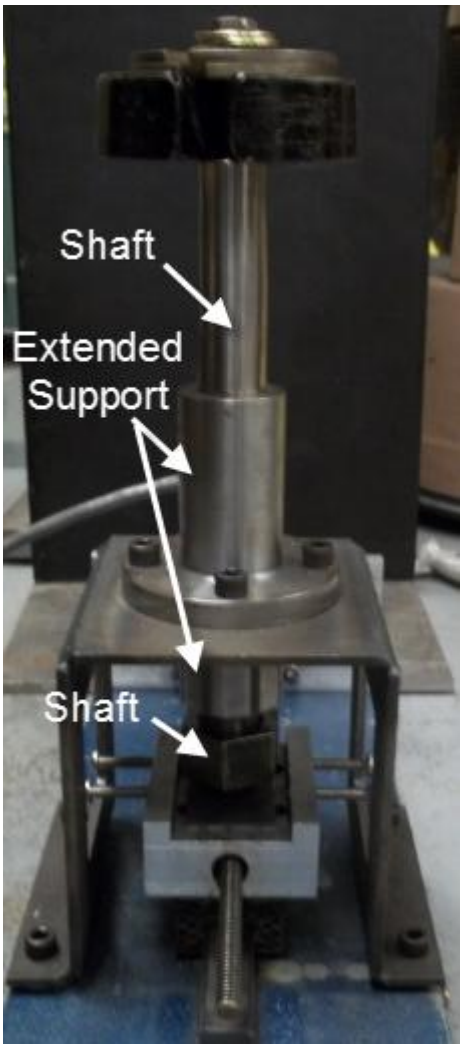

Figure E.2 Photograph of the wear equipment: (a) Overview and (b) Substrate holder close-up

The shaft was purchased as a precision ground steel rod with low variation in diameter (0.0005"). To minimize the tolerances between the shaft and the support, the support was drilled to a diameter close to the shaft diameter and then finished to the desired dimension using a reamer. The sides of the shaft were flattened to allow the use of a wrench. The weight is held simply by a bolt screwed in the top of the shaft. The ball is kept in position

with a special nut designed to let out the maximum of the 3/8" ball to maximized the distance between the nut and the substrate. This will help to avoid contact of the nut with the coating in case of high wear. The technical drawings of these components are shown in Figure E.3, E.4 and E.5.

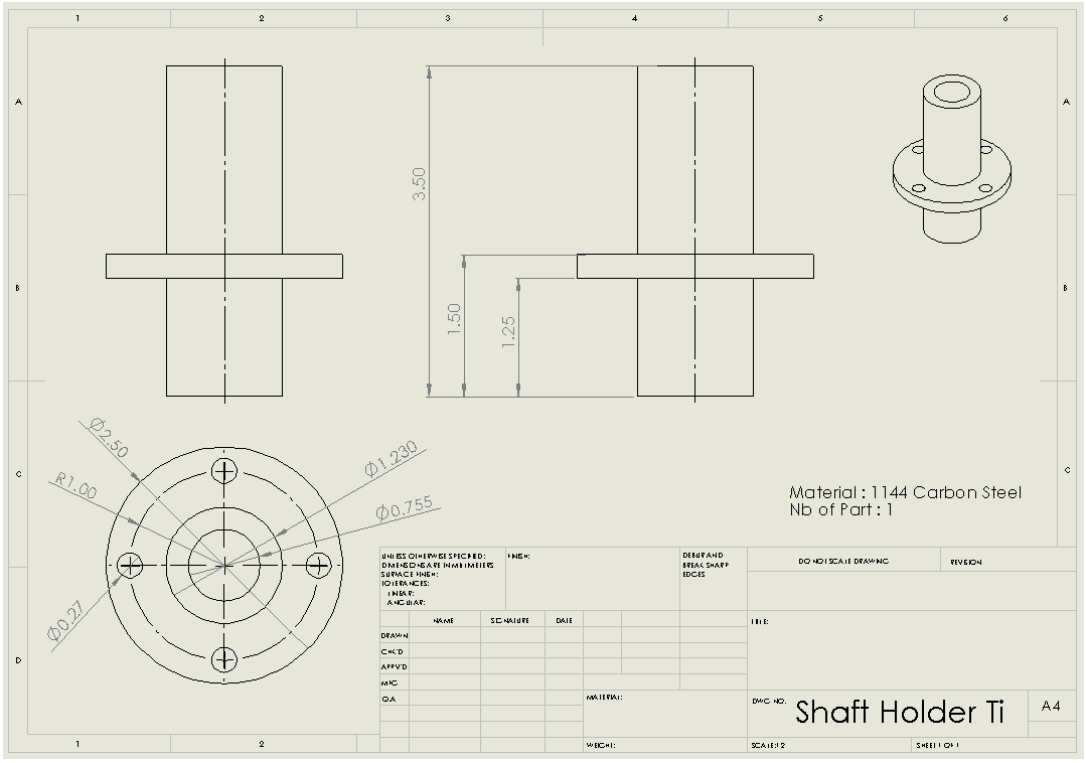

Figure E.3 Technical drawing of the shaft support

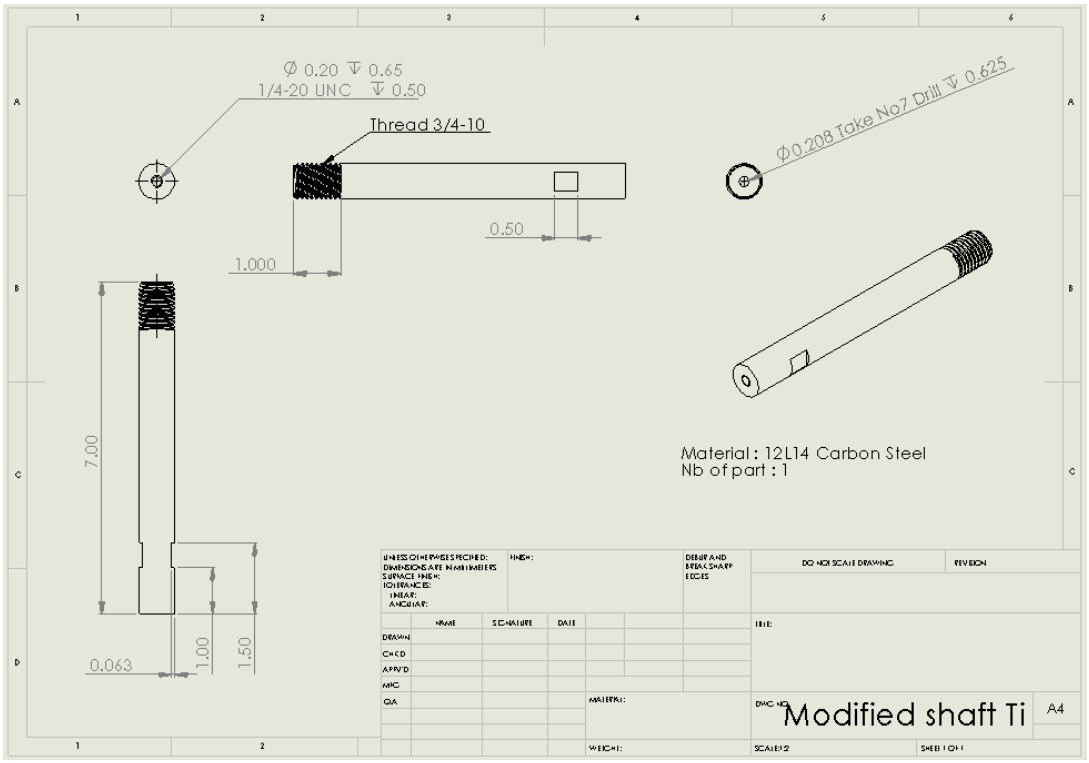

Figure E.4 Technical drawing of the shaft

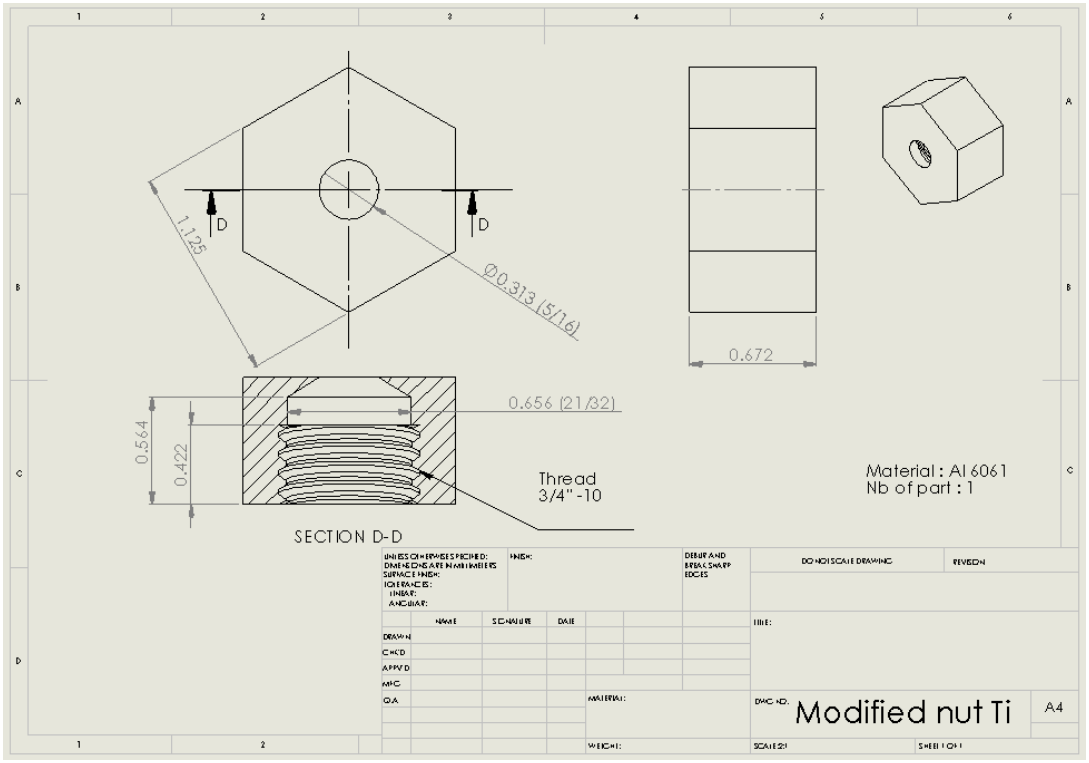

Figure E.5 Technical drawing of the ball holding nut

Appendix F - LPCS and PGDS Test plans

LPCS Test Plans Evolution

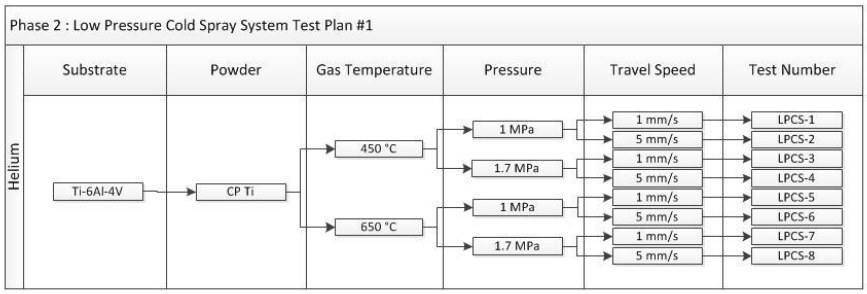

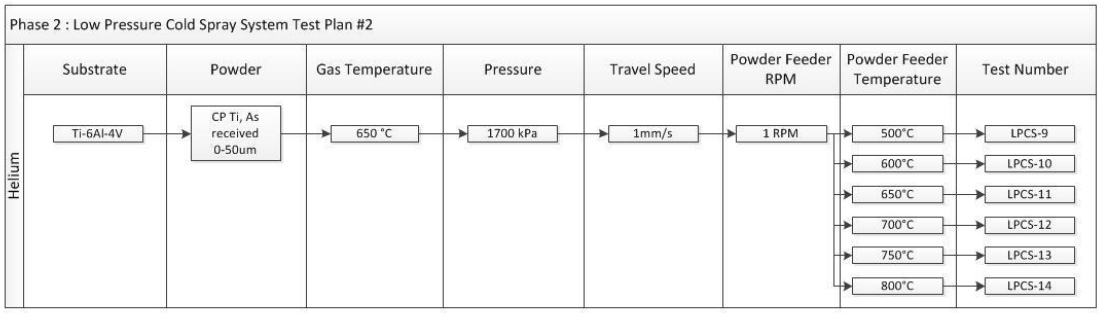

PGDS Test Plans Evolution

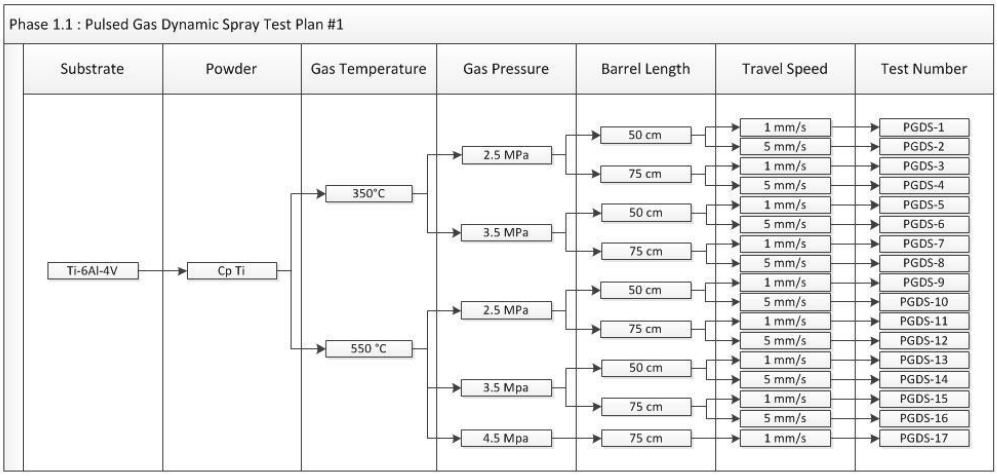

Following these experiments, few tests were performed using a barrel length of 100cm before the next test plan was performed.

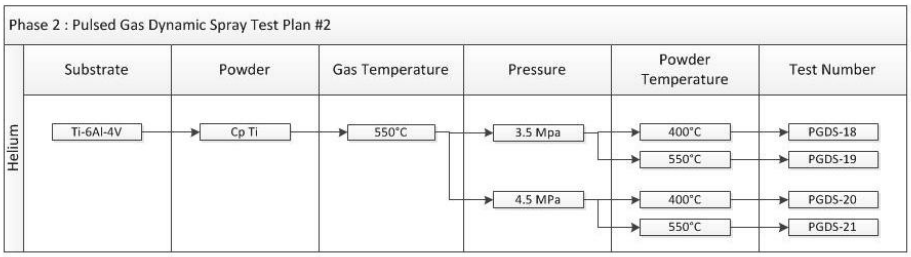

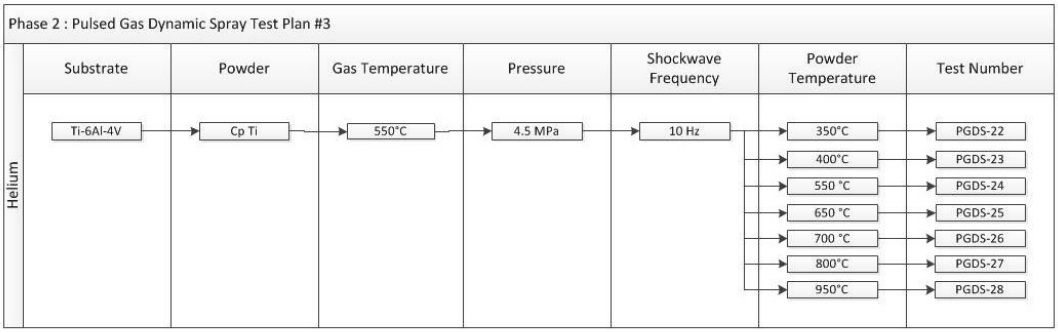

At this point, the commercial PGDS system from CenterLine was received and tests were conducted using higher gas temperatures (600 and 700°C) due to the high power of the new gas heater (14 kW). Tests were also conducted to verify that the new system produces coatings with similar microstructure than the old system using the same parameters. The next experimentations were conducted after this was confirmed.

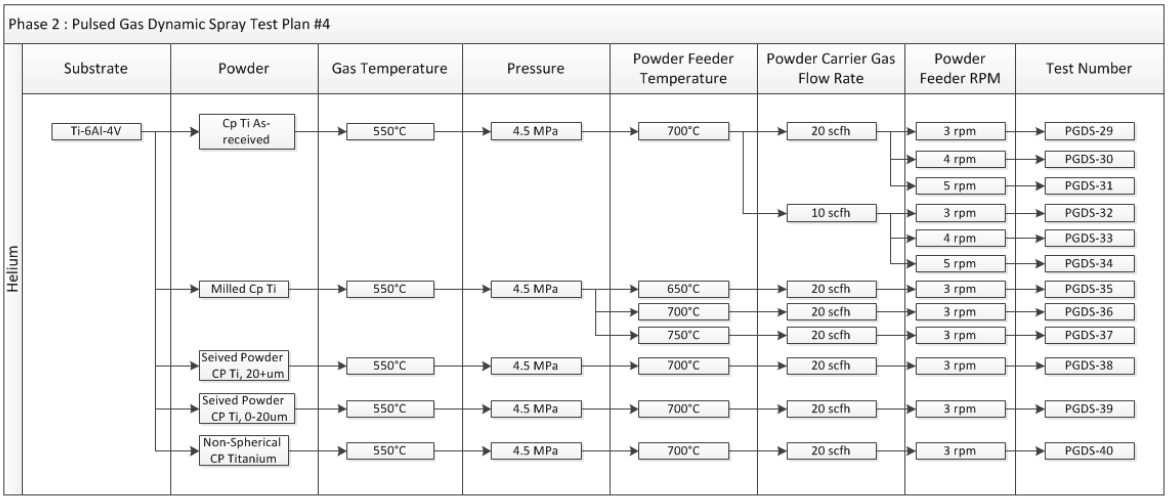
Phase 2 : Pulsed Gas Dynamic Spray Test Plan #4
Helium
Substrate
Powder
Gas Temperature
Pressure
Powder Feeder Temperature
Powder Carrier Gas Flow Rate
Powder Feeder RPM
Test Number
Ti-6Al-4V
Cp Ti As-received
550°C
4.5 MPa
700°C
20 scfh
3 rpm
PGDS-29
4 rpm
PGDS-30
5 rpm
PGDS-31
10 scfh
3 rpm
PGDS-32
4 rpm
PGDS-33
5 rpm
PGDS-34
Milled Cp Ti
550°C
4.5 MPa
650°C
20 scfh
3 rpm
PGDS-35
700°C
20 scfh
3 rpm
PGDS-36
750°C
20 scfh
3 rpm
PGDS-37
Seived Powder CP Ti, 20+um
550°C
4.5 MPa
700°C
20 scfh
3 rpm
PGDS-38
Seived Powder CP Ti, 0-20um
550°C
4.5 MPa
700°C
20 scfh
3 rpm
PGDS-39
Non-Spherical CP Titanium
550°C
4.5 MPa
700°C
20 scfh
3 rpm
PGDS-40

Appendix G - LPCS Parameter Optimization

This appendix includes the complete list of parameters for each of the different parameter optimization phase of the LPCS system. The parameter being optimized is shown in bold character.

Section 6.1.3.1 Gas-related Parameter Optimization

Table G.1 Parameters used for Table 6.3 Effect of nozzle inlet pressure on LPCS coating porosity

Category	Parameters Description	Preliminary Value
Gas	Nature	Helium
	Temperature	450°C
	Pressure	**1.0 and 1.7 MPa**
Powder	Material Nature	CP titanium
	Morphology	Spherical
	Size Distribution	0-50 μm
	Preheating Temperature	None
	Powder Feed Rate	2.0 g/min
	Powder Carrier Gas Nature	Helium
	Powder Carrier Gas Flow Rate	12.5 scfh
Substrate	Substrate Material Nature	Ti-6Al-4V
	Substrate Preparation	Acetone Cleaned/Degreased
	Substrate Temperature	Room Temperature
	Substrate Travel Speed	1 mm/s
	Gun Step Size	3 mm
	Substrate Stand-Off Distance	10 mm
Nozzle	Throat Diameter	2 mm
	Nozzle Geometry	Straight hydro formed
	Expansion/Area Ratio	10
	Nozzle Expansion Length	120 mm

Table G.2 Parameters used for Table 6.4 Effect of nozzle inlet temperature on LPCS coating porosity

Category	Parameters Description	Preliminary Value
Gas	Nature	Helium
	Temperature	**450°C and 650°C**
	Pressure	1.7MPa
Powder	Material Nature	CP titanium
	Morphology	Spherical
	Size Distribution	0-50 μm
	Preheating Temperature	None
	Powder Feed Rate	2.0 g/min
	Powder Carrier Gas Nature	Helium
	Powder Carrier Gas Flow Rate	12.5 scfh
Substrate	Substrate Material Nature	Ti-6Al-4V
	Substrate Preparation	Acetone Cleaned/Degreased
	Substrate Temperature	Room Temperature
	Substrate Travel Speed	1 mm/s
	Gun Step Size	3 mm
	Substrate Stand-Off Distance	10 mm
Nozzle	Throat Diameter	2 mm
	Nozzle Geometry	Straight hydro formed
	Expansion/Area Ratio	10
	Nozzle Expansion Length	120 mm

Section 6.1.1.2 Powder-related Parameters

Table G.3 Parameters used for Table 6.5 Effect of powder preheating temperature on LPCS coating porosity, microhardness and thickness

Category	Parameters Description	Preliminary Value
Gas	Nature	Helium
	Temperature	650°C
	Pressure	1.7MPa
Powder	Material Nature	CP titanium
	Morphology	Spherical
	Size Distribution	0-50 μm
	Preheating Temperature	**500°C to 800°C**
	Powder Feed Rate	2.0 g/min
	Powder Carrier Gas Nature	Helium
	Powder Carrier Gas Flow Rate	12.5 scfh
Substrate	Substrate Material Nature	Ti-6Al-4V
	Substrate Preparation	Acetone Cleaned/Degreased
	Substrate Temperature	Room Temperature
	Substrate Travel Speed	1 mm/s
	Gun Step Size	3 mm
	Substrate Stand-Off Distance	10 mm
Nozzle	Throat Diameter	2 mm
	Nozzle Geometry	Straight hydro formed
	Expansion/Area Ratio	10
	Nozzle Expansion Length	120 mm

Section 6.1.1.3 Substrate-related Parameters

Table G.4 Parameters used for Table 6.6 Effect of travel speed on LPCS coating porosity

Category	Parameters Description	Preliminary Value
Gas	Nature	Helium
	Temperature	650°C
	Pressure	1.7MPa
Powder	Material Nature	CP titanium
	Morphology	Spherical
	Size Distribution	0-50 μm
	Preheating Temperature	700°C
	Powder Feed Rate	2.0 g/min
	Powder Carrier Gas Nature	Helium
	Powder Carrier Gas Flow Rate	12.5 scfh
Substrate	Substrate Material Nature	Ti-6Al-4V
	Substrate Preparation	Acetone Cleaned/Degreased
	Substrate Temperature	Room Temperature
	Substrate Travel Speed	**1 mm/s and 5 mm/s**
	Gun Step Size	3 mm
	Substrate Stand-Off Distance	10 mm
Nozzle	Throat Diameter	2 mm
	Nozzle Geometry	Straight hydro formed
	Expansion/Area Ratio	10
	Nozzle Expansion Length	120 mm

Table G.5 Parameters used for Table 6.7 Effect of spray pattern on LPCS coating adhesion strength

Category	Parameters Description	Preliminary Value
Gas	Nature	Helium
	Temperature	650°C
	Pressure	1.7MPa
Powder	Material Nature	CP titanium
	Morphology	Spherical
	Size Distribution	0-50 μm
	Preheating Temperature	700°C
	Powder Feed Rate	2.0 g/min
	Powder Carrier Gas Nature	Helium
	Powder Carrier Gas Flow Rate	12.5 scfh
Substrate	Substrate Material Nature	Ti-6Al-4V
	Substrate Preparation	Acetone Cleaned/Degreased
	Substrate Temperature	Room Temperature
	Substrate Travel Speed	1 mm/s
	Gun Step Size	3 mm
	Substrate Stand-Off Distance	10 mm
Nozzle	Throat Diameter	2 mm
	Nozzle Geometry	Straight hydro formed
	Expansion/Area Ratio	10
	Nozzle Expansion Length	120 mm

Appendix H - PGDS Parameter Optimization

This appendix includes the complete list of parameters for each of the different parameter optimization phase of the PGDS system. The parameter being optimized is shown in bold character.

Section 6.2.2.1 Gas-related Parameter Optimization

Table H.1 Parameters used for Table 6.10 Effect of gas stagnation pressure on PGDS coating porosity

Category	Parameter Description	Preliminary Value
Gas	Nature	Helium
	Temperature	350°C
	Pressure	**2.5, 3.5 and 4.5 MPa**
Powder	Material Nature	CP titanium
	Morphology	Spherical
	Size Distribution	0-50μm
	Preheating Temperature	350°C
	Powder Feed Rate	7.0 g/min
	Powder Carrier Gas Nature	Helium
	Powder Carrier Gas Flow Rate	20 scfh
Substrate	Substrate Material Nature	Ti-6Al-4V
	Substrate Preparation	Acetone Cleaned/Degreased
	Substrate Temperature	Room Temperature
	Substrate Travel Speed	1 mm/s
	Step Size	2 mm
	Gun Stand-Off Distance	10 mm
Valve	Valve Frequency	10 Hz
	Barrel Length	75 cm
	Valve Opening Time	13 ms
	# Slots in disk	3

Table H.2 Parameters used for Table 6.11 Effect of gas heater temperature on PGDS coating porosity and microhardness

Category	Parameter Description	Preliminary Value
Gas	Nature	Helium
	Temperature	**350, 550, 600 and 700°C**
	Pressure	4.5 MPa
Powder	Material Nature	CP titanium
	Morphology	Spherical
	Size Distribution	0-50µm
	Preheating Temperature	700°C
	Powder Feed Rate	7.0 g/min
	Powder Carrier Gas Nature	Helium
	Powder Carrier Gas Flow Rate	20 scfh
Substrate	Substrate Material Nature	Ti-6Al-4V
	Substrate Preparation	Acetone Cleaned/Degreased
	Substrate Temperature	Preheating before spray
	Substrate Travel Speed	1 mm/s
	Step Size	2 mm
	Gun Stand-Off Distance	10 mm
Valve	Valve Frequency	10 Hz
	Barrel Length	75 cm
	Valve Opening Time	13 ms
	# Slots in disk	3

Section 6.2.2.2 Powder-related Parameter Optimization

Table H.3 Parameters used for Table 6.12 Effect of powder feed rate on PGDS coating porosity, microhardness and thickness

Category	Parameter Description	Preliminary Value
Gas	Nature	Helium
	Temperature	550°C
	Pressure	4.5 MPa
Powder	Material Nature	CP titanium
	Morphology	Spherical
	Size Distribution	0-50μm
	Preheating Temperature	700°C
	Powder Feed Rate	**7.0, 8.3 and 9.6 g/min**
	Powder Carrier Gas Nature	Helium
	Powder Carrier Gas Flow Rate	20 scfh
Substrate	Substrate Material Nature	Ti-6Al-4V
	Substrate Preparation	Acetone Cleaned/Degreased
	Substrate Temperature	Preheating before spray
	Substrate Travel Speed	1 mm/s
	Step Size	2 mm
	Gun Stand-Off Distance	10 mm
Valve	Valve Frequency	10 Hz
	Barrel Length	75 cm
	Valve Opening Time	13 ms
	# Slots in disk	3

Table H.4 Parameters used for Table 6.13 Effect of powder carrier gas flow rate on PGDS coating porosity and microhardness

Category	Parameter Description	Preliminary Value
Gas	Nature	Helium
	Temperature	550°C
	Pressure	4.5 MPa
Powder	Material Nature	CP titanium
	Morphology	Spherical
	Size Distribution	0-50µm
	Preheating Temperature	700°C
	Powder Feed Rate	7.0 g/min
	Powder Carrier Gas Nature	Helium
	Powder Carrier Gas Flow Rate	**10 and 20 scfh**
Substrate	Substrate Material Nature	Ti-6Al-4V
	Substrate Preparation	Acetone Cleaned/Degreased
	Substrate Temperature	Preheating before spray
	Substrate Travel Speed	1 mm/s
	Step Size	2 mm
	Gun Stand-Off Distance	10 mm
Valve	Valve Frequency	10 Hz
	Barrel Length	75 cm
	Valve Opening Time	13 ms
	# Slots in disk	3

Table H.5 Parameters used for Table 6.14 Effect of powder preheating temperature on PGDS coating porosity, microhardness and thickness

Category	Parameter Description	Preliminary Value
Gas	Nature	Helium
	Temperature	550°C
	Pressure	4.5 MPa
Powder	Material Nature	CP titanium
	Morphology	Spherical
	Size Distribution	0-50µm
	Preheating Temperature	**350 to 950°C**
	Powder Feed Rate	7.0 g/min
	Powder Carrier Gas Nature	Helium
	Powder Carrier Gas Flow Rate	20 scfh
Substrate	Substrate Material Nature	Ti-6Al-4V
	Substrate Preparation	Acetone Cleaned/Degreased
	Substrate Temperature	Preheating before spray
	Substrate Travel Speed	1 mm/s
	Step Size	2 mm
	Gun Stand-Off Distance	10 mm
Valve	Valve Frequency	10 Hz
	Barrel Length	75 cm
	Valve Opening Time	13 ms
	# Slots in disk	3

Section 6.2.2.4Valve-related Parameter Optimization

Table H.6 Parameters used for Figure 6.7 Effect of powder morphology on PGDS coating porosity and microhardness

Category	Parameter Description	Preliminary Value
Gas	Nature	Helium
	Temperature	550°C
	Pressure	4.5 MPa
Powder	Material Nature	CP titanium
	Morphology	Spherical
	Size Distribution	**Variable**
	Preheating Temperature	700°C
	Powder Feed Rate	7.0 g/min
	Powder Carrier Gas Nature	Helium
	Powder Carrier Gas Flow Rate	20 scfh
Substrate	Substrate Material Nature	Ti-6Al-4V
	Substrate Preparation	Acetone Cleaned/Degreased
	Substrate Temperature	Preheating before spray
	Substrate Travel Speed	1 mm/s
	Step Size	2 mm
	Gun Stand-Off Distance	10 mm
Valve	Valve Frequency	10 Hz
	Barrel Length	75 cm
	Valve Opening Time	13 ms
	# Slots in disk	3

Table H.7 Parameters used for Table 6.15 Effect of barrel length on PGDS coating porosity

Category	Parameter Description	Preliminary Value
Gas	Nature	Helium
	Temperature	550°C
	Pressure	3.5 MPa
Powder	Material Nature	CP titanium
	Morphology	Spherical
	Size Distribution	0-50µm
	Preheating Temperature	350°C
	Powder Feed Rate	7.0 g/min
	Powder Carrier Gas Nature	Helium
	Powder Carrier Gas Flow Rate	20 scfh
Substrate	Substrate Material Nature	Ti-6Al-4V
	Substrate Preparation	Acetone Cleaned/Degreased
	Substrate Temperature	Room Temperature
	Substrate Travel Speed	1 mm/s
	Step Size	2 mm
	Gun Stand-Off Distance	10 mm
Valve	Valve Frequency	10 Hz
	Barrel Length	**50, 75 and 100 cm**
	Valve Opening Time	13 ms
	# Slots in disk	3

Appendix I - LPCS Preliminary Test Using Nitrogen

The first deposition trials for CP titanium powder using the LPCS process were performed using nitrogen as the main processing gas. The parameters were chosen based on the literature and on the knowledge in the laboratory that has accumulated over years of cold spraying. The parameters used for these first trials, using nitrogen as the driver, are shown in the Table I.1. Unfortunately, these trials did not produce any coating. However, the powder heater had not been designed at the time that they were performed. With the use of the powder preheater, the enhanced ductility of the powder could lead to the formation of a coating. Now that this new feature is available, new trials could be performed using nitrogen.

Table I.1 Preliminary trials for CP titanium deposition using LPCS technique and nitrogen gas

Category	Parameters Description	Preliminary Value
Gas	Nature	Nitrogen
	Temperature	350°C
	Pressure	1.0 MPa
Powder	Material Nature	CP titanium
	Morphology	Spherical
	Size Distribution	0-50 μm
	Preheating Temperature	None
	Powder Feed Rate	2.0 g/min
	Powder Carrier Gas Nature	Nitrogen
	Powder Carrier Gas Flow Rate	12.5 scfh
Substrate	Substrate Material Nature	Ti-6Al-4V
	Substrate Preparation	Acetone Cleaned/Degreased
	Substrate Temperature	Room Temperature
	Substrate Travel Speed	1 mm/s
	Gun Step Size	None (single line)
	Substrate Stand-Off Distance	10 mm
Nozzle	Throat Diameter	2 mm
	Nozzle Geometry	Straight hydro formed
	Expansion/Area Ratio	10
	Nozzle Expansion Length	120 mm